Hydrogen energy storage in porous geological formations

–

Investigation of storage dimensioning, induced effects and monitoring methods

Dissertation
zur Erlangung des Doktorgrades
der Mathematisch-Naturwissenschaftlichen Fakultät
der Christian-Albrechts-Universität zu Kiel

vorgelegt von
Wolf Tilmann Pfeiffer
Kiel, März 2017

Erster Gutacher:	Prof. Dr. rer. nat. Sebastian Bauer
Zweiter Gutachter:	Prof. Dr.-Ing. Olaf Kolditz
Tag der mündlichen Prüfung:	04.05.2017
Zum Druck genehmigt:	04.05.2017

gez. Prof. Dr. rer. nat. Natascha Oppelt, Dekanin

EIDESSTATTLICHE ERKLÄRUNG

Hiermit versichere ich eidesstattlich, dass die vorliegende Arbeit, abgesehen von der Beratung durch den Betreuer, nach Inhalt und Form selbstständig und ohne unzulässige Hilfsmittel von mir angefertigt wurde.

Die vorliegende Arbeit hat weder in Teilen noch im Ganzen an anderer Stelle im Rahmen eines Prüfungsverfahrens vorgelegen und wurde nicht veröffentlicht oder zur Veröffentlichung eingereicht.

Weiterhin versichere ich, dass die Arbeit unter Einhaltung der Regeln guter wissenschaftlicher Praxis der Deutschen Forschungsgemeinschaft angefertigt wurde.

Kiel, 16.03.2017 Wolf Tilmann Pfeiffer

ABSTRACT

Power production from renewable sources is fluctuating, governed by the availability of the sources such as wind or solar radiation. Increasing the share of renewable sources can therefore lead to shortages in power production. Large-scale energy storage in porous geological formations, e.g. using hydrogen (H_2), produced during periods of ample power supply, could help mitigate offsets between supply and demand. In this thesis, hydrogen energy storage in porous geological formations is investigated using numerical scenario simulations with emphases on the quantification of storage dimensions, on induced hydraulic and thermal effects and on geophysical monitoring techniques.

For this end, a coupling approach for the scientific open source simulator OpenGeoSys and the proprietary reservoir simulator ECLIPSE is developed. The coupled simulator combines the multiphase-multicomponent flow and transport of ECLIPSE with the heat and geochemical reactive transport of OpenGeoSys. The implementation imposes no limitations regarding the considered components, thus providing a flexible platform. Furthermore, the Joule-Thomson effect is implemented in OpenGeoSys for gases consisting of N_2, O_2, H_2, CO_2 and CH_4. All implementations are successfully validated against reference simulations or data.

For the assessment of potential storage dimensions and induced hydraulic and thermal effects, a hypothetical storage operation is simulated at an existing structure in northern Germany. 25 realistic and heterogeneous parameter distributions are generated using a facies modelling approach. It is found that the simulated storage site can supply around 162 to 300 MW during a week-long production phase using 5 storage wells, depending on the distribution of the reservoir properties. Peak power output is higher, so that the amount of H_2 withdrawn during the production phase corresponds to about 41 000 to 55 900 MWh of energy. Increasing the volume of gas in place and adding storage wells results in a higher storage performance. Using 11 horizontal storage wells, the storage site can provide a continuous power output of 744 to 1147 MW in one week. The volume of H_2 withdrawn corresponds to an energy output of 210 400 to 234 300 MWh per storage cycle.

The distribution of the gas phase strongly depends on the reservoir heterogeneity and the geometry of the storage formation. In the simulated scenario, the gas phase is elongated, extending up to 7 km in one direction and less than 750 m perpendicular to that. The induced pressure perturbations reach further, with pressure increasing less than 3 bars 5 km from the storage wells. Near the wells, the pressure shows strong fluctuations of more than 10 bars around the initial hydrostatic pressure levels.

The assessment of induced thermal effects show that the Joule-Thomson effect only results in minuscule temperature variations of less than 1 °C during the H_2 storage operation. The primary process inducing thermal effects is the injection temperature of the gas, which is governed largely by the surface installations. Assuming an injection temperature of 50 °C, which is 25 °C above the initial reservoir temperature, results in thermal effects up to 50 m away from the storage wells in lateral direction and slightly less in vertical direction. Like the pressure signal, the cyclic operation of the storage site results in undulating temperature in the near well regions.

In addition to down-hole measurements, geophysical techniques such as seismic waveform inversion (FWI), electrical resistivity tomography (ERT) and gravity methods can be used for site monitoring. The virtual application of these methods to the simulated H_2 storage site shows that FWI and ERT methods can be used to map the gas phase distribution in the heterogeneous formation when using a high spatial density of receivers in a cross well geometry with distances between receivers of around 500 m. Both methods confirm each other. The gravity mapping also indicates anomalies due to the mass changes. However, monitoring the filling state cannot be achieved for the simulated storage with either method.

KURZFASSUNG

Die Stromproduktion aus erneuerbaren Energien unterliegt Schwankungen bedingt durch die variable Verfügbarkeit der Energieträger. Durch einen hohen Anteil von erneuerbaren Energien an der Gesamtproduktion können so Engpässe in der Stromproduktion entstehen, welche durch Energiespeicher ausgeglichen werden müssen. Hierfür kann Wasserstoff, mit Hilfe von Überkapazitäten synthetisiert, als chemischer Energieträger innerhalb von porösen geologischen Formationen gespeichert werden. In der vorliegenden Arbeit werden potentielle Dimensionen einer Wasserstoffspeicherung, die induzierten hydraulischen und thermischen Effekte sowie die Anwendung von geophysikalischen Monitoringmethoden mit Hilfe von numerischen Szenariensimulation untersucht.

Hierfür wurde zunächst eine Modellkopplung für den wissenschaftlichen Open-Source Simulator OpenGeoSys und den proprietären Reservoir-Simulator ECLIPSE (© Schlumberger) entwickelt. Der gekoppelte Simulator kombiniert die Mehrphasen-Mehrkomponenten Strömungssimulation von ECLIPSE mit dem Wärme- und Reaktiven-Transport-Modell von OpenGeoSys. Die Implementierung beinhaltet keine Einschränkungen bezüglich der berücksichtigten Komponenten im simulierten System und stellt somit eine flexible Plattform dar. Zusätzlich wurde das Wärmetransportmodell von OpenGeoSys durch den Joule-Thomson-Effekt für Gase, bestehend aus N_2, O_2, H_2, CO_2 und CH_4, erweitert. Alle vorgenommenen Modellentwicklungen wurden erfolgreich durch Referenzsimulationen oder -datensätze validiert.

Für die Abschätzung von möglichen Speicherdimensionen sowie der induzierten hydraulischen und thermischen Effekte wurde ein hypothetischer Speicherbetrieb, basierend auf einer existierenden geologischen Struktur in Norddeutschland, simuliert. Um die Variabilität der Verteilung geologischer Parameter abzubilden, wurden mit Hilfe eines Faziesmodells 25 realistische und gleich wahrscheinliche Parameterverteilungen erstellt. Der simulierte Wasserstoffspeicher kann, je nach Verteilung der hydraulischen Parameter, während einer einwöchigen Ausspeicherperiode eine Leistung von 162 bis 300 MW über 5 Speicherbrunnen kontinuierlich bereitstellen. Das während der Ausspeicherperiode geförderte H_2-Volumen entspricht dabei einer Energiemenge von 41 000 bis 55 900 MWh. Eine Erhöhung der Speicherkapazität und -leistung ist durch die Verwendung von zusätzlichen Speicherbrunnen sowie einer Vergrößerung des H_2-Volumens im Speicher möglich. So kann durch die Verwendung von 11 horizontalen Speicherbrunnen eine kontinuierliche Ausspeicherleistung von 744 bis 1147 MW über die einwöchige Ausspeicherphase erreicht. Das während dieser Zeit geförderte H_2-Volumen entspricht 210 400 bis 234 300 MWh.

Induzierte hydraulische Effekte ergeben sich durch die Ausdehnung der Gasphase im Untergrund sowie durch den Speicherbetrieb bedingte Druckspiegeländerungen. Die räumliche Verteilung der Gasphase wird stark durch die Heterogenität und die Geometrie der Speicherformation beeinflusst. Im Fall des simulierten Wasserstoffspeichers erreicht die laterale Ausdehnung der Gasphase maximal etwa 750 m x 7 km. Die Druckauswirkungen des Speicherbetriebes reichen weiter, mit Änderungen von maximal 3 bar 5 km von den Speicherbrunnen entfernt. Im Nahbereich des Speichers schwankt der Druckspiegel um mehr als 10 bar um den initialen hydrostatischen Druck.

Die Analyse induzierter thermischer Prozesse, zeigt, dass der Joule-Thomson-Effekt lediglich zu Temperaturschwankungen von weniger als 1 °C führt. Thermische Effekte werden daher primär durch die Injektionstemperatur des Gases induziert, welche von dem jeweiligen Obertageanlagen abhängig ist. Unter der Annahme einer Injektionstemperatur von 50 °C, was etwa 25 °C über der initialen Reservoirtemperatur liegt, zeigen sich thermische Effekte in den ersten 50 m um die Speicherbrunnen in lateraler und geringfügig weniger in vertikaler Richtung. Wie auch bei den

induzierten Druckeffekten resultiert der zyklische Speicherbetrieb in zeitlich stark variablen Auswirkungen.

Geophysikalische Methoden wie Seismik (seismic waveform inverion; FWI), Geoelektrik (electrical resistivity tomography; ERT) und Gravimetrie können zum Monitoring genutzt werden. Die Simulation der Anwendung dieser Methoden auf den hypothetischen Wasserstoffspeicher zeigt, dass mit Hilfe von FWI und ERT-Verfahren die Gasphase in der heterogenen Speicherformation abgebildet werden kann. Um die notwendige hohe Auflösung zu ermöglichen, müssen Bohrlochmessungen in einem Abstand von 500 m verwendet werden. Die Ergebnisse des FWI-Verfahrens werden durch die Ergebnisse der ERT-Messung bestätigt. Die Gravimetrie zeigt ebenfalls, bedingt durch die Masseänderung in der Speicherformation, Anomalien an. Die Bestimmung des Füllgrades des Speichers ist durch die getesteten Methoden nicht möglich.

ACKNOWLEDGEMENTS

I would like to use this opportunity to gratefully acknowledge those who have, directly or indirectly, supported me while working on my thesis.

First and foremost, I would like to thank my supervisor Prof. Dr. Sebastian Bauer for providing me with an environment from which my scientific development greatly benefited. His valuable input and scientific guidance through many fruitful discussions was a decisive factor for completing this thesis.

Also, I would like to thank my colleagues at Kiel University, especially Dr. Christof Beyer, for his always encouraging advice and support throughout the years. Furthermore, I would like to thank Dr. Jens-Olaf Delfs and Ph.D. Dedong Li for their highly valuable scientific input to my thesis.

I am also very grateful to Dr. Alina Kabuth for enduring me every day in our office, for plenty enlightening and encouraging talks and for a pleasant office climate in general.

My thanks are also directed to Steffi Popp, Katharina Benisch, Bo Wang, Anke Boockmeyer, Martón Berta and of course Tessa Strutz for many helpful and motivational discussions along the way.

Furthermore, I would like to thank Dr. Wolfgang Rübsam, Dr. Martin Stockhausen and Dr. Malte Heinemann for encouraging me and for the always enjoyable discussions and coffee breaks, which helped broadening my perspective more than once. I would also like to thank Christine Heinemann very much for working through and commenting my thesis.

I would also like to express my gratitude towards my parents, my brother and my sister who supported, motivated and encouraged me during all my years at the university.

Finally, I owe a great debt of gratitude to Anna for her endless support, understanding and caring every day.

TABLE OF CONTENTS

Abstract I
Kurzfassung II
Acknowledgements V

1 Introduction 1
1.1 Current and past research 4
1.2 Aims of this thesis 6
1.3 Structure of this thesis 7

2 Porous media hydrogen storage and interactions with other types of usage 9
2.1 Introduction to porous media gas storage 9
2.2 Storage dimensioning: Capacities, withdrawal rates 11
2.3 Induced effects 12
2.4 Affected pore space volumes 15

3 Model development for OGS-ECLIPSE 17
3.1 Introduction 17
3.2 Mathematical Model 18
3.3 OpenGeoSys 19
3.4 ECLIPSE 19
3.5 Simulator coupling 19
3.6 Model validation 22
3.7 The Joule-Thomson effect in OpenGeoSys 27
3.8 Application examples 28
3.8.1 Simulating geochemical reactions with OpenGeoSys-ECLIPSE 28
3.8.2 The Joule-Thomson effect during gas storage operations 30
3.9 Summary and Conclusions 32

4 Porous media hydrogen storage simulations at a realistic subsurface structure 35
4.1 Introduction 35
4.2 Storage scenario 36
4.3 Structural model of the storage site 37
4.4 Part I: Effect of reservoir heterogeneity 39
4.4.1 Heterogeneous rock model 39
4.4.2 Numerical simulation model 40
4.4.3 Simulation Results 43
4.4.4 Conclusions 50
4.5 Part II: Reservoir simulations using generalized properties 52
4.5.1 Generalized rock model & simulation setup 52
4.5.2 Comparison of heterogeneous and homogeneous simulation runs 55
4.5.3 Improved storage setup 62
4.5.4 Large-scale H_2 storage and combined use of a storage site 68
4.5.5 Conclusions 79

4.6 Part III: Thermal effects during storage operation 81
4.6.1 Simulation setup 82
4.6.2 Simulation results 84
4.6.3 Conclusions 87

5 Monitoring Aspects of porous media hydrogen storage 89
5.1 Introduction 89
5.2 Defintion of the storage demand 90
5.3 Storage site characterisation 90
5.4 Storage simulation setup 92
5.5 Storage simulation results 93
5.6 Geophysical monitoring 98
5.6.1 Seismic FWI results 98
5.6.2 ERT results 100
5.6.3 Gravity results 102
5.7 Conclusions 103

6 Summary and Conclusions 105

References 111
Enclosed Publications 121

LIST OF FIGURES

Fig. 1.1 Distribution of (a) the Rhaetian sandstone and (b) the Middle Buntsandstein in Schleswig-Holstein, representing potential porous storage formations, and (c) salt structures potential suitable for cavern storage sites (after Kaufhold et al. 2011) 3

Fig. 2.1 Depiction of typical structural traps for gas in the subsurface, being (a) simple anticlines and (b) reservoirs at salt dome flanks (after Katz et al. 1959) 9

Fig. 2.2 Schematic depiction of different usage options and protected entities (Kabuth et al. 2017). Solid black lines indicate the operational space of a usage option, dashed lines depict the affected space. The black dashed-dot line indicates the required monitoring space. The black arrows depict mutual interactions between different usages 15

Fig. 3.1 Process structure during a coupled OpenGeoSys-ECLIPSE simulation. Grey arrows indicate potential THMC feedback pathways 20

Fig. 3.2 Detailed overview on the OpenGeoSys-ECLIPSE coupling schematics during one iteration. Black arrows indicate the direction of data flow with p, v, S, ρ, μ and X representing pressure, velocity, saturation, density, viscosity and concentration of component n in phase α. T denotes the temperature. Δ denotes changes, which are added to the results from the last iteration stored in "temporary storage" as starting values for a new time step or iteration. The green and blue dots indicate the localization of the data in the mesh of OpenGeoSys and ECLIPSE, respectively 21

Fig. 3.3 (a) Gas saturation and (b) molar H_2 fraction in gas after 20 days in the OpenGeoSys–ECLIPSE simulation 24

Fig. 3.4 (a) Comparison of pressure, gas saturation and total component densities at an observation point 15 m from the injection well and 8.75 m from the top of the model. Lines represent the result obtained from the coupled OpenGeoSys-ECLIPSE simulator while symbols indicate the reference results from a pure ECLIPSE simulation. (b) Temporal evolution of the absolute as well as relative differences between the pressure and saturation as well as the total N_2 component density obtained with ECLIPSE and OpenGeoSys–ECLIPSE in the whole model domain. The relative differences are calculated based on the corresponding explicit values obtained at an element. Missing data points indicate a perfect match of the simulators with not differences observed 24

Fig. 3.5 (a) Aqueous H_2 concentration and (b) gas saturation after 1, 25 and 50 days of simulation 25

Fig. 3.6 Temporal evolution of the total H_2 content as well as the H_2 content in gas and water. The true value is the reference value calculated based on the applied production rate 25

Fig. 3.7 Comparison of the water densities and viscosities obtained for different temperatures at a constant pressure of 6.2 bars when using the IAPWS-IF97 formulation for density (Wagner et al. 2000) and the McDermott et al. (2006) formulation for fluid viscosity in OpenGeoSys with values obtained from ECLIPSE E300 26

Fig. 3.8 (a) Comparison of the temperature distributions in the validation benchmark including thermal feedback after 1.25 days and (b) 2.5 days along a horizontal slice at the top of the model (top) and a vertical slice along the heat plumes symmetry plane (bottom) obtained with the OpenGeoSys-ECLIPSE simulator (contour fill) and the solitary OpenGeoSys simulation (black lines) 26

Fig. 3.9 Simulation setup used for the validation of the implemented Joule-Thomson effect. The shaded area represents the low permeability zone so that $k_1 > k_2$. The cross marks the position of the observation point at which the temperature change is monitored. As $p_1 > p_2$, the temperature downstream of the low permeability zone is changing so that $T_1 \neq T_2$ 28

Fig. 3.10 (a) Aqueous H_2 concentration, (b) dissolved carbon, (c) dissolved CH_4 and (d) CH_4 in gas after 1, 15 and 50 days of simulation 30

Fig. 3.11 (a) Pressure distribution during injection and withdrawal phases and (b) temperature change occurring after 1, 5 and 10 storage cycles in the first 200 m of the model domain from the injection well 32

Fig. 4.1 (a) Structural model used for the reservoir simulation, (b) east-west cross section along the centre well and (c) thickness of the designated storage formation, the Main Sandstone of the Middle Rhaetian (after Pfeiffer and Bauer 2015). The black stars indicate the positions of the storage wells 38

Fig. 4.2 (a) Capillary pressure curves and (b) relative phase permeabilities of the individual facies used in the generation of the heterogeneous parameter distributions. The dashed lines depict the relative permeability of the gas phase while the solid lines represent the relative permeability of the liquid phase. 40

Fig. 4.3 Exemplary permeability distribution for the individual sub-formations in run #14. Please note that the Upper Shale of the Middle Rhaetian and the main sandstone of the Middle Rhaetian consist of five individual layers of which only three are displayed 41

Fig. 4.4 Evolution of the pressure change calculated based on the initial pressure distribution at the observation points at (a) 500 m, (b) 1000 m, (c) 2500 m and (d) 5000 m along a transect perpendicular to the well gallery and intersecting with the centre well and pressure change calculated based on the individual baseline simulations for the same observation points at (e) 500 m, (f) 1000 m, (g) 2500 m and (h) 5000 m. All observation points are located at the central layer of the storage formation. The solid black line depicts the median of all realisations, the dark grey shaded area the interval spanning between the 25th and 75th percentiles, the light grey shaded area the interval spanning between the 5th and 95th percentiles. The dashed lines indicate the absolute minimum and maximum values 44

Fig. 4.5 Initial hydrostatic pressure distribution in the storage formation (left) and observed pressure change (right) during the sixth storage cycle in run #14 45

Fig. 4.6 (a) Vertically averaged gas saturations and (b) vertically averaged molar fractions of H_2 in gas after the storage initialization and during the sixth storage cycle in run #14 46

Fig. 4.7 (a) Absolute gas saturations before the sixth production period and (b) change in gas saturation after the sixth storage cycle; (c) molar fractions of H_2 in gas before the sixth production period and (d) change of the molar fractions of H_2 in gas after the sixth production period (magnitudes) in the storage formation in run #14. The displayed formation is vertically exaggerated by a factor of 5. Each grid block is 50 by 50 m in lateral direction 47

Fig. 4.8 Vertically averaged gas saturations in the storage formation before the sixth production period in run #3 (a), #14 (b), #15 (c) and #19 (d) 48

Fig. 4.9 (a) Total storage flow rate, (b) volume averaged molar H_2 fraction in the produced gas phase per storage and (c) resulting H_2 flow rate as well as equivalent power output for storage cycles 1, 3 and 6. The solid black line depicts the median of all realisations, the dark grey shaded area the interval spanning between the 25th and 75th percentiles, the light grey shaded area the interval spanning between the 5th and 95th percentiles. The dashed lines indicate the absolute minimum and maximum values 49

Fig. 4.10 Generalised (a) capillary pressure and (b) relative phase permeability curves of the individual formations which are obtained when using the parameters given in Tab. 4.5 in combination with the formations of Brooks and Corey (1946) for capillary pressure and Burton et al. (2009) for relative phase permeability. The dashed lines depict the relative permeability curves the gas phase while the solid lines indicate the water relative permeability curves 54

Fig. 4.11 Evolution of reservoir pressures at observation points at (a) 500 m, (b) 1000 m, (c) 2500 m and (d) 5000 m along a transect perpendicular to the well gallery (compare Fig. 4.1). The grey shaded area marks the interval spanning between the 5th and 95th percentile of the heterogeneous ensemble. The curves for the lower and upper bound as defined by Cardwell Jr. and Parsons (1945) follow the same trend as the curves of obtained using the geometric mean (solid green) and the geometric mean of the vertical harmonic mean (short dashed green) but at even lower pressure levels and are thus omitted for easier visual distinction 56

Fig. 4.12 Comparison of the (a) average overpressure of the heterogeneous ensemble with the overpressure signals obtained with generalised rock models (b) using the geometric average of the arithmetic average of permeability [$k_{x,y,z} = k_{x,y}^{geom}(k_z^{arith})$], (c) using the arithmetic average [$k_{x,y,z} = k_{x,y,z}^{arith}$], (d) using the method proposed by Gutjahr et al. (1978) [$k_{x,y,z} = k_{x,y}^{geom}(1-\sigma^2/6)$] and (e) using the geometric mean [$k_{x,y,z} = k_{x,y,z}^{geom}$] prior to the sixth storage cycle at 1362 days 57

Fig. 4.13 Comparison of the (a) average of the gas saturation of the heterogeneous ensemble with the saturation distributions in the storage formation obtained with generalised rock models (b) using the geometric average of the arithmetic average of permeability [$k_{x,y,z} = k_{x,y}^{geom}(k_z^{arith})$], (c) using the arithmetic average [$k_{x,y,z} = k_{x,y,z}^{arith}$], (d) using the method proposed by Gutjahr et al. (1978) [$k_{x,y,z} = k_{x,y}^{geom}(1-\sigma^2/6)$] and (e) using the geometric mean [$k_{x,y,z} = k_{x,y,z}^{geom}$] prior to the sixth storage cycle at 1362 days 59

Fig. 4.14 Comparison of the (a) average of the H_2 fraction in gas in the heterogeneous ensemble with the distributions obtained with generalised rock models (b) using the geometric average of the arithmetic average of permeability [$k_{x,y,z} = k_{x,y}^{geom}(k_z^{arith})$], (c) using the arithmetic average [$k_{x,y,z} = k_{x,y,z}^{arith}$], (d) using the method proposed by Gutjahr et al. (1978) [$k_{x,y,z} = k_{x,y}^{geom}(1-\sigma^2/6)$] and (e) using the geometric mean [$k_{x,y,z} = k_{x,y,z}^{geom}$] prior to the sixth storage cycle at 1362 days 59

Fig. 4.15 Volume of (a) N_2 and (b) H_2 in place in the storage formation prior to the individual storage cycles. The grey shaded area marks the interval spanning from the 5th to 95th percentile in the heterogeneous simulations results. The data points of the simulations using the method of Cardwell Jr. and Parsons (1945) are omitted 60

Fig. 4.16 Evolution of (a) the storage flow rate, (b) the H_2 fraction in the produced gas and (c) the resulting H_2 flow rate and the power output from the storage in the first, third and sixth storage cycle. The curves for the lower and upper bound as defined by Cardwell Jr. and Parsons (1945) are omitted. They follow a similar trend as the curves obtained when using the geometric mean of the vertical harmonic mean (short dashed green). In addition to the median of the heterogeneous ensemble, the interval spanning the 5th and 95th percentile is indicated by the grey shaded area 61

Fig. 4.17 H_2 volume withdrawn in each storage cycle, equivalent amount of energy provided by the storage site and corresponding fraction of the defined storage demand (see Chapter 4.2). The data points of the simulations using the method of Cardwell Jr. and Parsons (1945) are omitted 62

Fig. 4.18 Target injection and withdrawal rates for N_2 and H_2 and amount of energy provided by the storage site in the optimized setup. Negative well flow rates indicate withdrawal phases with positive values representing injection phases 63

Fig. 4.19 Pressure response at observation points (a) 500 m and (b) 5000 m from the well gallery. For the location of the observation points see Fig. 4.1 64

Fig. 4.20 Distribution of (a) the gas saturation and (c) the molar fraction of H_2 in gas prior to the 11th storage cycle at 1683 days in the low permeability simulation case. Changes observed for (b) the gas saturation and (d) the H_2 fraction after the withdrawal. Each grid block is 50 by 50 m. The vertical dimension is exaggerated by a factor of 3 65

Fig. 4.21 N_2 and H_2 in place in the individual storage cycles prior to withdrawal in the individual storage cycles 66

Fig. 4.22 (a) Storage flow rate, (b) H_2 content in produced gas and (c) resulting H_2 flow rate and power output in all storage cycles. Crosses indicate the maximum value observed during the respective storage cycle with the rectangles representing the minimum values 67

Fig. 4.23 H_2 volume withdrawn and equivalent energy provided by the storage site in each storage cycle when using the improved storage setup 68

Fig. 4.24 Extended structural model created for the large scale H_2 storage simulation. The model is based on the previously described structural model (see Fig. 4.1). The grey colour indicates the underlying bedrock and thus represents areas in which the Rhaetian is not present 69

Fig. 4.25 Target injection and withdrawal rates for N_2 and H_2 as well as target storage capacity in the large-scale storage simulation with time. Negative well flow rates indicate withdrawal phases with positive values representing injection phases 71

Fig. 4.26 Pressure change in the storage formation in the low permeability simulation compared to the baseline pressure (a) before the 16th storage cycle at 2440 days, (b) after the gas withdrawal at 2458 days and (c) after the re-injection of H_2 at 2526 days. The storage wells are depicted as black circles, the blue diamonds indicate the water injection wells used in the combined usage scenario. The black cross depicts the observation point at which pressure differences are compared between the storage scenarios 72

Fig. 4.27 Evolution of the pressure change at observation points (a) 500 m, (b), 5000 m and (c) 9950 m from the well gallery for both simulations of the large-scale storage operation 73

Fig. 4.28 (a) Absolute gas saturation and (c) H_2 content in the gas in the centre layer of the Main Sandstone of the Middle Rhaetian prior to the 16th storage cycle in the low permeability simulation case and difference in (b) gas saturation and (d) H_2 fraction before and after the withdrawal 74

Fig. 4.29 N_2 and H_2 in place during the individual storage cycles for both simulations, representing the variability which can be expected due to formation heterogeneity 75

Fig. 4.30 (a) Storage flow rate, (b) H_2 content in produced gas and (c) resulting H_2 flow rate and power output in all storage cycles. Crosses indicate the maximum value observed during the respective storage cycle with the rectangles representing the minimum values 76

Fig. 4.31 H_2 volume withdrawn and equivalent energy provided by the storage site in each storage cycle 77

Fig. 4.32 Pressure difference between the simulation with and without water injection on the opposing anticline flank using the lower permeability estimate (a) prior to the water injection at 890 days, (b) after the water injection of 2 786 784 m^3 at 2034 days and (c) at 2526 days after the re-injection of H_2 in the 16th storage cycle. The black circles depict the location of the gas storage wells, the blue diamonds the location of the waste water injection wells. The observation point at which the differences in pressure is analysed is shown by the black circled-cross 78

Fig. 4.33 Pressure differences in the low and high permeability simulations at the observation point north of the H_2 storage site due to the storage operation (solid lines). The dashed lines depict the differences between the pressure signals obtained in the single usage scenario and the combined scenario. For positions of the observation points and the individual wells please refer to Fig. 4.26 and 4.31 79

Fig. 4.34 (a) Structural model used for the analysis of induced thermal effects. The caprocks above the Rhaetian formations are not shown. (b) Slice through the model domain along the I-axis at the well location. The caprocks are depicted by the grey formations 82

Fig. 4.35 Gas saturations at a vertical slice through the well position along the x-axis after (a) the first H_2 injection, (b) prior to the fourth storage cycle and (c) prior to the 11th storage cycle, the first cycle at full capacity 84

Fig. 4.36 Change in temperature to the initial distribution (a) after half of the N_2 is injected, (b) after the N_2 injection, (c) after the 30 day shut-in period and (d) after the initial filling with H_2 85

Fig. 4.37 Change in temperature compared to the initial storage temperature after the withdrawal and replenishment with H_2 in the first cycle (a, b), the fourth cycle (c, d) and of the 11th storage cycle (e, f) 86

Fig. 5.1 Vertically averaged porosity (top) and permeability (bottom) distribution of all sub-formations of the Rhaetian used in the scenario simulation. 91

Fig. 5.2 Pressure change observed in the middle plane of the reservoir formation, the Main Sandstone of the Middle Rhaetian, after the storage initialization (t=920 days) and during the sixth and last storage cycle (t=1361, 1369 and 1419 days respectively). The black lines depict one bar increments 94

Fig. 5.3 (a) Vertically averaged gas phase saturations and (b) molar fractions of H_2 in the gas phase after the storage initialization (t=920 days) and during the sixth and last storage cycle (t=1361, 1369 and 1419 days respectively) 95

Fig. 5.4 (a) Down-hole pressures and (b) achieved gas flow rates for all wells during the third storage phase, the cyclic storage operation. The first and the last storage cycles are enlarged. Stars mark the times at which the acoustic FWI (t1), ERT (t1) and gravity mapping (t1 & t2) is conducted 96

Fig. 5.5 Gas phase distribution in the model domain (left) and in a slice along the well gallery (right) before the second withdrawal period (t1=1009 days) which are used for the geophysical mapping modelling 98

Fig. 5.6 Comparison between the FWI mapping results, true P-wave velocity model Vp and relative error ΔVp for the H_2 storage formation using the VSP acquisition geometry (a)-(c) and crosswell acquisition geometry (d)-(f), respectively. Black dots denote receiver positions 99

Fig. 5.7 ERT mapping results for the simulated H_2 storage site. Shown is the input (a), inverted output models without constrains (b) with constraints in form of incorporated boundaries (c) and resistivity regions (d) outside the reservoir and the misfits Δρ corresponding to the output models (e-g). Black dots denote borehole electrodes 101

Fig. 5.8 Results of 3D gravity modelling showing anomalies of the vertical component ([Δg]z) for the reservoir filled with (a) N_2 and H_2 (b) and after the gas withdrawal and (c) as their difference ([ΔΔg]z). For the purpose of comparison, the distribution of average gas saturations before (d) and after (e) the withdrawal period are projected on the corresponding xy-plane 102

LIST OF TABLES

Tab. 3.1 Overview on the benchmarks used for testing the OpenGeoSys–ECLIPSE simulator 23

Tab. 3.2 Results of the validation runs for the implemented Joule-Thomson effect. The Joule-Thomson coefficients are calculated for a pressure drop of 5 bars. The NIST data is taken from Lemmon et al. (2016). At 298.15 K and 75 to 100 bars CO_2 is in the liquid state 29

Tab. 3.3 Properties assigned to the individual model units in the simulation regarding pressure-induced temperature changes 31

Tab. 4.1 Properties assigned to the individual facies components 39

Tab. 4.2 Values used for the calculation of the equation of state. Critical temperatures and pressures are taken from Lemmon et al. (2016), critical volumes from Kaye and Laby (2016) and acentric factors from Gasem et al. (2001). The values for the binary interaction coefficients are defaulted to 0 42

Tab. 4.3 Averaged results from the reservoir storage simulation for all six storage cycles (all values represent medians) 45

Tab. 4.4 Generalizing schemes for effective permeability tested in this analysis and corresponding permeability values 53

Tab. 4.5 Formation specific facies fractions based on the distributions of the heterogeneous ensemble and properties assigned to the individual formations in the generalised rock models 54

Tab. 4.6 Data of the horizontal wells used in the large-scale H_2 storage simulation 70

Tab. 4.7 Flow properties assigned to the individual formations of the simulation model used for the analysis of thermal effects 83

Tab. 5.1 Results from the reservoir storage simulation for all six storage cycles. The equivalent energy is calculated assuming a 60 % efficiency of the re-electrification process 97

1 INTRODUCTION

One way to mitigate climate change is to reduce greenhouse gas emissions. According to the fifth assessment report of the IPCC, 35 % of the total greenhouse gas emissions are contributed by the energy sector alone (IPCC 2014). Several mitigation pathways must be adopted to reduce the emissions of greenhouse gases, including extensive changes to energy systems away from fossil fuels. Scenarios in which atmospheric concentration levels below 450 to 500 ppm CO_2 equivalent are maintained, prospect a tripling to quadrupling increase of the share of zero- and low-carbon based energy production, e.g. by using renewable sources (IPCC 2014). Furthermore, even though considerable reserves of hydrocarbons such as oil and gas are still available, they are a limited resource. Consequently, power production from renewable sources is increasing worldwide. In 2015 alone a new net capacity of 150 GW was installed (IEA 2016).

As of 2015 a total of 164 countries have introduced renewable energy targets in one form or another (IRENA 2015). In the European Union, the EU Climate and Energy Package (Directive 2009/28/EC) adopted in 2009 defined mandatory targets to mitigate climate change, including 20 % renewables in the gross energy consumption at the EU level by 2020 (IRENA 2015). In Germany the so-called "Energiewende" resulted in an increase in the share of power production based on renewable sources in the total electricity consumption of Germany from 15.1 % in 2008 to 31.6 % in 2015, with the overall goal being more than 80 % by the year 2050 (BMWi 2016).

However, the availability of renewable sources used for power production such as solar radiation or wind fluctuate locally and with time (e.g. Klaus et al. 2010). Thus, increasing the share of power production based on renewable sources directly causes fluctuations in power supply within the system they are employed. Numerical simulations of a scenario in which 100 % of the power production in Germany is based on renewable sources, using actual meteorological data from the years 2007 and 2009, showed significant shortage periods of up to several days if unfavourable weather conditions prevail (Klaus et al. 2010). The extent and magnitude of such shortage periods can be reduced by load management and energy storage. However, even when including those factors Klaus et al. (2010) forecast a total deficit in power production of 84.7 TWh in the year 2050 based on the meteorological data of 2009, with a peak residual load of about 60 GW. Additional assumptions of the study are the non-existence of bottlenecks in the electrical grid which could hinder the transmission of electricity and a grid loss of 30 TWh annually. Other studies predict less storage requirements. Adamek et al. (2012) estimate the demand for short-term storage below 5 h to be 184 GWh and 26 TWh for long-term storage (several days) for Germany if 100 % of the power is generated using renewable sources. Again, a perfect grid with no transmission bottlenecks or losses is assumed. Per this study, reducing the share of renewable sources to 80 % would result in a decrease of the demand to 70 GWh for short-term storage and 7 TWh for long-term storage.

The storage demand and the grid extension are linked to each other in a manner that the storage demand in a perfect transmission grid with no bottlenecks is lower than in a scenario which considers a less optimal transmission grid (e.g. Steinke et al. 2013). Furthermore, given an imperfect transmission grid, energy storage can reduce the cost of the energy system by reducing the demand of conventional backup systems (Steinke et al. 2013). Although the values differ, energy storage is required in all scenarios.

Energy can generally be stored in form of a gravitational potential (e.g. pumped hydro), in batteries as electrochemical energy, in flywheels as kinetic energy, as electric field energy in capacitors, or as chemical or mechanical energy storage in gas (Pickard et al. 2009). The idea of producing and storing hydrogen gas during surplus periods and subsequently withdrawing and re-electrifying the stored hydrogen during shortage periods was

already introduced in the mid-1970s (Sørensen 1975). In turn of the increasing power generation from renewable sources, this idea of chemical energy storage - often referred to as power-to-gas - regained traction (e.g. Sørensen et al. 2004; Korpås and Greiner 2008; Klaus et al. 2010; Schiebahn et al. 2015).

The geological subsurface can be used for chemical energy storage by the means of gas storage in porous formation or leached salt caverns. Apart from this, energy can be stored in the subsurface as mechanical energy, e.g. in compressed air energy storages, or by heat storage, either in permeable or impermeable rock strata. So far the geological subsurface is already widely used for large scale chemical energy storage by the means of natural gas storage in porous formations and salt caverns (Evans and West 2008). These storage sites provide large storage capacities and long withdrawal periods lasting up to several months (e.g. Gregory and Pangborn 1976; Carden and Paterson 1979; Ogden 1999; Evans and West 2008; LBEG 2015). Natural gas, for example, is traditionally stored on a seasonal cycle with the gas being injected at the storage sites in the summer months and withdrawn during the high demand season in winter (e.g. Katz et al. 1959; Evans and West 2008; LBEG 2015). Additionally, gas storages, especially those constructed in salt caverns, are also used to cover peak demand as they can provide high deliverability (Evans and West 2008; Plaat 2009).

As of 2006, a total of 606 gas storage facilities with a total capacity of 333 235 million normal cubic metres (Nm^3; measured at 0 °C and 1.01325 bars) were operational world-wide (IGU/WOC 2006). The majority of the installed gas storage capacity is provided by permeable formations with depleted hydrocarbon fields contributing around 81.6 % and aquifers 14.5 % (IGU/WOC 2006). Leached salt caverns provide slightly less than 4 % of the total stored gas (IGU/WOC 2006). This is partly because suitable salt rock formations are not as abundant on world-wide perspective, making them a viable solution only for countries like Germany or Great Britain, which have access to suitable host formations. In Germany, currently around 20 natural gas storage facilities in porous formations are operational, which provide a total working gas volume of 9784 million Nm^3, with another 260 caverns providing about 14 315 million Nm^3 (LBEG 2015). Hence, compared with other energy storage technologies, power-to-gas in combination with subsurface storage and re-electrification can provide large capacities on long time scales (Gallo et al. 2016).

Currently hydrogen and methane are being discussed as potential energy carriers in a power-to-gas concept (Klaus et al. 2010; Schiebahn et al. 2015). Both methods rely on the production of hydrogen, e.g. by water electrolysis during times of high power production (Ursúa et al. 2012). The produced hydrogen gas could then either be used directly for power generation as a fuel for transportation or as an industrial resource. Thus far, the use of hydrogen is primarily limited to the use as the latter, with the former requiring at least some additional research and development. In a second step, the produced hydrogen can be turned into synthetic methane making use of the Sabatier-process (Schiebahn et al. 2015), e.g. for the direct use in the natural gas grid. Because of the second step of transforming the hydrogen into methane, a power-to-gas system based on methane has a round-trip efficiency of around 39 %, while a hydrogen based system has a higher efficiency of about 42 % (Klaus et al. 2010).

Until today pure hydrogen has only been stored in salt caverns for industrial use in Texas, USA and near Teeside, UK (Crotogino et al. 2010), thus only little practical experience with storing pure hydrogen is available. The storage of hydrogen rich town gas in an aquifer near Beynes, France, is the only documented field application of hydrogen storage in porous geological formations (Carden and Paterson 1979; Foh et al. 1979), although storing town gas was much more widespread. Technical issues arise from storing hydrogen instead of natural gas such as hydrogen induced embrittlement causing damage to steels and casings (Reitenbach et al. 2015; Schlichtenmeyer and Klafki 2016). Compared to natural gas, hydrogen has a higher compressibility factor, meaning that a higher pressure is required to store the same amount of gas in a given volume (Schlichtenmeyer and Klafki 2016). For the same reason the deliverability of hydrogen from a storage site can be expected to be lower than for a natural gas storage site at a given pressure difference. However, the low viscosity of hydrogen gas results in less dynamic pressure loss during injection or withdrawal from the storage

site to the well head (Schlichtenmeyer and Klafki 2016). Despite these differences, natural gas storage can be used as an analogue to porous media hydrogen storage due to the similarities of the underlying principles (Carden and Paterson 1979; Foh et al. 1979).

For the field deployment of a hydrogen based power-to-gas concept potential storage dimensions must be investigated. Given that the physical properties of natural gas and hydrogen differ, these metrics cannot be directly inferred from those of natural gas storage facilities. During the field deployment, the induced effects of the storage such as differences in pressures or fluid phase compositions can be used for a monitoring of the storage facility to ensure the proper and safe operation. Thus, the induced effects and in turn the applicability of different monitoring techniques should be evaluated prior to the field deployment. For such an a-priori assessment numerical simulations of the storage operation can be used, given that the required models are available and all necessary parameters are known sufficiently.

Potential storage formations for an application of power-to-gas using porous formations are widely available in the North German Basin and could thus provide large capacities (Fig. 1.1; Kaufhold et al. 2011; Reinhold and Müller 2011). Nevertheless, the available pore space of the subsurface does represent a limited resource for various usages. These comprise of groundwater abstraction in usually shallower formations, geothermal applications in various depths, large scale hydrocarbon exploration or energy storage as described in this work. All these potential subsurface uses induce, with varying magnitude, thermal, hydraulic, geomechanical, and geochemical (THMC) effects in the subsurface. The different usages are potentially competing for either the same storage site directly or through interactions with other usages. Thus, a subsurface spatial planning is required to allocate the limited space most effectively (Bauer et al. 2013; Kabuth et al. 2017). Such a planning scheme does include the determination of the dimensioning of the storage operation itself prior to its deployment. The dimensions of a storage operation are defined by the overall capacity of the storage site, which is the amount of energy which can be retrieved, and the rates with which the storage site can be operated. The storage flow

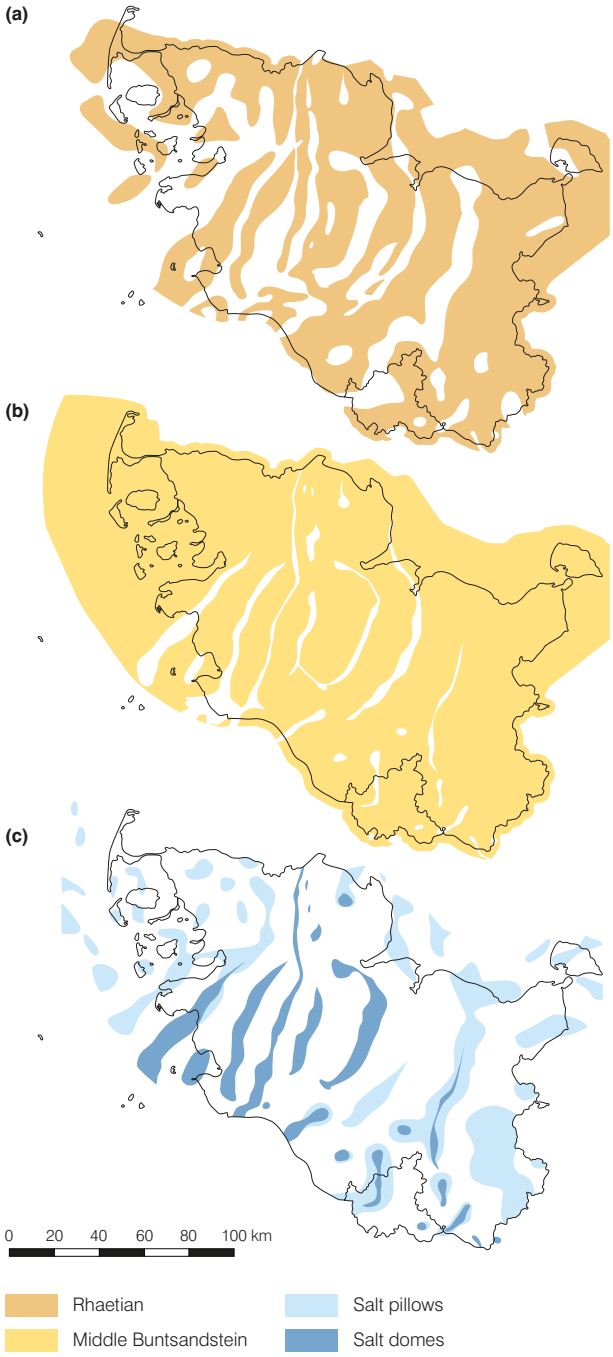

*Fig. 1.1 Distribution of **(a)** the Rhaetian sandstone and **(b)** the Middle Buntsandstein in Schleswig-Holstein, representing potential porous storage formations, and **(c)** salt structures potential suitable for cavern storage sites (after Kaufhold et al. 2011).*

rates, which can be achieved during withdrawal can then in turn be used to determine the power output the storage site can provide. For such a planning scheme to be sustainable, also the quantification of induced effects and the description of appropriate monitoring schemes is necessary

(Bauer et al. 2013). Other researches come to similar conclusions (e.g. Kahnt et al. 2015).

Given that adequate modelling tools are available, numerical scenario simulations based on generated "virtual realities" can be used to assess both the storage performance in terms of e.g. flow rates or power and the extent and magnitude of induced effects. The concept of such virtual realities has already been applied successfully to several geoscientific fields such as CO_2 storage (e.g. Bauer et al. 2012; Benisch and Bauer 2013) or contaminated aquifer evaluation and treatment (e.g. Schäfer et al. 2004; Bauer et al. 2006). A prerequisite for applying such scenario simulations for the estimation of e.g. storage capacities and induced effects are adequate input data.

1.1 Current and past research

With the increasing share of power production from renewable sources various energy storage concepts and technologies are increasingly discussed in scientific literature. For example, under the research initiative "Energiespeicher" in Germany, energy storage technologies ranging from small scale mobile storage applications to large scale power-to-gas energy storage are investigated. However, research regarding geological energy storage in systems with a high renewable penetration and hydrogen storage in particular is relatively scarce. As previously mentioned, the general concept was initially introduced in the mid-1970s by Sørensen (1975) and some additional work was done shortly thereafter regarding different subsurface hydrogen storage options (Foh et al. 1979) that remains relevant today. Concurrently the work of Carden and Paterson (1979) was published, focussing on aspects of porous media hydrogen in particular with an emphasis on potential losses of hydrogen. These can occur e.g. through capillary trapping of gas, essentially resulting in the gas being not available for withdrawal. Other potential losses include the dissolution of the hydrogen gas in the residual formation water and chemical reactions which result in a transformation of the stored hydrogen to another compound. Furthermore, the authors briefly discuss operating losses which are leakages of hydrogen from the storage site and energy losses e.g. due to friction of the gas during flow in the porous formation and the wells. The authors concluded that the physical and chemical problems associated with storing hydrogen in porous formation can be solved so that economic aspects are the major deciding factor for or against a storage operation. However, the authors do also point out that additional research is required regarding potential chemical reactions and the mechanics of hydrogen, having a low viscosity, displacing water. The latter is addressed in the work of Paterson (1983) in which experiments of hydrogen gas displacing formation water are presented and discussed. Paterson (1983) concludes that hydrogen is prone to fingering due to its low viscosity, which could result in additional losses during a storage operation, e.g. by fingers of gas snapping-off from the gas phase, resulting in capillary trapping of the gas. The use of a steeply dipping storage structure, reduced flow rates and alternative cushion gases could help mitigating such fingering.

From the late 1990s onwards additional research was done in the field of porous media hydrogen storage. While several publications are more focussed on the general concept of integrating energy storage in renewable grids (e.g. Ogden 1999; Sørensen et al. 2004; Crotogino et al. 2010; Gahleitner 2013; Carr et al. 2014), also some more detailed research was published. Panfilov (2010) for example investigated differences in chemical composition of hydrogen rich town gas stored in aquifers, which showed a decrease of hydrogen accompanied by an increase in methane. The author concluded that the reaction is caused by methanogenic bacteria and derived a mathematical model which describes the transformation reactions using bacteria population with a variable growth rate.

In recent years new research was published regarding issues arising from adding hydrogen to natural gas storage sites. Reitenbach et al. (2015) presented a review of technological aspects which must be considered when adding hydrogen to the existing natural gas storages and transportation pipelines, e.g. due to hydrogen embrittlement or chemical reactions. Based on literature data the authors concluded that the risk to the geological and technical integrity of the storage facility is primarily associated with the high diffusivity of hydrogen and the lower viscosity of the gas caused

by the addition of hydrogen. Furthermore, the authors suggest that the added hydrogen could promote a-biotic reactions of the hydrogen with the minerals of the caprock or the storage, causing dissolution of feldspar, carbonate, sulphate and clay minerals as well as precipitation of illites, iron sulphides and pyrrhotite. However, the most crucial risks are associated with microbial reactions, which could result in the production of hydrogen sulphide and acetic acid, both of which pose a risk to the environment and the safe operation of such hydrogen spiked natural gas storages.

Hagemann et al. (2015) and Feldmann et al. (2016) investigated the hydrodynamic and mixing processes of hydrogen gas stored in natural gas storages using numerical scenario simulations. Based on the simulations results obtained using homogeneous reservoir properties and in accordance with Paterson (1983), they concluded that the low viscosity of hydrogen results in significant gravity override if high flow rates are applied. According to Hagemann et al. (2015) hydrogen storage in stratified aquifers could reduce the risk of fingering and lateral spreading, resulting in an overall reduced risk of gas losses. Feldmann et al. (2016) concluded that hydrogen, being prone to gravity override and viscous fingering, complicates the displacement of formation water in aquifers. The authors furthermore state that these physical effects will be reduced in saturated gas reservoirs and will thus play a minor role during displacement in such systems. Hagemann et al. (2016) implemented a coupled mathematical model for the simulation of hydrodynamic transport and bio-chemical reactions of hydrogen in a depleted natural gas reservoir and applied the model to a homogeneous scenario simulation. Their conclusions regarding the hydrodynamic behaviour are comparable to those of Hagemann et al. (2015) and Feldmann et al. (2016). The authors further identified methanogenic archaea, acetogenic archaea, sulphate-reducing bacteria and iron-reducing bacteria as important hydrogenotrophic microorganism. Their simulations showed that a growth of microorganisms arises at the hydrogen injection front, resulting in a partial transformation of the hydrogen to methane. They further concluded, that the rate of bio-chemical reactions is dependent on the population number of the involved microorganisms, so that a correct description of the microbial growth and decay functions is important for modelling such bio-chemical reactions.

With little research overall being available on hydrogen gas storage in porous formations, research from related fields such as CO_2 sequestration can, to some extent, be related to. This is especially true for monitoring aspects of gas storages. The works of e.g. Birkholzer et al. (2009), Birkholzer et al. (2011), Benisch and Bauer (2013) and Birkholzer et al. (2015) for example provide estimates of large scale pressure perturbations caused by the injection of gas in aquifer structures. The studies show that regional-scale pressure build-up of several bars can be expected in the far field of the storage. Even though the volumes of stored gas are not directly comparable, these estimates can be seen as worst-case assumptions. Similarly, studies such as those by Birkholzer and Zhou (2009), Thibeau et al. (2014) and Mitiku and Bauer (2013) on CO_2 storage capacities can to some extent be applied to hydrogen gas storage. Given CO_2 has different physico-chemical properties than hydrogen such as a higher viscosity, research on the hydrodynamic behaviour of the gas displacing formation water (e.g. Taku Ide et al. 2007) cannot be transferred directly.

The issue of an increasing use of the subsurface and thus the requirement of a spatial planning of the limited subsurface space arose just in recent years. Previous works on subsurface spatial planning such as those by Roberts (1996), Rönkä et al. (1998) and Takasaki et al. (2000) focus primarily on engineered constructions in the subsurface such as tunnels, tanks or buildings. With the advent of subsurface energy storage in recent years, the requirement for a subsurface spatial planning is recognized in more recent publications (ARL 2012; Bauer et al. 2013; Kahnt et al. 2015; Schulze et al. 2015). For this, consistent and detailed data on the geological setting, the physical and chemical properties of the subsurface, e.g. fluid and rock compositions, porosities and permeabilities and the occurring anthropogenic and natural processes are required (ARL 2012). According to Bauer et al. (2013), an assessment of subsurface energy storage in the context of a spatial planning must consider induced effects of the storage operation itself and the monitoring associated with the storage operation. This can be done using numerical

simulations, given that adequate storage scenarios are defined, the relevant properties of the subsurface and the induced thermal, hydraulic, mechanical and geochemical processes are known, and appropriate modelling tools, which account for feedback reactions among the considered processes are available. The two studies published by Kahnt et al. (2015) and Schulze et al. (2015) for the German Federal Environment Agency discuss geological and regulatory issues regarding subsurface usage and spatial planning. According to Kahnt et al. (2015), the space allocated for a specific usage has to be defined in a way that no or only minimal effects are induced outside of the defined subsurface space. Furthermore, a spatial planning should include the quantification of potential storage dimensions, which in the case of energy storage includes capacities and achievable delivery rates. Establishing a new subsurface usage option, such as e.g. porous media hydrogen storage, should be accompanied by continuous monitoring (Schulze et al. 2015).

More recently an assessment tool for the selection of salt structures which can potentially be used for cavern storage of hydrogen or compressed air has been developed (Pollok et al. 2015). A similar tool does not exist for hydrogen storage in porous formations. However, the "Speicherkataster", a database of the distribution of rock strata potentially usable for CO_2 storage exists (Müller and Reinhold 2011), which can be used to infer areas of interest for hydrogen storage sites.

Only very little research has been published regarding hydrogen storage in porous formations. Of the published research the works Hagemann et al. (2015), Hagemann et al. (2016) and Feldmann et al. (2016) are the only publications which provide quantitative results on the hydrodynamic behaviour of hydrogen in porous formations, primarily focused at the displacement characteristics. Panfilov (2010) gives additional insight into the modelling of microbial hydrogen transformation reactions. Similarly Hagemann et al. (2016) quantify the effect of a-biotic and biotic reactions which could occur when adding hydrogen to a porous media natural gas storage. However, all the presented simulations used to infer the results on the hydrodynamic behaviour or occurring chemical reactions are done using a simplified geological model by assuming homogeneous rock properties. No research is thus far published regarding the applicability of monitoring techniques at a hydrogen storage site. So far only works from the field of CO_2 storage such as those of e.g. Birkholzer et al. (2009), Birkholzer et al. (2015) and Benisch and Bauer (2013) on pressure perturbations caused by gas injections and that of Benisch et al. (2015) on integrative geophysical monitoring techniques are available.

As noted previously, in the context of sustainable subsurface spatial planning one must determine storage dimensions, the induced thermal, hydraulic, mechanical and chemical effects and the monitoring requirements of hydrogen gas storage sites. The presented literature review indicates that several key aspects of porous media hydrogen storage are insufficiently or not investigated so far. For example, research is yet to be published on the potential dimensions of hydrogen storage in porous formations using a realistic geological setting. Furthermore, neither the thermal nor the mechanical effects caused by such a storage operation have been investigated. The research published on the hydraulic effects, such as the hydrodynamic behaviour, is based on simplified homogeneous rock models. There is an absence of published research on the pressure perturbations of a reasonably scaled hydrogen storage in an aquifer. Another deficit is the lack of research on monitoring techniques, which can be employed at a field site. Especially the applicability of integrated geophysical techniques, capable of providing multidimensional information, has not yet been determined.

1.2 Aims of this thesis

Several aspects of hydrogen storage in porous geological formations are investigated in this thesis, e.g. for an application in a subsurface spatial planning scheme. Based on the current state of research and knowledge the following research aims are deduced for this thesis:

- Quantification of potential storage dimensions, such as capacities and withdrawal rates, of porous media hydrogen storage for a realistic geological setting

- Development of modelling tools to assess effects induced during porous media hydrogen storage using scenario simulations of coupled hydraulic, thermal and chemical processes
- Assessment of hydraulic effects, i.e. of the magnitude and extent of the pressure perturbations and the distribution of the gas phase as a result of the storage operation
- Provision of a first estimate of induced thermal effects caused by a hydrogen storage operation
- Assessment of the applicability of geophysical monitoring techniques, namely seismic, geoelectric and gravimetric methods to porous media hydrogen storage operation at a realistic field site

For the quantification of potential storage dimensions, effects induced by the storage operation and the investigation of the applicability of geophysical monitoring techniques numerical scenario simulations of virtual realities are used. The required modelling tools are partly available. For the quantification of potential storage dimensions and induced hydraulic effects the reservoir simulator ECLIPSE E300 (Schlumberger 2015) is used, which is capable of solving multiphase-multicomponent problems. For the assessment of induced thermal effects and -albeit not included in this thesischemical effects the scientific open-source simulator OpenGeoSys (Kolditz et al. 2012a) is coupled to ECLIPSE. Furthermore, the Joule-Thomson effect (Joule and Thomson 1854) is implemented for the heat transport process of OpenGeoSys to account for temperature perturbations caused by isenthalpic pressure reductions during gas flow. All model development is validated using reference simulations or published data sets.

For the numerical simulations, a virtual storage scenario is defined. As a first step a storage demand is derived based on numerical simulations of the availability of power production from renewable sources. The simulations used to infer storage dimensions, induced effects and the applicability of geophysical monitoring techniques are based on a structural model of an existing geological structure in northern Germany. A realistic heterogeneous rock model is created using a facies modelling approach and 25 equally likely parameter distributions are derived. Subsequently, homogeneous rock models are derived from the heterogeneous ensemble.

The potential storage dimensions and the induced hydraulic effects are determined using both the heterogeneous and homogeneous rock models. The induced thermal effects are investigated based on homogeneous rock models. The applicability of seismic, geoelectric and gravimetric monitoring methods to a hydrogen storage operation is evaluated based on an integrative site investigation, using on the presented virtual storage scenario.

1.3 Structure of this thesis

Following this introduction (Chapter 1), fundamental principles and concepts used in this thesis are introduced in Chapter 2.
Chapter 3 consists of the description of model developments, including the development of the coupled OpenGeoSys-ECLIPSE simulator and the implementation of the Joule-Thomson effect.

In Chapter 4, potential storage dimensions and induced hydraulic and thermal effects of hydrogen storage in an aquifer structure are investigated using numerical scenario simulations. For this purpose, an existing geological structure is first parametrised realistically based on available literature data. Subsequently a storage scenario is defined, including the duration and magnitude of shortage periods which must be accounted for. The performance of the hypothetical storage operation is evaluated with respect to this defined scenario using numerical simulations of the heterogeneous parameter ensemble. Based on the findings of the heterogeneous ensemble, the storage setup is optimized to increase the storage performance. Homogeneous reservoir properties are calculated based on the parameter distributions in the heterogeneous ensemble and tested against the results obtained with the ensemble. A combined usage scenario is defined and simulated in which the hydrogen storage site is operated simultaneously to a brine injection in the same geological formation. The induced hydraulic effects linked to the storage operations are investigated based on the presented heterogeneous and homogeneous scenario simulations. For the estimation of induced

thermal effects, a slightly simplified scenario simulation based on the same geological structure is used. The corresponding coupled thermo-hydraulic simulations are carried out using the OpenGeoSys-ECLIPSE simulator described in Chapter 3.

In Chapter 5, geophysical monitoring methods, namely seismic, geoelectric and gravimetric monitoring techniques are tested with respect to their individual applicability at a porous media hydrogen storage site, using a heterogeneous simulation of the previously described ensemble (Chapter 4). The applicability of the individual geophysical monitoring methods is then tested by using the simulation results as input for forward simulations of the geophysical data acquisition. Based on the simulation results of the synthetic geophysical data, the different techniques are evaluated regarding the detectability of the gas within the storage and the current state of the storage operation itself.

In Chapter 6, the results of Chapters 3, 4 and 5 are discussed and summarized. The findings of this work regarding potential storage dimensions, the magnitude and extent of the induced hydraulic and thermal effects observed in the numerical simulations are then applied to the concept of subsurface usage spaces.

2 POROUS MEDIA HYDROGEN STORAGE AND INTERACTIONS WITH OTHER TYPES OF USAGE

In this chapter a short introduction into aquifer gas storage is given, which includes an overview of typical requirements and properties of such storage sites (Chapter 2.1). Typical dimensions of natural gas storage sites are given in Chapter 2.2 together with properties and requirements of the production and re-electrification of hydrogen. Chapter 2.3 consists of a short description of the concept of affected pore space volumes in the context of a subsurface spatial planning concept. Chapter 2.4 summarizes important induced hydraulic, thermal, geochemical and geomechanical effects which can be expected during the construction and operation of a porous media hydrogen storage.

2.1 Introduction to porous media gas storage

The first application of porous media gas storage dates back as far as 1915 with natural gas being injected into a depleted hydrocarbon reservoir in Canada (Foh et al. 1979; Evans and West 2008). In the following years the first natural gas storage was developed in the state of New York, USA, which is still in service today (Plaat 2009). The first porous media gas storage in Europe was completed in 1953 in the Engelborstel field, Germany (Plaat 2009). To present day around 100 porous media gas storage facilities are in operation within Europe with 20 in Germany (IGU/WOC 2006; Plaat 2009; LBEG 2015). Thus, natural gas has been stored in porous formations for more than a century.

Potential storage formations for gas are permeable aquifers, e.g. sandstones or carbonates, as well as depleted hydrocarbon fields (Plaat 2009). The main differences between these types of porous media gas storages are the initial chemical composition and the reservoir pressure levels. While the pore space of aquifer formations is occupied by formation water or brine, depleted hydrocarbon fields contain oil or natural gas which was not or could not be produced during the field exploration. As a consequence of the depletion the initial pressure in such fields is most likely reduced compared to the hydrostatic pressure level. A necessary prerequisite for a gas storage in a porous formation is the existence of a trap which retains the stored gas. In conventional hydrocarbon reservoirs such traps can either be stratigraphic or structural. At a site with a structural trap the gas is accumulating at the top of a structure and is retained from further movement by a tight caprock (Fig. 2.1). Contrary to that, a stratigraphic trap retains the gas within the stratum through a change in facies (Katz et al. 1959).

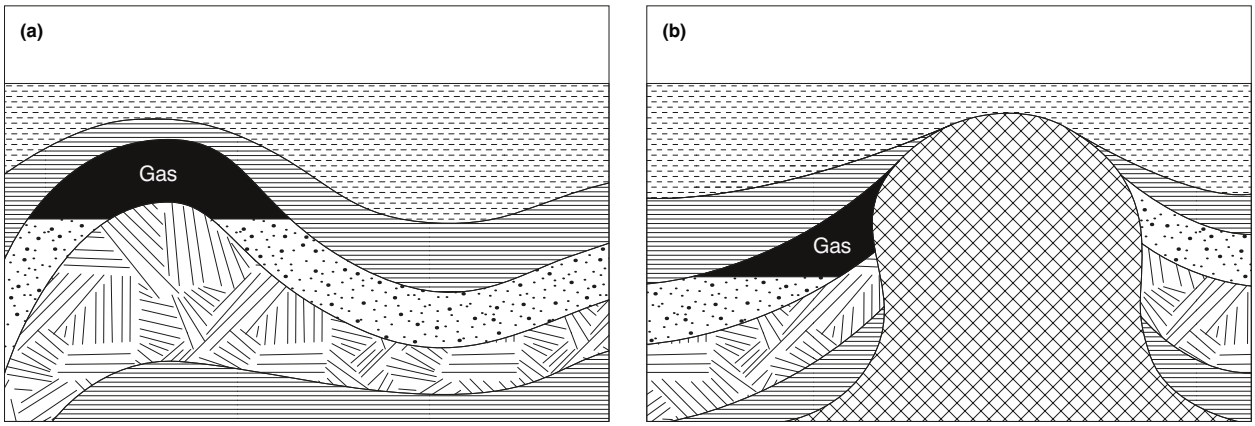

Fig. 2.1 *Depiction of typical structural traps for gas in the subsurface, being* ***(a)*** *simple anticlines and* ***(b)*** *reservoirs at salt dome flanks (after Katz et al. 1959).*

On a world-wide perspective, storage in depleted hydrocarbon fields provides the majority of the stored gas, with around 82 % (IGU/WOC 2006). Nevertheless, aquifers are more widespread than hydrocarbon fields and are thus of importance for energy storage.

The gas in place in a storage site, called inventory, can be split into two fractions, the working and the cushion gas (e.g. Katz et al. 1959; Plaat 2009). Of these two the working gas is the fraction of gas which is available for withdrawal. The cushion gas, also termed base gas, on the other hand is the fraction of gas which is not withdrawn during normal operation and stays within the storage formation. The primary objective of the cushion gas is to ensure the deliverability of gas from the storage during operation (Plaat 2009). Compared to other means of geological storage of gas, e.g. using salt caverns, porous formations generally provide larger storage capacities but simultaneously require more cushion gas to be in place for the storage operation (e.g. Evans and West 2008; Plaat 2009). The average cushion gas fraction of storage sites in Germany is more than 50 % with the storage of Allmenhausen having the highest fraction of more than 80 % (LBEG 2015). Cushion gas represents a one-time loss associated with the initial filling of the reservoir (Carden and Paterson 1979). If a storage is realised in a depleted natural gas field, the volume of additional cushion gas can be severely reduced if not completely unnecessary (Evans and West 2008). For gas storage in a depleted oil field, the gas cap that is often present above oil reservoirs is used for the storage operation (Plaat 2009). Different to these options, gas storage in aquifers does require a larger amount of cushion gas, mainly because the formation water, which is initially present in the storage, must be displaced by the gas injection. To reduce the cost of the cushion gas the use of inert substitutes to the actual working gas such as CO_2 or N_2 have been discussed in the literature and also used in practice (Laille et al. 1988; Dussaud 1989; Oldenburg 2003). In addition to potential cost savings due to a lower cushion gas requirement, depleted hydrocarbon fields already provide some proof regarding the tightness of the caprocks against gas migration and thus less exploration is required to characterise the storage formation.

However, the presence of a hydrocarbon field does not necessarily imply that the site can be used for gas storage. The requirements for porous media gas storage can be summarized as follows (Bennion et al. 2000):

1. Sufficient reservoir volume for the envisaged withdrawal rates and volumes
2. Proven tightness of the caprocks above and below the storage formation against migration of the stored gas resulting in structural or stratigraphic entrapment of the gas
3. Sufficient intrinsic permeability to support the scheduled storage flow rates
4. Low or no tendency for permeability reductions due to formation water encroachment, present hydrocarbons, drilling activities or geomechanical responses of the system, triggered by the cyclic storage operation
5. Absence and resistance against formation of corrosive H_2S gas
6. Technical feasibility of drilling

As the overall principals of storing any gas in porous formations are relatively similar, the storage of natural gas can to some extent be used as an analogue for storing hydrogen (Carden and Paterson 1979; Foh et al. 1979). However, due to its low viscosity H_2 is prone to fingering and gravity overrides (Paterson 1983; Hagemann et al. 2015; Feldmann et al. 2016). Consequently, a steeply dipping formation is favourable for a porous media H_2 storage (Paterson 1983).

In contrast to natural gas storage, practical experience from storing H_2 in porous formations is relatively scarce. So far the storage of H_2 rich town gas in an aquifer near Beynes, France, is the only field application documented in literature (Carden and Paterson 1979; Foh et al. 1979). The use of H_2 instead of natural gas or synthetic methane, which is very similar to natural gas, results in additional limitations regarding technical installations (Foh et al. 1979; Reitenbach et al. 2015; Schlichtenmeyer and Klafki 2016). Among those are the high mobility of H_2, which may require additional investigations regarding the tightness of borehole equipment and cements against migration. Furthermore, metals of the technical installations

might corrode when in contact with H_2. An overview on technical issues arising from the use of hydrogen instead of natural gas are given in Reitenbach et al. (2015). The arising technical issues can be solved (Schlichtenmeyer and Klafki 2016), which is further supported by hydrogen being already stored in salt caverns (Crotogino et al. 2010).

2.2 Storage dimensioning: Capacities, withdrawal rates

Currently 20 porous media storage facilities are in operation in Germany, providing a combined working gas volume of 9784 million Nm^3 (LBEG 2015). The largest of these storage facilities is located near Rheden in the state of Lower Saxony, providing a working gas volume of 4400 million Nm^3 alone which can be withdrawn with a peak flow rate of 2.4 million Nm^3/h using 16 storage wells (IGU/WOC 2006; LBEG 2015). On a global scale even larger porous media gas storage facilities exist, with the storage facility Severo-Stavropolskoe located in Russia having a total working gas volume of 23 000 million Nm^3 and a peak withdrawal rate of 6.7 million Nm^3/h using 810 storage wells (IGU/WOC 2006). However, these values represent only a small fraction of the storages in use. Several smaller gas storages are also operational. The storage Sandhausen in Germany for example has a comparably small working gas capacity of 30 million Nm^3 in a tertiary aquifer (LBEG 2015). The storage is operated using 5 storage wells providing a peak withdrawal rate of 45 000 Nm^3/h (IGU/WOC 2006; LBEG 2015).

Well flow rates clearly differ significantly for the individual storage sites. Compared with flow rates realized in conventional gas fields, the rates applied in gas storages may be significantly higher with the volume withdrawn and injected in a gas storage within a period of a few months equating to the volume of gas produced in a field over several years (Plaat 2009). To support such high well flow rates large diameter production casings are used (Plaat 2009). High well flow rates, however can introduce problems such as water coning, resulting in water production from the well, as well as sanding during which particles of the aquifer are transported within the gas flow, resulting in severe erosion of the equipment (Katz et al. 1959; Carlson et al. 1992; Evans and West 2008). For a given flow rate the amount of sanding depends on the viscosity of the fluid flowing through the formation (Carlson et al. 1992). The viscosity of hydrogen is lower than the viscosity of natural gas or air; thus, the use of hydrogen should support higher flow rates compared to natural gas before severe sanding occurs. For a given fluid the maximum well flow rate per well depends on site specific parameters such as the aquifer permeability and thickness. Such flow rates can be a-priori estimated using analytical functions, which however include several restricting assumptions such as steady-state flow, radial flow and constant aquifer thickness (see e.g. Katz et al. 1959; Wang and Economides 2009). For a more detailed investigation either numerical simulations making use of the actual geometry of the storage formation or well tests at a field site can be used. As obvious from the presented examples, high performance storage wells can reach flow rates in the region of several million cubic metre per day. Other documented cases of high productive storage wells quote values of slightly below 1 million Nm^3/d (Bary et al. 2002). For low permeability reservoirs, the deliverability can be increased by adding wells, which obviously introduces additional costs.

For use as an energy storage in the context of renewable power production, the hydrogen must be synthesised and injected into the storage during surplus periods and withdrawn and re-electrified during shortage periods. H_2 can be produced by water electrolysis (e.g. Smolinka et al. 2010; Ursúa et al. 2012). Readily available electrolyser modules, which are used in parallel stacks in H_2 production facilities, already reach production rates of up to 760 Nm^3/h (Smolinka et al. 2010). These production rates can be expected to increase in the next couple of years to values of 1500 Nm^3/h (Smolinka et al. 2010). Given the stack design, the output from H_2 production facilities greatly surpasses those of the individual modules. For example, the largest H_2 production plant currently in service can produce H_2 at a rate of 33 000 Nm^3/h (Smolinka et al. 2010). The re-electrification of the withdrawn H_2 can be achieved using either fuel cells or conventional gas turbines (Klaus et al. 2010; Büchi et al. 2014). Fuel cells capable of high power outputs are still in development with current modules reaching around 100 kW (Gahleitner 2013). Conventional gas turbine power plants

making use of natural gas reach power outputs of several hundred MW (Sterner and Stadler 2014). Gas turbines which can be fuelled with hydrogen rich gas are commercially available but are rarely used so far (Klaus et al. 2010). The real world efficiencies of re-electrification via fuel cells or gas turbines are quite similar at around 60 % (Klaus et al. 2010; Büchi et al. 2014). However, the options differ regarding their ability to tolerate H_2 impurities. While such impurities reduce the power output and could potentially damage fuel cells, a dilution of H_2 with for example N_2 is even required in gas turbines to meet emission regulations (Chiesa et al. 2005; Lee et al. 2012).

To conclude, porous media gas storage can be of considerable size, providing large storage capacities as well as high withdrawal rates, with smaller storages being on the order of around 30 million Nm^3 of working gas. Given the energy density of H_2 of about 124 MJ/kg (Carden and Paterson 1979), a gas density of 0.089885 kg/m^3 at normal conditions, i.e. a pressure of 1.01325 bars and a temperature of 0 °C (Lemmon et al. 2016), and assuming an efficiency of 0.6 for the re-electrification, the amount of energy stored at a H_2 storage site of similar size is around 55 729 MWh. Assuming the storage demand is 84.7 TWh as given by Klaus et al. (2010), slightly more than 1500 such storage facilities would be required. Assuming larger H_2 storage facilities, e.g. comparable in size to the storage facility Rheden, only around 11 storage sites would be required to cover for the whole demand. The power output from such storage sites would be, based on the peak withdrawal rates of the Rheden and Sandhausen gas storage sites, around 4460 MW and 84 MW, respectively. Clearly, the storage capacities and withdrawal rates highly differ at existing storage sites. In case of a storage formation providing only low withdrawal rates due to e.g. a low formation permeability, the delivery can be increased by adding storage wells.

2.3 Induced effects

The construction as well as the operation of a porous media gas storage facility induces – to varying extent – hydraulic (H), chemical (C), geomechanical (M) and thermal (T) effects in the subsurface. Such THMC-effects are in general linked to each other by feedback reactions, with the degree of coupling depending on the individual processes.

Fluid flow in the porous medium is a result of spatial pressure differences in the fluid. Hence, the injection or withdrawal of any fluid such as gas in the subsurface will result in hydraulic effects by a change of the pressure- and fluid phase distribution in the storage formation. Obviously, constructing as well as operating a porous media gas storage site will result in such hydraulic effects as the initially present fluid is displaced by the gas to be stored. The extent of the gas phase depends on the volume of the stored gas and the geometry of the storage formation. Thus, depending on the storage site, the extent of the gas phase can be highly anisotropic with the lateral extent being in the range of up to several km. Given that functional seals are a requirement for potential gas storage sites, the vertical extent of the gas phase is limited by the thickness of the formation and is thus on the order of several meters up to several 10s of meters.

For aquifer gas storage, i.e. not a depleted hydrocarbon field, the initial reservoir pressure has to be increased several bars for an active displacement of the formation water by gas (Katz et al. 1959). The reach and magnitude of such a pressure signal is highly dependent on the injected fluid volume as well as the geometry, extent and the hydraulic properties of the storage formation. Sealing faults can present a boundary to induced hydraulic effects, resulting in a reservoir compartmentalization (e.g. Zoback 2010; Birkholzer et al. 2011). The maximum allowable overpressure is governed by the local geomechanical stress state (e.g. Zoback 2010), indicating the strong interconnection of hydraulic and geomechanical effects. In Germany the average of the maximum allowable overpressure gradients at existing gas storage sites is 0.168 bar/m (Sedlacek 1999). According to the Schlumberger oilfield glossary (*www.glossary.oilfield.slb.com*), the normal hydrostatic pressure gradient for formation water (100 000 ppm total dissolved solids) is 0.10516 bar/m. Thus, the pressure envelope in which a storage site can be operated in generally increases with increasing formation depth. Little research is available on the reach or extent of pressure perturbations caused by aquifer gas storage. However, some knowl-

edge can be transferred from research on CO_2 injections in aquifer structures. Studies show that pressure effects induced by CO_2 injections can be expected in distances of several km, depending on the extent and permeability of the storage formations (e.g. Birkholzer et al. 2009; Birkholzer et al. 2011; Schäfer et al. 2012; Benisch and Bauer 2013; Thibeau et al. 2014). Hydraulic effects induced through a storage operation are strongly coupled with induced mechanical, thermal and chemical effects through the induced pressure perturbations causing fluid flow as well as the change in fluid phase distributions.

Induced hydraulic effects as described here can be monitored using storage and observation wells. For a detailed prognosis numerical scenario simulations can be used. In case of laminar flow of more than one fluid phase in a porous medium the mathematical-physical description is given by multiphase flow equations based on Darcy's law (see equation (1), Chapter 3.2). The applied models are well established in the oil and gas industry and can readily adapted to H_2 storage in aquifers, provided that the hydraulic parameters of storage formation are sufficiently well known.

As aforementioned, the change in fluid pressures within a formation results in a change in the local stress state of the rock-fluid system. Thus, hydraulic effects can result in a geomechanical response of the system. Geomechanical effects induced by aquifer storage of H_2 are complex and beyond the scope of this thesis. Nevertheless, a short overview on potentially important effects is given herein for completeness. Geomechanical effects can be a result of the storage operation itself but also the construction of the storage site through wellbore stability problems (Zoback 2010). During operation the excessive flow rates can result in sand production from the storage well during withdrawal or hydraulic fracturing during injection (Carlson et al. 1992; Zoback 2010). Such formation damage is clearly not desired and thus the storage operation is planned in a way that such effects do not occur. However, the pressure perturbations caused by the injection and withdrawal of gas can also result in large scale geomechanical effects such as movement of the land surface above a gas storage site, as observed e.g. for storage of natural gas (e.g. Teatini et al. 2011; Tenthorey et al. 2013) or the reactivation of existing but closed faults, which could in turn affect the integrity of the sealing formations (Rutqvist 2012). During withdrawal the land surface moves vertically down and horizontally towards the maximum pressure decline, while during injection the opposite is happening with the land surface being lifted and moving horizontally away (Teatini et al. 2011). Measurements of such movements can for example be obtained by satellite based radar scans. In the case of a seasonally operated natural gas storage in a depleted gas reservoir in northern Italy at a depth of around 1100 to 1500 m below the surface, vertical and horizontal movements of around 30 mm over the course of the approximately half-year long withdrawal period were measured (Teatini et al. 2011). Again, research from the fields of CO_2 storage (e.g. Rutqvist et al. 2008; Rutqvist 2012; White et al. 2014; Orlic 2016) or natural gas exploration (e.g. Hermansen et al. 2000; Nagel 2001; Hettema et al. 2002; Mallman and Zoback 2007) can be used to infer some knowledge on the geomechanical effects induced by storage operations.

Geochemical effects are induced directly by changing the fluid composition through dissolution of the injected gas in the connate formation water. Once dissolved, the hydrogen can react with other dissolved components in a-biotic and biotic reactions (see e.g. Cord-Ruwisch et al. 1988; Reitenbach et al. 2015). Hydrogen can for example react via methanogenesis or acetogenesis, resulting in the production of methane and acetate, respectively (Cord-Ruwisch et al. 1988). Hydrogen can furthermore be converted in sulphate reduction reactions, potentially resulting in the production of highly corrosive H_2S (e.g. Reitenbach et al. 2015). Such reactions obviously result in a reduction of the hydrogen in place in the storage formation, which could negatively impact the storage performance. Furthermore, acidic reaction products could result in mineral dissolution but also precipitation (Reitenbach et al. 2015). As a consequence of the dissolution and precipitation changes in the porosity and permeability of the storage formation can be expected. Such induced chemical reactions can obviously only occur if hydrogen is present. Thus, the spatial extent of the gas phase can be used as proxy for the space in which such chemical reactions may occur. However, induced chemical effects

in the near well bore regions are probably more significant for the storage operation as e.g. effects of porosity and permeability changes can significantly impair the individual performance of the well. It must be noted that most reactions occur in the water phase. Thus, a drying of the region near the well bore through the cyclic withdrawal of moist gas and the re-injection of dry gas will affect the induced chemical effects. Again, feedback between processes must be accounted for as e.g. the occurrence of biotic reactions is limited to the temperature window the microorganisms can work in. Furthermore, elevated temperatures could promote dry out zones near the wells, which could hinder geochemical reactions. Besides directly induced geochemical effects by the means of hydrogen reacting within the storage system, also indirect reactions are plausible. The injected gas could displace saline formation water through fault systems (e.g. Jolley et al. 2007), resulting in a disequilibrium between rocks and fluid triggering geochemical reactions (Zhao et al. 2007). Such indirectly induced geochemical effects could potentially occur in significant distances of several km from the gas storage and are thus far more wide spread than directly induced geochemical effects. Predictions of such indirect or direct geochemical effects induced by a storage operation can be assessed by scenario simulations. To achieve this, the contributing geochemical reactions must be quantified and coupled models capable of dealing with multiple geochemical reactions, heat transport and multiphase-multicomponent flow and transport must be available.

One factor which affects the induced thermal effects during a hydrogen storage operation is the temperature with which the hydrogen is injected into the storage. If the temperature of the hydrogen differs from that of the storage formation the gas injection results in temperature perturbations and thus induced thermal effects. The magnitude of such an induced thermal effect depends on the site-specific details. Assuming a geothermal gradient of around 0.03 °C/m, temperatures around 25 to 40 °C are given for typical storage formations depths of 500 to 1000 m. The temperature of the injected hydrogen depends on the site-specific surface installations such as the modules used to produce the hydrogen. Common modules used for hydrogen generation via water electrolysis have operating temperatures of up to 100 °C, with the efficiency generally increasing with temperature (Ursúa et al. 2012; Sterner and Stadler 2014). Thus, the hydrogen temperature after generation could differ significantly from the temperature of the storage formation. Commonly used electrolyser modules have maximum operating pressures of around 30 bars in alkaline electrolysis and around 50 bars during proton exchange membrane electrolysis (Ursúa et al. 2012; Sterner and Stadler 2014), which is at the lower end of hydrostatic pressures at typical storage depths. Thus, additional compression of the gas may be required prior to injection during which the gas will heat up (e.g. Katz et al. 1959). However, coolers might be used to lower the gas temperature (e.g. Wang and Economides 2009). The temperature perturbation caused by the injection temperature will be dampened by the heat capacities of the residual formation water and the solid phase. No barriers to heat transport exist, thus induced temperature perturbations will spread advectively and conductively within the storage formation and conductively into adjacent formations. Apart from the gas temperature during injection, thermal effects can be induced by the Joule-Thomson effect, which describes temperature changes in gas undergoing an isenthalpic pressure reduction (Joule and Thomson 1854). During injection and withdrawal periods the flowing gas is experiencing such a pressure reduction and thus temperature changes due to the Joule-Thomson effect can be expected. So far this effect has been studied for CO_2 storage (e.g. Oldenburg 2007; Singh et al. 2012), but not for a cyclic gas storage operation. At typical reservoir conditions hydrogen has a negative Joule-Thomson coefficient (Johnston et al. 1946). Thus, the Joule-Thomson effect will result in a temperature increase during a hydrogen storage operation. Lastly, the evaporation of residual formation water into the gas phase, which is subsequently removed from the storage during withdrawal, will result in a temperature decrease. Clearly, induced thermal effects are strongly linked to the induced hydraulic effects such as the distribution of the gas phase but also the pressure differences. Alike the flow equations, the heat transport in a porous medium can be described by partial differential equations (see equation (4), Chapter 3.2).

2.4 Affected pore space volumes

In Germany, the use of the subsurface is regulated by several laws, including the German mining law (Bundesberggesetz), which applies to the exploration of natural resources such as oil and gas. The currently employed method to allocate the limited space of the subsurface in Germany is to follow a principle of "first come-first serve" (Bovet 2014). Hence, no evaluation regarding the implication of the individual use on other potential usage options is required. No subsurface formations can by law be reserved for specific types of use. This could result in a potential storage formation for subsurface energy storage being unavailable due to other usages at the site or in its vicinity. Such competition can occur in form of a direct competition of different usage options for the same structure or in the form of an indirect competition where a given subsurface usage option prohibits the use of a structure for a porous media gas storage due to induced effects such as pressurized fluids or temperature perturbations (Kabuth et al. 2017). Thus, besides the dimensioning of a subsurface energy storage, also the induced effects as well as the specific monitoring requirements should be taken into account for a sustainable subsurface planning (Kahnt et al. 2015). For such an assessment, three major categories of volumes linked to each potential subsurface usage are identified. These are the "operational space", the "affected space" and the "monitoring space" (Kabuth et al. 2017). Of these the operational space is the volume of the subsurface which is directly used, e.g. the extent of the gas phase in a porous media gas storage (Fig. 2.2). The affected space on the other hand is the volume in which thermal, hydraulic, mechanical or chemical (THMC) effects may be induced by e.g. a storage operation. Lastly, the monitoring space is the volume of the subsurface required for the monitoring of the individual usage. Modelling tools are required to estimate such spaces prior to a storage operation based on e.g. threshold values such as tolerable pressure or temperature changes. During operation, these spaces can be monitored using the induced effects of the storage operation.

For the application of a subsurface spatial planning concept based on the previously introduced operational, affected and monitoring spaces, modelling tools and thus an accurate description of the various THMC-effects occurring during a storage operation are required. Given a proper and detailed parameterization of the individual processes (Dethlefsen et al. 2016), these effects can be simulated a-priori to a field application using commercial and scientific numerical modelling tools. This however, might necessitate additional model development if required processes or coupling links between processes are missing in the available modelling tools. Coupled scenario simulations can then be used to determine the necessity to consider a specific process or coupling link for e.g. the estimation of usage spaces of a porous media gas storage.

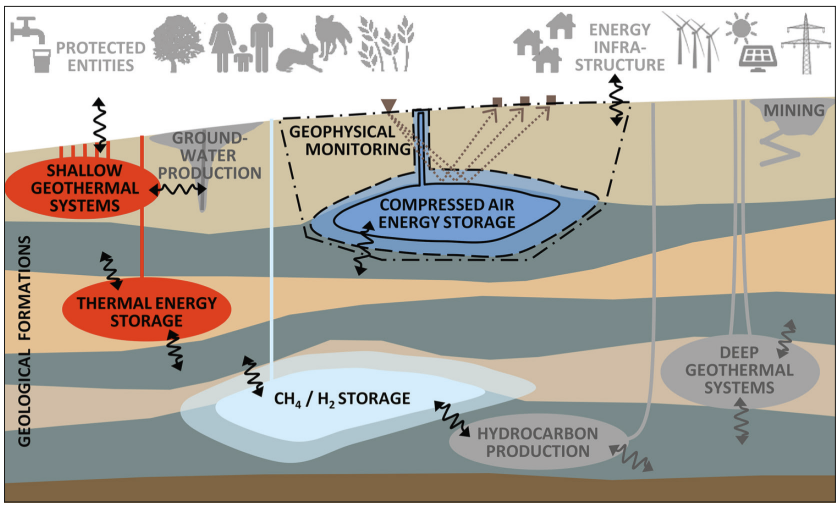

Fig. 2.2 Schematic depiction of different usage options and protected entities (Kabuth et al. 2017). Solid black lines indicate the operational space of a usage option, dashed lines depict the affected space. The black dashed-dot line indicates the required monitoring space. The black arrows depict mutual interactions between different usages.

3 MODEL DEVELOPMENT FOR OGS-ECLIPSE

In the following chapter a coupling approach for OpenGeoSys and ECLIPSE as well as the implementation of the Joule-Thomson effect in OpenGeoSys are presented. The underlying mathematical model is described in Chapter 3.2. A short description of the individual simulators is given in Chapter 3.3 and 3.4. The developed coupling scheme of the two simulators is explained in Chapter 3.5 and the implementations are verified in Chapter 3.6. The model development and validation of the Joule-Thomson effect in OpenGeoSys is presented in Chapter 3.7. The chapter is concluded with two application examples in which the coupled OpenGeoSys-ECLIPSE simulator is used for simulations in the context of subsurface porous media gas storage. Parts of this chapter are published as:

Pfeiffer WT, Graupner B, Bauer S (2016) The coupled non-isothermal, multiphase-multicomponent flow and reactive transport simulator OpenGeoSys-ECLIPSE for porous media gas storage. Environ Earth Sci 75:1347. doi: 10.1007/s12665-016-6168-2

3.1 Introduction

Complex thermal (T), hydraulic (H), geomechanical (M) and chemical (C) processes, are omnipresent in applications making use of the geological subsurface like oil and gas exploration, nuclear waste disposal, CO_2 storage and more recently geothermal energy storage as well as geoenergy storage (Bauer et al. 2013). As discussed previously, the latter two could be employed to mitigate shortages in power production arising from the extensive use of renewable sources. Potential storage options are high and low enthalpy heat storage systems using borehole heat exchanges or open well systems as well as mass storage technologies using either a chemical energy carrier such as H_2 or CH_4 or a mechanical energy storage, i.e. compressed air. Either of the storage technologies will, with varying magnitude, induce thermal, hydraulic, mechanical and chemical effects in the subsurface. The importance of the individual effect and therefore the process strongly depends on the investigated scenario, allowing case specific simplifications. However, the individual processes are in general coupled to each other by various parameters. Furthermore, these parameters typically also depend on the current state of the system, i.e. pressure, temperature and chemical composition. Thus, predictions of coupled effects are required for an adequate prognosis of induced effects. Several numerical simulators have been developed to address such problems e.g. the TOUGH codes (Pruess 2004), OpenGeoSys (Kolditz et al. 2016), DuMu^X (Freiboth et al. 2009; Flemisch et al. 2011), FEFLOW (Diersch 2014), ABAQUS (Börgesson 1996). However, not all codes can be used for general coupled THMC-systems due to code specific limitations. Instead of developing another code to fulfil this demand, two or several existing and well proven codes can be coupled together in order to benefit from their respective strengths such as implemented processes, numerical stability, flexibility or speed.

In this work, a coupling approach for the THMC-simulator OpenGeoSys and the proprietary reservoir simulation software ECLIPSE (© Schlumberger) is presented. OpenGeoSys is a scientific open source finite element code which is used in a variety of fields such as reactive transport modelling (e.g. Beyer et al. 2012; Shao et al. 2013), geothermal applications (e.g. Hein et al. 2016) and energy related research (e.g. Böttcher et al. 2012). ECLIPSE on the other hand is a reservoir simulation suite mainly used in the fields of hydrocarbon exploration as well as for CO_2 storage applications (e.g. Jessen et al. 2005; Kempka et al. 2010; Benisch and Bauer 2013; Ma et al. 2015). The main idea behind the coupled simulator is to harness the efficiency of the ECLIPSE simulator in solving multiphase-multicomponent problems and combining it with the flexibility of OpenGeoSys to account for geochemical and thermal feedback. The

principle of the coupled OpenGeoSys-ECLIPSE simulator presented here is based on a previously developed iteration of the OpenGeoSys-ECLIPSE simulator tailored specifically for use in CO_2 storage applications (Graupner et al. 2011). The coupled simulator is capable of dealing with complex THMC-systems such as those encountered in the field of subsurface energy storage utilizing hydrogen (H_2) or synthetic methane (CH_4), including thermal and chemical feedbacks on the flow and transport simulation. All implementations are validated against simulations conducted with one of the simulators individually to ensure the regularity of the coupled simulator. Furthermore, the Joule-Thomson effect (Joule and Thomson 1854), which describes temperature changes due to gas flow through a porous medium is implemented in OpenGeoSys, allowing for a more accurate estimation of induced thermal effects. Lastly two application examples of possible usage scenarios of the coupled OpenGeoSys-ECLIPSE simulator in the field of porous media hydrogen storage are constructed and simulated.

3.2 Mathematical Model

In the current state the OpenGeoSys-ECLIPSE simulator is capable of considering hydraulic, thermal and chemical coupling. Thus, the description of the mathematical model can be reduced to thermal, hydraulic and chemical processes, with each being described by a set of partial differential equations (PDEs). The general multiphase flow equation for a phase α is given as (Bear and Bachmat 1990)

$$\frac{\partial(\rho_\alpha n S_\alpha)}{\partial t} - \nabla\left(\rho_\alpha \frac{k_{r,\alpha}}{\eta_\alpha} k(\nabla p_\alpha - g\rho_\alpha)\right) - q_\alpha \rho_\alpha = 0 \tag{1}$$

with ρ_α [kg/m³] the density of the phase α, n [–] the porosity of the matrix, S_α [–] the phase saturation, k_r [–] the relative phase permeability, η_α [Pa × s] the viscosity of phase, k [m²] the intrinsic permeability, p_α [Pa] the phase pressure and g [m/s²] the gravitational acceleration. The individual phases are related to each other by the capillary pressure as well as the phase saturations which must sum up to unity. The relative phase permeability and the capillary pressure are usually described as a function of the phase saturations.

Mass transport of a component in a fluid phase can be through advective and diffusive-dispersive fluxes. The corresponding mass balance equation of component i in phase α is (e.g. Bear and Bachmat 1990)

$$\frac{\partial(n S_\alpha C_\alpha^i)}{\partial t} + \nabla\left(n S_\alpha\left(v_\alpha C_\alpha^i - D_\alpha^i \nabla C_\alpha^i\right)\right) - n S_\alpha Q_\alpha^i = 0 \tag{2}$$

with $C_\alpha{}^i$ [mol/m³] the concentration of the component, v_α [m/s] the phase velocity obtained by solving the flow equation (1), $D_\alpha{}^i$ [m²/s] the phase and component specific diffusion-dispersion coefficient and $Q_\alpha{}^i$ the sources/sink term of the component in phase α. The diffusion-dispersion coefficient is given as

$$D_\alpha^i = D_{diff,\alpha}^i \tau_\alpha + D_{disp,\alpha}^i \tag{3}$$

with $D_{diff,\alpha}{}^i$ [m²/s] the component specific molecular diffusion coefficient in phase α, τ_α [–] the tortuosity of phase α and $D_{disp,\alpha}{}^i$ [m²/s] the dispersion coefficient.

For the heat transport local temperature equilibrium is assumed between all phases including the porous matrix. Thus, all heat flux terms can be written in a single equation. In difference to the mass transport, the conductive transport of heat through the matrix has to be accounted for when solving heat transport problems. Following Bear and Bachmat (1990) multiphase heat transport can be described as

$$\frac{\partial(c\rho\, T)}{\partial t} + \sum_\alpha \nabla(n S_\alpha c_\alpha \rho_\alpha v_\alpha T) - \nabla(D^T \nabla T) + Q^T = 0 \tag{4}$$

with T [K] the temperature of the system, $c\rho$ [J/m³/K] the effective heat capacity, D^T [W/m/K] the thermal diffusion-dispersion coefficient and Q^T the sources and sinks of heat. The effective heat capacity is defined as

$$c\rho = (1-n)c_s\rho_s + \sum_\alpha (n S_\alpha c_\alpha \rho_\alpha) \tag{5}$$

with c_s [J/kg/K] the specific heat capacity of the solid phase and c_α [J/kg/K] the specific heat capacity of phase α. The thermal diffusion-dispersion coefficient is defined as

$$D^T = (1-n)\lambda_s + \sum_\alpha (nS_\alpha \lambda_\alpha) + \sum_\alpha (nS_\alpha D_\alpha^t) \quad (6)$$

where λ_s [W/m/K] is the thermal conductivity of the solid, λ_α [W/m/K] the thermal conductivity of phase α and $D_\alpha{}^t$ [W/m/K] the thermal dispersion coefficient in phase α. The PDEs (1), (2) and (4) are strongly coupled to each other by various parameters such as phase densities and viscosities. Numerical methods are commonly used for solving the PDEs as analytical solutions only exist when simplifying assumptions are made regarding the model geometry, parameter distributions and boundary conditions.

3.3 OpenGeoSys

OpenGeoSys is an open source, scientific code for the numerical simulation of THMC-processes in porous media (Kolditz et al. 2016). OpenGeoSys employs the standard Galerkin Finite Element (FE) method for the solution of partial differential equations and has been previously used for reactive transport modelling (e.g. Bauer et al. 2006; Beyer et al. 2006; Beyer et al. 2009; Shao et al. 2013; Ballarini et al. 2014), non-isothermal flow and geothermal energy systems (e.g. Boockmeyer and Bauer 2014; Hein et al. 2016) as well as for CO_2 storage (e.g. Böttcher et al. 2012; Kolditz et al. 2012; Beyer et al. 2012; Benisch et al. 2013; Singh et al. 2014). Apart from the already mentioned coupling to ECLIPSE, OpenGeoSys can also be used in combination with a variety of other well-known software packages such as GEMS (Kosakowski and Watanabe 2014), PHREEQC (Xie et al. 2006; He et al. 2015) or ChemApp (Li et al. 2014) for geochemical reactions. Besides those options, OpenGeoSys can also solve geomechanical and geochemical processes internally (Ballarini et al. 2014; Beyer et al. 2016). At the core OpenGeoSys employs a process oriented approach, meaning that the underlying PDEs of all processes can be solved using the same object functions (Kolditz and Bauer 2004). During an OpenGeoSys simulation run the considered coupled processes can be solved using a monolithic scheme or sequentially in each time step.

3.4 ECLIPSE

Together with the reservoir simulators IMEX and GEM (© Computer Modelling Group), ECLIPSE is one of the most widely used simulators in the exploration and production (E&P) industry and offers robustness as well as computational speed. Other applications of ECLIPSE are CO_2 storage simulations as well as other energy related research such as e.g. unconventional resources (e.g. Jessen et al. 2005; Kempka et al. 2010; Benisch and Bauer 2013; Ma et al. 2015). The ECLIPSE simulation suite consists of the ECLIPSE 100 and the ECLIPSE 300 simulators, which are a black oil and compositional model (Schlumberger 2015). Both simulators, from herein referred to as E100 and E300, and when undifferentiated as ECLIPSE, use a Finite Differences (FD) discretization scheme. Besides a fully implicit formulation and an implicit pressure, explicit saturation formulation (IMPES), a compromise termed adaptive implicit method, which uses a fully implicit solution for cells with a high throughput and an implicit pressure, explicit saturation scheme for the rest, can be used to solve the PDEs. By default the stable fully implicit solution procedure is used in E100. Different to that the default formulations used in E300 are the adaptive implicit method for compositional runs and the fully implicit scheme for black oil and thermal runs, respectively (Schlumberger 2015). Besides the OpenGeoSys-ECLIPSE simulator described in this work, ECLIPSE can also be used in conjunction with the finite-element geomechanics simulator Visage (© Schlumberger) through the interface ECL2VIS (Onaisi et al. 2002).

3.5 Simulator coupling

The process-oriented approach of OpenGeoSys is reflected in Fig. 3.1. For a combined multiphase flow, species and heat transport simulation, first the flow equations are solved, termed flow process, followed by the solution of a transport equation for each component in each fluid, gas or sol-

id phase. While local temperature equilibrium is assumed for the heat transport resulting in the system temperature being the primary variable, each species in each phase is represented by its own primary variable. Consequently, phase disequilibrium conditions can be accounted for in the mass transport.

In a coupled simulation, the flow process of OpenGeoSys is replaced by an ECLIPSE simulation while the individual mass transport processes can either be handled in OpenGeoSys subsequent to the flow simulation or completely in ECLIPSE together with the flow simulation, if the component is a major phase constituent (Fig. 3.1). Therefore, it is possible for transported components to exist in only one of the simulators, if the component is not a major phase constituent, or in both simulators, when component concentrations are exchanged between the simulators. This is represented in Fig. 3.1 by showing the OpenGeoSys Mass Transport twice, either in combination with the flow simulation and within the interface, if it is a major phase constituent, or further down in the process list outside the interface. This can be useful either to minimize the computational effort required during the simulation as less data has to be handled or to overcome simulator limitations regarding the choice of components, i.e. dissolved species cannot be directly included in an ECLIPSE simulation.

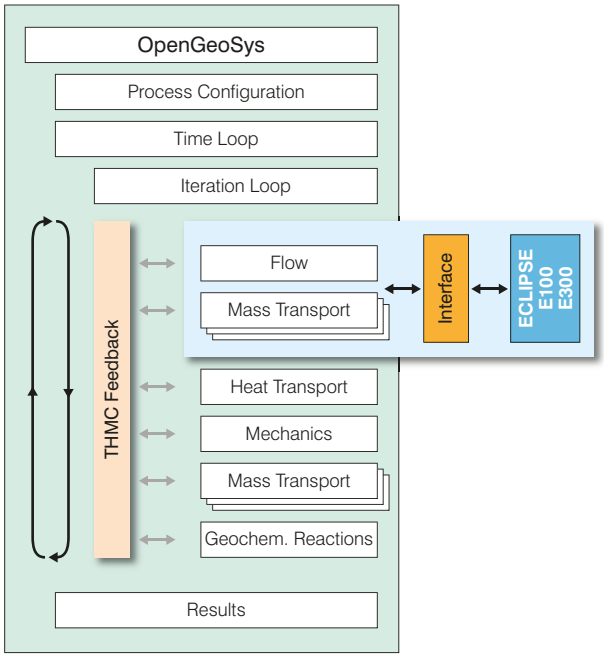

Fig. 3.1 Process structure during a coupled OpenGeoSys-ECLIPSE simulation. Grey arrows indicate potential THMC feedback pathways.

The coupling of the two simulators follows an operator splitting approach in which OpenGeoSys provides the overall framework of the simulation controlling the ECLIPSE execution and setting the absolute length of each time step for the flow and transport processes handled in ECLIPSE. However, ECLIPSE is still capable of splitting the time step into smaller intervals if required. The results of the ECLIPSE simulation run are then transferred to OpenGeoSys, which subsequently solves all remaining processes equations (Fig. 3.1). In addition to this basic sequential coupling of the two simulators in which ECLIPSE is called once per time step, also an iterative coupling scheme is available. Here the coupled simulator loops over ECLIPSE and all processes solved for in OpenGeoSys within one time step until the user provided error tolerance is reached. The coupling error is calculated based on the maximum change observed for any primary variable between the current and the initial iteration in each time step. The non-iterative sequential coupling can be sufficient for simulation of loosely coupled processes, e.g. simulations in which the time scale of changes differs largely between the processes (Rutqvist et al. 2002). The iterative coupling allows the simulation of cases with strongly coupled processes which require an iterative coupling (Taron and Elsworth 2009). Initial and boundary conditions have to be specified in the respective simulator used to solve the process, i.e. boundary conditions for the flow simulation have to be set in the ECLIPSE simulator. If a component is handled in both simulators, consistent initial and boundary conditions have to be applied in each simulator. To maintain consistency in fluid properties across both simulators even when feedback processes are included, e.g. when coupling heat transport and fluid flow, the phase densities and viscosities calculated in ECLIPSE are transferred to OpenGeoSys after each execution of ECLIPSE and used there in the subsequent process simulations of the corresponding coupling or time step.

Due to the different numerical schemes used in OpenGeoSys (FE) and ECLIPSE (FD), interpolating the results in each time step is mandato-

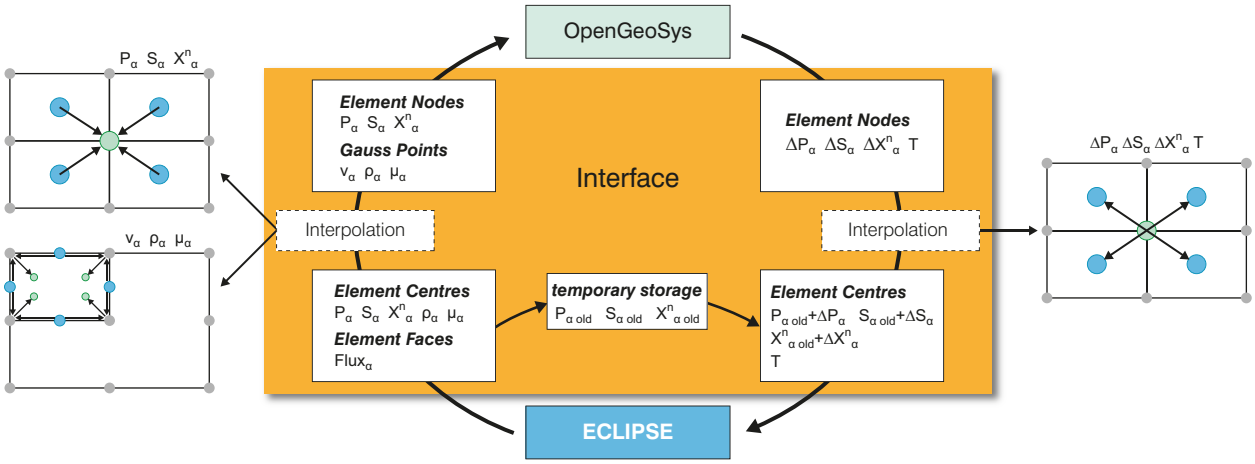

Fig. 3.2 Detailed overview on the OpenGeoSys-ECLIPSE coupling schematics during one iteration. Black arrows indicate the direction of data flow with p, v, S, ρ, μ and X representing pressure, velocity, saturation, density, viscosity and concentration of component n in phase α. T denotes the temperature. Δ denotes changes, which are added to the results from the last iteration stored in "temporary storage" as starting values for a new time step or iteration. The green and blue dots indicate the localization of the data in the mesh of OpenGeoSys and ECLIPSE, respectively.

ry even if the most restrictive approach of using corresponding grids in both simulators, consisting purely of regular hexahedron elements, is applied as the numerical solutions are valid at different spatial points. However, when matching the simulation grid to complex subsurface structures regular hexahedrons are suboptimal. The FE approach used in OpenGeoSys allows the use of several element types, namely lines, triangles, tetrahedrons, prisms, pyramids and hexahedrons to closely match such structures. ECLIPSE can accomplish more complex gridding tasks by collapsing or distorting the hexahedron elements in the grid following the corner-point gridding approach (Schlumberger 2015). To aid the process of grid generation a mesh converter was developed which translates even such complex ECLIPSE grids to a corresponding OpenGeoSys mesh consisting of hexahedrons, pyramids, tetrahedrons and prisms by splitting distorted elements if required (Wang and Bauer 2016). The implemented interface in OpenGeoSys is capable of ensuring correct data handling even in these geometrically complicated cases, which allows the simulation of real field sites with complex structural features. While data such as pressure, saturation and component concentrations are valid on the FD cell centres in ECLIPSE and have to be interpolated to the FE grid nodes in OpenGeoSys, the flow data has to be transferred from the cell faces in ECLIPSE to the gauss points of the OpenGeoSys elements. All interpolations are done using an inverse volume weighted approach. The phase velocities required by OpenGeoSys to solve mass or heat transport processes are calculated directly from the flow data taken from ECLIPSE instead of relying on recalculating the velocities based on the pressure distribution in the model domain which would be less accurate.

In the current version of the interface the data transfer between ECLIPSE and OpenGeoSys is done through the result output and the flexible restart functionality of ECLIPSE. In each time step or iteration, subsequent to the ECLIPSE simulation, all required output variables are read by OpenGeoSys from the ECLIPSE result file and stored element wise in an internal data structure (Fig. 3.2). Additionally the ECLIPSE grid file is read in the first time step to allocate and populate necessary data structures holding information on element faces and nodes for later use. After all additional processes have been solved in OpenGeoSys, the simulation is advanced to the next time step or, if the iterative coupling scheme is selected, to the next coupling iteration as long as the coupling error tolerance is not reached. Prior to the next call of ECLIPSE, the data entries in the ECLIPSE result file from the previous run used for the restart simulation are altered to account for feedback on the flow simulation (Fig. 3.2). This is done by first

calculating the changes in phase pressure, phase saturation and component concentrations due to the coupled processes in OpenGeoSys such as e.g. chemical reactions or heat transport. In a second step, these changes are interpolated from the element nodes to the element centres and added to the results from the previous ECLIPSE run, which are kept in temporary storage (Fig. 3.2). This approach is chosen, because interpolating only the variable changes instead of their absolute values further reduces the interpolation error.

SI units have to be used in OpenGeoSys and metric units in ECLIPSE, with the necessary unit conversions being carried out by the interface. The number of keywords which have to be read and thus the data which has to be transferred in each time step depends on the individual simulation. If ECLIPSE is solely used as a replacement for the flow process in OpenGeoSys, only pressures, saturations and the corresponding phase flow rates are transferred. However, if components are transported in ECLIPSE the number of required keywords depends on whether the E100 or E300 simulator is utilized as different variables are used to describe component concentrations in the individual phases. In either case, all additionally necessary variables to convert the results are taken directly from ECLIPSE in order to eliminate conversion errors. OpenGeoSys supports chemical reactions in and between all phases. As E100 does not allow gas dissolution in the water phase, the oil phase is treated as the water phase in a coupled E100-OpenGeoSys simulation. The concentration of the gas component in the "aqueous" phase thus is

$$C_n = \frac{RS * \rho_{g,surf}}{BO * MW_n} \tag{7}$$

with C_n [mol_n/m_{aq}^3] the concentration of component n in the aqueous phase, RS [$m_{g,\,surf}^3/m_{o,\,surf}^3$] the gas to oil ratio, $\rho_{g,\,surf}$ [$kg_g/m_{g,\,surf}^3$] the gas density at surface conditions, BO [$m_{o,\,res}^3/m_{o,\,surf}^3$] the oil formation volume factor and MW_n [kg_n/mol_n] the molar weight of the component. When using the compositional simulator E300 each component of the system apart from water is treated as a hydrocarbon component, which besides building up the oil and gas phases can also dissolve in the water phase if required. In an E300 simulation the concentrations of a component in the different phases are calculated as

$$C_{n,w} = \frac{MLSC_n * 1000}{S_w} - S_g \frac{YFW_n * \rho_{g,res}}{MW_n * S_w} - S_o \frac{XFW_n * \rho_{o,res}}{MW_n * S_w} \tag{8}$$

$$C_{n,g} = \frac{YFW_n * \rho_{g,res}}{MW_n} \tag{9}$$

$$C_{n,o} = \frac{XFW_n * \rho_{g,res}}{MW_n} \tag{10}$$

with $C_{n,\,\alpha}$ [mol/m_α^3] the concentration of component n in phase α, $MLSC_n$ [$kmol/m_{pv}^3$] the molar density of the component in the total pore volume of an element, S_α [–] the saturation, MW_n [kg/mol] the molar weight of the component, $\rho_{\alpha,\,res}$ [kg/m_α^3] the density of phase α at reservoir conditions as well as YFW_n [kg_n/kg_g] and XFW_n [kg_n/kg_o] the mass fraction of the component in the gas and oil phase, respectively. Indices w, g, o represent the water, gas and oil phase. The variables used to return the altered concentration data back to ECLIPSE are the RS and the $MLSC_n$ for E100 and E300, respectively. ECLIPSE then allocates the correct amount of component to the individual phases depending on the equation of state specified in the ECLIPSE simulation.

The thermal coupling is implemented as a one-way coupling between OpenGeoSys and ECLIPSE. Heat transport is solved in OpenGeoSys, subsequent to the ECLIPSE flow simulation, which provides the phase velocities and saturations. The temperature field as result of the heat transport simulation is transferred to ECLIPSE for the next time step (or iteration) and used as input for calculating temperature dependent variables such as phase densities or viscosities.

3.6 Model validation

The described OpenGeoSys-Eclipse interface has to be validated to ensure adequate simulation results when using the coupled simulator. Several test cases are created to test the individual functionalities of the interface of which four are presented here (Tab. 3.1). Because the respective simulators are well tested themselves (e.g. Kolditz

Tab. 3.1 Overview on the benchmarks used for testing the OpenGeoSys–ECLIPSE simulator.

#	Description	ECLIPSE	Dim.	Grid	Phases	Transport
1	Single phase radial flow and mass transport	E100	2	Cartesian	1	Conservative
2	Multiphase flow and mass transport	E100	2	Cartesian	2	Conservative
3	Multiphase flow	E100	2	Radial	2	–
4	Single phase flow and heat transport	E300	3	Cartesian	1	Heat
5	Multiphase flow and mass transport	E300	2	Radial	2	Conservative
6	Multiphase flow and reactive mass transport	E300	2	Radial	2	Non-conservative
7	Multiphase flow and reactive mass transport	E100	2	Cartesian	2	Non-conservative
8	Multiphase flow and reactive mass transport	E300	2	Cartesian	2	Non-conservative

Benchmarks 4, 5 and 8 are presented in this work

et al. 2015; Kolditz et al. 2016), the validation process can be reduced to tests comparing the results of the coupled simulator with those obtained from either a pure ECLIPSE or OpenGeoSys simulation of the same test case.

To validate the data transfer from ECLIPSE to OpenGeoSys, a 2D radial, multiphase-multicomponent simulation (#3) representing a gas injection into a sloped aquifer is used (Fig. 3.3). The total model extent is 200 m in lateral and 20 m in vertical direction using a discretization of 5 and 2.5 m, respectively. The upper most layer of the model drops from 500 m depth at the top to slightly more than 555 m at the flank of the model. Initially a hydrostatic pressure distribution is assumed throughout the aquifer with no gas in place. Boundary conditions for flow and mass transport processes are an injection of N_2 for the first 10 days followed by 10 days of H_2 injection using a constant rate of 50 m^3/day of gas at reservoir conditions. The pressure at the far side of the model domain is set constant. No additional processes are considered in OpenGeoSys. Because the boundary conditions are applied in the ECLIPSE simulator, the test case validates the data exchange from ECLIPSE to OpenGeoSys.

As the gas is injected, the pressure within the aquifer increases and the formation water is displaced towards the lower model boundary (Fig. 3.3 a). The change of injection composition after 10 days results in a zonation of the gas phase composition with high molar fractions of H_2 in the gas phase near the well and low values at the injection front of the gas phase (Fig. 3.3 b, Fig. 3.4 a). The comparison of the OpenGeoSys-ECLIPSE simulator using the basic sequential coupling scheme with a pure ECLIPSE simulation does not show visible differences (Fig. 3.4 a). However, small differences between the two simulations do exist with the absolute errors obtained for the N_2 component density being no more than 10^{-12} mol/m^3 prior to the switch in injection gas and 2×10^{-5} mol/m^3 after (Fig. 3.4 b). The corresponding relative error is about 0.00001 % and 0.003 % for the first and second stage of the simulation, respectively. The error regarding the H_2 component density is in a similar range. Phase saturations and pressures exhibit an even better match with no differences between the two simulators for most of the simulation time (Fig. 3.4 b). Only towards the end of the simulation phase pressures diverge once reaching an absolute error of 10^{-5} bar, which is 0.00001 % of the pressure observed at the respective element. The largest absolute error observed for the phase saturations is about 2×10^{-8} m^3/m^3, while the maximum relative errors stays below 0.0003 %. Given the good accuracy of the comparison, the validation of the data transfer from ECLIPSE to OpenGeoSys in the coupled simulator is shown.

The feedback from OpenGeoSys on the component transport in ECLIPSE is tested by changing component concentrations in OpenGeoSys and checking the corresponding feedback in the coupled ECLIPSE simulation. For this, H_2 is produced in the aqueous phase which should lead to a generation of a H_2 gas phase. The scenario thus represents a leakage scenario in which dissolved H_2 dif-

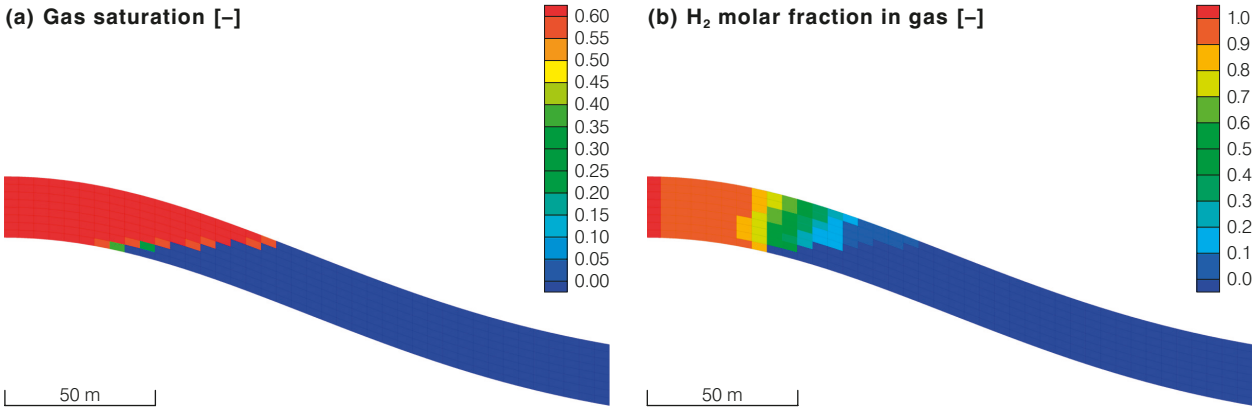

Fig. 3.3 (a) Gas saturation and (b) molar H_2 fraction in gas after 20 days in the OpenGeoSys–ECLIPSE simulation.

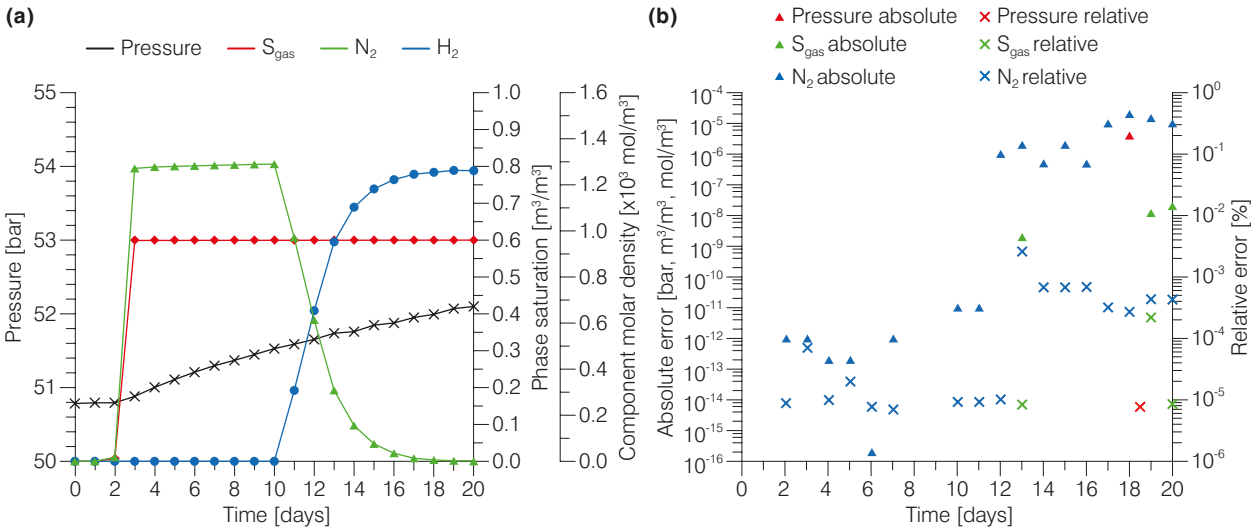

Fig. 3.4 (a) Comparison of pressure, gas saturation and total component densities at an observation point 15 m from the injection well and 8.75 m from the top of the model. Lines represent the result obtained from the coupled OpenGeoSys-ECLIPSE simulator while symbols indicate the reference results from a pure ECLIPSE simulation. (b) Temporal evolution of the absolute as well as relative differences between the pressure and saturation as well as the total N_2 component density obtained with ECLIPSE and OpenGeoSys–ECLIPSE in the whole model domain. The relative differences are calculated based on the corresponding explicit values obtained at an element. Missing data points indicate a perfect match of the simulators with not differences observed.

fuses into a shallow aquifer at a constant rate and accumulates there. The 2D test model consists of 20 by 5 cells with a spatial discretization of 0.5 m in horizontal direction and 0.4 m in vertical direction, respectively (Fig. 3.4). Model width is 1 m. A hydrostatic pressure distribution is assumed at the beginning of the simulation with constant pressure boundary conditions applied at both sides of the model domain. Within the source zone from 4 to 6 m along the base of the model domain H_2 is produced in the water phase at a rate of 200 mol/m^3_w/day. The addition of dissolved H_2 in the water phase results in increasing concentrations with time (Fig. 3.5a | 1day; Fig. 3.6). No H_2 gas phase is present at this stage (Fig. 3.5b | 1 day). Due to the continuous production, the H_2 concentration in the water increases until the solubility limit is reached. Then, a H_2 gas phase is generated and additional H_2 partitions into the gas phase. The H_2 gas saturation thus increases further, becoming larger than the value of the residual saturation of 0.1. From this point onward the H_2 gas is mobile, so that H_2 transport is mainly through the gas phase (Fig. 3.5 | 50 days). While the total content of H_2 in the model increases steadily, a sharp change in the H_2 content in the gas and water phase is

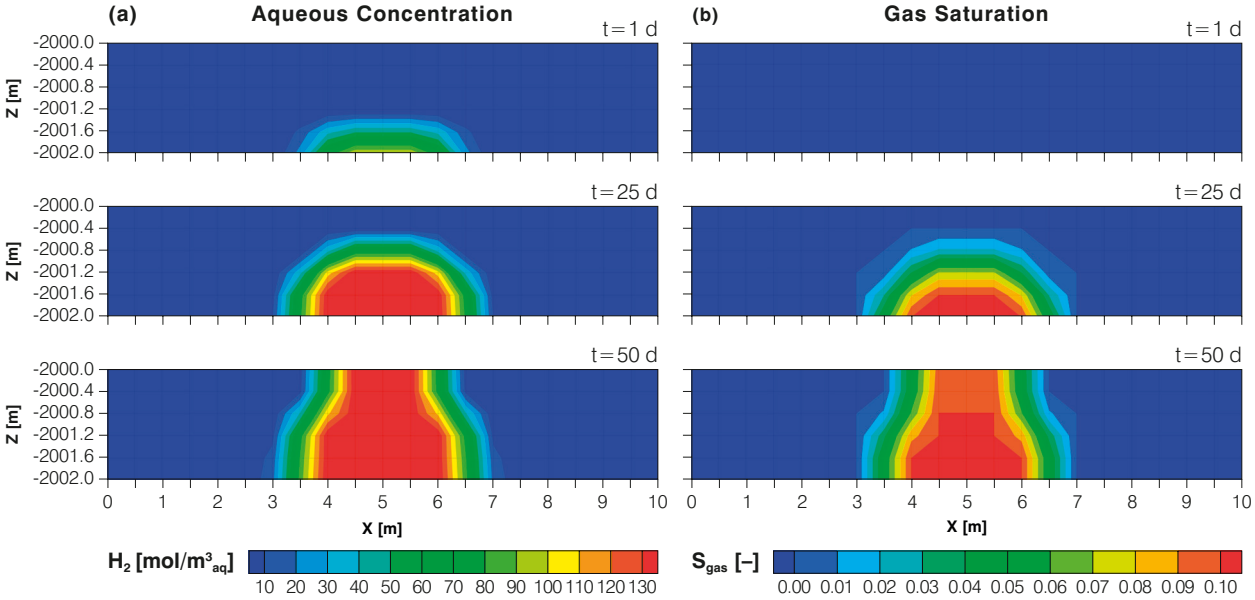

Fig. 3.5 (a) Aqueous H_2 concentration and (b) gas saturation after 1, 25 and 50 days of simulation.

observed whenever the H_2 gas can spread into a previously water saturated element (Fig. 3.6). The comparison of the evolution of the molar content in ECLIPSE and the theoretical value calculated from the specified production rate shows only a very slight offset reaching a maximum of -0.0014 % at the end of the simulation (Fig. 3.6). This is most likely due to small interpolation errors as well as inaccuracies in the flexible restart functionality of ECLIPSE, which accumulate over the course of the simulation. Even though the simulated process of a H_2 generation does not qualify as a realistic geochemical reaction, the feedback of the change in chemical composition on the flow process in ECLIPSE, in the coupled simulation as tested in this benchmark is validated.

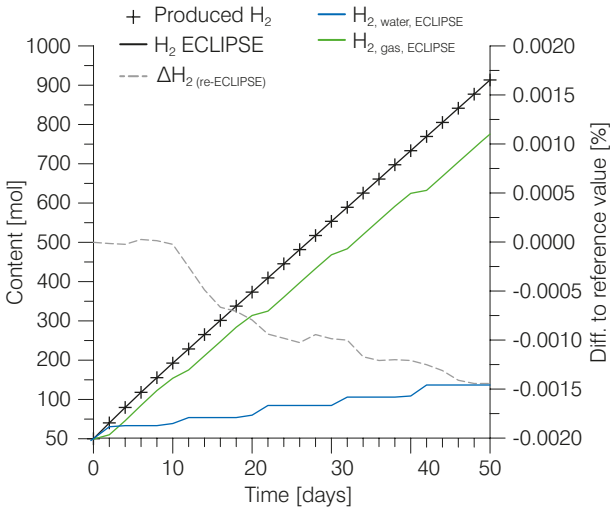

Fig. 3.6 Temporal evolution of the total H_2 content as well as the H_2 content in gas and water. The true value is the reference value calculated based on the applied production rate.

The thermal coupling of the OpenGeoSys-ECLIPSE simulator is validated by comparing the results obtained for a heat transport simulation with the coupled simulator to those of a pure OpenGeoSys simulation. In addition to using constant fluid properties, also the feedback of the heat transport on the fluid flow through variable fluid density and viscosity is taken into account in a second validation run. The model setup for both comparisons is identical using a 3D model of 10 by 3.1 by 3.1 m which is uniformly discretised in all spatial directions in steps of 0.1 m. A hydraulic gradient of 0.05 m/m parallel to the longest model extension is assumed. The flow in the simulation is controlled by using a constant influx and constant pressure boundary conditions on the left and right hand side of the model, respectively. In both model setups the initial temperature of the aquifer is set to 295 K. A heat source is placed at 2 m into the model from the left-hand side, which is represented by a constant temperature condition of 340 K. If no feedback of the temperature signal on the fluid parameters is considered, the viscosity and density are constant at 1000 kg/m³ and 0.0012956 Pa × s, respectively. When the feedback of the heat transport is taken into account, the flu-

id properties are calculated depending on the current temperature and pressure in each element.

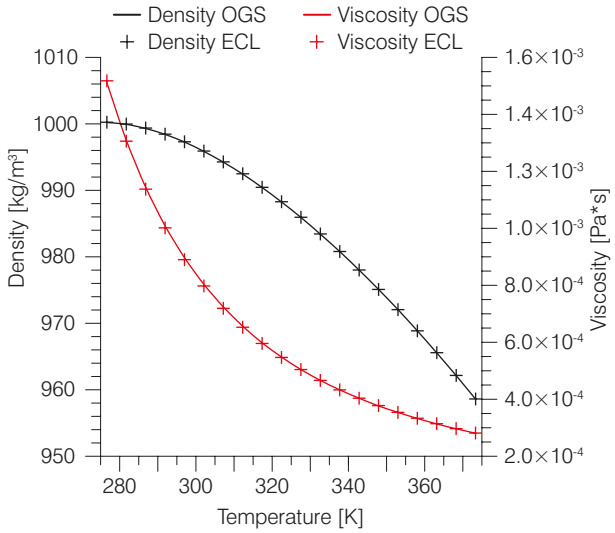

Fig. 3.7 Comparison of the water densities and viscosities obtained for different temperatures at a constant pressure of 6.2 bars when using the IAPWS-IF97 formulation for density (Wagner et al. 2000) and the McDermott et al. (2006) formulation for fluid viscosity in OpenGeoSys with values obtained from ECLIPSE E300.

In the OpenGeoSys simulation, the fluid density is calculated based on the 1997 industrial formulation of the International Association for the Properties of Water and Stream (IAPWS-IF97) (Wagner et al. 2000) while the fluid viscosity is calculated according to McDermott et al. (2006). The chosen formulations yield very similar density and viscosity values as compared to values used in ECLIPSE E300, with maximum relative differences in fluid viscosity and density being 0.7 % and 0.000029 %, respectively (Fig. 3.7).

Due to the groundwater flow, heat is transported away from the heat source and a temperature plume develops (Fig. 3.8). Because of the temperature dependency of fluid density and viscosity, an upward motion of the water is induced near the point of heat injection. The temperature distributions obtained for the simulation with no temperature feedback show a very good match (not shown) with nodal temperatures differing by less than ±0.005 K, which is 0.0015 % of the corresponding grid block temperature. Using the basic sequential coupling, slight offsets in the temperature distribution in the range of +0.247 K to -0.905 K, translating to 0.07 % and -0.28 %,

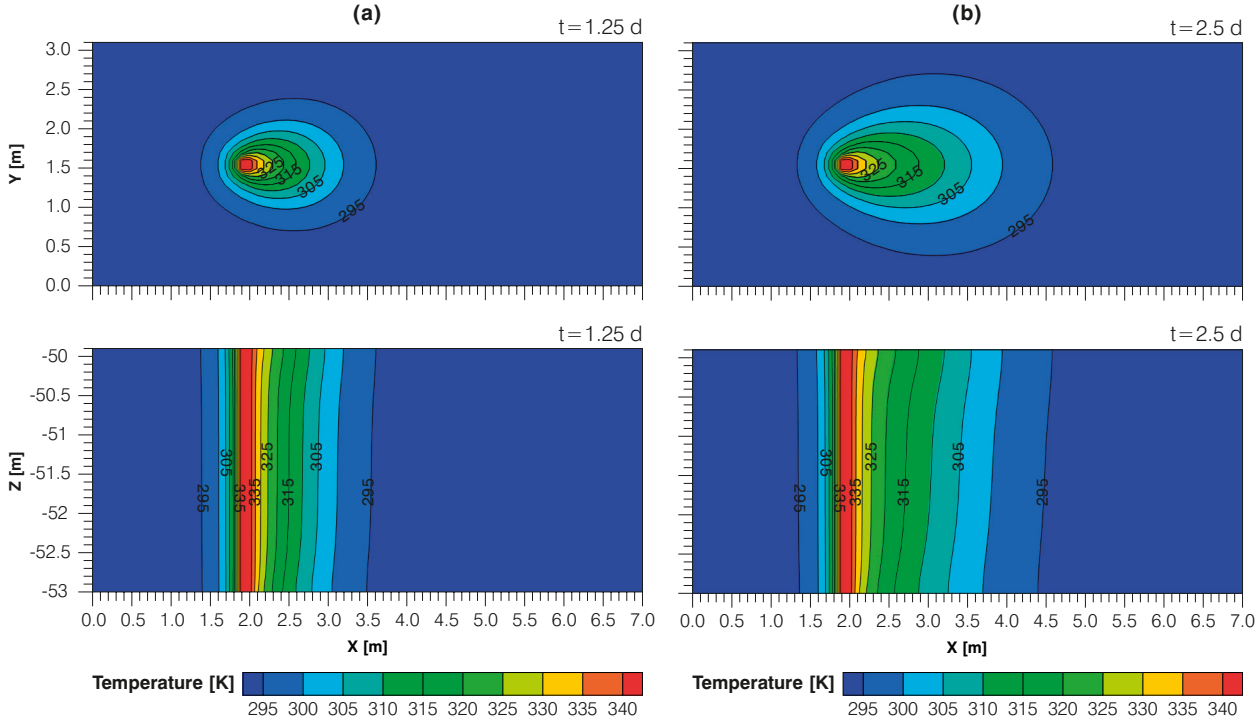

Fig. 3.8 (a) Comparison of the temperature distributions in the validation benchmark including thermal feedback after 1.25 days and (b) 2.5 days along a horizontal slice at the top of the model (top) and a vertical slice along the heat plumes symmetry plane (bottom) obtained with the OpenGeoSys-ECLIPSE simulator (contour fill) and the solitary OpenGeoSys simulation (black lines).

respectively, are visible between the two simulators when thermal feedback on the fluid flow is taken into account. The differences are restricted to within one grid block (Fig. 3.8 b). The largest differences can be observed in the vicinity of the heat source towards the top of the model domain. The average absolute difference between both simulations across all nodes, which experienced a change in temperature compared to the initial condition is 0.0345 K and the standard deviation, is 0.0761 K.

Using the implemented iterative coupling approach does not increase the accuracy significantly. The average of the absolute differences decreases to 0.0257 K with the standard deviation being 0.0718 K. However, the benefits of the iterative approach become more apparent when the time step size of the simulation is increased. In the validation test case, increasing the time step size by a factor of 10 results in maximum relative discrepancies of 1.45 % between OpenGeoSys and the coupled OpenGeoSys-ECLIPSE simulator in sequential mode. Using the iterative approach the maximum relative error between the two simulators decreases to 0.41 %. The persistent differences between the simulators can to some extent be attributed to the slight differences in fluid densities and viscosities used in both simulation runs. Since the overall differences are relatively small, the benchmark shows that the coupling of heat transport and fluid flow including thermal feedback can be simulated with a good accuracy using the coupled OpenGeoSys-ECLIPSE simulator.

3.7 The Joule-Thomson effect in OpenGeoSys

In a porous media gas storage, substantial flow rates can occur in the reservoir during injection and withdrawal phases. The gas flow from regions of higher pressure to lower pressure results in the gas expanding along the flow path. Assuming isenthalpic conditions, i.e. the change of temperature within the gas phase is faster than the exchange with the storage formation, the expansion of a real gas results in a change of temperature due to the Joule-Thomson effect (Joule and Thomson 1854; Oldenburg 2006). The ratio between the change in temperature for a given pressure drop yields the Joule-Thomson coefficient (JTC)

$$\left(\frac{\partial T}{\partial P}\right)_H = \mu_{JT} \tag{11}$$

The value of the JTC depends on the gas composition as well as the initial temperature and pressure conditions. Below the component specific Joule-Thomson inversion curve the JTC has a positive sign which leads to a cooling of the gas upon expansion as the pressure change is always negative. Above the inversion curve the JTC is negative which results in the gas heating up during expansion. To account for these effects in reservoir simulations using the OpenGeoSys-ECLIPSE simulator, the Joule-Thomson effect is implemented in OpenGeoSys for a system which may contain the components N_2, O_2, H_2, CH_4 and CO_2. This is done by first calculating the change in heat in the gas phase due to isenthalpic expansion

$$\Delta Heat_g = \mu_{JT}\, \Delta p\, c_g \rho_{\,g}\, V_g \tag{12}$$

with μ_{JT} [K/Pa] the JTC at the given pressure and temperature conditions, Δp [Pa] the pressure change, c_g [J/kg/K] the heat capacity of the gas and V_g [m³] the volume of gas. The obtained changes in the heat content are added to the heat transport equation (4) as nodal source terms. The required JTC can either be supplied through a look-up table or can be calculated during the simulation run using the methods of Span et al. (2000), Schmidt and Wagner (1985), Leachman et al. (2009), Setzmann and Wagner (1991) and Span and Wagner (1996), for N_2, O_2, H_2, CH_4 and CO_2, respectively. For a system consisting of a mixture of the components the effective JTC is calculated based on the molar fraction of each individual component in the system.

To validate the implementations a model setup similar to that used by Oldenburg (2007) for the validation of the Joule-Thomson effect in the TOUGH code is created (Fig. 3.9). The model resembles the original Joule-Thomson experiment, in which a thermally isolated gas is flowing from a high pressure region through a porous plug to a low pressure region and the temperature differences between the two regions are recorded. This setup is transferred to the validation model consisting of three zones, two high permeability zones separated by a low permeability zone in between.

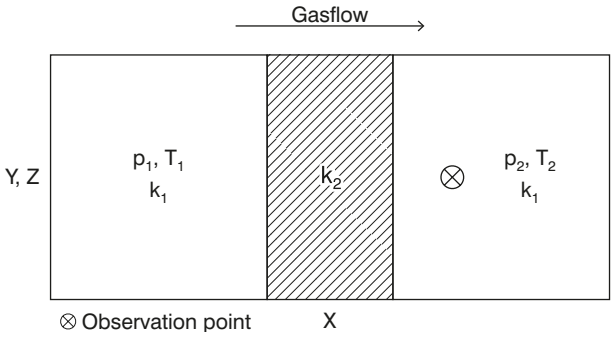

Fig. 3.9 Simulation setup used for the validation of the implemented Joule-Thomson effect. The shaded area represents the low permeability zone so that $k_1 > k_2$. The cross marks the position of the observation point at which the temperature change is monitored. As $p_1 > p_2$, the temperature downstream of the low permeability zone is changing so that $T_1 \neq T_2$.

Using equation (11), the change in temperature in the downstream high permeability zones divided by the pressure difference between the upstream and the downstream zone should yield the JTC of the individual component at the given initial pressure and temperature.

The total model dimensions are $10 \times 1 \times 1$ m, discretised in all spatial directions in 0.5 m. The low permeability zone, marked k_2 in Fig. 3.9, starts 3 m into the model domain and has a thickness of 1 m. The absolute permeabilities of the low and high permeability zones are 10^{-15} m^2 and 10^{-12} m^2, respectively. Porosity and gas saturation are 1, thus dampening effects due to the heat capacity of the solid or liquid phases are neglected. The validation runs are conducted for all available gas components for initial pressures from 10 to 100 bars and initial temperatures of 298.15 K and 323.15 K (Tab. 3.2). The pressure in the model domain is controlled via constant pressure boundaries on the left and right hand side of the model domain, with the left-hand boundary being kept constant at the initial pressure value and the right hand boundary being set to 5 bars below initial pressure upon the simulation start. The pressure reduction and thus the region of temperature change is mainly restricted to the low permeability zone. As a result of the pressure decrease during the gas flow through the low permeability zone, the temperature in the downstream high permeability zone differs from the initial temperature. This temperature change, in combination with the given pressure drop of 5 bars, is used to determine the JTC.

The calculated values are in very good agreement with the values given in the NIST webbook (Lemmon et al. 2016), with differences being within a few percent (Tab. 3.2). The greatest discrepancy between the published data and the results obtained with OpenGeoSys relative to the published data is 3.7 % for CO_2 at 298.15 K and 10 bars, which is well within uncertainties commonly accepted for equations of state (Oldenburg 2007). For CH_4, N_2, O_2 and H_2 the greatest relative differences in the calculated JTC relative compared to the published data are less than 1.2 %, 1.1 %, 0.65 % and 2.3 %, respectively. As the differences between the published data and the results obtained with OpenGeoSys are relatively small, the implementation of the Joule-Thomson effect in OpenGeoSys provides accurate results.

3.8 Application examples

Two application examples for the coupled simulator OpenGeoSys-ECLIPSE in the field of subsurface energy storage are given in this work. The first application example showcases the use of the coupled simulator for models of geochemical effects, which could occur during a porous media gas storage operation. The second example deals with thermal effects of such an operation by simulating the temperature change as a result of a cyclic flow pattern resulting from frequent storage cycles.

3.8.1 Simulating geochemical reactions with OpenGeoSys-ECLIPSE

Large scale subsurface energy storage of synthetic gases such as H_2 storage in porous formations could potentially be used to mitigate shortages originating from the extensive use of renewable energy sources (e.g. Sørensen 1975; Kroniger and Madlener 2014). However, due to the increasing use of the subsurface for various applications induced effects and impacts of such a porous operation should be assessed (Bauer et al. 2013). Furthermore, processes such as transformation reactions of H_2 to CH_4 as observed in gas storages containing H_2 rich town gas (Panfilov 2010) could potentially limit the applicability of a storage op-

Tab. 3.2 *Results of the validation runs for the implemented Joule-Thomson effect. The Joule-Thomson coefficients are calculated for a pressure drop of 5 bars. The NIST data is taken from Lemmon et al. (2016). At 298.15 K and 75 to 100 bars CO_2 is in the liquid state.*

T_1 [K]	p_1 [bar]	$\mu_{JT} - N_2$		$\mu_{JT} - O_2$		$\mu_{JT} - H_2$		$\mu_{JT} - CH_4$		$\mu_{JT} - CO_2$	
		NIST [K/bar]	OGS [K/bar]	NIST [K/bar]	OGS [K/bar]	NIST [K/bar]	OGS [K/bar]	NIST [K/bar]	OGS [K/bar]	NIST [K/bar]	OGS [K/bar]
298.15	10	0.2081	0.2097	0.2638	0.2649	-0.0304	-0.0301	0.4326	0.4350	1.0976	1.0572
298.15	25	0.1968	0.1983	0.2555	0.2566	-0.0311	-0.0308	0.4223	0.4251	1.1035	1.0630
298.15	50	0.1774	0.1790	0.2402	0.2414	-0.0325	-0.0320	0.3996	0.4030	1.0884	1.0540
298.15	75	0.1580	0.1595	0.2235	0.2248	-0.0339	-0.0333	0.3687	0.3725	–	–
298.15	100	0.1389	0.1404	0.2057	0.2070	-0.0353	-0.0345	0.3298	0.3339	–	–
323.15	10	0.1732	0.1744	0.2245	0.2252	-0.0345	-0.0342	0.3638	0.3655	0.8935	0.8623
323.15	25	0.1635	0.1647	0.2172	0.2180	-0.0351	-0.0348	0.3541	0.3560	0.8927	0.8622
323.15	50	0.1473	0.1485	0.2043	0.2051	-0.0362	-0.0358	0.3346	0.3368	0.8763	0.8488
323.15	75	0.1312	0.1324	0.1905	0.1914	-0.0373	-0.0368	0.3104	0.3130	0.8097	0.7909
323.15	100	0.1156	0.1167	0.1761	0.1771	-0.0384	-0.0377	0.2820	0.2847	0.5614	0.5709

eration and should thus be quantified prior to any field deployment. The first example presented here simulates such a possible transformation reaction during a porous media hydrogen storage operation. The model used for the simulation resembles the gas filled part of a dipping anticline storage formation into which H_2 is injected. The simulation includes both multiphase-multicomponent flow handled by E300 and the simulation of chemical reactions carried out in OpenGeoSys. The radial model domain extends 200 m in horizontal and 15 m in vertical direction and is uniformly discretised in 0.5 m increments. The top of the storage formation is 500 m below the land surface at the centre and dips down to around 540 m towards the flank. A homogeneous parameter distribution is assumed with a permeability of 500 mD and a porosity of 0.2. The residual water saturation is set to 0.4. The initial gas saturation within the storage formation is 0.6, hence no mobile water is present. Initially the gas is purely composed of N_2, which is used as cushion gas, as it can be assumed cheap due to its great abundance and is relatively inert to chemical reactions (Oldenburg 2003; Oldenburg and Pan 2013). A hydrostatic pressure distribution is assumed throughout the model domain prior to the gas injection. With the storage well being located at the top of the structure, the far boundary is assumed open by setting constant pressures. H_2 is injected with a constant rate of 10 m^3/d at reservoir conditions for a period of 50 days. An initial dissolved organic carbon concentration $C_{diss} = 5$ mol/m^3 is assumed as a reaction partner for the H_2 transformation to CH_4. CH_4 production is assumed to follow the reaction stoichiometry of methanogenesis:

$$4H_2 + C_{diss} \rightarrow CH_4 + 2H_2O \tag{13}$$

The transformation reaction is simulated by a Monod type kinetic reaction

$$\frac{dC_i}{dt} = kS_i \frac{H_2}{H_2+M} \frac{C_{diss}}{C_{diss}+M} \tag{14}$$

with C_i [mol/m_w^3] and S_i [–] as the concentration and stoichiometry coefficient of reaction educt or product i according to the methanogenesis reaction, the maximum reaction rate $k = 1 \times 10^{-7}$ mol/m^3_w/s and a Monod-constant $M = 0.1$ mol/m^3_w for both dissolved H_2 and C_{diss}. It has to be noted that the assumed reaction rate does not represent a detailed kinetic model of methanogenesis but is chosen to mimic the overall behavior. A realistic simulation of geochemical impacts of a H_2 injection would require consideration of interacting reactions like e.g. acetogenesis, nitrate reduction and sulphate reduction (e.g. Hagemann et al. 2016). The reaction is simulated at all nodes

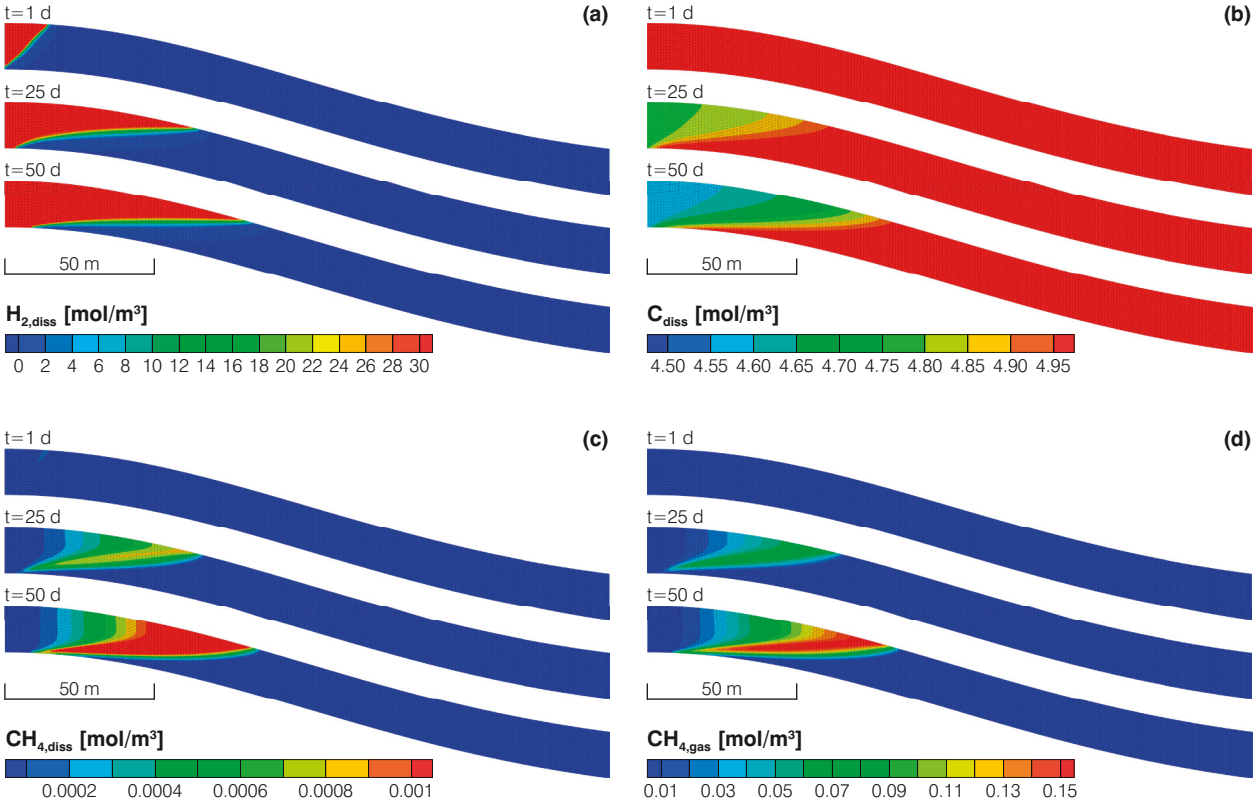

Fig. 3.10 (a) Aqueous H_2 concentration, (b) dissolved carbon, (c) dissolved CH_4 and (d) CH_4 in gas after 1, 15 and 50 days of simulation.

in OpenGeoSys, and the changes in gas phase composition are fed back to ECLIPSE through the interface of the coupled simulator. All gas components can dissolve into the connate water according to the solubility as defined in ECLIPSE. The injection of the H_2 changes the gas composition near the injection well as the N_2 is displaced.

The pressure in the model domain remains relatively constant as a result of the constant pressure boundary condition on the far side (not shown). Obviously, no change in gas saturation can be observed as the maximum gas saturation is already reached prior to the injection. As soon as the H_2 is injected, it dissolves in the connate water and dissolved CH_4 is produced at the expense of H_2 and aqueous carbon (Fig. 3.10 a, b). However, a decrease in the aqueous H_2 concentration is not visible as it is constantly replenished from the gas phase and the continuous H_2 injection. The concentrations of CH_4 near the injection well are low with higher concentrations obtained further away from the injection well (Fig. 3.10 c, d). This can be attributed to the CH_4 being stripped out of the water phase, as its partial pressure is low due the absence of CH_4 in the gas phase in this region. As the gas phase is mobilized the produced CH_4 is transported away from the injection well. Consequently, the highest concentrations of dissolved CH_4 are obtained at the front of the H_2 gas plume. As soon as the injection stops and the continuous supply of H_2 ceases, the CH_4 concentrations near the injection well will increase and eventually approach similar high values. Even though the chemical reaction considered in this simulation is not detailed per se, the resulting multiphase-multicomponent system is relatively complex. The simulated problem thus gives a good example of a potential use of the coupled OpenGeoSys-ECLIPSE simulator as neither simulator is capable of individually solving the stated problem without further simplifications.

3.8.2 The Joule-Thomson effect during gas storage operations

Thermal effects can have significant effects on fluid parameters and in consequence greatly influenc-

Tab. 3.3 Properties assigned to the individual model units in the simulation regarding pressure-induced temperature changes.

Model unit	k [m^2]	n [–]	$c\rho$ [J/m^3/K]	λ [W/m/K]	ρ [kg/m^3]
Storage	5.62546×10^{-13}	0.33	349	3.0	2650
Caprock	9.86923×10^{-20}	0.10	792	2.1	2500
Gravel pack	4.93462×10^{-12}	0.40	272	1.5	2400
Casing	9.86923×10^{-22}	0.01	888	2.0	2650

The thermal parameters are taken from VDI (2010)

ing fluid flow, mass transport and chemical reactions. Therefore, thermal effects occurring during a gas storage operation have to be considered in order to assess the importance of the individual feedback mechanisms. The second application example simulates temperature changes induced as a result of frequent changes in storage operation by including the Joule-Thomson effect, which describes isenthalpic temperature changes caused by throttling of a gas flow through e.g. a porous plug (Joule and Thomson 1854; Oldenburg 2007).

The simulation of pressure induced temperature effects includes multiphase-multicomponent flow, which is simulated by ECLIPSE, and heat transport simulated in OpenGeoSys. The radial model consists of four units, two of which are geological layers namely the storage formation, the overlying caprock and the well casing within the caprock and an open hole gravel pack in the storage formation. The overall model dimensions are 400.3 m by 25 m with the storage formation and the caprock being 10 m and 15 m, respectively. The top of the model is at 585 m depth. In radial direction the model is discretised using variable increments increasing from 0.1 m to 100 m towards the far boundary. The vertical discretization of the model is 1 m constant. Homogeneous parameter distributions are applied for each model unit (Tab. 3.3). Prior to the simulated storage operation, a hydrostatic pressure distribution is assumed throughout the model domain. Furthermore, an initial H_2 gas saturation of 0.7 is set for the storage formation while no gas is present in the caprock. Thus, no mobile water is present in the storage prior to injection. Initial formation temperature is assumed to be 298.15 K in the whole model domain. The temperature and the pressure at the far side of the model domain are held constant during the simulation. The storage simulation is performed for 10 cycles, each consisting of an injection of H_2 with a constant rate of 300 000 sm^3/d for 30 days and a production phase with a constant rate of -900 000 sm^3/d for 10 days. The production and injection phases are separated from each other by shut-in periods of 10 days. During the injection phases the borehole temperature is set constant to 298.15 K, thus the changes in temperature can be solely attributed to the Joule-Thomson effect included in the heat transport simulation in OpenGeoSys.

As the H_2 gas is injected into the storage formation, the pressure in the model increases (Fig. 3.11 a). Along the flow path the pressure of the gas phase decreases resulting in temperature changes due to gas expansion (Fig. 3.11 b). At the given temperature and pressure conditions, H_2 has a negative Joule-Thomson coefficient (Johnston et al. 1946; Michels et al. 1964), thus a positive temperature change occurs. During the injection phase the heat spreads by advection and conduction within the storage formation. As no flow occurs in the caprock, heat transport is purely conductive in this region. In the subsequent shut-in period, conductive heat transport leads to a reduction of the temperature signal within the storage formation. During the production period the pressure gradient is reversed pointing towards the storage well (Fig. 3.11 a). The temperatures in the system increase further as the gas flow is again throttled along the flow path (Fig. 3.11 b). Thus, during both injection and production, the gas temperature and with that the formation temperature rises. Consequently, the observed temperature increases with the number of storage cycles. However, the conductive spreading of heat into the caprock considerably dampens the observable magnitude of the signal. Based on these results, the effect of pressure induced temperature chang-

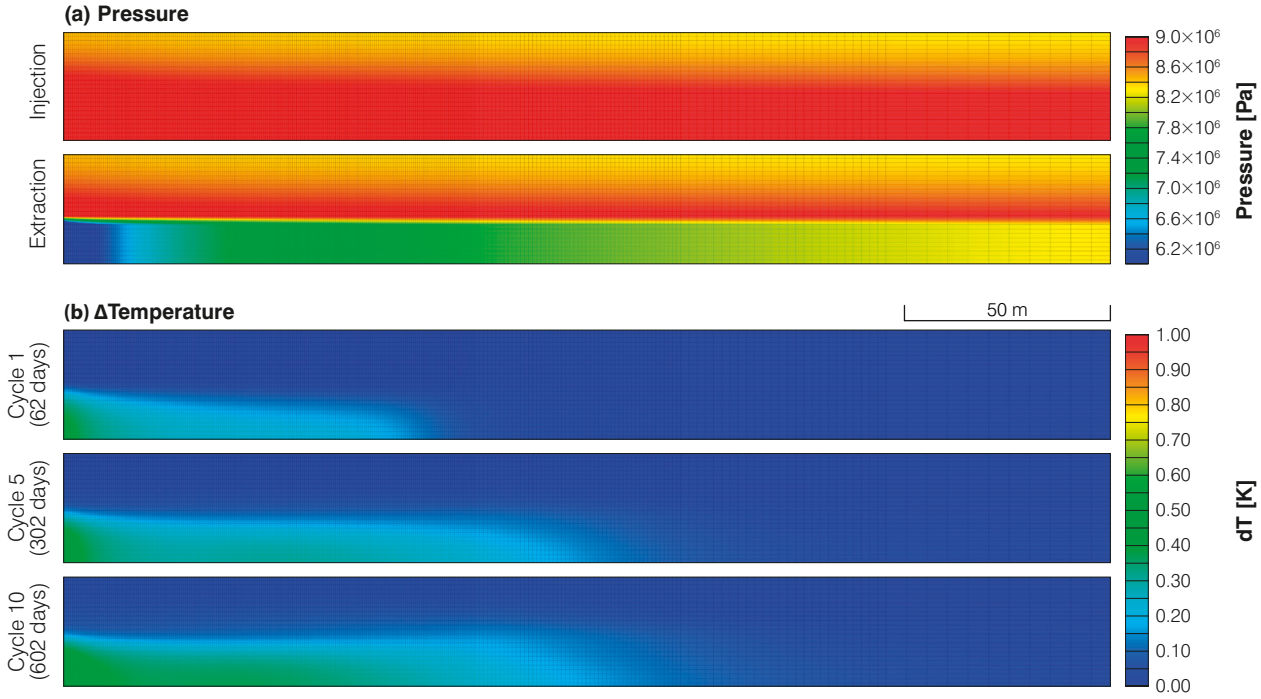

Fig. 3.11 (a) Pressure distribution during injection and withdrawal phases and (b) temperature change occurring after 1, 5 and 10 storage cycles in the first 200 m of the model domain from the injection well.

es during a porous media hydrogen storage can be expected to be insignificant when compared to i.e. the thermal effects introduced when the temperature of the injected gas differs from the initial reservoir temperature. Other gases typically show a positive Joule-Thomson coefficient at the given pressure and temperature conditions so that a reservoir cooling can be expected during cyclic gas storage operations. Also, using different injection and withdrawal regimes will alter the magnitude of the induced temperature changes.

3.9 Summary and Conclusions

The processes occurring during subsurface porous media energy storage are complex and include various feedback effects. Adequate modelling tools capable of dealing with such THMC-systems, are required for a correct prognosis of induced effects. In this work, a coupling interface for OpenGeoSys and ECLIPSE is presented, which is capable of dealing with THMC-systems including chemical and thermal feedbacks. Furthermore, the Joule-Thomson effect, which describes a temperature change due to pressure reduction during gas flow, is implemented in OpenGeoSys and validated against published data. In a coupled simulation ECLIPSE is used to solve the multiphase flow and component transport in case of a multicomponent-multiphase flow system. OpenGeoSys solves for additional mass transport processes of non-major phase constituents in the fluid phases and the solid phase. Furthermore, OpenGeoSys solves for induced geochemical reactions and heat transport, including processes such as the Joule-Thomson effect, in all phases in order to account for feedback on the multi-phase flow.

The coupled simulator is validated using a series of specific benchmarks. Slight differences between the reference simulations and results obtained with the coupled OpenGeoSys-ECLIPSE simulator arise due to interpolation inaccuracies when transferring data between the finite element and finite differences meshes used. The differences between the results obtained with the coupled OpenGeoSys-ECLIPSE and those of the reference simulations are small with the absolute differences in pressures, saturations and component densities staying below 1×10^{-5} bar, 2×10^{-8} m^3/m^3 and 2×10^{-5} mol/m^3, respectively. Taking the local element values as reference, the corresponding relative errors of the respective variables are within 1 × 10-5 %, 2 × 10-4 % and 0.003 %, and thus

relatively small. For the thermal coupling of the two simulators the inaccuracies introduced by the coupling are about ±0.005 K or 0.0015 % when no thermal feedback on the flow is considered. If however thermal feedback is included in the simulations, the observed differences increase while staying within 0.91 K which translates to 0.28 % of the observed temperature in the respective element. However, the average of the absolute error calculated at all nodes which are affected by the heat plume is less than 0.035 K with the standard deviation being less 0.072 K. Using the implemented iterative coupling scheme the errors could be reduced slightly. The persistent differences could be due to the slightly different formulations used for the calculation of fluid densities and viscosities in each simulator. If consistency in the fluid properties is ensured, the coupled simulator allows for an accurate representation of the governing THC-processes occurring during subsurface storage operations as the inaccuracies introduced by the data interpolation and data handling are within a reasonable range.

The Joule-Thomson effect is implemented by calculating the change in the heat content in the flowing gas phase, which is then added to the simulation via the nodes of the mesh. The implementation is validated by simulating model which closely represents the original Joule-Thomson experiment. The resulting temperature change in the model is used to calculate effective Joule-Thomson coefficients which are then compared to available literature values. The Joule-Thomson coefficients calculated from the model results obtained with OpenGeoSys are in very good agreement with the published data, with the maximum differences relative to the absolute values of the Joule-Thomson coefficients being 1.1 %, 0.65 %, 2.3 %, 1.2 % and 3.7 % for N_2, O_2, H_2, CH_4 and CO_2, respectively.

To demonstrate possible applications of the coupled simulator, a hydrogen storage simulation including a basic transformation reaction of H_2 to CH_4 by methanogenesis as well as a simulation of pressure induced temperature changes during storage operation are presented. The chemical reaction model considered in the first application example is too simplified to infer the importance of such transformation reactions when assessing a potential storage operation, but demonstrates the potential of the coupled OpenGeoSys-ECLIPSE simulator. The pressure induced temperature changes in the second application example are caused by the Joule-Thomson effect, which in the case of H_2 results in positive temperature changes within the storage formation. These temperature changes occur as a result of both gas injection and extraction and can thus accumulate during cyclic operation of such a storage reservoir. The magnitude of the temperature change induced is determined by the Joule-Thomson coefficient, the number of storage cycles and the conductive heat transport from the storage formation into the caprocks above and below. The newly developed coupled simulator offers the required flexibility for site specific simulations taking into account individual injection / withdrawal schemes.

The presented application examples, albeit simplified, showcase the complexity which has to be dealt with when assessing induced effects from subsurface geoenergy storage applications such as porous media H_2 storage. The developed and validated coupled OpenGeoSys-ECLIPSE simulator is a viable tool for such an assessment as both, realistic subsurface structures as well as the governing hydraulic, thermal and chemical processes, as already demonstrated in the work of (Li et al. 2014), can be represented in the coupled simulator.

4 POROUS MEDIA HYDROGEN STORAGE SIMULATIONS AT A REALISTIC SUBSURFACE STRUCTURE

The following chapter deals with scenario simulations of hydrogen storage operations at a realistically parametrised field site in Schleswig-Holstein, Northern Germany. The underlying storage scenario is presented in Chapter 4.2 with the structural model of the storage site being described in Chapter 4.3. Chapter 4.4 consists of heterogeneous scenario simulations which are used to infer the performance of the investigated hydrogen storage as well the induced hydraulic effects. For further analysis generalised rock models are used, which are described in Chapter 4.5. Results obtained with the homogeneous simulations are compared to those of the heterogeneous ensemble. In addition to this, an optimized simulation setup and a large scale hydrogen storage scenario are presented in this chapter. In Chapter 4.6 thermal effects of a porous media hydrogen storage are simulated using the previously described, coupled OpenGeoSys-ECLIPSE simulator. Parts of this chapter are published as

Pfeiffer WT, Beyer C, Bauer S (2017) Hydrogen storage in a heterogeneous sandstone formation - Dimensioning and induced hydraulic effects. Petroleum Geoscience doi: 10.1144/petgeo2016-050

4.1 Introduction

One option to reduce carbon dioxide emissions is to increase the share of electricity produced from renewable sources. Currently 27.4 % of the electricity consumed in Germany in 2014 is produced from such sources with the overall target of the "Energiewende" being 80 % by the year 2050 (BMWi 2015). Locally, in areas of strong wind energy production, about 100 % of electricity is provided by renewables. Electricity produced from renewable sources, however, is subject to strong fluctuations due to the local weather conditions. Shortages in power production will thus occur which could last up to several days (Klaus et al. 2010). The idea of an economy based on renewable power production and using hydrogen (H_2) as a storage medium was already introduced in the mid-1970s (Sørensen 1975). In recent years more research has been conducted in this field, e.g. Sørensen et al. (2004) investigated several usage scenarios for H_2 as an energy carrier in the context of Denmark's plan at that time to cover 50 % of its total energy supply by renewable sources by 2030. Klaus et al. (2010) discussed scenarios for a 100 % renewable power supply by 2050 for Germany which include energy storage utilizing H_2. However, power-to-gas concepts using H_2 are investigated worldwide with 48 projects in 15 countries being either planned or already realised (Gahleitner 2013). Depending on the characteristics of the shortage periods, large storage capacities and high power supply rates are necessary. The geological subsurface is already used for bulk energy storage as natural gas storage, as it can offer very large storage capacities and long withdrawal periods (e.g. Gregory and Pangborn 1976; Carden and Paterson 1979; Ogden 1999; Evans and West 2008). Experience in the field of subsurface H_2 storage, however, is scarce. So far, pure H_2 gas has been stored in salt caverns in Texas, USA, and in Tesside, UK (Crotogino et al. 2010). Even less experience has been gained regarding porous media storage of H_2. The storage of H_2-rich town gas is the only application in which H_2 has been stored in porous geological formations. Albeit much more widespread, the aquifer storage of town gas near Beynes, France is the only field application documented in literature (Carden and Paterson 1979; Foh et al. 1979) and has been referenced to in subsequent publications investigating geochemical effects (e.g. Panfilov 2010). Even though technical issues arising from the use H_2 instead of natural gas are diverse, such as corrosion of installations and potential impacts on well and formation integrity (Reitenbach et al. 2015), natural gas storage can be used as an analogue for porous media H_2 storage as the overall principles are comparable (Carden and Paterson 1979; Foh et al. 1979).

As more and more types of use in the subsurface, ranging from groundwater abstraction over geothermal applications to large scale energy storage, compete for the limited suitable space, analyses of induced effects and impacts should be conducted additionally to an assessment of storage capacity and retrieval rates (Bauer et al. 2013). To achieve this, an integrated concept for site investigation and monitoring can be used, as e.g. explained in Bauer et al. (2012) for the application of CO_2 storage. In this approach, synthetic but realistically parametrised storage sites are used to simulate the impacts and induced effects, like e.g. the pressure increase in the subsurface. These model results are then used to test and improve investigation and monitoring methods. This approach has been applied by Benisch and Bauer (2013) for pressure monitoring and by Benisch et al. (2015) for assessing geophysical monitoring methods for gas phase detection in the context of CO_2 geological storage. Pfeiffer et al. (2016) could successfully transfer this concept to geophysical monitoring of H_2 gas storage, which is described in the subsequent Chapter 5.

This work therefore aims at assessing the hypothetical application of a porous media H_2 gas storage, utilising an existing anticline structure in the North German Basin, which provides a realistic geological setting and parameters. A likely usage scenario is derived using a projection of typical fluctuations of renewable energy production and the energy demand to define the storage demand and then simulating the hypothetical storage operation.

At the selected storage site, the Rhaetian sandstones are chosen as the designated storage formation, which are overlain by the deposits of the Middle Jurassic and the Lower Cretaceous representing possible cap rocks (Hese 2011; Hese 2012). At the storage site formation thickness is up to 20 m with the formation depth being about 450 to 500 m. A heterogeneous and realistic parameter set consisting of 25 equally likely realisations is used to investigate the effect of the reservoir heterogeneity on the storage operation. Required storage dimensions and retrieval rates are determined for the ensemble. Additionally, the hydraulic impact of the storage operation due to induced pressure perturbations is investigated. Subsequently, various generalised rock models are developed based on the parameter distributions of the heterogeneous ensemble. Results obtained with these generalised rock models are then compared to those of the heterogeneous ensemble and used for further analysis of an optimized storage setup, increased storage sizes and thermal effects during storage operation.

4.2 Storage scenario

For a scenario analysis of subsurface energy storage, an estimation of the storage demand is necessary. This can be broken down into the required power output that has to be sustained for a given period of time and the frequency with which such periods of demand occur due to the fluctuating nature of the renewable energy production. Storage demand is thus mainly controlled by the fluctuating renewable power production and the deployment of load balancing schemes, which reduce the storage requirements by shifting energy demands on smaller time scales of up to hours. Numerical simulations of renewable power production in Germany based on actual meteorological data in a scenario, in which 100 % of the electricity is produced by renewable sources, indicate that power shortage periods of up to 14 days in a year may occur frequently (Klaus et al. 2010). However, it can be expected that several storage options or backup systems such as conventional power plants will be employed during such prolonged shortage periods, which essentially reduces the time span in which one storage has to operate at its maximum capacity. Thus, a typical shortage period of one week is assumed in this analysis, but the analysis can easily be extended to other shortage scenarios.

For determining the required delivery rate from a porous medium H_2 storage, the power delivered is compared to the average weekly demand of electricity of the state of Schleswig-Holstein, Northern Germany, with a population of about 2.8 million people. In 2011, a total of 42.82 million GJ of electricity was consumed in Schleswig-Holstein (MELUR 2013). Thus, a week long shortage period would result in a deficit of 0.82 million GJ (228 113 MWh) of electricity, corresponding to an average load of 1356 MW. Klaus et al. (2010) estimated the roundtrip efficiency of a H_2 storage

system to be around 42 %, incorporating conversion of electric power to gaseous H_2 and from H_2 back to electric power. The analysis in this paper is focused on the deliverability of power from the porous medium H_2 storage and thus only the re-electrification process is considered, which can be technically accomplished either through fuel cells (Büchi et al. 2014) or gas turbines (Forsberg 2009). The efficiency of the re-electrification process is assumed to be 60 % as this can be achieved with either method. Assuming an energy density of H_2 of about 124 MJ/kg (Carden and Paterson 1979) and the corresponding H_2 density of 0.085207 kg/m³ at surface conditions defined as 1 bar and 15 °C, the volume of H_2 which has to be stored to cover for the complete deficit of 0.82 million GJ in a week long shortage period equates to 129 million m³ of H_2 gas at surface conditions (sm³).

4.3 Structural model of the storage site

Several criteria have to be fulfilled at a given site in order to qualify a geological structure as a potential porous gas storage formation. Besides providing sufficient reservoir volume, a potential storage site should provide competent sealing formations above and below the storage formation in order to prevent gas migration into adjacent formations. Also a high intrinsic permeability is required to ensure well deliverability (Bennion et al. 2000). In addition, the depth of the storage formation is important as it affects the operational pressure range of the storage and the well deliverability. While deeper formations potentially allow a broader operating pressure range, reducing the well length by choosing a shallow storage formation reduces the pressure drop occurring within the well during gas flow and thus increases the overall well deliverability (Carden and Paterson 1979; Wang and Economides 2009). H_2 gas is prone to fingering in the porous formation as a result of its specific properties, making a steeply dipping structure is favourable (Paterson 1983). Conventional aquifer gas storages used for storing hydrocarbons are typically located in depths of 800 to 1000 m in formations of 15 to 40 m thickness which provide permeabilities greater than 600 mD (Sedlacek 1999).

The anticline used in this analysis (Fig. 4.1, Fig. 4.24) is based on an actual structure found in Schleswig-Holstein, northern Germany. The storage operations, however, are purely hypothetical. The subsurface of northern Germany is strongly affected by movements of the Zechstein salt deposits (Doornenbal and Stevenson 2010). Halokinesis of these salt deposits, which led to the formation of the structure, started in the Triassic period (Baldschuhn et al. 2001). The Rhaetian sandstones of the Upper Triassic (Exter formation) have been investigated as a potential host formation for CO_2 sequestration (Hese 2011; Hese 2012). Furthermore, the overlying deposits of the Middle Jurassic and the Lower Cretaceous are regarded as possible cap rocks (Hese 2011; Hese 2012). Apart from being investigated as potential CO_2 storage formations, the Rhaetian deposits are proven reservoir formations for natural gas exploration in northwest Germany (Fahrion and Betz 1991). Several northwest-southeast oriented faults cut through the centre of the anticline as a result of changes in the local stress state. In this work, the faults are assumed tight and represented as a hydraulically closed model boundary.

During the Rhaetian the depositional system of the North German Basin changed from the non-marine environment of the Late Triassic to the marine environment of the Early Jurassic (Doornenbal and Stevenson 2010). As a result, the depositional system changed spatially from a non-marine system in the east through a paralic system to a marine setting in the west of the North German Basin (Doornenbal and Stevenson 2010). The study site is assumed to lie in the paralic facies belt, consisting of shallow-marine, deltaic and coastal sandstones and separating the non-marine facies in the east from the marine facies to the west (Doornenbal and Stevenson 2010).

In general, the Rhaetian deposits are made up of several distinct sandstone layers of varying thickness with intermediate shale layers (Gaupp 1991; Doornenbal and Stevenson 2010; Hese 2011; Hese 2012). Multiple classifications of the Rhaetian appear in literature of which most include a separation into Lower, Middle and Upper Rhaetian (Battermann 1989; Gaupp 1991; DSK 2005). The Lower Rhaetian consists of cyclic coarsening-upwards successions of mudstones to sandstones (Gaupp 1991). The Middle Rhaetian, also known as the Conterta succession, comprises five units, namely the Lower Shale, the Main Sandstone,

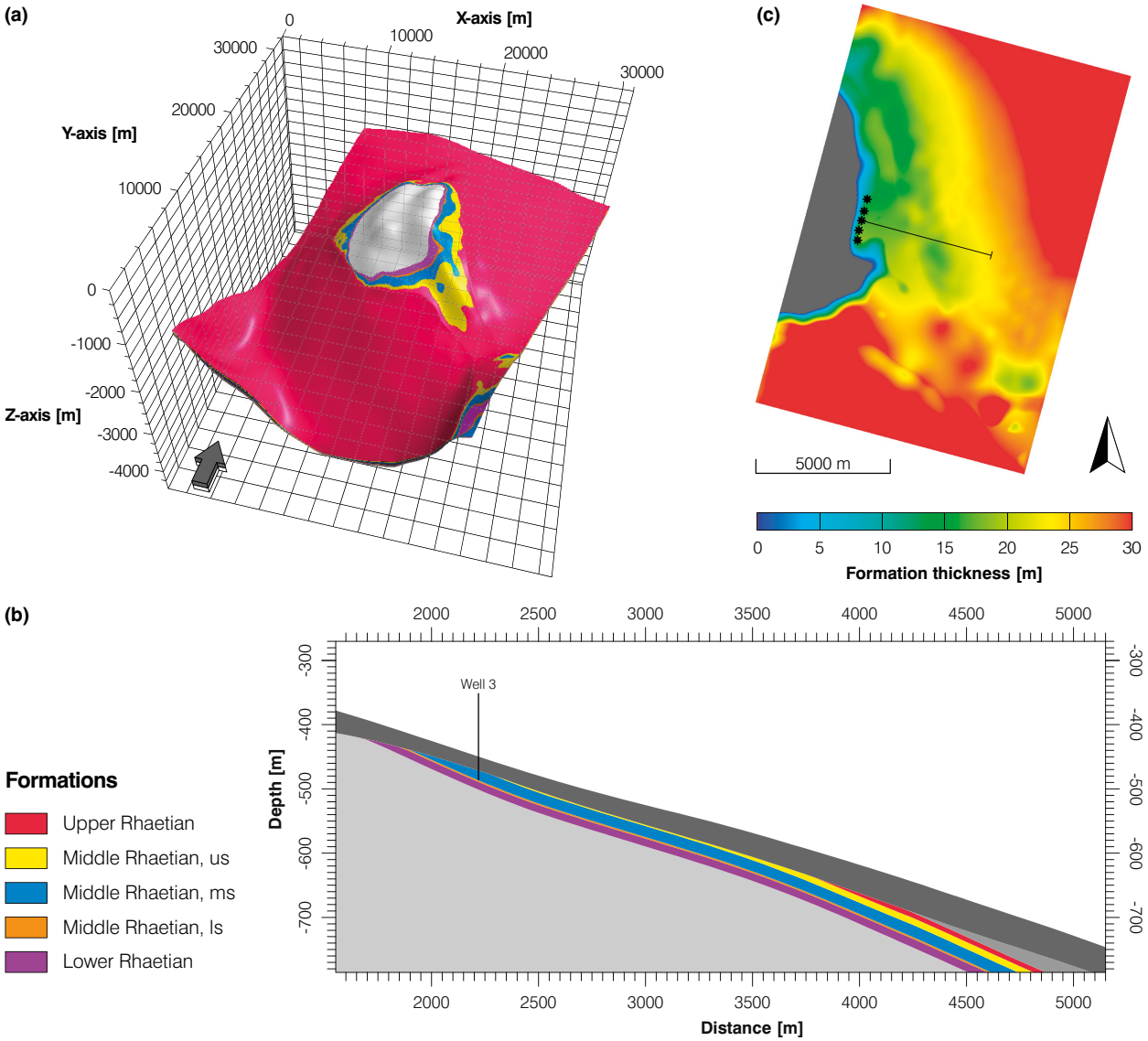

Fig. 4.1 (a) Structural model used for the reservoir simulation, (b) east-west cross section along the centre well and (c) thickness of the designated storage formation, the Main Sandstone of the Middle Rhaetian (after Pfeiffer and Bauer 2015). The black stars indicate the positions of the storage wells.

the Middle Shale, the Flaser Sandstone and the Upper Shale. Similar to the Lower Rhaetian, the Upper Rhaetian shows a coarsening-upward succession from mudstones at its base to sandstones in the upper parts of the formation (Gaupp 1991; DSK 2005; Doornenbal and Stevenson 2010). The Main Sandstone of the Middle Rhaetian has the highest potential for use as an underground gas storage site, as it shows in general a thickness of several meters and consists of middle to coarse grained relatively pure quartzite (Fahrion and Betz 1991; Gaupp 1991; DSK 2005; Hese 2011; Hese 2012).

A regional structural model developed by Hese (2012) is used as a basis for the geological site model created for this study. The distribution and extent of the Rhaetian deposits beyond the boundaries of the original model developed by Hese (2012) were calculated based on the distribution of the residual thickness of the Rhaetian deposits in the North German Basin given in Baldschuhn et al. (2001) in combination with the minimum depth data of the cap rocks covering the Rhaetian, which were merged from the surfaces of the Jurassic and Cretaceous sediments presented in Hese (2012). In order to get a more

Tab. 4.1 Properties assigned to the individual facies components.

Component	Permeability [mD]			Porosity [–]			Sr_w [–]	kr_{gmax} [–]	p_d [bar]
	mean	min	max	mean	min	max			
Shale	5×10^{-5}	1×10^{-6}	1×10^{-5}	0.05	0.01	0.1	0.6	0.015	15
Fine Sand	5	0.1	10	0.25	0.2	0.3	0.4	0.3	0.5
Medium Sand	250	10	500	0.35	0.3	0.4	0.4	0.5	0.2
Coarse Sand	1000	500	2500	0.35	0.3	0.4	0.3	0.9	0.1

realistic presentation of the storage formation, the internal succession of the Rhaetian was included in the model. For this, Lower Rhaetian and the lower shale of the Middle Rhaetian, the main sandstone of the Middle Rhaetian, the upper shale of the Middle Rhaetian and Upper Rhaetian were integrated into the structural model, based on facies descriptions given by Gaupp (1991) and Hese (2011, 2012).

At the storage site used in this analysis, the depth of the Rhaetian deposits varies from around 400 m near the top of the structure to more than 3000 m at the flanks of the anticline. Halokinesis and the early Cimmerian uplift and transgressional tectonics resulted in varying thickness of the Upper Triassic sediments throughout the North German Basin (Baldschuhn et al. 2001; Doornenbal and Stevenson 2010). As a consequence, parts of the Rhaetian deposits are missing in the study area. The potential storage site hence represents a capped dome structure. Due to its shallower depth, the eastern flank of the structure is selected to accommodate the H_2 gas storage site.

4.4 Part I: Effect of reservoir heterogeneity

To study the effect of the reservoir heterogeneity on the storage performance and the hydraulic effects induced by the storage operation multiple simulations are required to assess the variability of the results. To minimize the simulation time the structural model of the storage site was reduced to the eastern part of the anticline, i.e. the shallower side of the structure at which the storage wells are located. At the given site the Main Sandstone of the Middle Rhaetian exhibits a thickness of around 15 to 20 m near the top of the structure and a thickness greater than 30 m at the flanks (Fig. 4.1).

4.4.1 Heterogeneous rock model

The heterogeneous geological model of the storage site is obtained by facies modelling based on the described structural model and accounting for lateral and vertical trends. Doornenbal and Stevenson (2010) determined the major direction of sediment influx during the Rhaetian for the study region to be around 70°. While deltaic facies such as those found at the study site can extent several tens of km (Morse 1994), the lateral correlation lengths were set to 2500 m in the major direction and to 500 m perpendicular in the minor direction in the absence of direct site specific data. The facies descriptions given by Gaupp (1991) and Hese (2011, 2012) are used to obtain correlation lengths corresponding to the coarsening-upwards of the individual sub-formations. The data is used to create 25 equally probable facies distributions. The final heterogeneous parameter distributions are obtained in a second step by assigning the parameters based on the facies distributions in combination with the parameter ranges assigned to each individual facies component (Tab. 4.1, Fig. 4.2). One distribution of permeability for the geological model is depicted in Fig. 4.3, which shows the vertically evenly distributed values in the storage formation, the Main Sandstone, compared with the stronger coarsening-upwards trends in the remaining sub-formations.

Site specific data on hydraulic properties of the Rhaetian deposits is scarce. Parameter ranges for porosity and intrinsic permeability are available as on-site (Hese 2011; Hese 2012) and off-site data from the North German Basin (Gaupp 1991). Capillary pressure and relative phase permeability data for the Rhaetian, however, are not openly accessible. Hence, the necessary parameters like residual saturations, displacement pressures, maximum gas phase permeabilities and pore dis-

tribution indices are derived from values typically found in literature for rocks of similar characteristics (e.g. Hildenbrand et al. 2002; Hildenbrand et al. 2004; Bachu and Bennion 2008; Wollenweber et al. 2010). Based on this the relative phase permeability data is calculated using Corey-type equations by Burton et al. (2009), while capillary pressure is calculated using the standard Brooks & Corey formulation (Brooks and Corey 1946). To account for differences phase properties, the capillary entry pressure data taken from the literature was scaled to the phases used in the simulation using the Laplace equation (e.g. Helmig 1997). Assuming temperature and pressure conditions which can be expected in the storage (25 °C; 50 bars), the interfacial tensions calculated for H_2 and N_2 using the empirical formulation by Massoudi and King (1974) are 0.068 and 0.071 N/m, respectively. Consequently, the entry pressures for both gas components are comparable and thus phase composition is not taken into account for calculating the capillary pressure data.

The realisations generated here are used to obtain a first estimate of the effects of geological formation sub-structure and heterogeneity on the storage operation, especially the pressure evolution and the gas phase distribution as well as the well deliverability rates. They are not intended as a full-scale uncertainty assessment, as this would require more knowledge on site specific data as well as more realisations

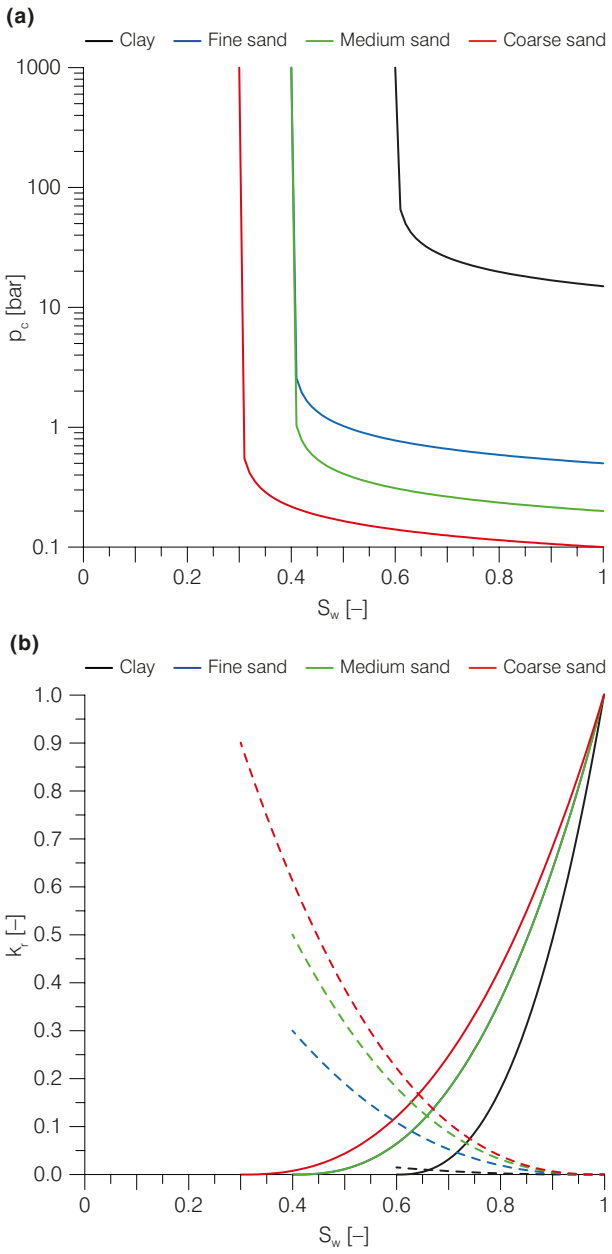

*Fig. 4.2 **(a)** Capillary pressure curves and **(b)** relative phase permeabilities of the individual facies used in the generation of the heterogeneous parameter distributions. The dashed lines depict the relative permeability of the gas phase while the solid lines represent the relative permeability of the liquid phase.*

4.4.2 Numerical simulation model

The geological model of the storage site is transferred to a simulation model using a discretization of 50 by 50 m laterally, 0.2 to 5 m vertically and a constant number of layers for each sub-formation. Initially, a hydrostatic pressure distribution and a fully water saturated pore space is assumed throughout the model domain. The initial pressure distribution in the central plane of the storage formation is shown in Fig. 4.5, where the steeply dipping anticline suitable for H_2 storage can be discerned from the hydrostatic pressure distribution. In order to get a representative pressure response in the far field of the storage, a pore volume multiplier and permeability factor equal to the reciprocal of the pore volume multiplier were applied to the boundary elements of the simulation grid to represent the lateral extent of the storage formation. Based on the distribution of the Rhaetian deposits given in Baldschuhn et al. (2001) the extent towards the north, east and south were set to 48, 20 and 20 km, respectively. The boundary to the west is assumed to be closed to the fault system apart from the most southern

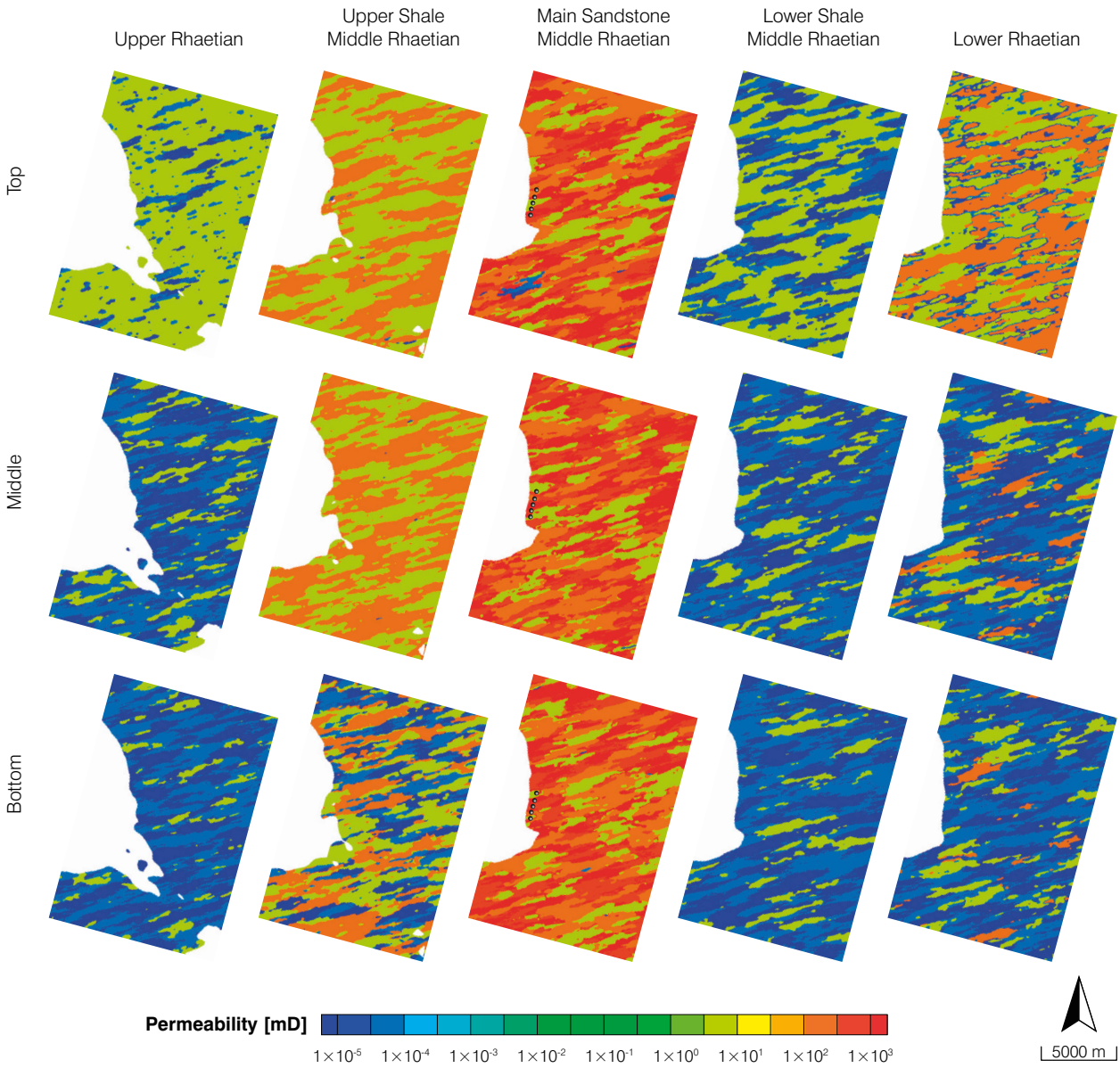

Fig. 4.3 Exemplary permeability distribution for the individual sub-formations in run #14. Please note that the Upper Shale of the Middle Rhaetian and the main sandstone of the Middle Rhaetian consist of five individual layers of which only three are displayed.

part of the western boundary in which the storage formation is continuous beyond the model boundary for 14 km. Furthermore, the caprocks above and below the Rhaetian deposits are assumed impermeable and are thus omitted from the simulations. The storage operation is simulated using five wells, labelled 1 to 5 from north to south (compare Fig. 4.1). Preliminary simulations using homogeneous test cases showed that the individual screen length should be at least 12 m in order to sustain the storage rates required in this scenario. Placement of the storage wells can furthermore affect the theoretical maximum storage capacity of a structure as shown for CO_2 storage by Mitiku and Bauer (2013) with the highest usable potential being available when the wells are placed at the top of a structure. Thus, the storage wells are placed at the shallowest depth possible near the top of the structure while at the same time fulfilling the minimum reservoir thickness criterion of 12 m. The individual reference depths of the storage wells are 493, 481, 479, 463 and 474 m for wells 1 through 5 with the corresponding initial hydrostatic bottom hole pressures (BHP) being

Tab. 4.2 Values used for the calculation of the equation of state. Critical temperatures and pressures are taken from Lemmon et al. (2016), critical volumes from Kaye and Laby (2016) and acentric factors from Gasem et al. (2001). The values for the binary interaction coefficients are defaulted to 0.

Component	T_{crit} [K]	P_{crit} [bar]	V_{crit} [m^3/mol]	Ω [–]
N_2	126.192	33.958	8.95×10^{-5}	0.039
H_2	33.200	12.970	6.50×10^{-5}	-0.220

calculated at 50.5, 49.3, 49, 47.5 and 48.6 bars, respectively. Placing the wells further down the anticline would allow for higher injection and extraction rates, but also require a larger gas storage volume.

The necessity of cushion gas injection prior to the storage operation represents a costly one-time loss for a porous media gas storage (Carden and Paterson 1979; Evans and West 2008). Using a cheaper alternative such as inert N_2 or CO_2 instead of the working gas thus can reduce the cost of the storage and has been discussed and already successfully conducted for natural gas storage (e.g. Laille et al. 1988; Dussaud 1989; Oldenburg 2003) as well as compressed air energy storage (Oldenburg and Pan 2013). The use of N_2 as a cushion gas in a porous media H_2 storage also helps to reduce the extremely sharp density contrast between the H_2 and the formation water. On the other side, using a separate cushion gas does introduce the risk of impurities of the produced gas phase. While such impurities should be avoided if fuel cells are used for re-electrifying the H_2 as they e.g. result in a reduction in power output (Borup et al. 2007; Nachiappan and Kalaignan 2013), the dilution of the H_2 with for example N_2 is required if gas turbines are used to meet emission requirements (Chiesa et al. 2005; Lee et al. 2012).

The model simulations are carried out using the multiphase-multicomponent reservoir simulator ECLIPSE E300 (© Schlumberger). The simulation takes into account two-phase immiscible flow and pressure dependent dissolution of both gas components in the water phase at the reservoir temperature. Evaporation of water into the gas phase is not included in the simulations. The solubility data of H_2 and N_2 was determined prior to the simulation using solubility data from Young (1981) and Battino (1982). Phase densities and viscosities are calculated using a generalised formulation of the Peng-Robinson equation of state (Schlumberger 2015). For a temperature of 25 °C and pressures from 30 to 70 bars, which are representative conditions at the simulated storage site, the equation of state yields densities within 1.9 % and 1.3 % of the values given in Lemmon et al. (2016) for H_2 and N_2, respectively. The parameters used are given in Tab. 4.2. Compared to the reference values given in Lemmon et al. (2016), the calculated viscosities deviate by less than 13.9 % for H_2 and 1.9 % for N_2. Nevertheless, the obtained values are within the uncertainty interval specified in Lemmon et al. (2016).

Diffusion and dispersion processes between the two immiscible fluids or the gas components are neglected in this study. In a porous geological formation, diffusion is reduced compared to free atmosphere diffusion as a result of high pressure, porosity and tortuosity effects (see e.g. Oldenburg et al. 2004). With the given parameters of the storage site, the diffusion coefficient of H_2 would be about 3.6×10^{-7} m^2/s, corresponding to a diffusion length of less than 2 m during one storage cycle. As the H_2 gas moves by about 100 m during one cycle due to injection and extraction, this effect can be considered small and is thus neglected in this study. Mechanical dispersion, which represents mixing due to sub scale hydraulic heterogeneity not explicitly represented in the model, is a macroscopic, scale dependent effect. This process is also not included in the simulation, as the major contribution to mixing, being the heterogeneity of the hydraulic permeability of the formation, is explicitly accounted for in the model approach. In case of a homogeneous reservoir representation, Feldmann et al. (2016) show that effects of dispersion should be considered.

For each of the 25 realisations the storage operation is simulated in three stages. In the first stage, the gas storage site is initialized by injecting the N_2 serving as cushion gas for 710 days with a target injection rate of 55 625 sm^3/d/well. The time span of 710 days is required for initial filling of the reservoir compares well with reported times by e.g. Dussaud (1989), and shows that this initial period requires considerable effort. This is followed by the initial filling of the reservoir with H_2 for another 210 days with a target rate of 155 000 sm^3/d/well. Subsequent to the first two

stages, the actual storage operation consisting of 6 storage cycles is simulated. Each cycle consists of a production phase of one week at a target rate of 1 000 000 sm^3/d/well followed by a short one day shut-in period. Consequently, the simulated storage should suffice to provide about 370 MW under ideal conditions, which is around 27 % of the total demand defined in the scenario. The storage then is replenished with H_2 gas for 50 days with the target rate set to 150 000 sm^3/d/well, followed by a 30 day shut-in period. Thus, the frequency of the extraction periods is roughly 3 months, representing a strong withdrawal period every three months, with a longer time required to replenish the extracted gas by H_2 produced from surplus power.

The depth of the uppermost connections, which are used as a reference for defining the maximum BHPs are 493, 481, 479, 463 and 474 m at wells 1 through 5, respectively. The corresponding initial BHPs are 50.5, 49.3, 49, 47.5 and 48.6 bars, respectively. Determining accurate overpressure limits requires in-depth knowledge on the local stress state (Zoback 2010). While such detailed data is not openly available for the storage site, Röckel and Lempp (2003) estimated the minimum horizontal stress gradient in the North German Basin (NGB), which is often used in combination with a safety factor to obtain reasonable pressure limits in such cases (e.g. Thibeau et al. 2014). The lower and higher estimate of the minimum horizontal stress gradient of sediments above the Zechstein salts, which applies to the storage site, given in Röckel and Lempp (2003) is 15 and 20 MPa/km, respectively. The average of the maximum pressure gradients found in porous media gas storages in Germany lies within this interval being 16.8 MPa/km (Sedlacek 1999). Due to the lack of site specific data, the maximum BHP is set to 65 bars in all wells. The maximum overpressure of about 17.5 bars at the shallowest well 4 thus is equal to about 80 % of the maximum allowable overpressure of 22 bars if the lower estimate of the minimum horizontal stress by Röckel and Lempp (2003) is used. If the upper pressure limit was to be calculated by using the average of the maximum pressure gradient of existing storages in Germany, the maximum overpressure would equate to 30 bars. Thus, the estimated upper BHP limit provides a conservative estimate. For the remaining wells the gradients would allow an even larger overpressure due to the greater depth of the uppermost connection in those wells. The lower BHP limit was set to 30 bars to provide sufficient overpressure for technical installations. If the storage operation results in a violation of these limits in one of the wells, the injection / withdrawal rate applied in this well is automatically adjusted so that the BHP limit is respected.

4.4.3 Simulation Results

At the beginning of the simulation ECLIPSE is set to calculate an initial hydrostatic pressure distribution within the reservoir assuming the model to be fully water saturated. During the equilibrium calculation ECLIPSE calculates the water pressures based on the fluid densities and brings the fluid saturations into equilibrium based on the provided capillary pressure curves. Due to the different entry pressures of the various facies (compare Fig. 4.2 a), the local pressure varies slightly. This disequilibrium results in small pressure changes even if no fluid is injected or withdrawn. To assess the effect of this inaccuracy of the simulator, a baseline simulation is conducted for each heterogeneous simulation. These simulations are identical to the storage simulations without the storage operation. The difference in the pressure changes relative to the initial quasi-hydrostatic pressure distribution (Fig. 4.4 a–d) and the case specific baseline simulations (Fig. 4.4 e–h) are relatively small being generally less than 0.2 bars. Consequently, the pressure perturbations caused by the storage operation as calculated using the initial pressure distribution do only differ slightly from those calculated using the baseline simulations and thus no further differentiations are made regarding the way the pressure change is calculated.

The consecutive injection of N_2 and H_2 gas in the first two stages of the simulation results in a quick pressure increase within the storage formation (Fig. 4.4, 4.5), with the maximum overpressure being 20 bars as governed by the BHP limits of the storage wells. The pressure responses of the individual wells strongly depend on the distribution of the high and low permeability zones at and close to the injection wells in the individual heterogeneous realisations (not shown). Ulti-

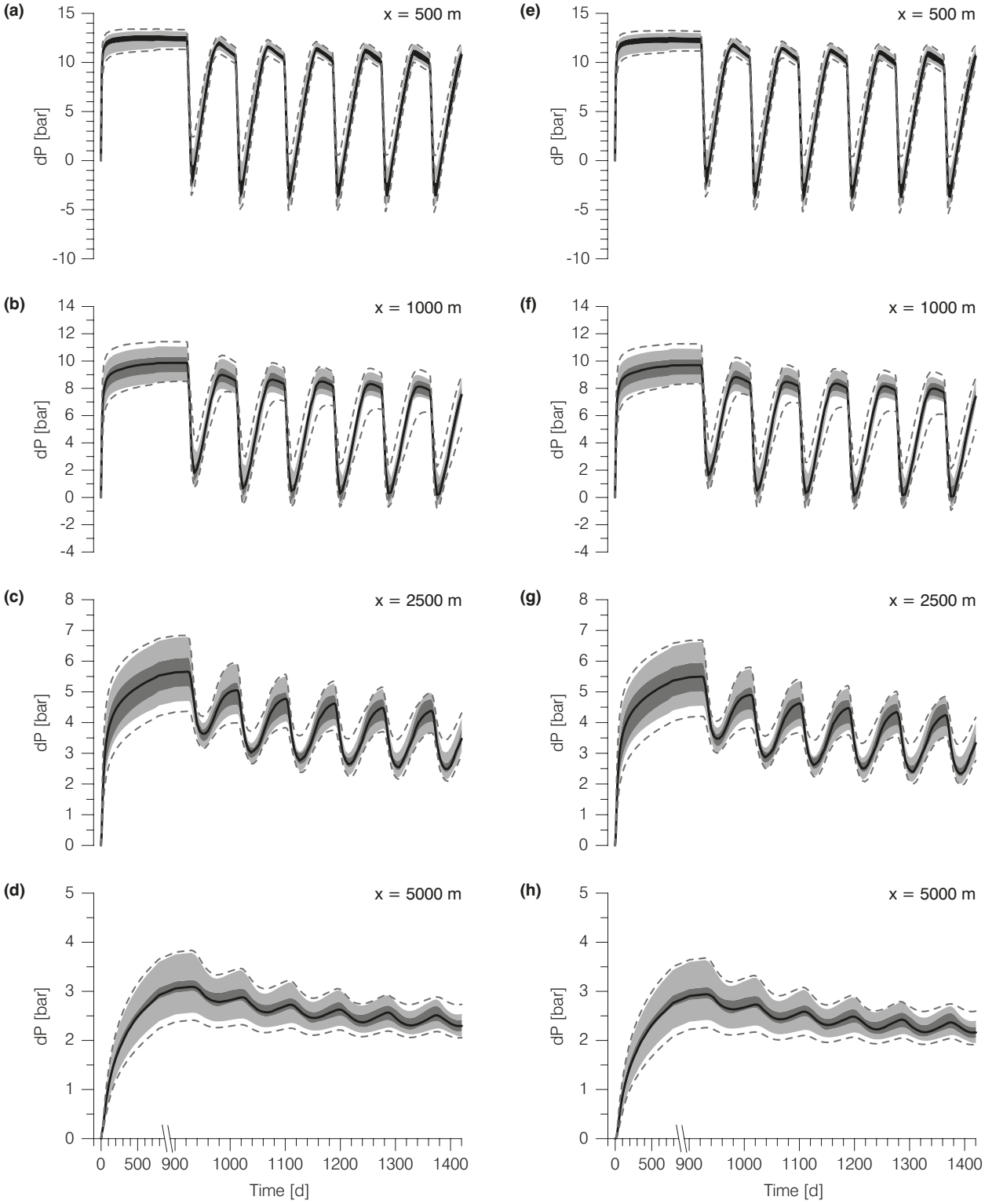

Fig. 4.4 *Evolution of the pressure change calculated based on the initial pressure distribution at the observation points at* ***(a)*** *500 m,* ***(b)*** *1000 m,* ***(c)*** *2500 m and* ***(d)*** *5000 m along a transect perpendicular to the well gallery and intersecting with the centre well and pressure change calculated based on the individual baseline simulations for the same observation points at* ***(e)*** *500 m,* ***(f)*** *1000 m,* ***(g)*** *2500 m and (h) 5000 m. All observation points are located at the central layer of the storage formation. The solid black line depicts the median of all realisations, the dark grey shaded area the interval spanning between the 25th and 75th percentiles, the light grey shaded area the interval spanning between the 5th and 95th percentiles. The dashed lines indicate the absolute minimum and maximum values*

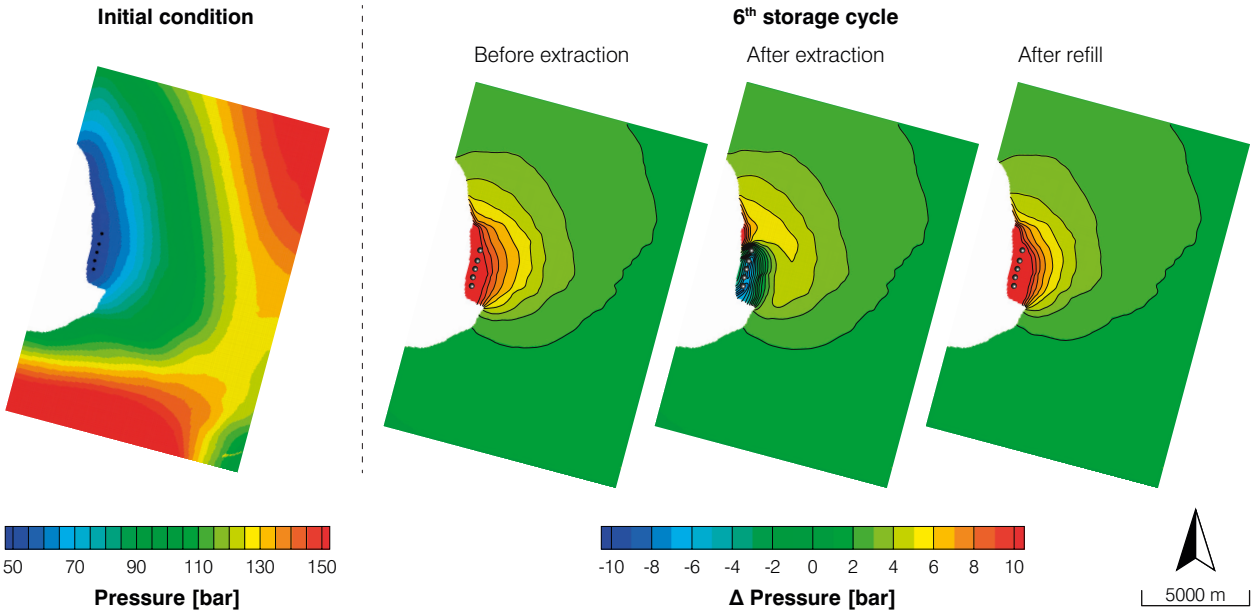

Fig. 4.5 Initial hydrostatic pressure distribution in the storage formation (left) and observed pressure change (right) during the sixth storage cycle in run #14.

mately the upper BHP limit of 65 bars is reached in all wells in every realization, resulting in an automatic reduction of the well flow rates. The pressure continues to increase over the course of the initial filling stage of the simulation at the observation points (see Fig. 4.1 for observation point positions), with the signal at 500 m reaching a maximum of slightly less than 12.5 bars.

With increasing distance to the injection points the overpressure signal is dampened considerably (Fig. 4.4). Furthermore, the arrival time of the pressure signal at the observation wells in 2500 and 5000 m is delayed, resulting in the maximum pressure being observed after the initial filling is completed and the first storage cycle well under way. The variability in the pressure signal from the 25 realisations is more or less constant throughout the first stage of the simulation with a range between the 5th and 95th percentiles of about ±1.5 bars around the median at the observation points in 500 and 1000 m distance to the well gallery and of about ±1 bar around the median at the distant observation points.

At a distance of 5000 m to the well gallery the median of the maximum pressure perturbation caused by the storage reaches 3.1 bars with the 95th percentile being 2.6 bars and the 5th percentile being 3.8 bars.

The injected gas accumulates in the top of the structure due to its lower density compared with the formation water (Fig. 4.6, 4.7). The gas phase composition exhibits a clear zonation as

Tab. 4.3 Averaged results from the reservoir storage simulation for all six storage cycles (all values represent medians).

Cycle	N_2 in place [$\times 10^6$ sm^3]	H_2 in place [$\times 10^6$ sm^3]	Max. continuous gas extraction rate [$\times 10^6$ sm^3 d^{-1}]	Max. continuous power output [MW]	Cum. H_2 produced [$\times 10^6$ sm^3]	Cum. power output [MWh]
1	82.7549	21.7480	3.4667	78	13.6438	24104
2	66.9309	40.1481	3.5087	131	21.1357	37340
3	58.4265	51.9373	3.5984	169	24.3144	42955
4	52.6588	61.1223	3.7265	201	26.6927	47157
5	47.6881	70.4376	3.9083	225	28.0505	49556
6	43.7333	77.4331	4.0271	245	29.4465	52022

the N_2 is injected prior to the H_2. While the N_2 is spread throughout the stored gas phase, reaching up to 2 km from the injection wells in northern direction, the H_2 gas is concentrated around the injection wells (Fig. 4.6). The distribution of the gas phase saturations in lateral and vertical direction indicates the strong influence of the formation heterogeneity (Fig. 4.6, 4.7, 4.8). As result of the upper BHP limit being reached in all wells during the storage initialization, the median of the injected N_2 is just 82.75 million sm^3, with the median of the injected H_2 volume being 21.75 million sm^3. This represents just about 42 % and 13 % of the intended injection volume of N_2 and H_2. Consequently, less H_2 gas than intended is available for extraction in the first storage cycle (Tab. 4.3). This clearly shows in the composition of the gas phase in the storage prior to the first extraction period with the only significant H_2 fractions in gas being found in close proximity to the wells (Fig. 4.6)

The third stage of the simulation consists of the actual storage operation represented by six storage cycles. The production of gas from the storage formation results in sharp and pronounced pressure drops in and around the storage wells by more than 20 bars. This results in pressure levels more than 10 bars below the initial hydrostatic levels, while local pockets of over pressurized fluid are persistent in some realisations over the course of the extraction periods (Fig. 4.5). The minimum theoretical pressure that can occur is again governed by the BHP limits of the storage wells and thus equates to 30 bars.

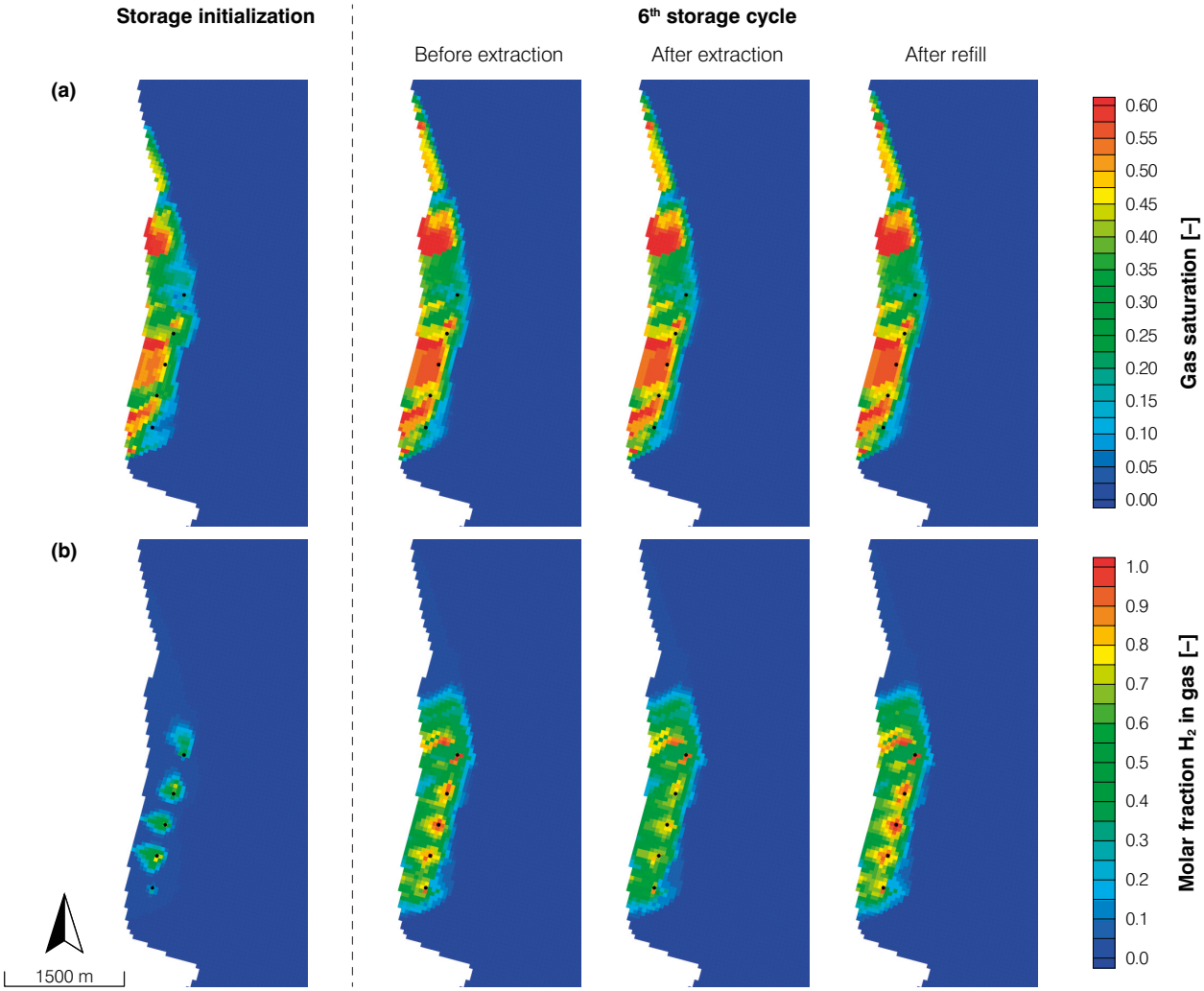

*Fig. 4.6 **(a)** Vertically averaged gas saturations and **(b)** vertically averaged molar fractions of H_2 in gas after the storage initialization and during the sixth storage cycle in run #14.*

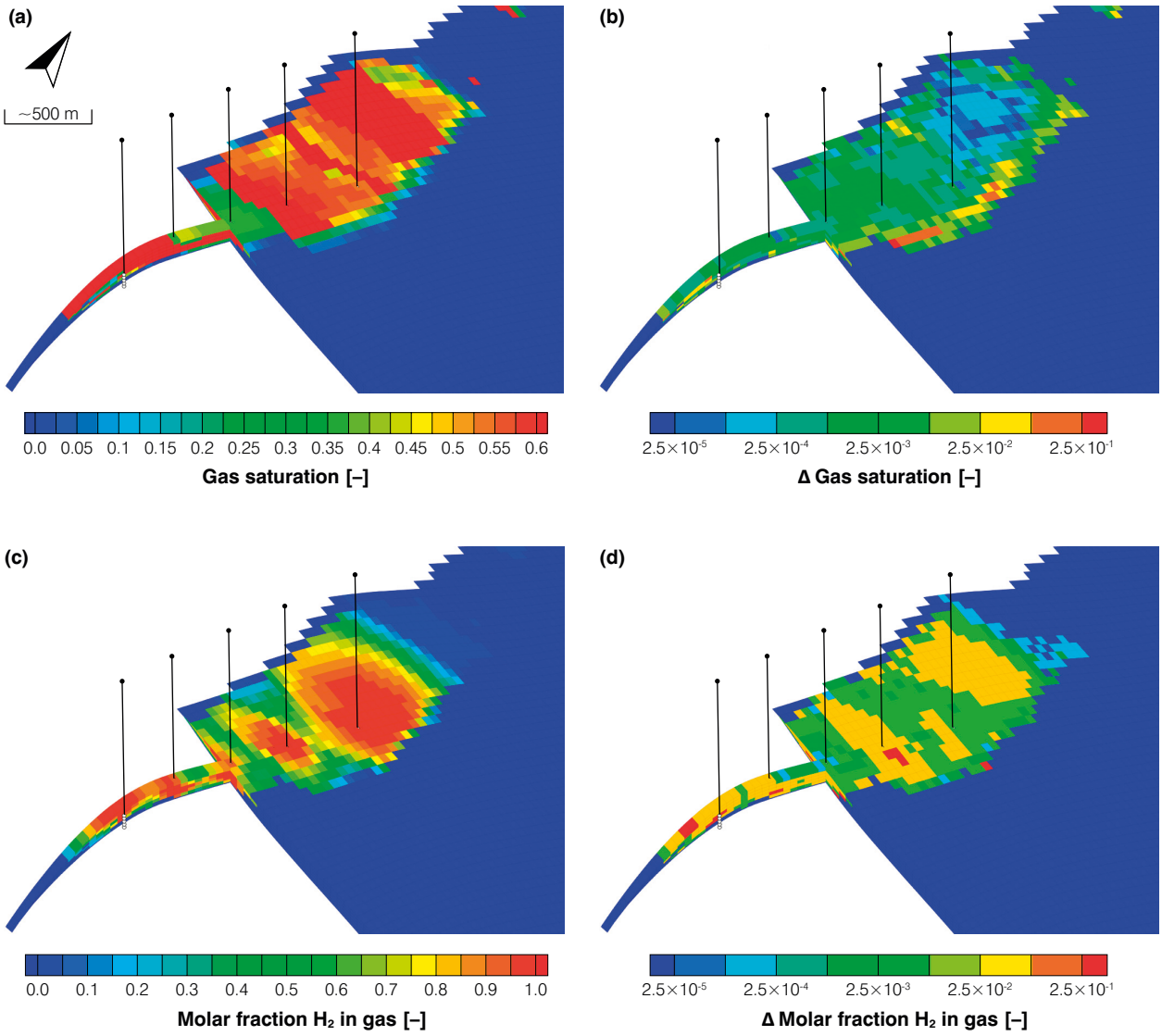

*Fig. 4.7 **(a)** Absolute gas saturations before the sixth production period and **(b)** change in gas saturation after the sixth storage cycle; **(c)** molar fractions of H_2 in gas before the sixth production period and **(d)** change of the molar fractions of H_2 in gas after the sixth production period (magnitudes) in the storage formation in run #14. The displayed formation is vertically exaggerated by a factor of 5. Each grid block is 50 by 50 m in lateral direction.*

The pressure change observed at the observation points 500 and 1000 m distant to the well gallery during the first storage cycle from day 923 to 930 exhibits a similar characteristic compared to the storage wells with the median pressure dropping about 14 and 8 bars, respectively (Fig. 4.4). Consequently, the pressure at 500 m is already below the initial hydrostatic pressure at the end of the extraction period while the observation well at 1000 m still shows a slight median overpressure of about 1.8 bars. The variability of the pressure change as determined by the spread between the 5th and 95th percentiles around the median varies but stays within ±2.7 bars at the observation point in 500 m distance, while the variability in 1000 m distance is ±1.0 bar. The more distant observation points again show a delayed pressure response to the gas extraction and smaller amplitudes (Fig. 4.4). The refill of the storage with H_2 from day 932 to 982, subsequent to the gas extraction, again results in a pressure increase in the vicinity of the storage wells (Fig. 4.5). Even though the amplitude of the pressure increase is greater than during the initial fill, the maximum value of the median pressure observed is lower than the value reached during the storage initialization, as

the pressure level prior to the refill is lower than the initial pressure (Fig. 4.4). The rate of the pressure change during the storage refill is lower than during the production phase because the gas flow rates applied at the wells and thus the gradient imposed on the system is considerably smaller. The variability in the pressure signal during the storage refill periods is nearly identical with the variability observed during the production phases. During the subsequent 30 day shut-in phase the pressure slowly declines towards the initial value in the injection wells (not shown). This behaviour is also visible at the observation points in 500 and 1000 m with a pressure decrease of about 1 bar and 0.5 bars, respectively. Contrary to that a slight pressure increase resulting from the H_2 refill can be observed at 2500 and 5000 m during this period (Fig. 4.5). The subsequent pressure drop at 1020 days is already a result of the second production period. Thus, the pressure signal of the 30 day shut-in period separating the storage cycles is not visible at the distant observation points as the strong pressure gradient imposed on the system during production outpaces it. The variability of the pressure signal during the shut-in period is similar to the refilling period.

With increasing number of storage cycles, the pressure signal from the initial filling of the storage dissipates slowly as a result of the constant pressure boundary conditions (Fig. 4.4). The maximum and minimum pressures observed during the storage cycles decrease as well while the variability of the pressure signal is more or less constant throughout the simulation.

While both gas injection and extraction are clearly visible in the pressure distribution, little to no visible differences are observable in the gas saturation (Fig. 4.6, 4.7), indicating a relatively stable gas-water contact during the storage cycles. This shows, that the storage operation is mainly supported through gas expansion and compression and is therefore controlled by the gas compressibility. This conclusion is further supported by the observed changes in gas density of around 20 % during each storage cycle. The total gas in place increases with the number of storage cycles as slightly more gas is injected than extracted during each cycle (Tab. 4.3, Fig. 4.6). Nevertheless, the strong effect of the formation heterogeneity is persistent throughout the simulation with the distribution of the gas phase being highly variable between the individual realisations until the last storage cycle (Fig. 4.8). While few realisations show a relatively homogeneous gas phase distribution (e.g. run #15, Fig. 4.8), most realisations display a more variable pattern. Well placement in a heterogeneous reservoir can thus result in individual wells being more or less separated from the main storage (e.g. centre well 3 in run #3 & #19, Fig. 4.8). This well-known effect has to be checked for in the field during well testing.

The composition of the produced gas phase changes considerably during each extraction period (Fig. 4.6, 4.8). As more H_2 is injected than

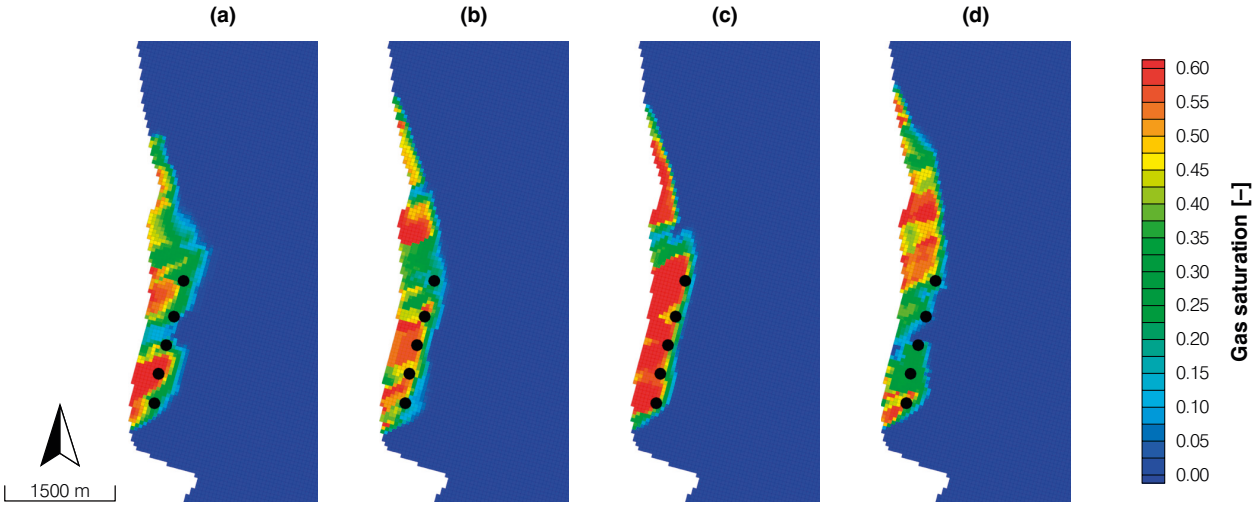

*Fig. 4.8 Vertically averaged gas saturations in the storage formation before the sixth production period in run #3 **(a)**, #14 **(b)**, #15 **(c)** and #19 **(d)**.*

extracted in each storage cycle, the H_2 in place increases with the number of cycles (Fig. 4.6). While the absolute molar fractions of H_2 in gas show high values at the top of the storage formation (Fig. 4.8), the vertically averaged values are considerably lower in most of the storage site (Fig. 4.6). Thus, a density contrast driven vertical separation of the two gas components is occurring with H_2 occupying the upper parts of the reservoir and N_2 making up the gas phase in the lower parts of the storage formation.

During the first extraction period, the lower BHP limit is reached in at least one well in almost every realization, resulting in reduced well flow rates and thus reduced gas extraction rates for the whole storage site (Tab. 4.3, Fig. 4.9). The median of the achieved gas flow rate is above 4 million sm^3/d for most of the first extraction period, ultimately dropping down to about 3.5 million sm^3/d towards the end. The variability of the storage gas flow rate is large with the range between the 5th to 95th percentiles being about ±1.4 million sm^3/d

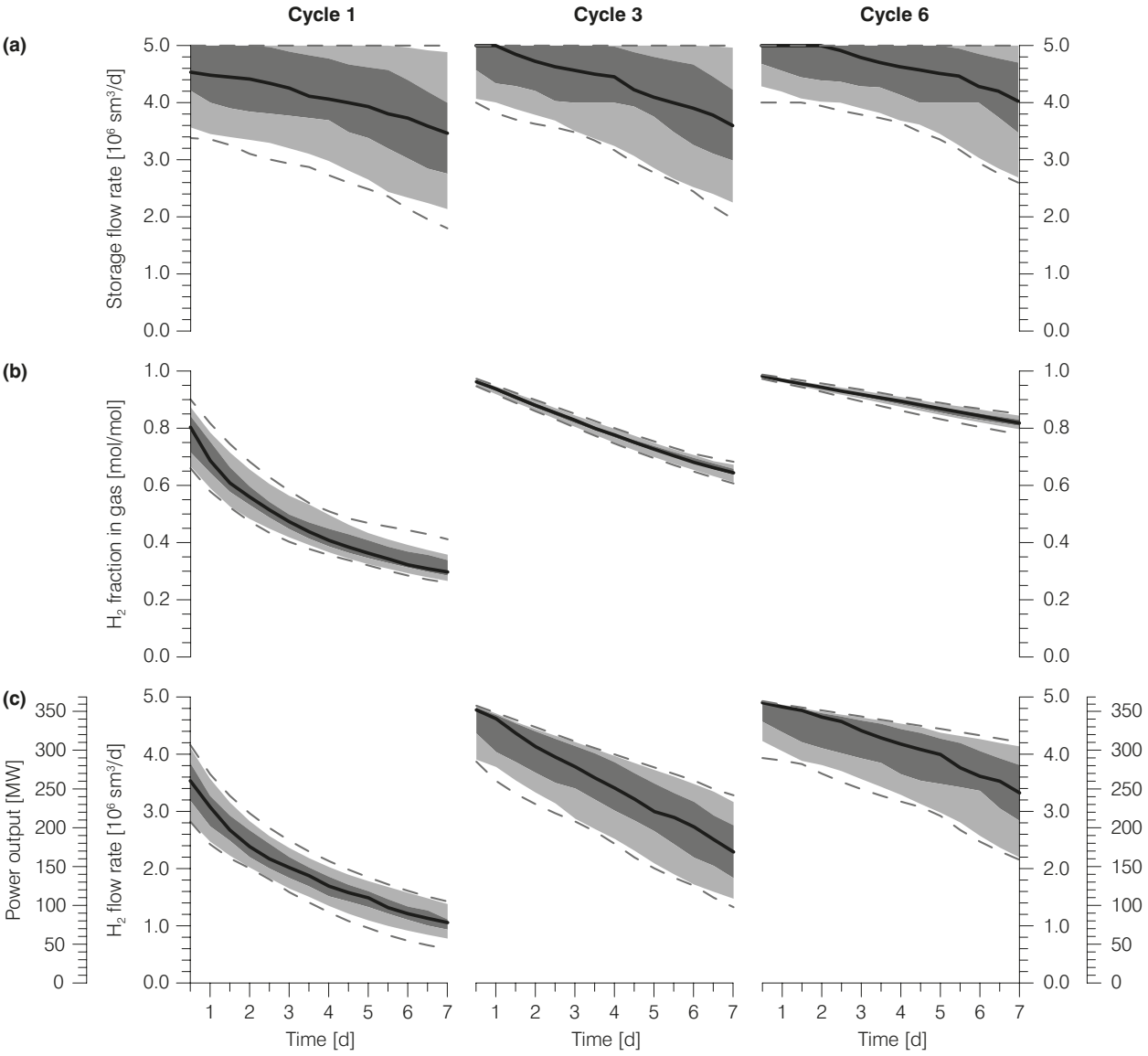

*Fig. 4.9 **(a)** Total storage flow rate, **(b)** volume averaged molar H_2 fraction in the produced gas phase per storage and **(c)** resulting H_2 flow rate as well as equivalent power output for storage cycles 1, 3 and 6. The solid black line depicts the median of all realisations, the dark grey shaded area the interval spanning between the 25th and 75th percentiles, the light grey shaded area the interval spanning between the 5th and 95th percentiles. The dashed lines indicate the absolute minimum and maximum values.*

around the median value. The composition of the gas phase in the storage formation and also in the produced gas changes considerably during each production period (Fig. 4.6, 4.8, 4.9). While the molar fraction of H_2 in the produced gas phase initially is 0.8, fractions of about only 0.3 are reached at the end of the extraction period (Fig. 4.9). The variability in the data stays more or less constant and within ±0.05 of the median. Consequently, the median of the achieved H_2 flow rate drops considerably from initially 3.5 million sm^3/d to slightly less than 1.1 million sm^3/d at the end of the production phase (Fig. 4.9). The power output from the storage site thus drops from initially about 260 MW to 78 MW over the course of the withdrawal period. The cumulative H_2 volume produced during the withdrawal is 13.64 million sm^3, which corresponds to 24 104 MWh (Tab. 4.3). Thus, the storage site is capable of supplying around 11 % of the required storage demand defined in this analysis. However, taking the median power output at the end of the production phase of 78 MW as an approximation of the potential continuous power output of the storage, the storage can only supply 5.7 % of the continuous power demand of 1356 MW specified in the scenario.

In the subsequent storage cycles the median of the achieved storage flow rates increases slightly with the lowest value obtained at the end of the last storage cycle being 4.0 million sm^3/d (Fig. 4.9). With the exception of the last day of the third storage cycle, the 95th percentile remains at the maximum value of 5.0 million sm^3/d throughout the third and sixth storage cycle. Thus, the best 5 % of all simulation runs can sustain the envisaged extraction rate of 1 million sm^3/d/well from the third storage cycle onwards. The variability of the storage flow data decreases slightly with the number of storage cycles. Compared with the first storage cycle, the median value of the molar H_2 fraction in the produced gas and thus the H_2 flow rate of the storage increases considerably in the later cycles with the median of being 3.32 million sm^3/d at the end of the sixth cycle, corresponding to a power output of about 245 MW (Fig. 4.9). This means that the storage is capable of continuously delivering 18 % of the required power in this scenario in the last storage cycles. The total withdrawn H_2 volume corresponds to 52 022 MWh, which is nearly 23 % of the total demand specified in the scenario. The storage performance is greatly increased compared to the first few storage cycles (Tab 4.3)

The variability of the H_2 flow data is increased compared to the first cycle with the 5th to 95th percentiles ranging from 2.19 to 4.14 million sm^3/d in the sixth production period, providing about 162 and 305 MW, respectively. Thus, the minimum and maximum power output, which can be sustained over the whole sixth production period, equates to 11.9 and 22.5 % of the required delivery rate of power. The variability in the data of the H_2 flow rate is mainly due to the variability in the total gas flow rate as the data of the molar H_2 fractions in the produced gas shows only a small spread (Fig. 4.9). Thus, the storage performance strongly depends on the distribution of the gas saturation in the storage formation. An approximately homogeneous gas phase distribution as e.g. observed in run #15 (Fig. 4.8) allow for high H_2 gas flow rates and thus a power output twice as large as for a strongly varying as phase as i.e. in run #3 (Fig. 4.8). Thus, the performance of the storage site is mainly governed by the distribution of the H_2 gas phase within the storage formation, which in turn depends strongly on formation heterogeneity.

4.4.4 Conclusions

The heterogeneous parameter distribution of the storage system affects the behaviour of the storage on the short and on the long term. In the first two stages of the simulated storage operation (initial fill with the cushion and working gases) the heterogeneity of the hydraulic parameters results in reduced injection rates as a consequence of the pressures in the injection wells reaching the specified upper BHP limit. Even if good injection properties of the reservoir are given, the volume of H_2 that can be provided for the first storage cycle is lower than intended. This in part can be attributed to the injection of inert N_2 in the first stage prior to the first H_2 injection, resulting in already elevated pressures in the storage formation and thus reducing the amount of H_2 that can be injected in the second stage. Changing the injection pattern such that the N_2 is injected at the side of

the structure purely for pressure mitigation after the initial filling with the H_2 could potentially improve the storage performance of the first cycles. The N_2, however, is also acting as an inert barrier between the formation water and the H_2 which could help minimizing chemical and microbial reactions. Other techniques such as additional shut-in periods during the storage initialization to reduce the formation pressure could also help increasing the H_2 volume available prior to the first storage cycle. The relatively slow dissipation of the overpressure signal, however, requires long shut-ins during which the storage cannot be used. Starting the storage operation even if the performance is sub-par in the first cycles does result in comparable or even better storage performances after the same timespan with the added benefit that the storage is, albeit on a smaller scale than intended, already in use. Alternatively, the overpressures can be actively mitigated by producing fluid from the storage formation.

The heterogeneous distribution of the gas phase in combination with the varying composition results in reduced storage flow rates and N_2 gas as impurity in the produced H_2 gas. Furthermore, the simulation of the storage operation clearly shows that the storage is not operating at its full potential in the first storage cycles, as the extracted H_2 volume and thus the power output increases consistently with the number of completed storage cycles. The increase in storage performance is due to the fact that more H_2 is injected than extracted in each cycle.

Even though the achieved H_2 extraction rates increase with the number of completed cycles, the variability among the heterogeneous realisations stays more or less constant. This is due to the gas phase distribution being strongly spatially heterogeneous throughout the whole simulation. Consequently, the explicit simulation of the storage initialization as opposed to defining an initial homogeneous gas phase distribution is very important in order to obtain valid storage flow rates later in the simulation. Monitoring of the gas phase distribution, e.g. by a combination of seismic and hydraulic methods as reported in Pfeiffer et al. (2016) or Benisch et al. (2015) could thus enhance the understanding of the storage formation and help with optimizing the storage operations.

As every simulation run exhibits a decrease in the H_2 fraction in the produced gas in the week-long production period and most simulation runs also show a reduction in storage flow rate, the H_2 flow rate and thus the power output from the storage is not constant. Using the lowest value as a reference, it can be concluded that the simulated storage site can supply a continuous power output of around 245 MW for one week when using five storage wells while peak performance can be as high as 363 MW. Thus, the storage is sufficient to provide 18 % of the total delivery rate required in the defined scenario, which assumes no power production from renewable sources at all during the one week period. If favourable parameter distributions and thus homogeneous, high saturation gas phase distributions close to the wells prevail, the storage formation can supply up to 300 MW continuously, corresponding to about 22.5 % of the required rate. Increasing the power output requires more wells to be used as the storage performance is clearly limited by the achieved flow rates. Storage capacity is not limiting, as the spill points of the structure are not yet reached by the injected gas, so that the stored gas volume could be increased easily. Dispersion effects, which are not included in this simulation via dispersivities but rather by explicitly representing formation heterogeneity, can be used to represent mixing processes during gas storage and may have considerable impact on the component distribution in certain settings, as found by e.g. Feldmann et al. (2016). A site and model approach specific evaluation of these mixing effects should thus be conducted, which however requires site specific determination of dispersivities. In case of higher mixing than represented in this work, fractions of H_2 in the produced gas may slightly decrease.

The pressure response of the reservoir to the storage operation is far reaching with a pressure increase of about 3 bars being observed in distances of 5 km and the storage operation being visible in the recorded pressure signals. These signals could thus be used to monitor the storage site and the injection and extraction periods, as e.g. Benisch and Bauer (2013) did for CO_2 storage. Pressure changes in such distances from the storage wells caused by other usages, however, will most likely leave the storage operation unaf-

fected as the observed storage induced pressure change is already relatively low.

4.5 Part II: Reservoir simulations using generalized properties

Reservoir simulations using a heterogeneous ensemble of properties, as presented in Chapter 4.4, can be used to obtain knowledge regarding the variability of the storage performance as well as any induced effects in cases where the exact parameter distribution is largely unknown. However, due to the large ensemble size required to obtain reliable results, such simulations are time intensive and require significant computational resources. While approximations of reservoir behaviour do exist for simple cases with many assumptions, e.g. for estimating deliverability from storage wells (e.g. Katz et al. 1959), full scale reservoir simulations are required for complex real world geometries of storage formations and storage operations. To investigate effects of different storage simulation setups, i.e. varying well positions or injection/withdrawal rates, on the storage dimensions or induced effects, a generalised rock model can be useful as it reduces the number of required simulations. To begin, first several generalised rock models are created based on the parameter distributions of the heterogeneous ensemble. In a second step simulation results obtained with these rock models are compared to those of the heterogeneous simulations for identical storage setups. Based on the comparison, the effect of a new storage setup is tested with regard to the achievable storage performance and the induced hydraulic effects. Finally, the storage performance and the induced hydraulic effects of a large scale H_2 storage operation, capable of supplying 100 % of the defined storage demand, is investigated. Furthermore, potential mutual interactions between the large scale H_2 storage operation and a use of the storage formation for brine disposal are investigated.

4.5.1 Generalized rock model & simulation setup

To obtain a set of effective parameters which yields equivalent results compared to the conducted heterogeneous simulations, the rock properties such as the intrinsic permeability, porosity and the multiphase-flow characteristics must be averaged. Several methods and schemes of different complexity for calculating equivalent permeability are available and have been discussed in the literature (e.g. Renard and de Marsily 1997). In a simple system, in which the fluid flow is parallel or perpendicular to homogeneous rock layers, a correct estimation of the effective permeability exists in the form of the arithmetic (15) or harmonic (16) average of permeability for the former and latter case, respectively (e.g. Ringrose and Bentley 2015):

$$k_{arith} = \frac{\sum_1^n k_i t_i}{\sum_1^n t_i} \tag{15}$$

$$k_{harm} = \left[\frac{\sum_1^n \frac{t_i}{k_i}}{\sum_1^n t_i}\right]^{-1} \tag{16}$$

With n denoting the sample size and k_i and t_i the permeability and thickness of layer i, respectively. Such perfect systems in which rock layers are continuous and flow is either perfectly perpendicular or parallel rarely exist. Nevertheless, the arithmetic and harmonic averages do specify the upper and lower bound in which the effective permeability lies (e.g. Renard and de Marsily 1997; Ringrose and Bentley 2015). Similar to this, Cardwell and Parsons used an electric analogy to show that the equivalent permeability is bound by the arithmetic mean of the harmonic means of permeability parallel to the flow direction and the harmonic mean of the arithmetic means perpendicular to the flow direction (Cardwell Jr. and Parsons 1945). Thus, assuming flow is in x direction:

$$\begin{aligned} k_z^{arith}\left(k_y^{arith}(k_x^{harm})\right) \leq\ & k_{eff} \\ k_{eff} \leq\ & k_x^{harm}\left(k_y^{arith}\left(k_z^{arith}\right)\right) \end{aligned} \tag{17}$$

For more complex rock and flow geometries the geometric mean (18) is often suggested as an approximation (e.g. Ringrose and Bentley 2015):

$$k_{geom} = exp[\textstyle\sum_1^n \ln k_i / n] \tag{18}$$

For low variance, 3D-permeability distributions which have a low spatial correlation, i.e. the correlation lengths must be significantly smaller than the averaging volume (Ringrose and Bentley 2015), Gutjahr et al. (1978) showed that the effective permeability can be expressed using the geometric mean of the permeability and the corresponding variance of the natural logarithm of permeability:

$$k_{eff} = k_{geom}\left(1 - \frac{\sigma^2_{\ln k}}{6}\right) \quad (19)$$

However, the assumption of a purely stochastic permeability distribution with a low variance does not hold in the investigated scenarios as vertical and horizontal trends are used to obtain the heterogeneous parameter fields. The many choices of averaging schemes already imply that there is in fact no scheme which produces the correct effective permeability in all cases. Thus, instead of relying on one generalization scheme, 10 schemes are used to obtain generalised rock models (Table 4.4). The simulation results obtained with the different models are then compared with the heterogeneous results described previously in Chapter 4.4. As the heterogeneous simulations display a layered structure within each formation (compare Fig. 4.3), the effect of anisotropy in permeability was tested in cases 3 and 7 by assuming the permeability in z-direction being the arithmetic mean of the harmonic means. The reasoning for the harmonic mean is that a vertical movement of the gas is perpendicular to the layered structure of the formations (also compare Chapter 4.3).

Using the various averaging schemes results in differences in assumed effective permeability of several orders of magnitude for the same rock formation (Tab. 4.4). Low permeability zones can have significant impacts on the calculated effective permeability when using geometric or harmonic means. Thus, the magnitude of the variations in the effective permeabilities depends strongly on the degree of heterogeneity of the rock formation. Comparatively homogeneous formations such as the Main Sandstone of the Middle Rhaetian thus show smaller variations in the calculated effective permeabilities than e.g. the highly heterogeneous Lower Rhaetian.

For the storage formation, the Main Sandstone of the Middle Rhaetian, the estimated effective permeabilities vary from just around 20 mD to nearly 600 mD depending on the selected averaging scheme (Tab. 4.4). For the remaining rock formations, the variability in the estimated effective permeability is larger with the differences being on the order of several magnitudes.

Indifferent to the averaging scheme for permeability, the porosity is always calculated using the

Tab. 4.4 *Generalizing schemes for effective permeability tested in this analysis and corresponding permeability values.*

#	Methods used for averaging permeability	Permeability [mD]				
		Upper Rhaetian	Upper Shale Middle Rhaetian	Main Sandstone Middle Rhaetian	Lower Shale Middle Rhaetian	Lower Rhaetian
1	$k_{x,y,z} = k_{x,y,z}^{arith}$	1.806×10^{0}	1.204×10^{2}	5.984×10^{2}	1.341×10^{0}	4.687×10^{1}
2	$k_{x,y,z} = k_{x,y}^{arith}(k_z^{harm})$	3.942×10^{-1}	2.766×10^{1}	3.180×10^{2}	3.272×10^{-1}	4.940×10^{0}
3	$k_{x,y} = k_{x,y}^{arith}$ $k_z = k_{x,y}^{arith}(k_z^{harm})$	1.806×10^{0} 3.942×10^{-1}	1.204×10^{2} 2.756×10^{1}	5.984×10^{2} 3.180×10^{2}	1.341×10^{0} 3.272×10^{-1}	4.687×10^{1} 4.940×10^{0}
4	$k_{x,y,z} = k_{x,y,z}^{geom}$	3.090×10^{-3}	1.049×10^{1}	2.370×10^{2}	1.040×10^{-3}	1.167×10^{-2}
5	$k_{x,y,z} = k_{x,y}^{geom}(k_z^{harm})$	1.600×10^{-4}	1.433×10^{-1}	8.566×10^{1}	1.300×10^{-4}	2.800×10^{-4}
6	$k_{x,y,z} = k_{x,y}^{geom}(k_z^{arith})$	3.857×10^{-1}	7.085×10^{1}	4.748×10^{2}	2.079×10^{-2}	2.858×10^{0}
7	$k_{x,y} = k_{x,y}^{geom}(k_z^{arith})$ $k_z = k_{x,y}^{geom}(k_z^{harm})$	3.857×10^{-1} 1.600×10^{-4}	7.085×10^{1} 1.433×10^{-1}	4.748×10^{2} 8.566×10^{1}	2.079×10^{-2} 1.300×10^{-4}	2.858×10^{0} 2.800×10^{-4}
8	$k_{x,y,z} = k_{x,y}^{geom}\ (1-\sigma^2/6)$	1.930×10^{-2}	4.439×10^{1}	4.130×10^{2}	5.720×10^{-3}	9.905×10^{-2}
9	$k_{x,y,z} = k_z^{arith}(k_y^{harm}(k_x^{harm}))$	9.960×10^{-3}	3.651×10^{0}	2.603×10^{1}	4.000×10^{-5}	3.400×10^{-4}
10	$k_{x,y,z} = k_x^{harm}(k_y^{arith}(k_z^{arith}))$	6.209×10^{-1}	4.004×10^{1}	2.106×10^{2}	4.824×10^{-1}	1.689×10^{1}

Tab. 4.5 Formation specific facies fractions based on the distributions of the heterogeneous ensemble and properties assigned to the individual formations in the generalised rock models.

Formation	Porosity [–]	Sr_w [–]	kr_{gmax} [–]	p_d [bar]	Facies fractions			
					Shale	Fine Sand	Medium Sand	Coarse Sand
Upper Rhaetian	0.126	0.5268	0.1193	9.6932	63.40 %	36.60 %	0.00 %	0.00 %
Upper Shale, Middle Rhaetian	0.280	0.4183	0.3696	1.6833	9.15 %	43.00 %	47.85 %	0.00 %
Main Sandstone, Middle Rhaetian	0.332	0.3469	0.6770	0.2146	0.10 %	17.85 %	28.77 %	53.28 %
Lower Shale, Middle Rhaetian	0.108	0.5457	0.0923	11.0644	72.86 %	27.14 %	0.00 %	0.00 %
Lower Rhaetian	0.154	0.5165	0.1711	8.8877	58.23 %	23.25 %	18.52 %	0.00 %

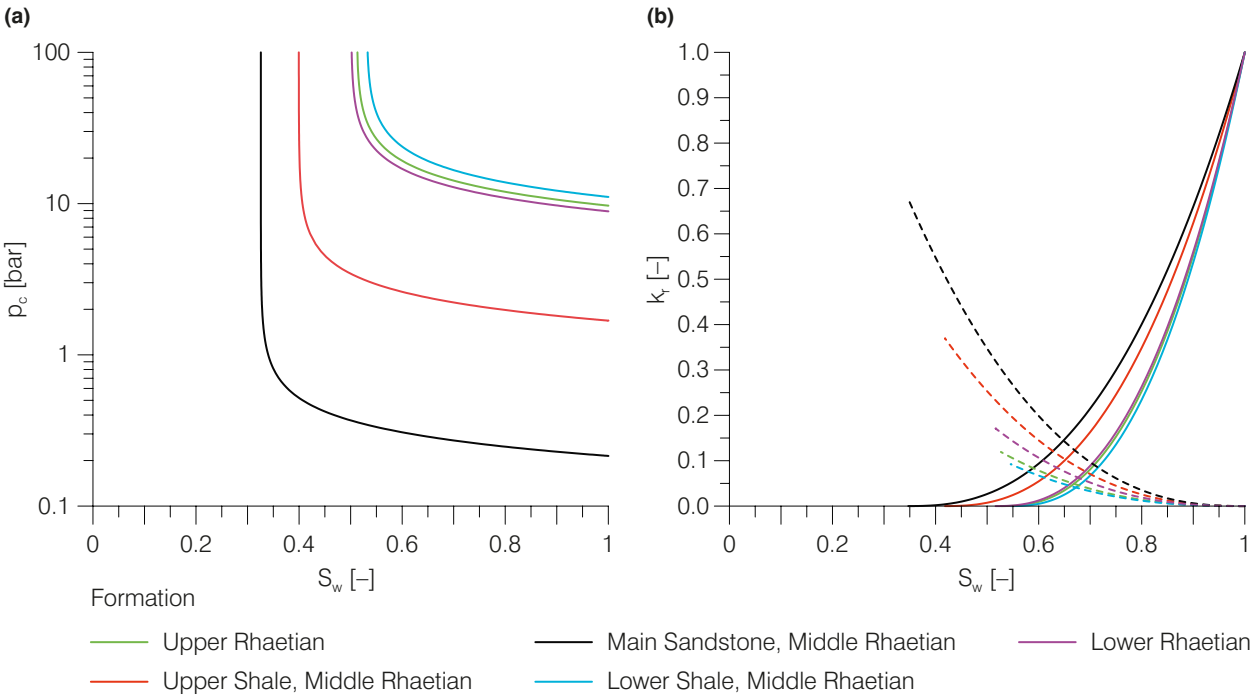

*Fig. 4.10 Generalised **(a)** capillary pressure and **(b)** relative phase permeability curves of the individual formations which are obtained when using the parameters given in Tab. 4.5 in combination with the formations of Brooks and Corey (1946) for capillary pressure and Burton et al. (2009) for relative phase permeability. The dashed lines depict the relative permeability curves the gas phase while the solid lines indicate the water relative permeability curves.*

arithmetic mean of the porosity values in all 25 heterogeneous simulations. Also, identical multiphase flow properties such as relative phase permeabilities and capillary pressures are used in all simulations. The multiphase flow properties are determined by calculating effective input parameters for the respective equations by Brooks and Corey (1946) for capillary pressure and Burton et al. (2009) for relative phase permeability by a weighted arithmetic mean, with the weights being the fractions with which the individual facies occurred in each formation (Tab. 4.5, Fig. 4.10). Albeit hydrodynamic dispersion is a factor contribution to mixing processes, ECLIPSE cannot consider gas in gas dispersion and thus this process is not represented in the simulations.

4.5.2 Comparison of heterogeneous and homogeneous simulation runs

Given the variety of available methods to estimate effective permeability, first the applicability of the individual methods for the given storage scenario should be tested. This is done by comparing the results obtained in the various homogeneous simulation cases to those of the heterogeneous ensemble regarding the storage performance and the induced hydraulic effects. Based on this analysis, results obtained for homogeneous scenario simulations of e.g. different well setups can then be used to provide a first estimate the variability of which can be expected due to the formation heterogeneity.

For the comparison of the heterogeneous and the homogenous simulations all simulation data apart from the hydraulic properties (Tab. 4.4, 4.5) such as e.g. phase properties, well setup and boundary conditions are carried over from the heterogeneous scenario simulations described in Chapter 4.4. Hence, the storage operation consists of three phases. The simulation starts with the initial injection of N_2 at a target rate of 55 625 sm^3/d/well for 710 days, followed by the first H_2 injection at 155 000 sm^3/d/well for 210 days. These two first stages are followed by the storage operation comprising of 6 cycles with each cycle consisting of a withdrawal period of 1 week followed by an injection phase of 50 days and a shut-in period of 30 days. The target well flow rate for the withdrawal is and the injection periods are 1 000 000 sm^3/d/well and 150 000 sm^3/d/well, respectively. Assuming ideal conditions, i.e. all the withdrawn gas is H_2, the volume of gas produced per storage cycle should be 35 million sm^3, which equates to about 27 % of the weekly demand defined if the efficiency of the re-electrification is 60 % (see Chapter 4.2). During injection phases the pressure in the storage wells is limited to 65 bars. The lower BHP limit is set to 30 bars. The simulations are carried out using the Eclipse E300 reservoir simulator (© Schlumberger).

Induced hydraulic effects

The homogeneous simulations exhibit the same effect of small scale pressure changes because of the different endpoints of the capillary pressure curves of the individual formations as the heterogeneous simulations (compare Chapter 4.4.3). However, larger pressure differences of up to nearly 1 bar are present in the baseline simulations when using the various homogeneous parameter distributions. Thus, all pressure perturbations shown in the following are calculated using reference pressures obtained with the individual baseline simulations instead of relying on the initial pressure distribution calculated by ECLIPSE.

Identical to the simulations using the heterogeneous parameter distributions, the injection of the N_2 and the H_2 in the first two stages of the storage formation results in a pronounced pressure increase in the storage formation as the water is displaced by gas (Fig. 4.11, 4.12). The maximum overpressure in the storage formation is about 20 bars above the initial pressure, being bound by the upper BHP limit assigned to the storage wells. During the storage initialization phase the upper BHP limits are reached in all wells, independent of the estimation of permeability (not shown). As a direct result the well flow rates are reduced. Consequently, the overpressure signals close to the injection site do not vary significantly among the simulations during the initial injection until 920 days. Apart from the very low permeability cases, all simulations show overpressures in the interval spanning from the 95th percentile to the median up to 1000 m from the injection wells during the initial injection (Fig. 4.11 a,b). Only the simulations of lower permeability values, i.e. when permeability is estimated by the method of Cardwell Jr. and Parsons (1945) or by an geometric average of the harmonic mean, show an even lower pressure increase (not shown).

With increasing distance to the well gallery, the overpressure signal is dampened and delayed so that the maximum pressure changes at 2500 m and 5000 m are observed after the initial filling of the storage site is completed. Again, the pressure signals in most simulations are within the interval spanning from the 95th percentile to the median of the heterogeneous ensemble during the first 920 days (Fig. 4.11 c,d). In the far field of the storage wells the median pressure signal of the initial gas injection is reasonably well matched when the effective permeability is estimated using a simple arithmetic mean.

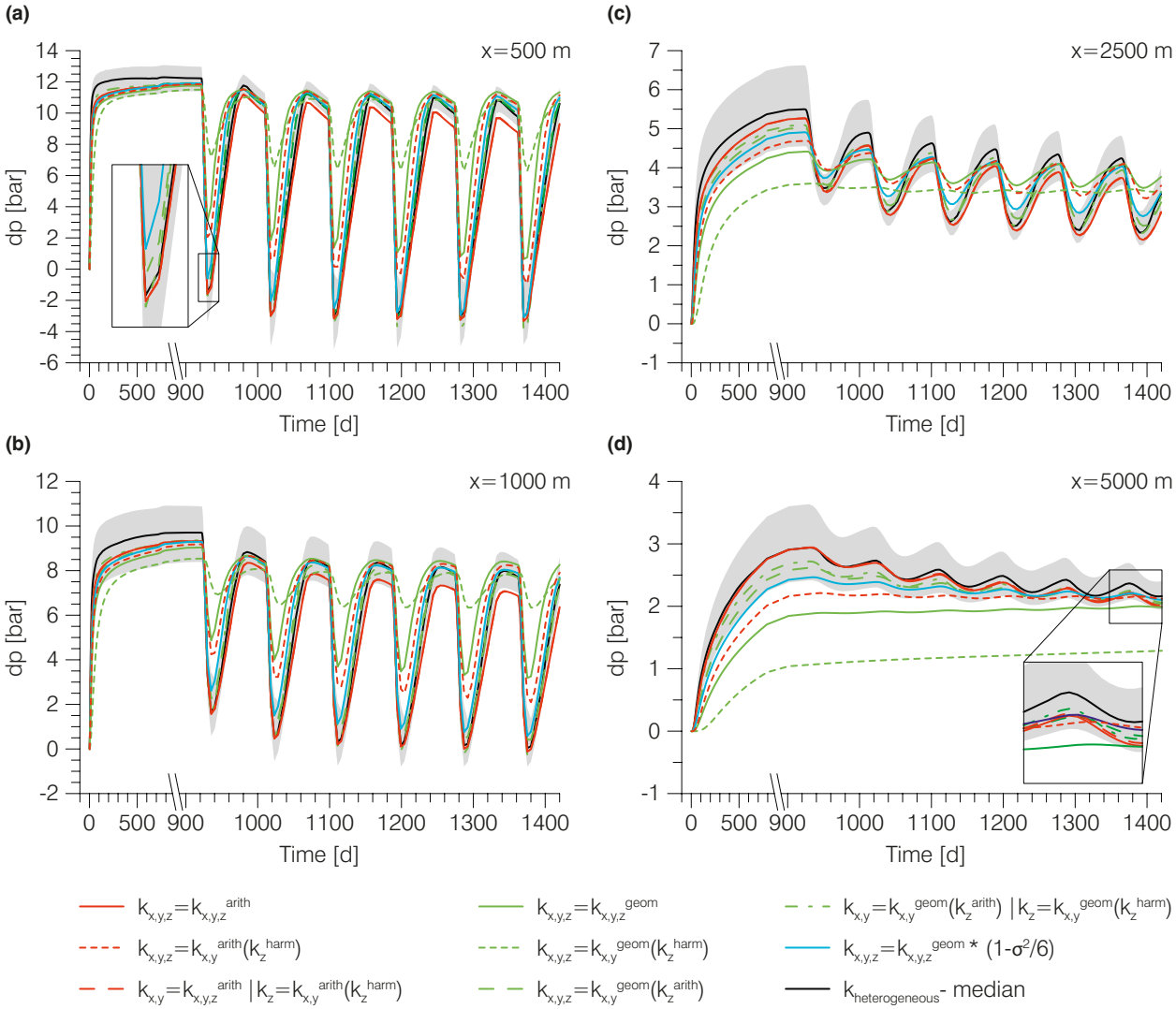

Fig. 4.11 *Evolution of reservoir pressures at observation points at* ***(a)*** *500 m,* ***(b)*** *1000 m,* ***(c)*** *2500 m and* ***(d)*** *5000 m along a transect perpendicular to the well gallery (compare Fig. 4.1). The grey shaded area marks the interval spanning between the 5th and 95th percentile of the heterogeneous ensemble. The curves for the lower and upper bound as defined by Cardwell Jr. and Parsons (1945) follow the same trend as the curves of obtained using the geometric mean (solid green) and the geometric mean of the vertical harmonic mean (short dashed green), but at even lower pressure levels and are thus omitted for easier visual distinction.*

The low permeability simulations, e.g. when using a geometric average, the pressure perturbations are significantly dampened, resulting only slight overpressures which are persistent until the end of the simulation. The heterogeneous ensemble and the higher permeability homogeneous cases show a decline in the overpressure in the far field during the storage operation following the maximum pressure increase after the storage initialization.

During the storage operation, the variation in the pressure signals obtained in the different homogeneous simulations differs significantly, especially during the withdrawal periods (Fig. 4.11 a,b). This is because the duration of the withdrawal periods is short, resulting in only slight pressure changes in the low permeability simulations. Using a simple arithmetic mean to estimate permeability provide the best fit to the median of the heterogeneous ensemble during withdrawal periods in the near and the far field of the storage wells. During injection phases, estimating the effective permeability by the method of Gutjahr et al. (1978) provides the better fit to the median of the heterogeneous ensemble (Fig. 4.11 a,b; solid blue line).

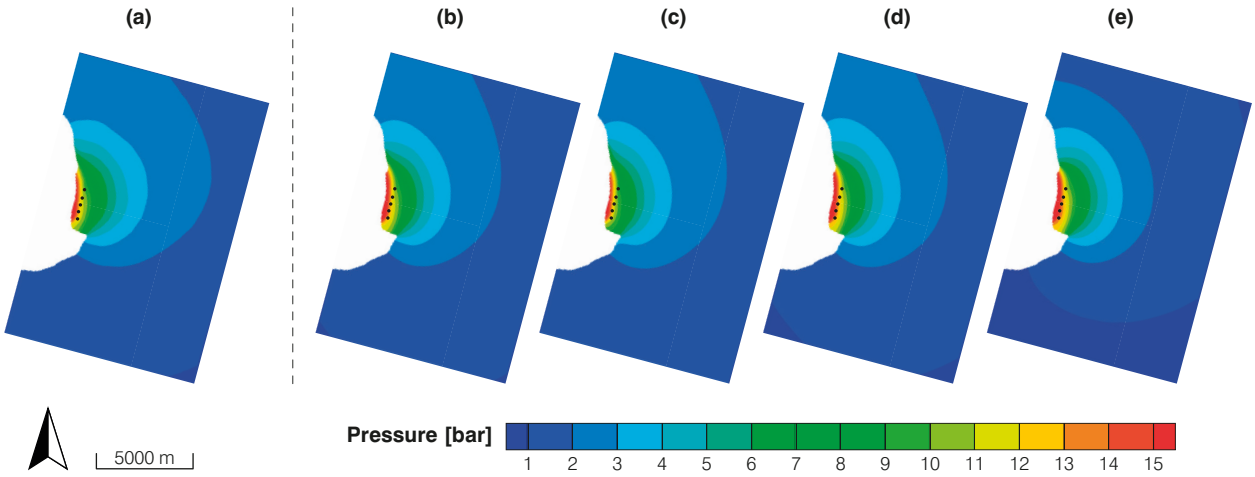

Fig. 4.12 Comparison of the ***(a)*** *average overpressure of the heterogeneous ensemble with the overpressure signals obtained with generalised rock models* ***(b)*** *using the geometric average of the arithmetic average of permeability [$k_{x,y,z} = k_{x,y}^{geom}(k_z^{arith})$],* ***(c)*** *using the arithmetic average [$k_{x,y,z} = k_{x,y,z}^{arith}$],* ***(d)*** *using the method proposed by Gutjahr et al. (1978) [$k_{x,y,z} = k_{x,y}^{geom}(1-\sigma^2/6)$] and* ***(e)*** *using the geometric mean [$k_{x,y,z} = k_{x,y,z}^{geom}$] prior to the sixth storage cycle at 1362 days.*

With increasing permeability of the individual simulation, the overpressures dissipate quicker (Fig. 4.11 c,d). Nevertheless, the predicted overpressure at the end of the sixth storage cycle is similar for most cases with the difference being less than 0.5 bars in 5000 m while being close to the 95th percentile of the heterogeneous ensemble (Fig. 4.11 d). However, the overpressures caused by the storage operation are on the order of about 2 bars and thus not in itself not high compared to the absolute pressures being around 150 bars and more.

Thus, the tested homogeneous simulation cases can only serve as lower estimate of the overpressure persistent at the end of the storage operation. The maximum pressure increase in the far field can, however, be adequately represented in the given scenario when permeability is estimated by a simple arithmetic average. The magnitude of the induced pressure changes in the near field of the storage site are governed by the applied BHP limits and thus not directly affected by the formation permeability in the tested scenario. The extent of the space in which higher overpressures can be expected is, however, dependent on the formation permeability.

While the pressure response of the storage operation is still visible in the simulation based on the method of Gutjahr et al. (1978) and consequently also the higher permeability simulations, the lower permeability simulations do not show a clear response and thus do not allow for a distinction of the current storage operation based on the pressure signal.

Regarding the distribution of the overpressure neither methods results in a very good representation of the median of the heterogeneous ensemble (Fig. 4.12). Nevertheless, the simulations in which permeability is estimated by an arithmetic mean, by the geometric mean of the vertical arithmetic means or by the method of Gutjahr et al. (1978) provide the best fit for the presented simulations (Fig. 4.12 b,c,d). In the low permeability simulations, e.g. when using a geometric mean of the vertical harmonic means or the method of Cardwell Jr. and Parsons (1945) the extent of the pressure perturbation is underestimated (Fig. 4.12 e).

For the given storage setup, the absolute magnitude of the induced pressure perturbations in the near field of the storage site is governed by the defined BHP limits and thus little affected by the permeability. However, the propagation of the pressure signal is affected by formation permeability so that the space in which high pressure differences occur varies. Compared to the median of the heterogeneous ensemble the overpressure distribution in the near field of the storage site is reasonably well matched in the homogeneous simulations in which permeability is either estimated by a simple arithmetic mean or the ge-

ometric average of the vertical arithmetic means. In the far field the induced pressure perturbations are slightly underestimated in all homogeneous simulation cases compared to the median of the heterogeneous ensemble towards the end of the storage operation. However, the magnitude of the induced overpressure in the far field is reasonably well approximated in the simulation in which the effective permeability is estimated by a simple arithmetic average.

The injected gas accumulates at the top of the structure as it is more buoyant than the denser formation water with the extent of the gas phase in the different homogeneous simulations varying depending on the injected gas volumes (Fig. 4.13). The extent of the gas phase in the heterogeneous ensemble is best matched by the simulation in which a simple arithmetic mean is used (compare Fig. 4.13 a and c). Thus, the reach of directly induced hydraulic effects by the gas injection is best estimated by the simulation using a simple arithmetic mean. The H_2 is concentrated around the storage wells at the end of the storage initialization phase at 920 days, with again the simulations using an arithmetic mean provide the best fit to the heterogeneous ensemble (Fig. 4.14). The overall behaviour of the storage site is identical to the previously discussed heterogeneous simulations with the withdrawal of the gas being mainly supported by the compressibility of the gas phase with only little water movement (compare Fig. 4.7).

Storage performance

The storage performance is greatly affected by the injectivity of the storage formation, which depends on the reservoir properties such as the permeability and the formation thickness (e.g. Plaat 2009). For formations with lower injectivity higher injections pressures are required to inject the same volume of fluid per time at a given number of wells compared to a formation with a higher injectivity. Given the maximum pressure is constrained by the applied BHP limits, less gas is injected in simulations in which the storage formation has only a low permeability. Consequently, less gas is available for withdrawal from the first cycle onwards (Fig. 4.15). In the simulations in which permeability is estimated by a simple arithmetic mean high injection rates are achieved during the storage initialization phases, resulting in more than 90 million sm^3 of N_2 and nearly 26 million sm^3 of H_2 being injected (Fig. 4.15a,b). These injection volumes are close to the 5th percentile interval of the heterogeneous ensemble. The lower interval limit, taken as the 95th percentile, is well matched in the simulation cases which use the geometric mean of the vertical arithmetic means with about 68 million sm^3 of N_2 and 19 million sm^3 of H_2 being in place prior to the first storage cycle at 920 days (Fig. 4.15 a,b). Assuming an anisotropy in permeability does not change the results significantly. The remaining simulation cases show reduced gas volumes in place which are not within the range of the variability of the heterogeneous simulations.

Even though the discrepancies between the different simulations are getting smaller with the number of storage cycles, the overall trend remains unchanged with the simulations in which permeability is estimated by an arithmetic mean providing a good estimate of the 5th percentile of the heterogeneous ensemble (Fig. 4.15 a,b). The 95th percentile is again well matched in the simulations in which the geometric mean of the vertical arithmetic means is used to estimate the effective permeability. No estimation technique results in a good match to the median of the heterogeneous ensemble.

The general trend storage flow rates achieved in the heterogeneous ensemble is not matched well in any of the tested homogeneous simulations, showing a tendency to more pronounced drops in the achieved flow rates toward the end of the withdrawal periods (Fig. 4.16a). This is due partly to the results of the heterogeneous simulations being the average of several runs which are hence already smoothed. Nevertheless, the high permeability simulations, e.g. when an arithmetic average or a geometric average of the vertical arithmetic averages is used, provide the closest fits the results of the heterogeneous ensemble. Regarding the sustainable storage flow rate, that is the lowest rate achieved during a withdrawal cycle, the simulations in which permeability is estimated by a simple arithmetic average provide a good fit to the 5th percentile of the heterogeneous ensemble during the later storage cycles. The simulations in which permeability is estimated by the geometric mean of the vertical arithmetic averages show

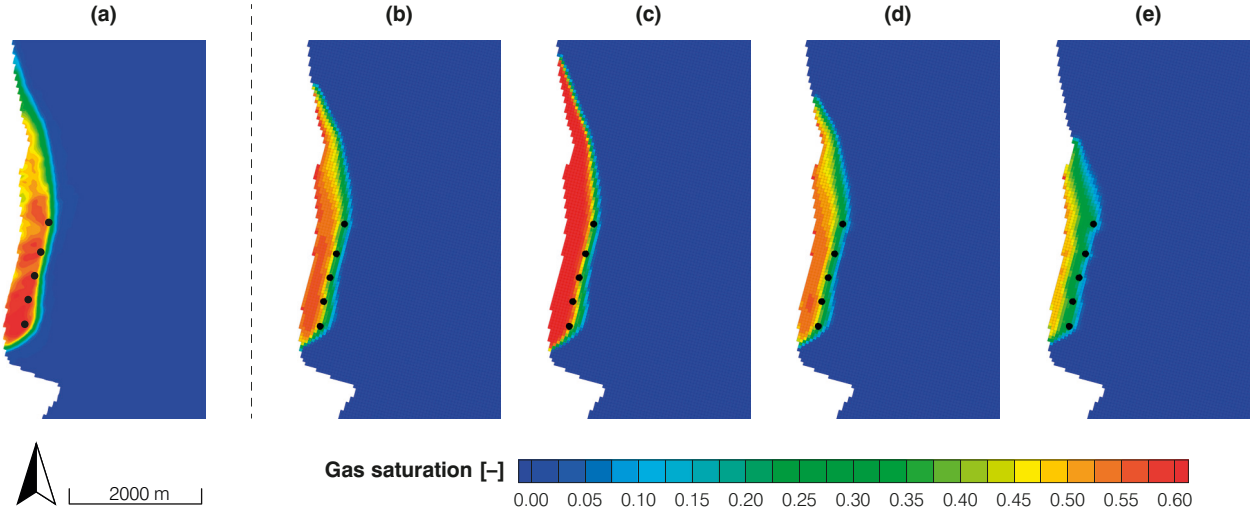

*Fig. 4.13 Comparison of the **(a)** average of the gas saturation of the heterogeneous ensemble with the saturation distributions in the storage formation obtained with generalised rock models **(b)** using the geometric average of the arithmetic average of permeability [$k_{x,y,z} = k_{x,y}^{geom}(k_z^{arith})$], **(c)** using the arithmetic average [$k_{x,y,z} = k_{x,y,z}^{arith}$], **(d)** using the method proposed by Gutjahr et al. (1978) [$k_{x,y,z} = k_{x,y}^{geom}\ (1\text{-}\sigma^2/6)$] and **(e)** using the geometric mean [$k_{x,y,z} = k_{x,y,z}^{geom}$] prior to the sixth storage cycle at 1362 days.*

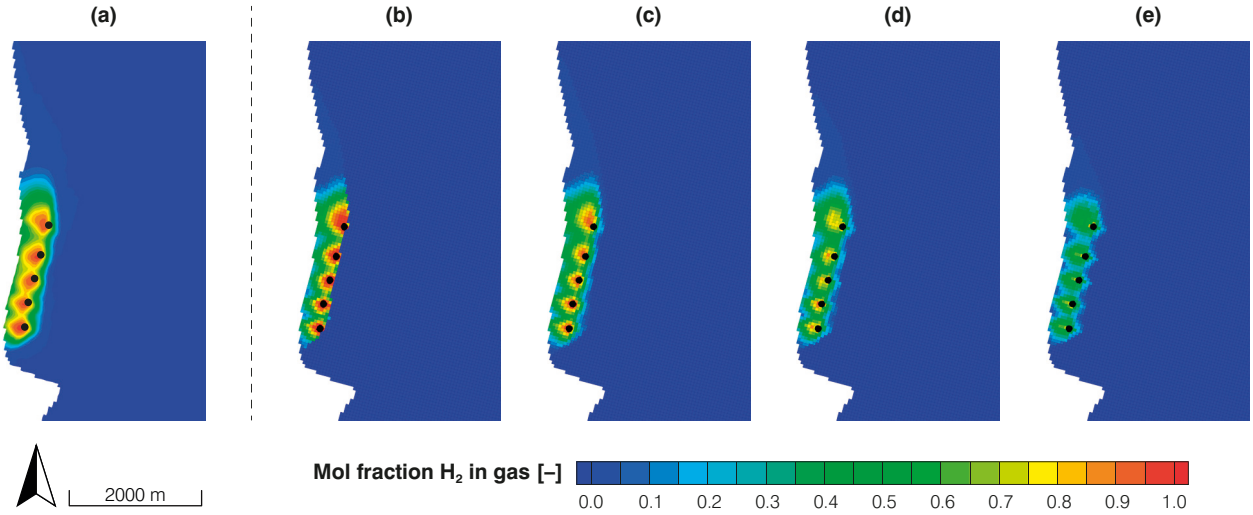

*Fig. 4.14 Comparison of the **(a)** average of the H_2 fraction in gas in the heterogeneous ensemble with the distributions obtained with generalised rock models **(b)** using the geometric average of the arithmetic average of permeability [$k_{x,y,z} = k_{x,y}^{geom}(k_z^{arith})$], **(c)** using the arithmetic average [$k_{x,y,z} = k_{x,y,z}^{arith}$], **(d)** using the method proposed by Gutjahr et al. (1978) [$k_{x,y,z} = k_{x,y}^{geom}\ (1\text{-}\sigma^2/6)$] and **(e)** using the geometric mean [$k_{x,y,z} = k_{x,y,z}^{geom}$] prior to the sixth storage cycle at 1362 days.*

storage flow rates comparable to the 95th percentile. Thus, simulations using these two averaging schemes provide a good upper and lower estimate of the storage flow rates achieved in the heterogeneous ensemble.

The H_2 fractions in the produced gas volume vary significantly over the course of the first storage cycle in each simulation, with the discrepancies among the simulations being relatively small (Fig. 4.16b). Initially values of around 80 to 90 % are achieved in all cases, which is slightly more than the median of the heterogeneous ensemble.

The H_2 flow rate, being the product of the storage flow rate and the H_2 fraction in the produced gas, follows the trend of the storage flow rates with the rates decreasing over the course of the withdrawal periods (Fig. 4.16c). With the number of storage cycles the overall performance in terms of achieved storage flow rates as well as H_2 fractions, and with that also the H_2 flow rate, in-

crease as more H_2 is available in the storage formation prior to the production periods (compare Fig. 4.15). In case of the simulations in which the permeability is estimated by an arithmetic mean, the H_2 volume in place increases nearly threefold, from the initial 26 million sm^3 to about 76 million sm^3, prior to the sixth storage cycle. Because of the variability in the H_2 fractions being minuscule among the homogeneous simulations, the simulations in which permeability is estimated using an arithmetic mean again provide a reasonable estimate of the 5th percentile of the heterogeneous ensemble towards the later storage cycles with the H_2 flow rate being about 3.8 million sm^3/d, which corresponds to roughly 280 MW (Fig. 4.16c). The 95th percentile is again well matched by the simulations in which permeability is estimated by the geometric mean of the vertical arithmetic means, with an H_2 flow rate of 2.2 to 2.4 million sm^3/d. These flow rates translate to a power output of 170 to 180 MW. Even though the amount of H_2 in place also increases significantly in the remaining simulations, the achieved values are below the 95th percentile and thus do not provide a good fit.

With the H_2 flow rate increasing with the storage cycles (Fig. 4.16), also the H_2 volume withdrawn and thus the cumulative power output from the storage site increases in each cycle (Fig. 4.17). In the simulation in which the effective permeability is estimated by an arithmetic mean a total of about 31 million sm^3 of H_2 is produced in the last storage cycle, corresponding to about 55 000 MWh, which is 24 % of the total storage demand outlined in Chapter 4.2. Once more this simulation provides results close to that of the 5th percentile of the heterogeneous ensemble. Contrary to the other metrics, the 95th percentile of the heterogeneous ensemble is not well matched by any of the homogeneous simulations.

The comparison of the different homogeneous simulations with the results of the heterogeneous ensemble shows that none of the tested averaging methods yields a parameter distribution which adequately represent the median of the heterogeneous ensemble regarding storage performance. However, using an arithmetic mean to estimate the effective permeability yields simulations results which are in a good agreement with the 5th percentile of the heterogeneous ensemble storage

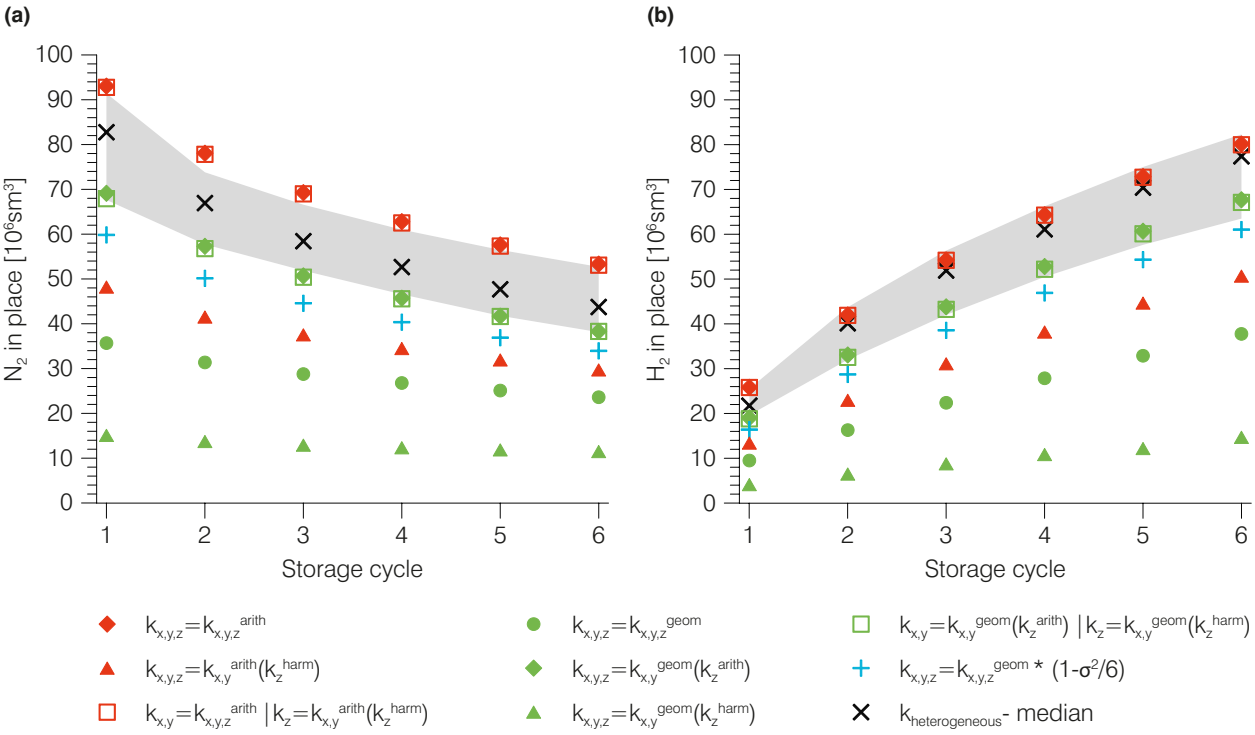

Fig. 4.15 Volume of (a) N_2 and (b) H_2 in place in the storage formation prior to the individual storage cycles. The grey shaded area marks the interval spanning from the 5th to 95th percentile in the heterogeneous simulations results. The data points of the simulations using the method of Cardwell Jr. and Parsons (1945) are omitted.

or H_2 flow rates. Thus, data on the storage performance obtained with this parameter distribution can be interpreted as the upper bound to the variability which must be expected when considering variability in the distribution of the reservoir properties as in the presented heterogeneous ensemble. Comparably, the lower bound to the variability of most storage performance metrics can be estimated by a simulation in which the geometric average of the vertical arithmetic averages of permeability is used, as the results are in good agreement with the 95th percentile of the hetero-

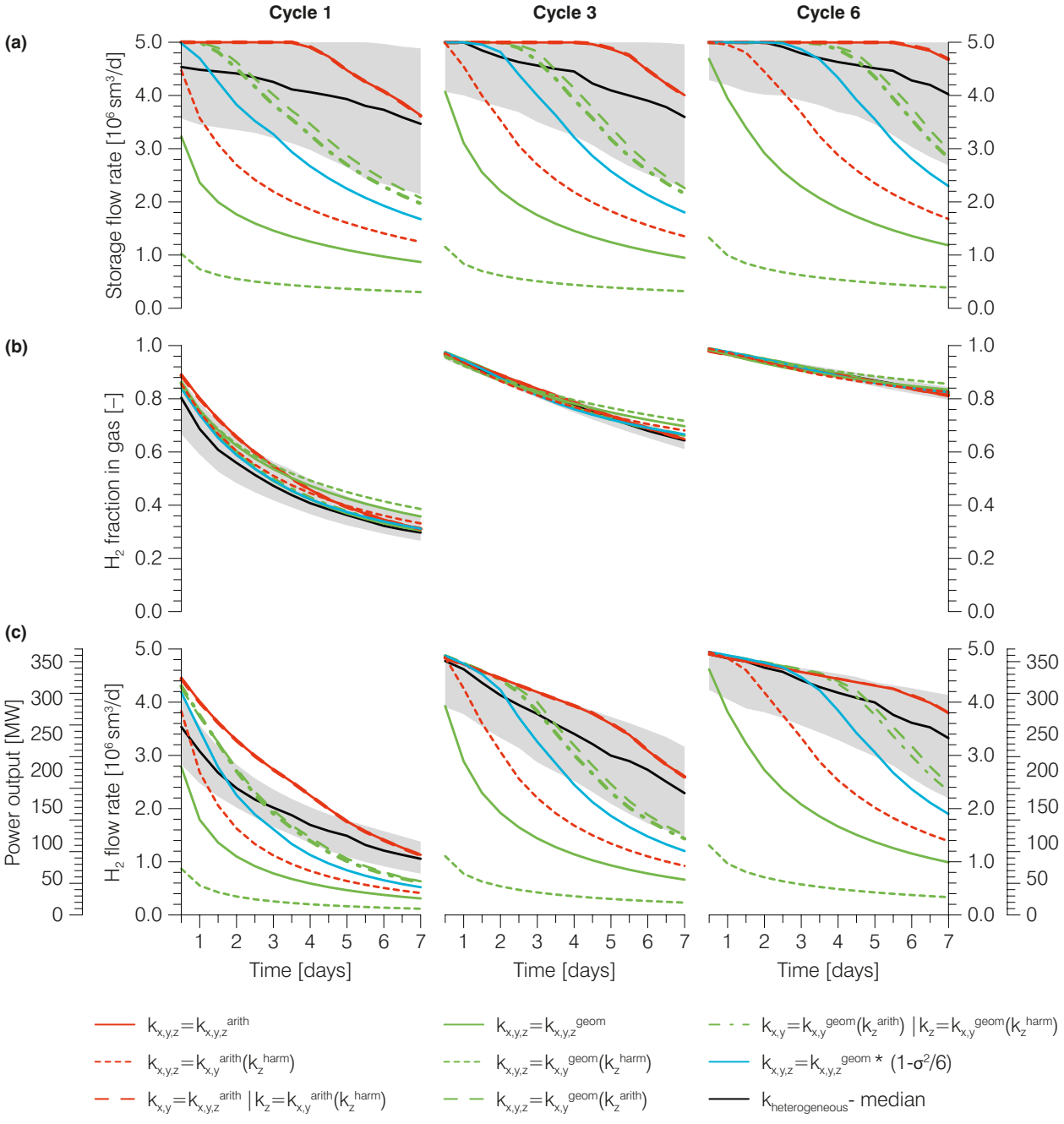

Fig. 4.16 Evolution of ***(a)*** *the storage flow rate,* ***(b)*** *the H_2 fraction in the produced gas and* ***(c)*** *the resulting H_2 flow rate and the power output from the storage in the first, third and sixth storage cycle. The curves for the lower and upper bound as defined by Cardwell Jr. and Parsons (1945) are omitted. They follow a similar trend as the curves obtained when using the geometric mean of the vertical harmonic mean (short dashed green). In addition to the median of the heterogeneous ensemble, the interval spanning the 5th and 95th percentile is indicated by the grey shaded area.*

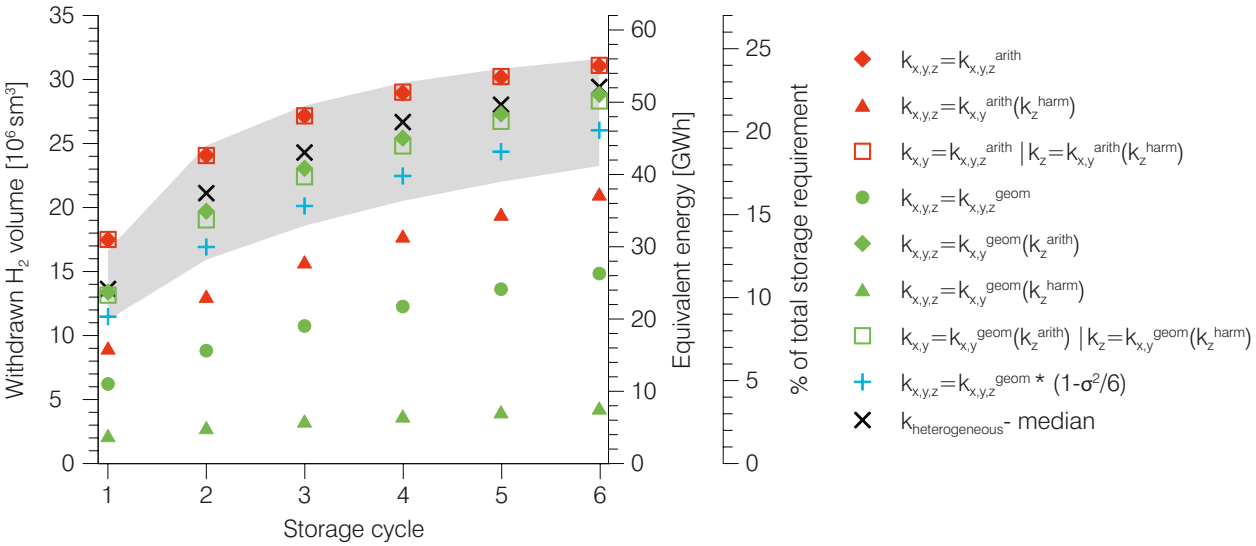

Fig. 4.17 H_2 volume withdrawn in each storage cycle, equivalent amount of energy provided by the storage site and corresponding fraction of the defined storage demand (see Chapter 4.2). The data points of the simulations using the method of Cardwell Jr. and Parsons (1945) are omitted.

geneous ensemble. Including an anisotropy does not significantly affect the simulation results.

4.5.3 Improved storage setup

The results of the heterogeneous and the homogeneous simulations deviate from the targets defined in the simulation setup (see Chapter 4.4.2) and the storage scenario (see Chapter 4.2). While the latter is in part a result of the simulation setup, i.e. the number of wells and the target rates used in this first analysis, the former is a result of the simulation storage setup being inadequate for the given storage structure. For example, the storage flow rate and the H_2 fraction in the produced gas varies greatly during the first storage cycle in the heterogeneous ensemble and the homogeneous simulations (Fig. 4.16). Besides being inconsistent with time, also the volume of H_2 withdrawn and thus the storage capacity of the site is lower than the target of 35 million sm^3 being on average only about 13.5 million sm^3 in the first storage cycle of the heterogeneous simulations (Fig. 4.17). With more gas in place the storage performance increases, both in terms of flow rates as well as H_2 fraction in gas (Fig. 4.15, 4.16, 4.17). However, even in the last storage cycle after 1365 days about 29 million sm^3 of H_2 are retrieved from the storage site on average, which corresponds to slightly more than 52 000 MWh and thus about 23 % of the total storage demand as defined in the scenario (Fig. 4.17, also compare Chapter 4.2). In addition to the lower storage capacity, the sustainable output, as taken by the lower endpoint of the H_2 flow rate, differs drastically from the maximum power output at the beginning of each withdrawal phase (Fig. 4.16c). Taking the median of the sustainable power output from the storage of all heterogeneous simulations during the sixth storage cycle of about 250 MW (compare Fig. 4.9c or 4.16.c), the storage capacity is around 42 000 MWh, which is only about 18.5 % of the total storage demand. Hence, the first step to increase the storage performance is to obtain a better consistency in both the achieved well flow rates and the H_2 fraction in the withdrawn gas. For this, a new simulation setup is required as the current storage site is rate limited.

Simulation model

As it is obvious from the simulation results shown in Chapter 4.4.3 and 4.5.2, the volume of H_2 in place in the storage formation is not sufficient at the beginning of the storage operation. Increasing the well flow rates during the injection phases, including the initial filling of the storage formation,

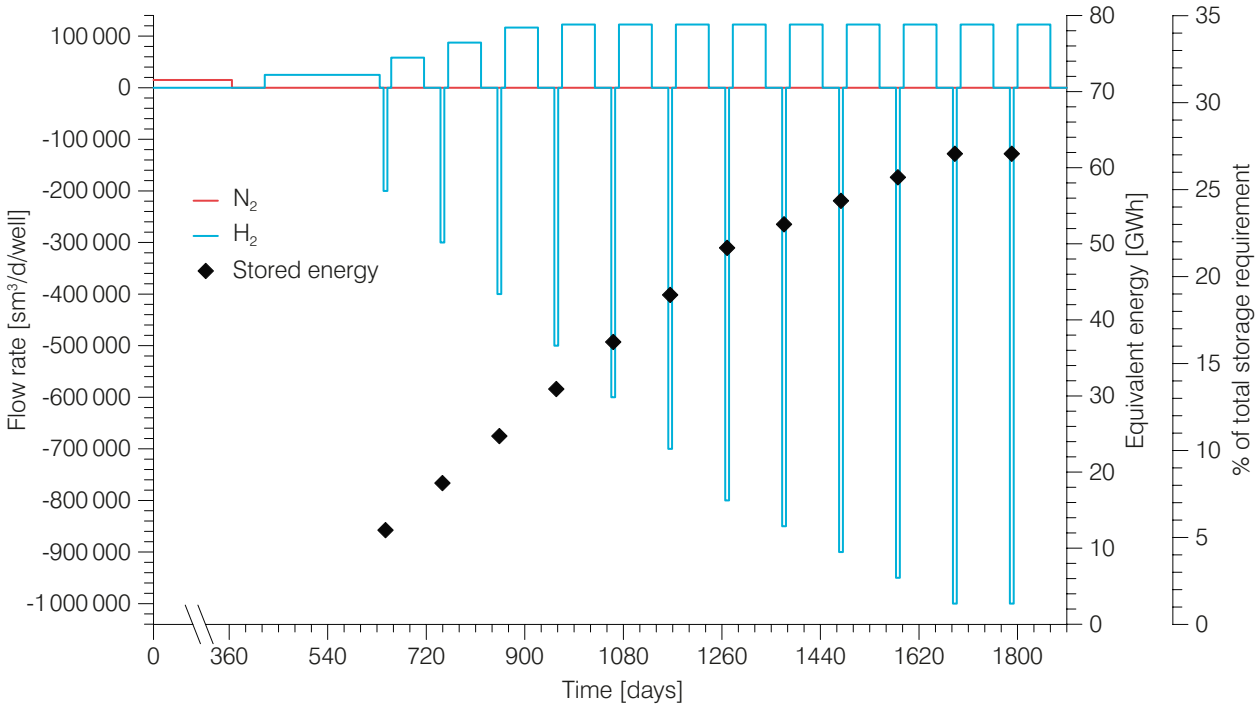

Fig. 4.18 *Target injection and withdrawal rates for N_2 and H_2 and amount of energy provided by the storage site in the optimized setup. Negative well flow rates indicate withdrawal phases with positive values representing injection phases.*

is not possible as the wells already operate at the maximum BHP during injection. To increase the amount of gas available for the storage operation, either the initial filling of the storage site can be prolonged considerably or the rates applied during the individual storage cycles can be increased stepwise from low rates in the beginning to the target rate of 1 000 000 sm³/d/well at the end. The latter approach should allow for a greater injection rates due to the pressure reduction caused by the individual withdrawal phases. Using this scheme the storage is gradually increased in size, providing at least some usable storage capacity early in the build-up phase, while the former option would result in considerable time required before the storage can be used.

Consequently, a new storage setup is developed, in which the first production cycle is already after 642 days compared to the 920 days of the previously used setup (Fig. 4.18). The number of wells, their position and the associated properties such as BHP limits are carried over from the previous storage setup. The overall schematics of an initial N_2 injection to displace the formation water around the wells followed by a first H_2 injection are also kept.

The N_2 is injected at a rate of 15 000 sm³/d/well for 365 days. After a shut-in period of 60 days, H_2 is injected at a rate of 25 000 sm³/d/well for 210 days. Following a short shut-in period of 7 days the storage operation starts, consisting of 12 storage cycles in total. Instead of applying the final target withdrawal rate in all cycles, the applied rate is increased over the course of 11 storage cycles from initially 20 % (200 000 sm³/d/well) to 80 % of the designated value (800 000 sm³/d/well) in 10 % increments. From there onwards the flow rate is increased in 5 % increments until the final target withdrawal rate of 1 000 000 sm³/d/well is reached. While the length of the withdrawal phases are kept constant at 7 days, the duration of the storage refill subsequent to the withdrawal are increased to 60 days. Shut-in phases of 7 days and 30 days are following the individual withdrawal and injection phases, respectively. The injection rates are increased stepwise as well, from 58 333 sm³/d/well in the first storage cycle to the final target rate of 122 500 sm³/d/well in the fourth (Fig. 4.18). Doing so results in considerably more gas being injected compared to what is withdrawn at the beginning of the storage operation. Under ideal con-

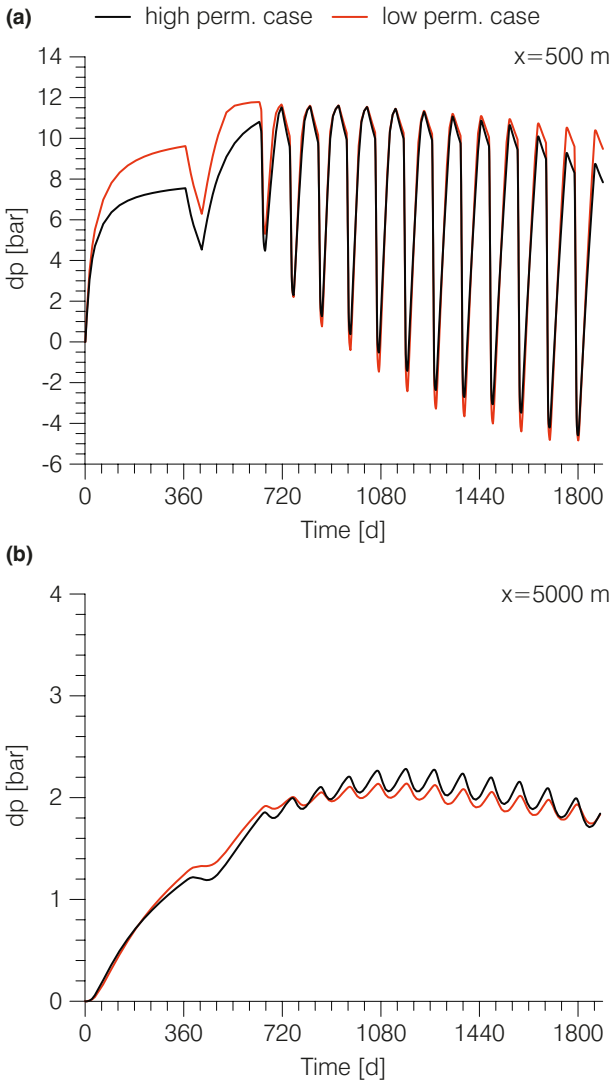

*Fig. 4.19 Pressure response at observation points **(a)** 500 m and **(b)** 5000 m from the well gallery. For the location of the observation points see Fig. 4.1.*

ditions the volume H_2 in place prior to the first full rate cycle should be about 145 million sm^3. The target injection volume of N_2 is 27.4 million sm^3. Thus, about 24 % of the total H_2 in place is produced during withdrawal when the storage site operates at its full capacity with the target withdrawal rate being 1 000 000 sm^3/d/well.

The simulation setup is tested for two homogeneous parameter distributions to approximate the variability of the simulation results which must be expected due to uncertainties in the distribution of the reservoir properties (see Chapter 4.4). The hydraulic properties used for the simulations are chosen based on the comparison presented in Chapter 4.5.2. For the given scenario, estimating the effective permeability by an arithmetic average of the heterogeneous permeabilities (Table 4.4, #1) provided simulation results in good agreement to the 5th percentile of the heterogeneous ensemble regarding storage performance metrics. Comparably, the 95th percentile of the heterogeneous ensemble is reasonably well matched by simulations in which the effective permeability is calculated using a geometric average of the vertical arithmetic averages of the heterogeneous permeabilities (Table 4.4, #6). From herein the two simulation cases are referred to as the low and high permeability simulation, with the storage formation having a permeability of 598 mD in the latter and 475 mD in the former case.

While the selected homogeneous rock models can provide a reasonable estimate of metrics linked to the storage performance, the persistent overpressure in the far field of the storage towards the end of the simulation will most likely be slightly underestimated (compare Fig. 4.11c,d). Nevertheless, based on the comparison on the small-scale model, it can be assumed that the maximum pressure perturbation in the far field is represented adequately in the high permeability simulation case. The remaining simulation setup is identical to that described previously (see Chapter 4.4.2 and 4.5.1).

Simulation results

The injection of the gas results in a pressure increase in the near and far field of the storage formation (Fig. 4.19). As expected, the pressure increase near the injection wells is slightly reduced compared to the previously discussed simulation setup with the maximum overpressure during the initial filling of the storage being about 10.5 bars in the high permeability simulation and 11.5 bars in the low permeability simulation (Fig. 4.19a, compare Fig. 4.11a). The pressure response due to the gas withdrawal and re-injection in the first two storage cycles from 642 to 850 days are nearly identical for both simulations. However, with increasing number of storage cycles the pressure fluctuations near the storage wells in the high permeability simulation are lower than in the low permeability simulation as the formation is providing less resistance to pressure propagation. Consequently the overpressure in the far field is greater in case of the higher

permeability simulation, being slightly more than 2.2 bars compared to about 2 bars in the lower permeability simulation (Fig. 4.19b). The overall pressure increase in the far field is comparable to the pressure perturbation seen in the previously presented simulations (compare Fig. 4.11d). A key difference is that due to the early start of the storage operation during which the storage is still developed, the maximum pressure increase in the far field does not coincide with the initial filling of the storage. In case of the high permeability simulation maximum pressure increase is reached around the fifth storage cycle while the low permeability simulation shows the largest pressure increase around the fourth cycle (Fig. 4.19b).

The spatial distribution of the pressure perturbations is qualitatively identical to the previous simulations and thus omitted at this point (compare Fig. 4.12b,c).

The distribution of the gas phase also shows a close resemblance with the previous simulations models. However, the fraction of N_2 in the total gas in place is lower in this setup, with around 27.4 million sm^3 being injected in both simulation cases (Fig. 4.20; Fig. 4.21). This also shows in the distribution of the gas components within the storage formation with the highest N_2 fractions at the bottom and towards the northern and southern outskirts of the gas phase (Fig. 4.20). The volume of H_2 available for withdrawal prior to the

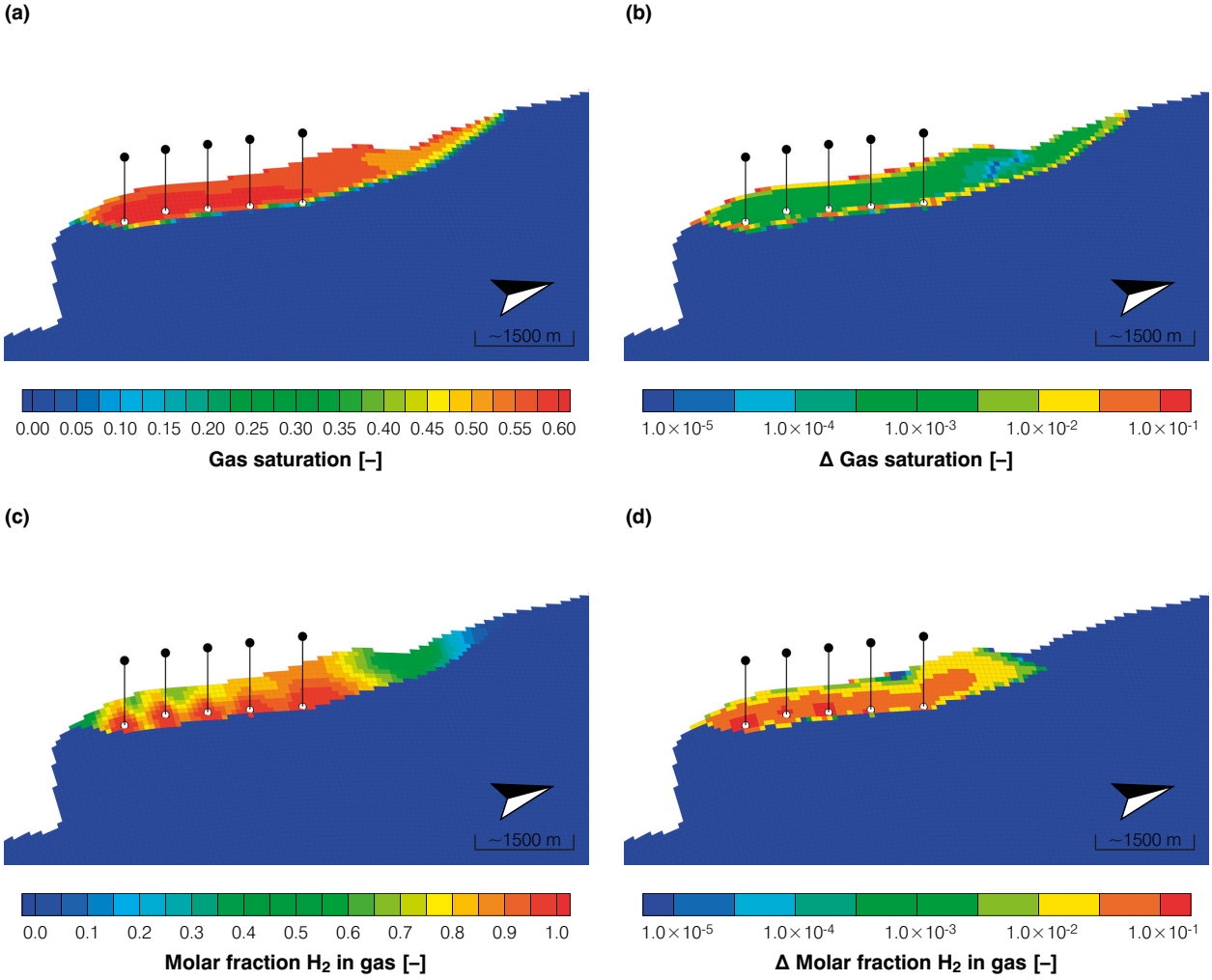

Fig. 4.20 Distribution of ***(a)*** *the gas saturation and* ***(c)*** *the molar fraction of H_2 in gas prior to the 11th storage cycle at 1683 days in the low permeability simulation case. Changes observed for* ***(b)*** *the gas saturation and* ***(d)*** *the H_2 fraction after the withdrawal. Each grid block is 50 by 50 m. The vertical dimension is exaggerated by a factor of 3.*

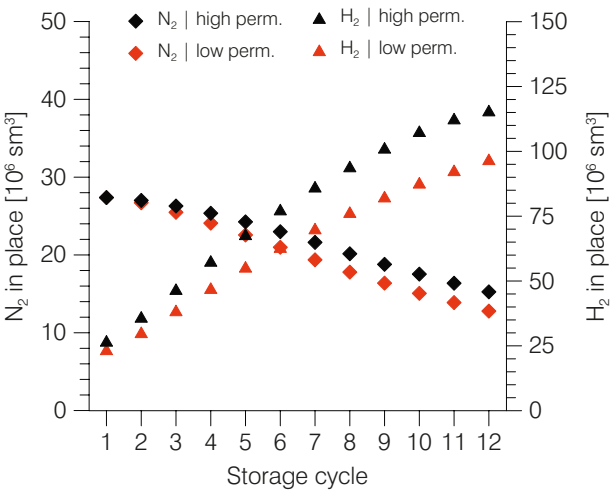

Fig. 4.21 *N_2 and H_2 in place in the individual storage cycles prior to withdrawal in the individual storage cycles.*

first storage cycle differs between both simulations being in the range of 23 to 26.3 million sm³. Thus, while the target H_2 volume is successfully injected in the high permeability case prior to the first storage cycle, only about 87 % of the target volume of 26.3 million sm³ are injected in the low permeability case.

Despite slightly less gas being in place in the low permeability simulation, the storage flow rates achieved during the first withdrawal period are identical in both simulations and consistent throughout the whole production phase, with the storage flow rate being 1 000 000 sm³/d (Fig. 4.22a). The fraction of H_2 in the withdrawn gas differs with time and between the simulation cases (Fig. 4.22b). In case of the high permeability simulation the H_2 fraction in the withdrawn gas reaches a minimum of about 89 % in the first cycle, while the low permeability simulation shows a slightly smaller minimum value of 81 %. Nevertheless, both values are well above those obtained with the previous simulation setup in which fractions of about 30 % are achieved. The resulting H_2 flow rate also varies slightly with time as well as between the simulation cases (Fig. 4.22c). The respective minimum H_2 flow rates are 880 000 sm³/d and 810 000 sm³/d for the high and low permeability simulation, which corresponds to a power output of about 65 MW and 60 MW. The withdrawn H_2 volume in the first storage cycle corresponds to about 11 MWh and 12 MWh for the low and high permeability simulation, respectively (Fig. 4.23).

In the subsequent storage cycles the volume of gas in place increases with ultimately 112 million sm³ H_2 being available in the storage formation prior to the first withdrawal at the final target rate (cycle #11) after 1689 days in case of the high permeability simulation (Fig. 4.21). This is about 20 % more than in the low permeability simulation in which 96 million sm³ of H_2 are in place at the same point in time. Thus, the variability in gas in place between the low and high permeability simulation cases increases with the number of completed storage cycles.

The differences in the achieved storage flow rates are relative small during the first four cycles until which only very little reductions in the flow rates can be observed (Fig. 4.22a). However, from the fifth cycle onwards (1065 days) the storage flow rates of the simulations vary increasingly during the individual withdrawal phases, following the same trend as the previously discussed homogeneous simulations (Fig. 4.16a). The high permeability simulation shows only a small decrease in the storage flow towards the end of the simulation with the minimum flow rate being 4.77 million sm³/d in the 11th storage cycle. Compared with this, the storage flow rate achieved in the low permeability simulation shows a more pronounced decrease with the minimum rate being just 3.47 million sm³/d.

Nevertheless, the sustainable storage flow rates are still greater than those during the last storage cycle in using the previous simulation setup, which were 2.99 and 4.68 million sm³/d for the low and high permeability simulation respectively (compare Fig. 4.16a). As more H_2 is injected than withdrawn in each storage cycle, the fraction of H_2 in the produced gas phase becomes more uniform with the number of storage cycles completed, with the values being constantly above 90 % from the eighth cycle onwards, showing a near linear decrease (Fig. 4.22b). Compared with the previous simulation setup the purity of the produced gas is thus higher and more stable (compare Fig. 4.16b).

The H_2 flow rates differ between the two simulation cases, primarily because of the differences in the storage flow rates (Fig. 4.22c). The sustainable power output from the storage during the first full-scale withdraw is in the range of 238 to 331 MW depending on the formation permeability. In the second full-scale storage cycle the sus-

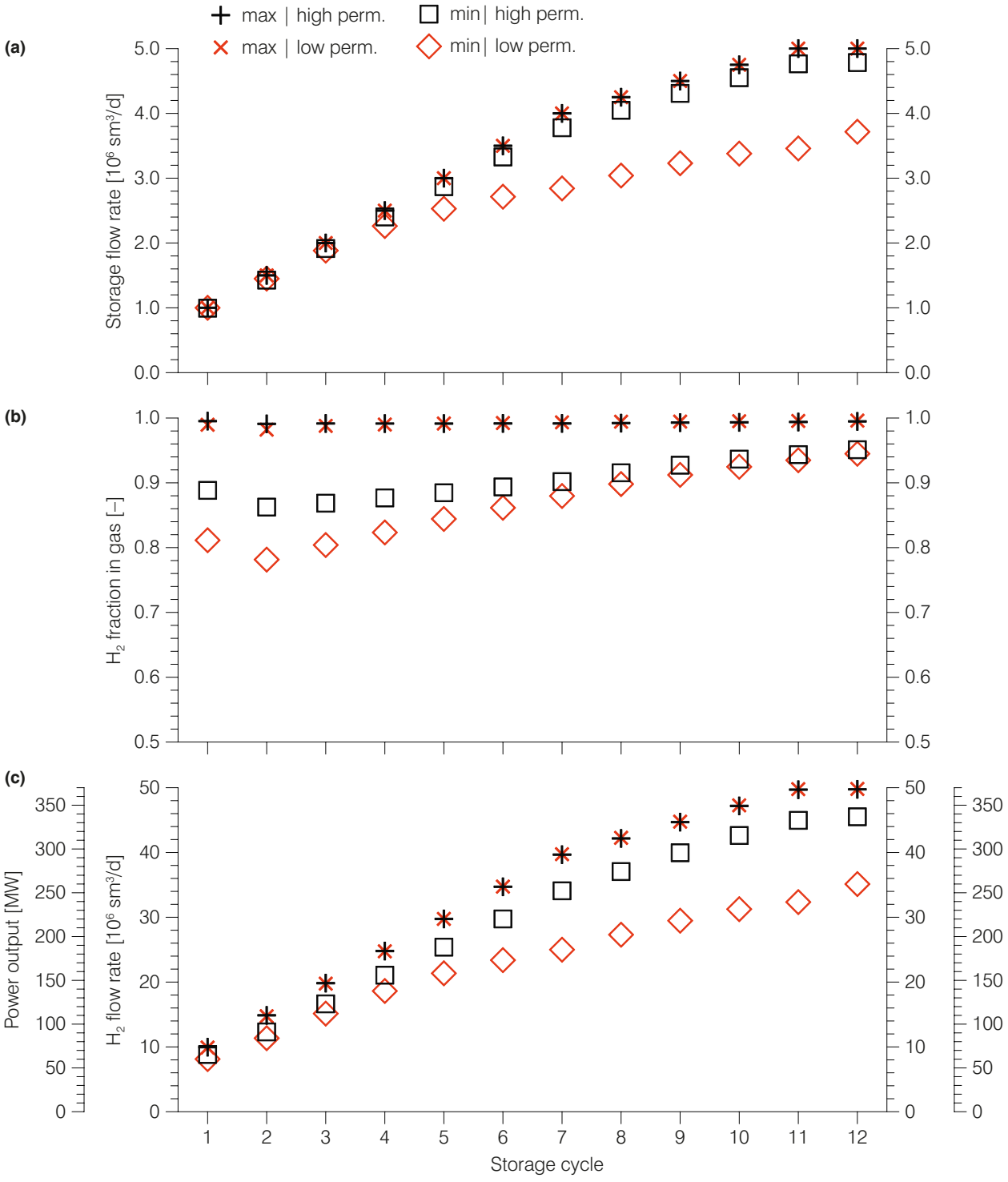

Fig. 4.22 (a) Storage flow rate, (b) H_2 content in produced gas and (c) resulting H_2 flow rate and power output in all storage cycles. Crosses indicate the maximum value observed during the respective storage cycle with the rectangles representing the minimum values.

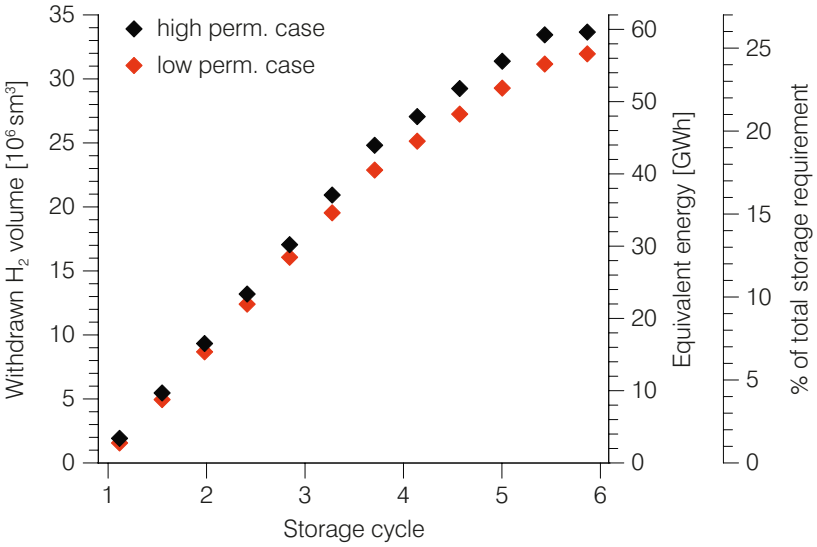

Fig. 4.23 H_2 volume withdrawn and equivalent energy provided by the storage site in each storage cycle when using the improved storage setup.

tainable power output increases to 259 MW and 335 MW, respectively. Thus, using the improved storage setup, the low permeability simulation, which provides a good fit to the 95th percentile of the homogeneous ensemble in the previous setup, surpasses the median of the ensemble (250 MW) during the last storage cycle (compare Fig. 4.16c). The storage site can therefore supply around 19 to 25 % of the average power demand of 1356 MW defined in this study.

The H_2 volume withdrawn per cycle storage capacity follows the same trend as e.g. the storage flow rate with the differences between the two simulations increasing slightly with time (Fig. 4.23). At the final storage capacity, H_2 equivalent to around 57 000 to 60 000 MWh are withdrawn from the storage formation during the week-long production period depending on the permeability of the storage formation. Thus, the simulated storage site is capable of supplying about 25 % to 26 % of the total storage demand in energy defined in this study.

4.5.4 Large-scale H_2 storage and combined use of a storage site

The storage setup used in the scenario simulations presented in the previous chapters included 5 vertical storage wells with a screen length of at least 12 m (compare Chapter 4.4.2), which were operated at a target withdrawal rate of 1 000 000 sm^3/d/well. Thus, under ideal conditions the storage would suffice to provide 35 million sm^3 of H_2 during the week-long shortage period defined in the storage scenario (Chapter 4.2). With the assumption of a 60 % efficiency in the re-electrification, this volume corresponds to about 61 833 MWh, which is only about 27 % of the total storage demand in the defined scenario. To cover for the complete shortage in power production, a total of 228 113 MWh must be provided, which corresponds to a H_2 volume of slightly more than 129 million sm^3. The required average load during the week-long production period is thus 1356 MW.

To supply a greater volume of gas in a given period of the time, either the target flow rates and/or number of wells used in the storage have to be increased. Either way, the volume of gas in place in the storage formation would have to be increased accordingly. At the investigated site this is possible as the spill points of the structure are not yet reached by the injected gas. While the storage rates applied in the previously used setup are already high and comparable to the high productivity wells used in conventional gas storages (Bary et al. 2002; IGU/WOC 2006), the number of active storage wells in this example is on the lower end compared to existing storages (see also Chapter 2.2). Furthermore, the well flow rates during injection and withdrawal already result in the BHP limits being reach in most storage wells, which results in an automatic reduction of the rates. Thus, at the given structure increasing the power output from the storage is best done us-

ing more storage wells rather than increasing the flow rates applied per well.

To get an adequate representation of the pressure perturbation caused by the enlarged storage operation, a larger simulation model is necessary and thus constructed. This model is also used to simulate the effect of a combined usage scenario, demonstrated by a brine injection at the western flank of the structure, opposite to the H_2 gas storage site. Brine or waste water originating from conventional hydrocarbon exploration (Clark et al. 2005) or the leaching of salt caverns (Zemke et al. 2005) is commonly injected into saline formations. Depending on the injected fluid volume, such an injection can result in a large scale pressure perturbation as well as trigger brine movement in adjacent formations if suitable pathways are available (Delfs et al. 2016). The pressure perturbation caused by the water injection may impair a nearby storage operation by overlapping pressure signals.

Simulation model and storage setup

To accommodate the larger storage operation, the previously used structural model of the anticline is increased in size (Fig. 4.24). This requires knowledge of the distribution of the Rhaetian, being once more the designated storage formation, beyond the model domain as defined in the underlying regional model of Hese (2012). Without the aid of additional on-site data, the depth data of the Rhaetian is calculated based on the distribution of the overlying caprocks as given in the large scale structural model by Hese (2012) and the residual thickness of the Rhaetian given in Baldschuhn et al. (2001). Subsequently, the Upper Rhaetian, the Upper Shale of the Middle Rhaetian, the Main Sandstone of the Middle Rhaetian, the Lower Shale of the Middle Rhaetian and the Lower Rhaetian are included in the model based on facies descriptions given by Gaupp (1991) and Hese (2011, 2012). A high and low permeability

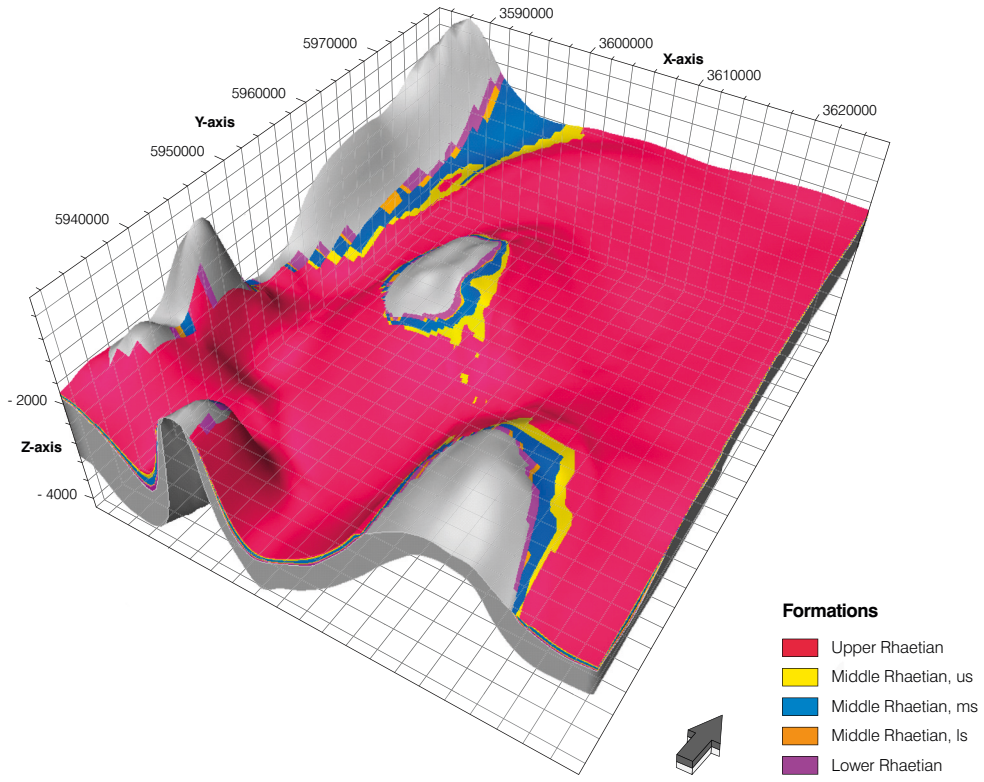

Fig. 4.24 *Extended structural model created for the large scale H_2 storage simulation. The model is based on the previously described structural model (see Fig. 4.1). The grey colour indicates the underlying bedrock and thus represents areas in which the Rhaetian is not present.*

Tab. 4.6 *Data of the horizontal wells used in the large-scale H_2 storage simulation.*

	Well										
	1	**2**	**3**	**4**	**5**	**6**	**7**	**8**	**9**	**10**	**11**
Reference depth [m]	546.11	532.34	518.96	510.06	505.64	502.39	489.35	474.63	467.26	463.58	482.54
Maximum BHP [bars]	73.70	71.90	70.10	68.90	68.30	67.80	66.10	64.10	63.10	62.60	65.10
Minimum BHP [bars]	30.00	30.00	30.00	30.00	30.00	30.00	30.00	30.00	30.00	30.00	30.00

homogeneous rock model are used to evaluate the storage performance and the extent and magnitude of the induced hydraulic effects. Consistent with the previous chapter, the effective permeability in the low permeability simulation is estimated using the geometric mean of the vertical arithmetic means of the heterogeneous ensemble discussed in Chapter 4.4. The permeability of the high permeability simulation is estimated using a simple arithmetic mean of the heterogeneous permeability distributions.

The dimensions of the created simulation model are about 41 km by 48 km in lateral direction. The discretization of the simulation model is 50 m to 1000 m in the lateral directions and 0.2 to more than 15 m vertically with a constant number of layers in each formation. The Rhaetian deposits strike out towards the west, the south and the south east of the model domain (Fig. 4.24). The extent of the Rhaetian beyond the model domain is included by applying a pore volume multiplier and a permeability reduction factor, being the reciprocal of the pore volume multiplier, to the boundary elements of the simulation grid. The lateral extent of the Rhaetian towards the north increases from 3.5 km in the western part to 16 km in the eastern part of the northern boundary, while the extent towards the east is estimated to be at least 10 km. The southern and western model boundaries already include gaps in the distribution of the Rhaetian. The extent of the Rhaetian towards the south is estimated at 8 km, 10 km and 3.5 km in the three sections, from east to west, in which the Rhaetian reaches the model boundary. Towards the west the extent of the Rhaetian is set to 12 km. Identical to the previous simulations, the sealing formations above and below the storage formation are assumed tight against N_2 and H_2 and are thus excluded from the simulation for the sake of minimizing the computational effort.

The storage operation is carried out using 11 horizontal wells located at the eastern half of the anticline (Fig. 4.24, 4.27). The screen length of all wells ranges from about 300 m to 425 m depending on the orientation in the simulation grid. Compared to horizontal wells deployed in the oil and gas industry this is relatively short (Nurmi et al. 1996). The individual well trajectories are along the centre layer of the Main Sandstone of the Middle Rhaetian. By using the horizontal wells, the well positioning is more flexible because the minimum horizontal thickness of 12 m as required in the simulations using the vertical wells can be neglected.

Due to the strong difference in the depth of the wells, the maximum allowable overpressures (upper BHP limits) were calculated individually for each well. For this the lower estimate of the minimum horizontal stress gradient of 15 MPa/km for the sediments above the Zechstein salts of the North German Basin (Röckel and Lempp 2003) is used in combination with a safety factor 0.9, similar to what is used in other studies (e.g. Thibeau et al. 2014). At the shallowest well 10, the resulting upper BHP limit is 62.6 bars, which is slightly lower than what is used in the previous study. In contrast, the deepest wells being 1 to 3 at the north end of the storage, allow a higher BHP of about 70.1, 71.9 and 73.7 bars. The lower BHP limit, being governed in part by the surface installations, was set 30 bars and is thus identical to the previous simulations using vertical wells.

The setup for the large scale H_2 storage simulations is similar to the optimized simulation setup presented in the previous chapter with the well flow rates being increased stepwise over the

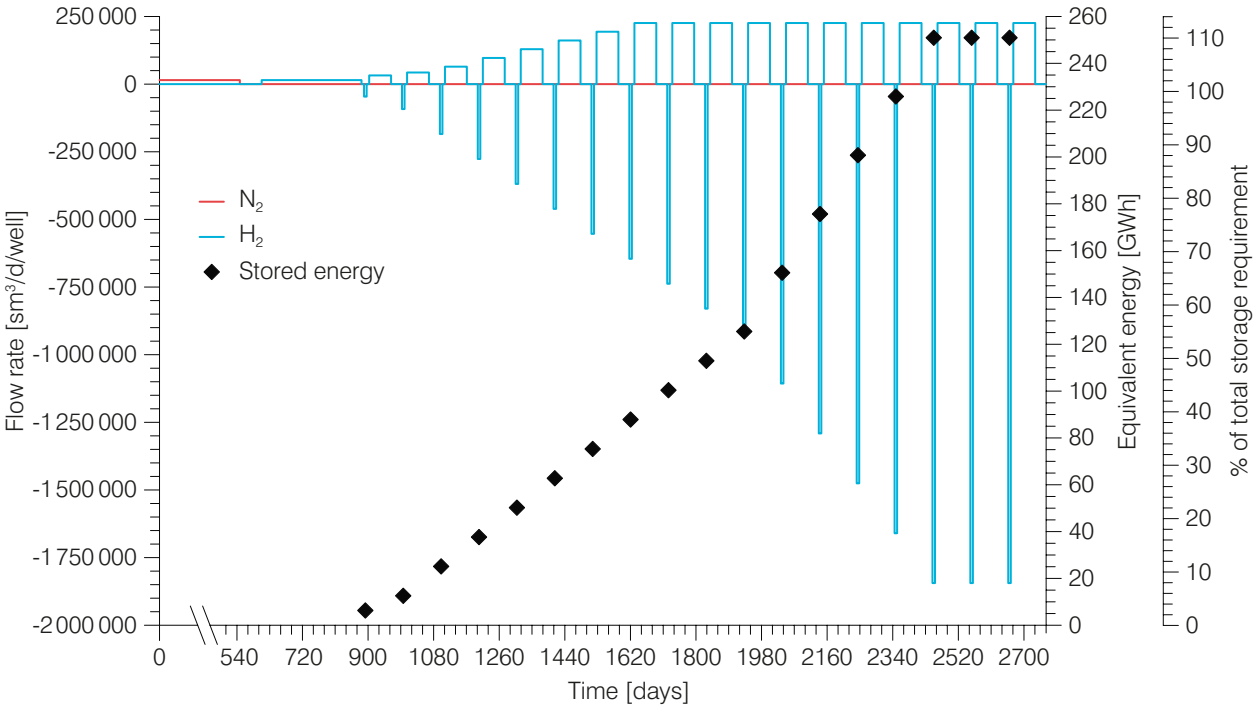

Fig. 4.25 *Target injection and withdrawal rates for N_2 and H_2 as well as target storage capacity in the large-scale storage simulation with time. Negative well flow rates indicate withdrawal phases with positive values representing injection phases*

course of 15 storage cycles until the storage is at its final capacity (Fig. 4.25).

Each storage cycle consists of a withdrawal period of 7 days and an injection period of 60 days. In between the withdrawal and the injection period a short shut-in of 7 days is included. Subsequent to the replenishment of the storage with H_2, another shut-in period of 30 days is included before the next storage cycle. Prior to the first cycle the storage is initialized by an N_2 injection at 15 000 $sm^3/d/well$ for 548 days, a short shut-in period of 60 days and an H_2 injection at 15 000 $sm^3/d/well$ for 274 days (Fig. 4.25). Following this, the target withdrawal rates for the first storage cycle from 889 to 903 days are set to 46 114 $sm^3/d/well$, with the injection rates being 32 280 $sm^3/d/well$. In this cycle the storage can thus only provide a maximum of about 3.55 million sm^3 of H_2, corresponding to about 6273 MWh. The storage capacity in the first cycle is therefore less than 5 % of the total storage requirement defined in Chapter 4.2. In the subsequent 14 storage cycles the applied well flow rates are increased until the final target rate of 1 844 577 $sm^3/d/well$ is applied in the 16th storage cycle after 2449 days of operation. Assuming pure H_2 is withdrawn and all wells operate at the target rate, the power output from the storage should equate to 1494 MW, which is 110 % of the average power demand defined in this study. Thus, at full capacity, the storage site should be able to provide H_2 equivalent to around 251 000 MWh (Fig. 4.25).

The underlying scenario of the combined usage scenario is an injection of waste water originating from a cavern being leached, potentially for a short-term gas storage. The dimensioning of the waste water injection is loosely based on the leaching rate and time which were required to construct the Huntorf compressed air energy storage (e.g. Crotogino et al. 2001; Bary et al. 2002). The Huntorf caverns have a volume of about 300 000 m^3 and were constructed over a period of slightly more than 3 years (Leith 2001). The time required to leach a salt cavern depends on the solubility of the salt and the volume of the cavern, with the required fresh water volume being typically 7 to 8 times that of the salt volume (Leith 2001; Bary et al. 2002).

The waste water is injected into the Main Sandstone of the Middle Rhaetian at the opposite site of the anticline used for the porous media hH_2

storage site. Two vertical wells are used for the water injection located at depths of 2073 and 2319 m, respectively (Fig. 4.26). The BHP limits of the injection wells are determined using the same reasoning as for the storage wells, resulting in the pressure limits being 278.7 bars for the norther injection well and 311.7 bars for the southern well. The water injection starts at 890 days and thus after the first injection of N_2 and H_2 is completed. Over the course of the next 11 storage cycles, spanning 1144 days, the injection rate is kept constant at 1218 sm^3/d/well. The total volume of water injected is 2 786 784 sm^3, which is about 9 times the volume of the Huntorf caverns and therefore slightly more than what would regularly be injected to dispose of waste water originating from leaching similar sized cavers.

Simulation results of the large-scale H_2 storage operation

Identical to the previous homogeneous simulations all pressure changes are evaluated relative to a baseline simulation to account for numerical inaccuracies in the automatic equilibration of ECLIPSE due to the different endpoints of the capillary pressure curves.

The overall behaviour of the large-scale storage is comparable to that of the smaller H_2 storage with the optimized simulation setup (see Chapter 4.5.3). Again, the maximum overpressure is governed by the upper BHP limit, resulting in the maximum pressure increase being less than 20 bars. Compared to the smaller scale storage simulations, the area of a noteworthy pressure increase of more than 5 bars is larger due to the increased number of storage wells and the associated storage volume (Fig. 4.26a, c). At a distance of 500 m the maximum overpressure during the storage initialization phase is just under 10 bars in the low permeability simulation, while about 8.5 bars are reached in the high permeability simulation (Fig. 4.27a). However, the differences between the two simulations regarding the overpressure are negligible after three storage cycles with about 10 bars being reached in both simulations. At 5000 m from the storage wells towards the eastern boundary of the model domain, the pressure signals of both simulations are much the same during the N_2 injection phase up to 548 days (Fig. 4.27b). Minor differences towards the end of the N_2 injection and a stronger pressure decline during the shut-in period following the N_2 injec-

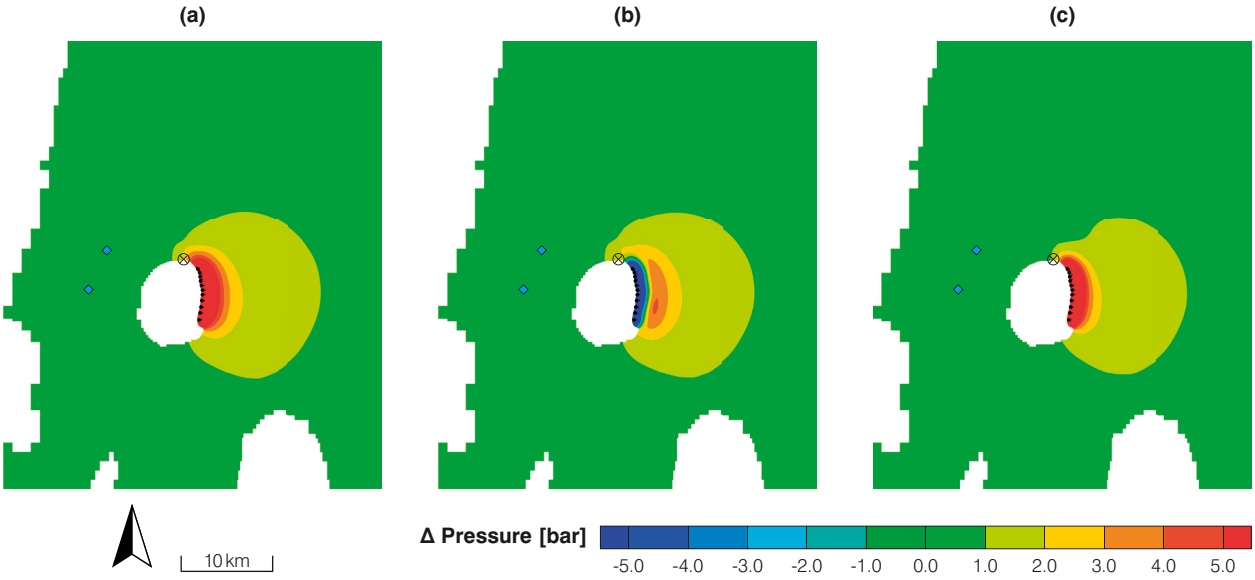

*Fig. 4.26 Pressure change in the storage formation in the low permeability simulation compared to the baseline pressure **(a)** before the 16th storage cycle at 2440 days, **(b)** after the gas withdrawal at 2458 days and **(c)** after the re-injection of H_2 at 2526 days. The storage wells are depicted as black circles, the blue diamonds indicate the water injection wells used in the combined usage scenario. The black cross depicts the observation point at which pressure differences are compared between the storage scenarios.*

tion result in a somewhat lower overpressure in the high permeability simulation compared to the low permeability case. However, the pressure perturbations are about 2.5 and 2.2 bars and thus bear a close resemblance relative to the absolute pressure at the given observation point, which is more than 150 bars.

With increasing distance, the discrepancies between the simulations are marginal with both simulations showing an overpressure of about 0.9 bars at 9950 m at the end of the first H_2 injection after 882 days (Fig. 4.27c). The pressure perturbations caused by the storage operation are similar in the magnitude, albeit larger due to the increased volume of gas in the storage formation when compared with the smaller H_2 storage simulation.

The withdrawal of the gas during the production phases results in a significant pressure reduction in the near field of the storage (Fig. 4.26b, 4.26a). This results in a pressure zonation with the lowest pressures close the storage wells followed by a zone of overpressure, which reduces in magnitude with increasing distance to the storage (Fig. 4.26b). During the first couple of storage cycles, the minimum pressure observed during the withdrawal phases 500 m from the well gallery still shows an overpressure (Fig. 4.27a). However, at the end of the sixth production period at 1517 days, the pressure at this observation point is lower than the hydrostatic pressure by about 0.5 bars in case of the low permeability simulation. It takes until the end of the seventh storage cycle for the pressure to be below the hydrostatic pressure in the high permeability simulation.

The overpressures during the refilling phases of the storage operation are more or less constant throughout the simulation time, showing only a slight decrease of about 1 bar compared to the maximum value at 500 m (Fig. 4.27a). The minimum pressures observed during the withdrawal phases decrease with each storage cycle, ultimately reaching about -14 bars in both simulations, due to the increasing well flow rates (Fig. 4.27a).

At 5000 m from the storage wells the pressure signals observed in the two simulations are quite similar, clearly showing the individual storage cycles (Fig. 4.27b). Over the course of the simulation, the pressure levels in the far field of the storage decrease (Fig. 4.26c, 4.26b, c). However,

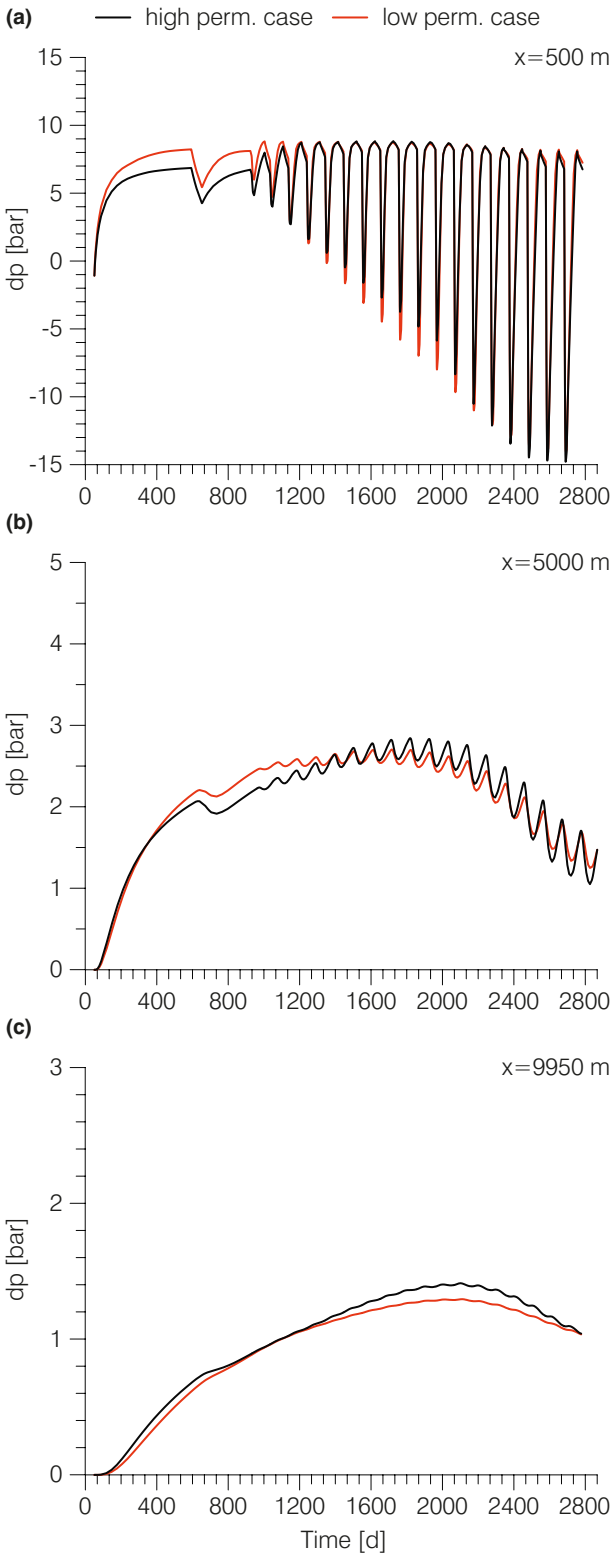

*Fig. 4.27 Evolution of the pressure change at observation points **(a)** 500 m, **(b)**, 5000 m and **(c)** 9950 m from the well gallery for both simulations of the large-scale storage operation.*

a slight overpressure of about 1 to 1.5 bars, depending on the current storage phase, is persistent at the end of the simulation at 2761 days. At greater distances of 9950 m the storage cycles can still be recognized in the pressure signals of the simulations, however the differences between injection and withdrawal are minuscule being less 0.01 bars (Fig. 4.27c). Pressure differences of such small magnitudes can be difficult to detect at field sites. Both simulations predict the same overpressure of about 1 bar at the end of the individual storage simulations. During the storage operation, the region of overpressures of more than 1 bar decreases in size as the pressure signal of the initial injection slowly dissipates (compare Fig. 4.26a and c).

The injected gas accumulates in the top of the structure, with the comparatively large volume of H_2 in the storage formation resulting in an evenly distribution of H_2 of more than 90 % throughout the main parts of the storage (Fig. 4.28a,c). Thus, the comparatively low volume of N_2 injected is not sufficient to act as a barrier between the H_2 and the formation water in this case. The evenly distribution of the N_2 can also be accounted to mixing processes during the storage operation, which might be lower in a heterogeneous reservoir. The total gas in place is not sufficient to completely support the storage operation through the compressibility of the gas. While the gas saturations at the depth layer of the storage wells only decrease slightly during the withdrawal

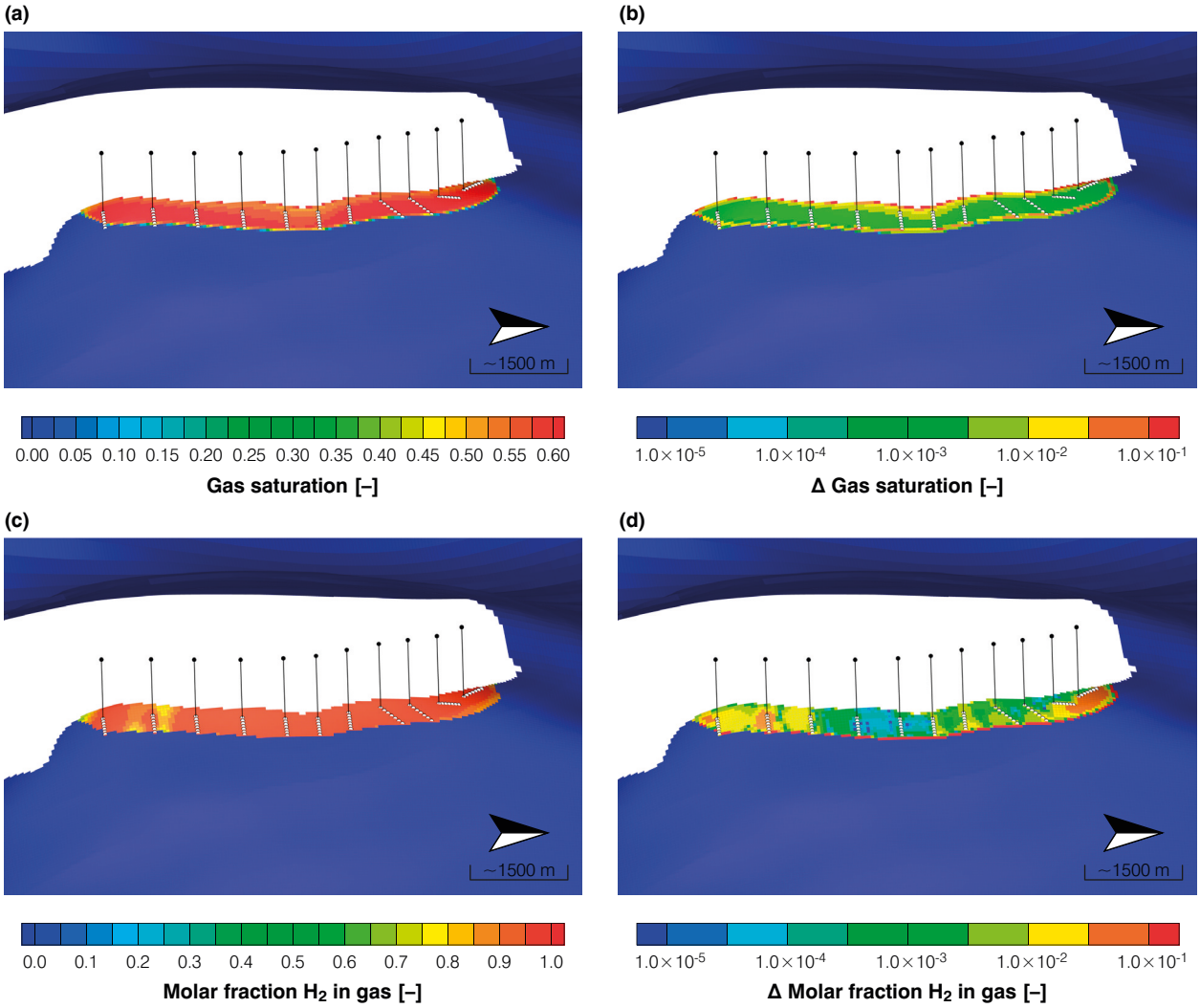

*Fig. 4.28 **(a)** Absolute gas saturation and **(c)** H_2 content in the gas in the centre layer of the Main Sandstone of the Middle Rhaetian prior to the 16th storage cycle in the low permeability simulation case and difference in **(b)** gas saturation and **(d)** H_2 fraction before and after the withdrawal.*

(Fig. 4.28b), the gas-water contact at the bottom of the storage moves several m (not shown). Such cyclic displacement of formation water with gas and vice versa can result in increased gas trapping due to hysteresis which could negatively impact the storage performance. This process is not represented in this scenario. The storage operation is visible in the H_2 fraction in gas, with changes of less than 20 % at the fringes of the gas phase (Fig. 4.28d). The overall lateral extent of the gas phase is about 7 km by 750 m (Fig. 4.28 a).

The volume of N_2 injected at the beginning of the storage operation does not show a great variability with about 83 to 90 million sm³ of N_2 being in place at the end of the storage initialization phase, depending on the formation permeability (Fig. 4.29). The volume of H_2 in place prior to the first storage cycle is 42 million sm³ and 45 million sm³ for the low and high permeability case, respectively. During the first nine storage cycles the storage flow rates are nearly identical in both simulations, with the individual target flow rates of the various storage cycles being reached most of the time (Fig. 4.30a). The gas volume in place is therefore sufficient to support the target rates independent on the formation permeability. The maximum H_2 fraction in the produced gas during the first cycle is just 90 % with values of around 76 % and 78 % towards the end of the withdrawal period in the low and high permeability case, respectively (Fig. 4.30b). However, the volume of produced gas in the first cycle is about 3.55 million sm³ (compare Fig. 4.25), which is considerably less than the total volume of H_2 in place in either simulation case (Fig. 4.29). Thus, it can be assumed that the distribution of the H_2 within in the formation is not ideal at the beginning of the storage operation. The resulting H_2 flow rates are in the range of about 456 000 sm³/d to 390 000 sm³/d in the low permeability case (Fig. 4.30c). In the high permeability simulation the H_2 flow rates decrease from initially 460 000 to 380 000 sm³/d.

In the next storage cycle, the target storage flow rates are almost perfectly matched (Fig. 4.30a). However, the H_2 fractions in the withdrawn gas reach maximum values of just around 80 %, which once more results in reduced H_2 flow rates (Fig. 4.30b,c). In the subsequent storage cycles the storage performance increases with higher and more consistent H_2 fractions in the withdrawn gas

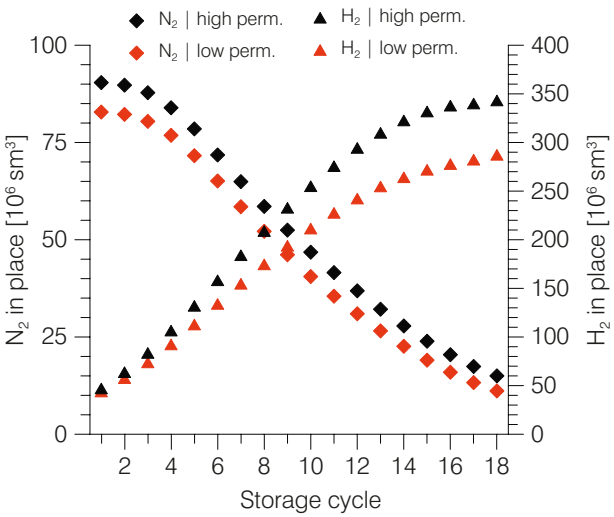

Fig. 4.29 *N_2 and H_2 in place during the individual storage cycles for both simulations, representing the variability which can be expected due to formation heterogeneity.*

throughout each cycle (Fig. 4.30b). This is a result of the volume of H_2 in the storage increasing with time as more H_2 is injected in each storage cycle during the build-up (Fig. 4.29). However, the discrepancies between the low and high permeability simulation increase as well. Furthermore, the volume of N_2 in place decreases significantly due to the high fractions of N_2 in the withdrawn gas (Fig. 4.29). From the 10th storage cycle onwards the storage flow rates start to decrease towards the end of the individual withdrawal periods in each cycle (Fig. 4.30a). The gas in place is insufficient to the support the envisaged target rates from this point onwards.

During the 16th storage cycle, being the first cycle at the final target rate of 1 844 577 sm³/d/well, the minimum storage flow rate in the low permeability simulation is just 9.85 million sm³/d, while the maximum flow rate is about 20.29 million sm³/d (Fig. 4.30a). The trend of the storage flow rates is comparable to the previously presented homogeneous simulations (compare Fig. 4.16a). The H_2 fractions in the produced gas are close to 100 % with the minimum value being 94 % (Fig. 4.30b). As a consequence of these two metrics the H_2 flow rate varies from about 20 million sm³/d at the beginning to 9.47 million sm³/d at the end of the withdrawal period of the 16th storage cycle in the low permeability simulation (Fig. 4.30c). Thus, the sustainable power output, taken as the lowest value obtained in this withdrawal period, is 697 MW.

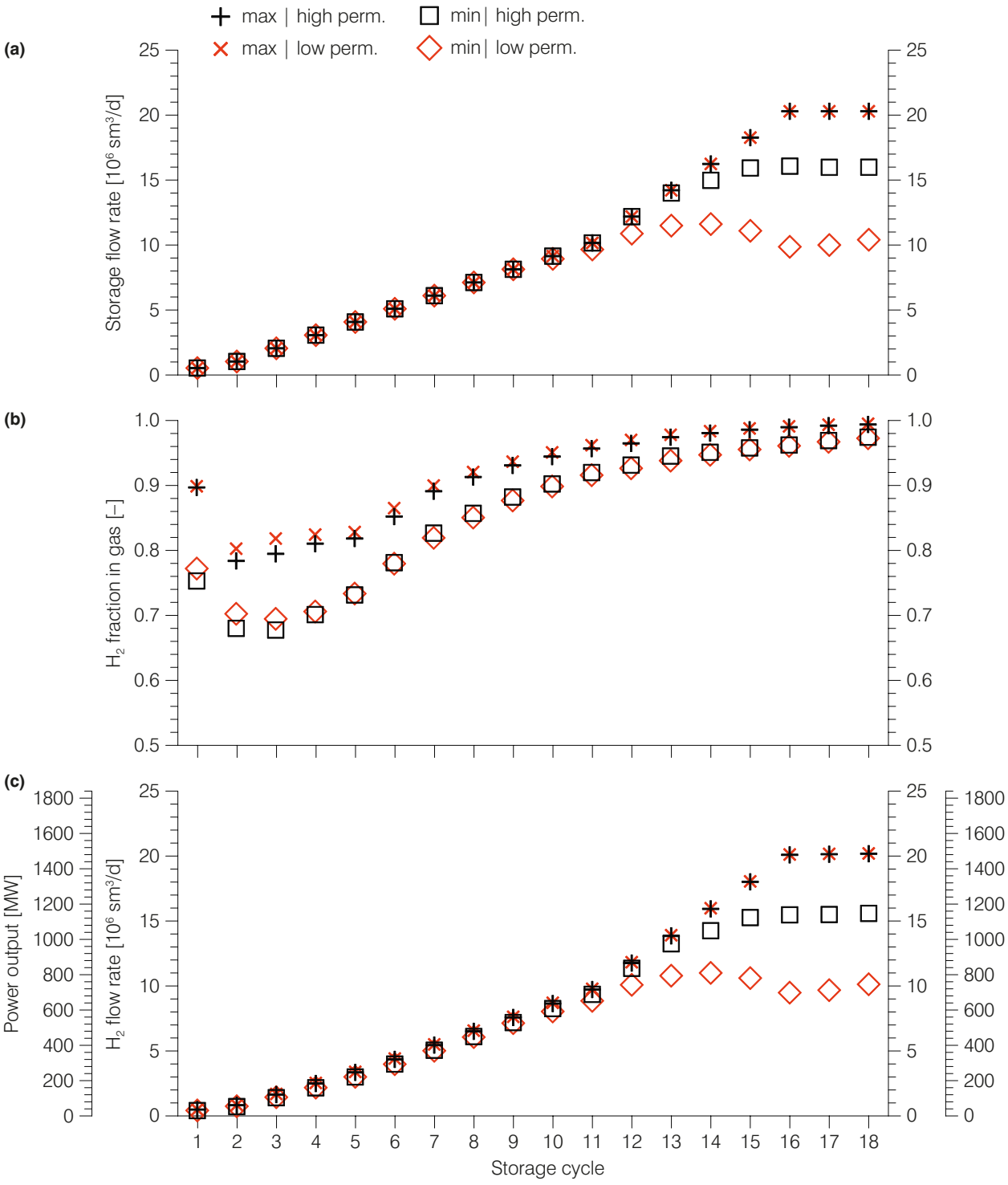

Fig. 4.30 (a) Storage flow rate, (b) H_2 content in produced gas and (c) resulting H_2 flow rate and power output in all storage cycles. Crosses indicate the maximum value observed during the respective storage cycle with the rectangles representing the minimum values.

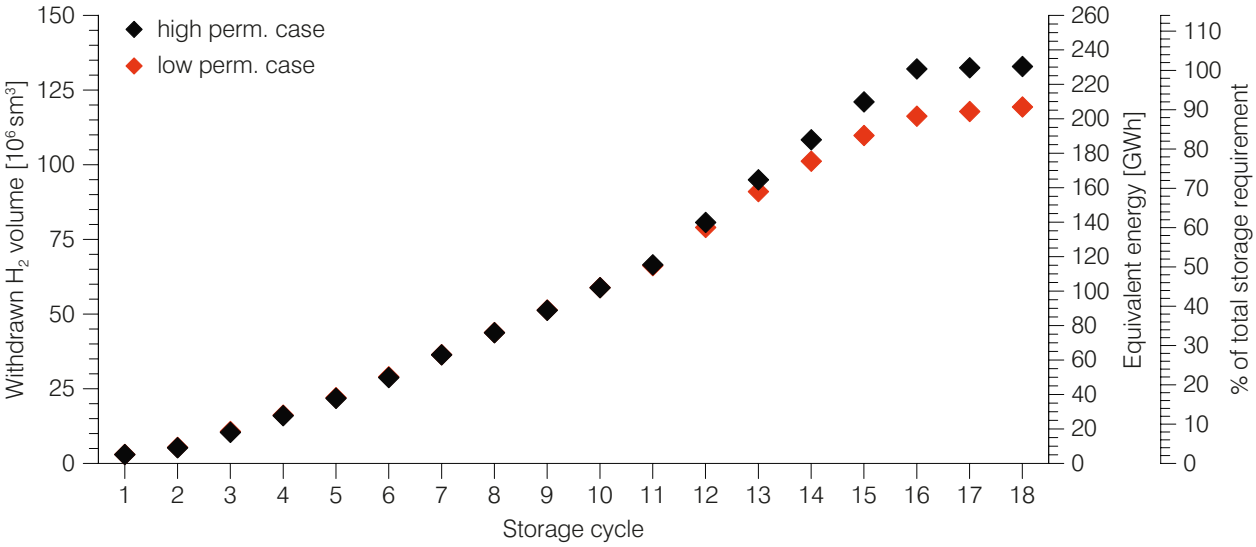

Fig. 4.31 *H_2 volume withdrawn and equivalent energy provided by the storage site in each storage cycle.*

The high permeability simulation shows an improved performance with the storage flow rate remaining more stable over the course of the same withdrawal period, varying from 20.29 to 16.06 million sm³/d (Fig. 4.30a). This transfers directly to the achieved H_2 flow rates as the H_2 fractions are in general high and do not show a strong variability, being more or less identical to the low permeability simulation (Fig. 4.30b). Hence, the lowest H_2 flow rate achieved in the first full scale storage cycle in the high permeability simulation case is 15.56 million sm³/d, corresponding to a sustainable power output of around 1138 MW (Fig. 4.30c). In the high permeability simulation the storage can thus provide nearly twice as much power at the end of the 16th storage cycle than the low permeability simulation. Nevertheless, the sustainable power output from the storage site falls short of the target power output defined as 1356 MW in either case. The sustainable power output from the storage site can only cover for 51 to 84 % of the specified demand. This trend continues in the following storage cycles as the sustainable H_2 flow rates remain relatively constant level in either simulation, with the storage being capable of supplying 744 to 1147 MW, which is about 55 to 85 % of the defined power demand (Fig. 4.30c).

The H_2 volume withdrawn from the storage site during the first 11 cycles and thus the storage capacity is strikingly alike in both simulations, showing next to no influence of the reservoir permeability (Fig. 4.31). From the 12th cycle onwards the volume of H_2 withdrawn in each cycles starts to differ with about 116 million sm³ and 132 million sm³ of H_2 being withdrawn in the 16th storage cycle in the low and high permeability case, respectively. Given the conversion factors assumed in this work, the equivalent energy output from the storage site is in the range of 204 952 to 232 860 MWh. The storage site is thus capable of delivering about 102 % of the defined total storage demand in energy (see Chapter 4.2) when a favourable reservoir permeability is given. In case of a less optimal reservoir permeability the storage site can provide about 90 % of the defined total demand in energy with this simulation setup (Fig. 4.31). These values differ dramatically in their magnitude and variability compared the fractions of the power demand which the storage site can provide for, indicating a rapid decrease in the storage flow rates towards the end of the withdrawal periods given that the H_2 fractions do not vary much (compare Fig. 4.30a,b). Like the power output, the amount of energy withdrawn from the storage remains relatively constant during the following storage cycles (compare Fig. 4.30, 4.31).

Simulation results of the combined usage scenario

The overall simulation setup of the combined usage scenario is not altered from the previously described scenario, except for the addition of two injection wells at the opposing site of the anticline (Fig. 4.26, 4.32). For that reason, the storage performance and behaviour are only discussed briefly.

As a result of the water injection starting at 890 days and continuing for 1144 days, the pressure on the western side of the anticline increases (Fig. 4.32). The initial formation pressure at the northern and southern injection well is about 205 bars and 228 bars, respectively. Over the course of the injection the pressure in both wells increases by about 7 bars, which is also the maximum pressure change observed in the western flank of the storage formation (not shown). With increasing distance to the injection wells the overpressure dissipates (Fig. 4.32). The pressure propagation is greatest towards the north and south as a result of the western model boundary being de-facto closed due to the erosion of the Rhaetian formations.

The overpressure envelopes of the water injection at the western flank and the storage operation at the eastern flank of the structure overlap north of the theoretical apex of the structure (Fig. 4.32). At an observation point which is about 2 km form the northern end of the H_2 storage site and about 8.5 km from the northern water injection well (see Fig. 4.32, 4.25), the initial filling of the storage site in the first 890 days is visible in the pressure signal, with the pressure increasing compared to the baseline simulation by around 1.9 to 2.3 bars (Fig. 4.33 solid lines). During the storage operation, the pressure increases further, reaching a maximum value of about 3.5 bars independent of the permeability of the formation at around 1400 days. From there onwards the pressure levels decrease slowly with the pressure fluctuating between about -1 bar and +2.5 bars at the end of the simulation at 2762 days. The water injection has only a very little effect on the pressure signal at this observation point with the differences between the cases with simultaneous water injection and those without being less than 0.8 bars throughout (Fig. 4.33 dashed lines).

The storage flow rates and the H_2 fractions in the produced gas are more or less the same as in the simulation without the additional water injection. The beginning of the 12th storage cycle coincides with the end of the water injection at 2034 days.

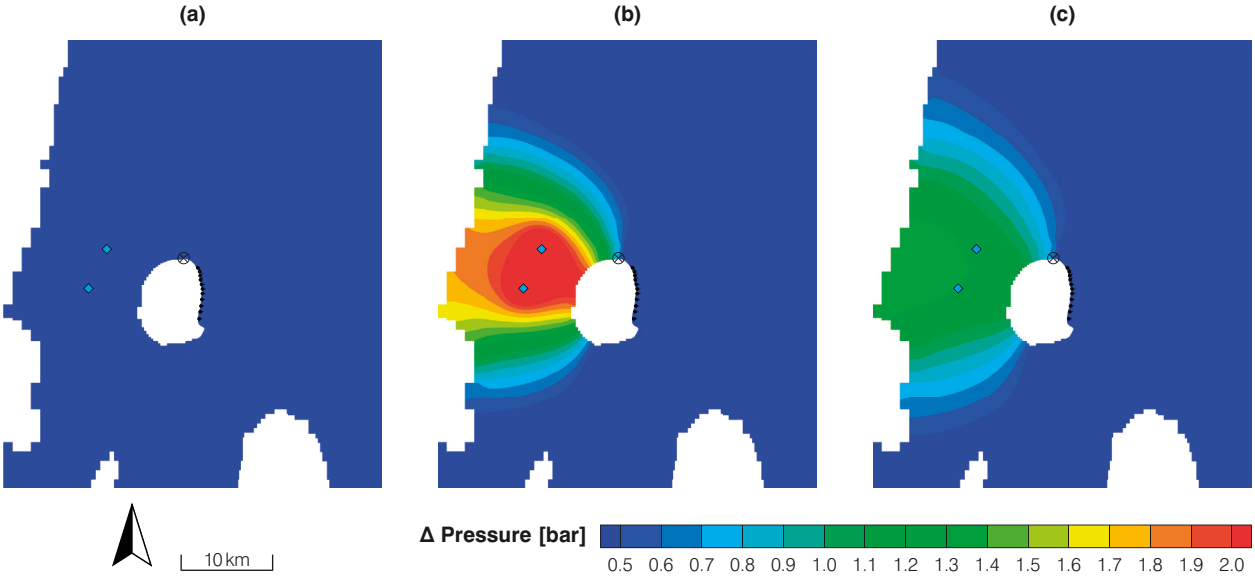

*Fig. 4.32 Pressure difference between the simulation with and without water injection on the opposing anticline flank using the lower permeability estimate **(a)** prior to the water injection at 890 days, **(b)** after the water injection of 2 786 784 m^3 at 2034 days and **(c)** at 2526 days after the re-injection of H_2 in the 16th storage cycle. The black circles depict the location of the gas storage wells, the blue diamonds the location of the waste water injection wells. The observation point at which the differences in pressure is analysed is shown by the black circled-cross.*

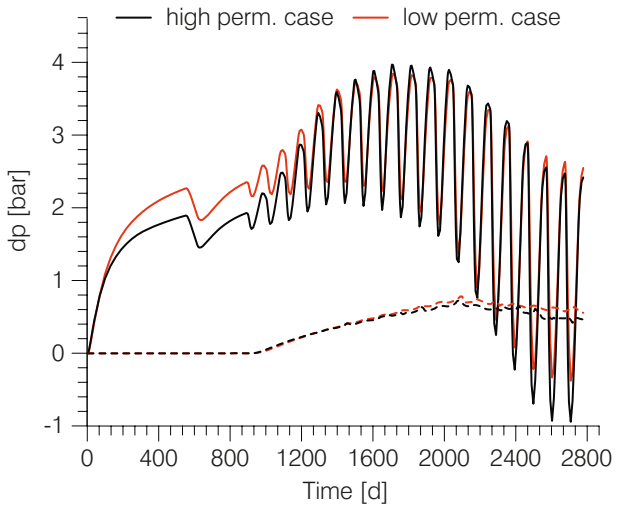

Fig. 4.33 *Pressure differences in the low and high permeability simulations at the observation point north of the H_2 storage site due to the storage operation (solid lines). The dashed lines depict the differences between the pressure signals obtained in the single usage scenario and the combined scenario. For positions of the observation points and the individual wells please refer to Fig. 4.26 and 4.31.*

At this time the pressure perturbation caused by the injection is largest (compare Fig. 4.33), however, the average storage flow rates differ by only 0.02 % in case of the low permeability simulations and are identical in the high permeability simulations. In terms of the storage capacity, the results obtained in the combined usage scenario are in the range of 139 175 to 142 157 MWh, depending on the assumed permeability and thus the distribution of the reservoir properties. Compared to the single usage scenario, in which the storage capacity is in the range of 139 245 to 142 189 MWh, the combined usage of the storage structure results in a decrease of the storage capacity by about 0.05 %. The power output from the storage site is decreasing about 0.1 % and thus equally negligible.

In the final storage cycle storage cycle, the upper estimate of the storage capacity in the combined usage scenario is 232 820 MWh and thus 490 MWh below that of the single usage scenario. The lower estimate of the storage capacity is 209 723 MWh of energy, which is 690 MWh below the lower estimate in the single usage scenario. Given these small reductions, the storage site can still provide around 90 to 102 % of the total energy demand defined in this study. The sustainable power output from the storage site is in the range of 733 to 1139 MW, which is 54 to 84 % of the power demand defined in this study. Thus, the combined use of the storage structure results in a reduction in the sustainable power output from the storage of about 1 %.

Clearly, the different uses of the storage formation simulated in this scenario do not affect each other. The additional overpressure caused by the water injection of less than 1 bar in 2 km from the H_2 storage is not enough to affect the storage performance. Nevertheless, if good reservoir properties such as high formation permeabilities are available, the pressure signals of the individual uses are reaching farther and thus result in stronger mutual interactions. Also, more severe interactions can be expected when the water injection rate is increased or the injection is prolonged. In simulations in which formation heterogeneity is explicitly included, the orientation of the geological structures and thus the distribution of the properties may also effect the severity of the mutual interactions. Nevertheless, the presented simulations show that effects of a combined use of a single geological structure can be analysed using such numerical scenario simulations.

4.5.5 Conclusions

The storage schedule considered in the heterogeneous scenario simulations results in the storage performance being initially poor as a result of insufficient gas being in place. This is due to the upper BHP limits being reached in all wells during the initial gas injection, resulting in a reduction in flow rates. Because of the low volume of gas in place, the storage flow rate and the H_2 fraction in the withdrawn gas vary greatly over the course of the withdrawal periods.

For a quick assessment of potential strategies to increase the storage performance homogeneous scenario simulations can be used given they are adequately representing the behaviour of the heterogeneous ensemble. For the heterogeneous rock model used in this analysis a set of homogeneous parameter distributions is found which can serve as an estimate of the variability that must be expected due to the variability in the heterogeneous parameter distribution.

It is found that employing a storage setup in which the storage capacity is increased stepwise, using the intermediate withdrawal periods for overpressure mitigation, results in increased storage flow rates and higher H_2 fractions in the withdrawn gas in each individual storage cycle. In direct comparison with the previously used storage setup, the new scheme results in the storage site being already partially usable after around 642 days. At the final capacity, which is reached after about 1777 days, the storage site can provide a sustainable H_2 flow rate corresponding to a power output of 259 to 335 MW for one week, depending on the reservoir properties. The sustainable power output from the storage is thus equivalent to about 19 to 25 % of the average power demand as defined in this study. The volume of H_2 withdrawn during the week-long production phase corresponds to about 57 200 to 60 000 MWh of energy, which is around 25 to 26 % of the total storage demand in energy defined in this study. The differences in the relative storage performance (fractions of power and energy demand supplied by the storage site) are due to storage flow rate decreasing quickly towards the end of the individual withdrawal periods. Thus, the power output from the storage site drops considerably towards the end of the withdrawal. In addition to providing some useful storage capacity early into the development, the H_2 fraction in the gas is more consistent throughout the individual storage cycles when the optimized setup is used. This allows for an easier planning and operation of the power plant connected to the storage.

As the spill points of the structure are not yet reached, the storage performance can be further increased by adding storage wells and raising the well flow rates, which requires increasing the volume of gas in place. Using 11 horizontal storage wells the storage is then capable of delivering about 119 to 133 million sm^3 of H_2, corresponding to a storage capacity of 210 413 to 234 310 MWh. With that storage capacity, this site alone can supply about 102 % of the electricity demand of the state of Schleswig-Holstein in one week if good reservoir conditions prevail. If slightly less favourable reservoir permeabilities are given, the storage is still capable of supplying around 90 % of the demand. The sustainable H_2 flow rate during this withdrawal cycle is in the range of 10.1 to 15.6 million sm^3/d, which corresponds to a power output about 744 to 1147 MW. Thus, the storage site can provide about 55 to 85 % of the average power demand defined in this study. Compared to the smaller scale H_2 storage operation the differences in the fractions of the power and energy demand the storage site can provide for are greater. This can be attributed to the total gas volume in the large-scale storage simulation being too low, also shown by the undulating gas-water contact during the storage operation. However, the storage performance can be further increased as the spill points of the structure are not yet reached. Thus, even if less favourable reservoir conditions are given, it can be postulated that the storage site can supply 100 % of the power and energy demand defined in this scenario when additional storage wells are added.

The lateral extent of the gas phase is about 7 km by 750 m. The reach and the magnitude of the pressure perturbations caused by the storage operations are like those obtained in the heterogeneous ensemble. Near the injection wells the maximum pressure increase is governed by the applied BHP limits. In the presented scenario, a maximum increase of slightly less than 11 bars over the initial pressure at distances of 500 m from the storage wells can be observed. In the far field of the storage wells the maximum pressure increase is less than 3 bars in all simulated cases. For the large-scale storage operation, the induced pressure perturbations are estimated at approximately 1 bar in around 10 km. Compared to the initial hydrostatic pressures, which are above 150 bars, the induced pressure perturbations are small.

Potential hydraulic interactions of competing usages are investigated by an injection of waste water at the opposing flank of the storage structure for the large-scale storage operation. The total injected water volume is about 9 times the cavern volume of the Huntorf compressed air energy storage site, which is a conservative estimate of the volume required to leach caverns of this size. The water injection rate was set so that the duration of the water injection represents the construction time of said cavern storage site. Even though the induced effects of both usages are far reaching, the distance between the gas storage site and the waste water injection site is enough so that the overpressure envelopes only slightly overlap. At an observation point about 2 km from the

gas storage site the waste water injection results in an additional pressure increase during the storage operation of less than 1 bar. This small additional pressure increase does not majorly affect the performance of the gas storage site, so that the storage site can still provide around 209 723 to 232 820 MWh over a period of one week depending on the reservoir permeability, which is about 90 to 102 % of the total energy demand defined in this study. The sustainable power output from the storage site is in the range of 733 to 1139 MW in the combined usage scenario, which represents a reduction of about 1 % compared to the single usage scenario. Nevertheless, increasing the water injection volume, the injection rate or repositioning the injection site closer to the gas storage could result in increased interferences of the two usage options. The presented scenario simulations can easily be adapted to investigate the effect further increasing the size of the gas storage operation or to quantify mutual interaction between the storage operation and other, potentially competing, uses of such a geological structure.

4.6 Part III: Thermal effects during storage operation

Besides hydraulic effects, as shown in Chapters 4.4 and 4.5, an underground gas storage operation may also induce thermal effects through the temperature of the injected gas and pressure induced temperature changes such as the Joule-Thomson effect. The latter will most likely only result in slight temperature changes in the storage formation due to the small Joule-Thomson coefficients of H_2 (see also Chapter 3.7 and 3.8). Additionally thermal effects can also be caused by the temperature with which the gas is injected, with the injection temperature itself depending on the pressure and temperature of the gas prior to injection and the pressure differences between the gas and the reservoir. For gas to flow into the storage formation during injection, the pressure of the gas must be higher than the pressure of the reservoir. Thus, the gas may have to be compressed prior to injection, during which the temperature of the gas increases (e.g. Katz et al. 1959; Wang and Economides 2009). Even though coolers are used in between compression stages to optimise the efficiency of the compression (e.g. Wang and Economides 2009), the temperature of the gas could differ from the reservoir temperature prior to injection.

The pressure and temperature of the H_2 gas prior to any such compression depends on the setup of the surface installations such as the technology used to produce the required H_2 (see Chapter 2.2). The most promising methods may be alkaline electrolysis (AEL) and proton exchange membrane electrolysis (PEM) due to the individual maturity of these technologies and the foreseeable technology development. Modules used for AEL-electrolysis are operated at temperatures between 0 to 100 °C and pressures of up to 30 bars (Ursúa et al. 2012). While the operating temperatures of PEM-electrolyser modules is similar to that of AEL-modules (20 to 100 °C), the operating pressure can be as high as 50 bars for already commercially available units (Sterner and Stadler 2014). Operating at a higher temperature may also be beneficial as the efficiency of the H_2 production by water electrolysis increases with rising temperature (Sterner and Stadler 2014). The pressure and temperature of the H_2 prior to injection may then vary considerably depending on the setup of the H_2 generation plant. The final injection temperature of the H_2 gas is not well defined if the specific subsurface installations are unknown. Nevertheless, any difference in reservoir and gas temperatures will result in a temperature perturbation within the storage formation and the caprock

Given the range of the operating temperatures and the fact that the efficiency of the process of H_2 generation increases with temperature, it can be expected that the injection temperature of the gas might differ several °C from the reservoir temperature even if additional compression is not required. The magnitude of induced thermal effects by the injection temperature may be much more than the Joule-Thomson effect. Consequently, the effect of the injection temperature has to be analysed to determine induced thermal effects.

For the estimation of thermal effects a new simulation grid is required as formations overlying and underlying the storage formation will be affected by conductive heat transport and thus the exclusion of these rock strata as done in the previous scenario simulations does not result in an realistic representation of the investigated

process. The simulation is carried out using the coupled OpenGeoSys-ECLIPSE simulation described in Chapter 3 of this thesis, in which the flow process is simulated by ECLIPSE and the heat transport is solved for in OpenGeoSys.

4.6.1 Simulation setup

To maintain consistency among the scenario simulations the new simulation model is based on the same structural model as the previous simulations (see Chapter 4.3), albeit with a reduced lateral extent to minimize the computational load. The model is constructed around the central well 3 of the small capacity H_2 storage simulation (Fig. 4.34) with the overall dimensions being 7.5 km in x-direction and 450 m in y. The model is discretised using 116 elements of 1 to 200 m in x-direction and 45 elements of 1 to 15 m in y-direction, with the increments increasing from the well positions towards the model boundaries. The vertical extent of the model varies due to the depth and thickness of the individual layers but is in general around 900 m. In vertical direction the model is discretised using 59 layers with each geological strata consisting of a constant number of layers. The resulting element thicknesses are in the range of 0.5 to 270 m depending on the local thickness of the individual rock formation. Near the simulated well the element thicknesses are about 2 m within the storage formation.

The intrinsic permeability, porosity and the multiphase flow properties such as the residual phase saturations, the maximum relative gas permeability and the capillary entry pressure are assumed to be homogeneous within each formation. Permeability is assumed to be isotropic. The values assigned to the individual formations of the Rhaetian are calculated based on the parameter distributions in the heterogeneous ensemble using a simple arithmetic mean for permeability (Tab. 4.7).

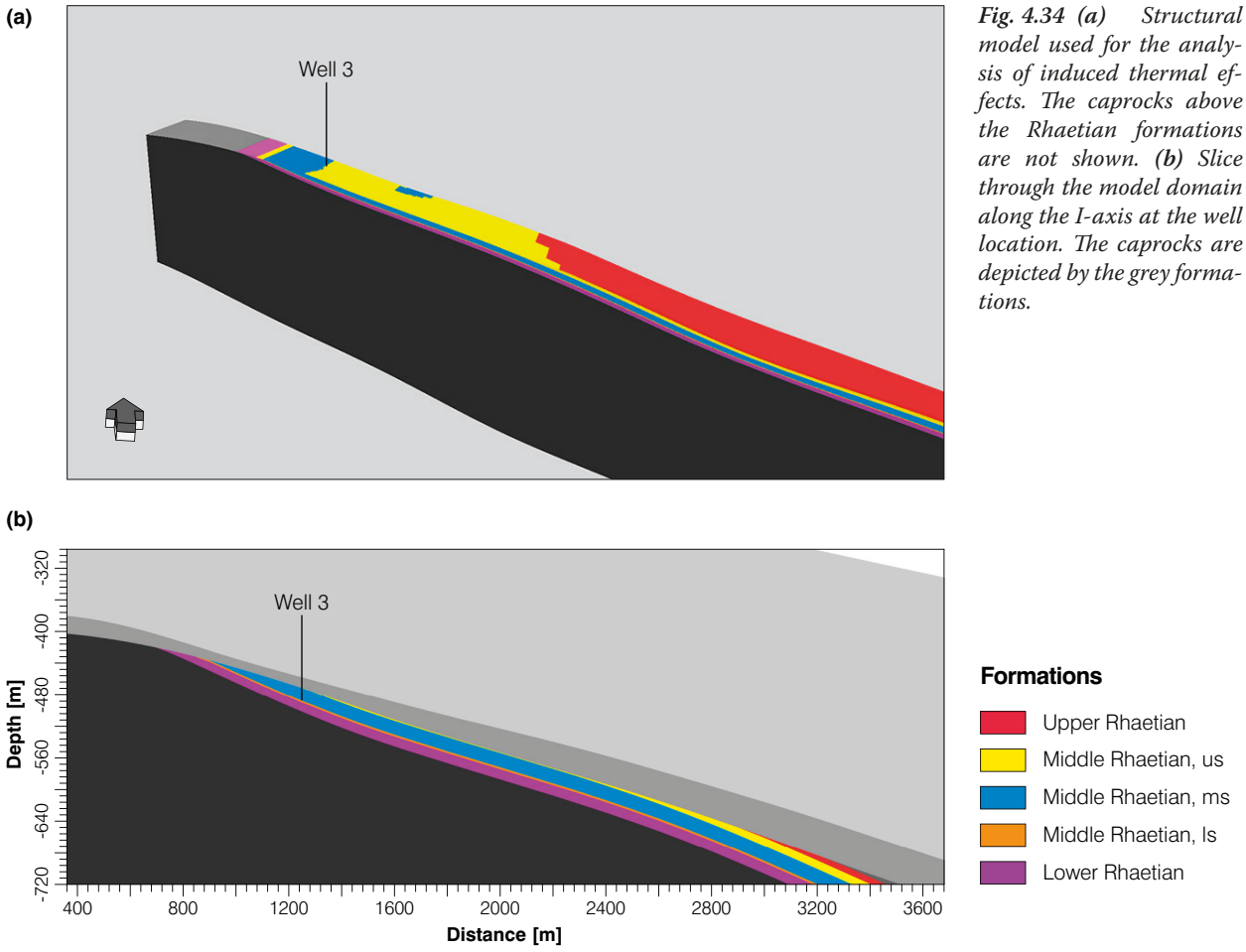

Fig. 4.34 (a) Structural model used for the analysis of induced thermal effects. The caprocks above the Rhaetian formations are not shown. (b) Slice through the model domain along the I-axis at the well location. The caprocks are depicted by the grey formations.

Tab. 4.7 Flow properties assigned to the individual formations of the simulation model used for the analysis of thermal effects.

Formation	Permeability [mD]	Porosity [–]	Sr_w [–]	kr_{gmax} [–]	p_d [bar]
Jurassic/Cretaceous	1×10^{-5}	0.10000	0.6000	0.0150	15.0000
Upper Rhaetian	1.806×10^{0}	0.12569	0.5268	0.1193	9.6932
Upper Shale, Middle Rhaetian	1.204×10^{2}	0.27929	0.4183	0.3696	1.6833
Main Sandstone, Middle Rhaetian	5.984×10^{2}	0.33188	0.3469	0.6770	0.2146
Lower Shale, Middle Rhaetian	1.341×10^{0}	0.10840	0.5457	0.0923	11.0644
Lower Rhaetian	4.687×10^{1}	0.15389	0.5165	0.1711	8.8877
Lower / Middle Triassic	1×10^{-5}	0.10000	0.6000	0.0150	15.0000

No data on the thermal properties of the individual formations at the given site is publicly available, so the thermal properties had to be assigned based on values in available literature. The heat capacity of the solids of the Main Sandstone of the Middle Rhaetian is assumed to be 725 J/kg/K while the heat conductivity is taken as 3.75 W/m/K. The heat capacity and the thermal conductivity of the formation water is assumed to be 4185 J/kg/K and 0.56 W/m/K, respectively. Given that the formation is fully water saturated the heat capacity of the storage formation thus equates to about 2.6 MJ/m³/K, which is the upper estimate given by VDI (2010) for sandstones. For the gas the heat capacity is set to 14.3 kJ/kg/K, while the thermal conductivity of the gas is assumed to be 0.1869 W/m/K, respectively. For the pressure and temperature conditions given in the simulation, the chosen values correspond to the values given in Lemmon et al. (2016) for H_2. For the sake of simplicity all thermal properties are assumed to be homogeneous throughout the model domain. According to the VDI (2010) the thermal conductivities of clay stones are 1.1 to 3.4 W/m/K, while sandstones fall in the range of 1.9 to 4.6 W/m/K. The volumetric heat capacities of clay stones are specified to be around 2.1 to 2.4 MJ/m³/K, while those of sandstones are 1.8 to 2.6 MJ/m³/K. Consequently, the thermal conductivities and heat capacities of the shales or sandstones rich in clay are slightly overestimated in the simulation compared to literature data by the assumption of homogeneous thermal parameters. To ensure numerical stability a heat dispersivity is set to 50 m, which results in a dampening the heat pulses caused by the intermittent injection.

Initially, the storage formation is completely water saturated with the pressure being hydrostatic. The initial temperature distribution in the model follows a geothermal gradient of 0.03 °C/m with the temperature near the surface being 10 °C. Given this gradient the initial temperature proximal to the storage well is around 24 °C.

As the model only includes one storage well, representing a central section of the H_2 storage simulated in Chapter 4.3 and 4.4, the model boundaries to the south, west, and north are assumed to be closed while pore volume multipliers are used at the eastern boundary to mimic the extent of the Rhaetian beyond the model domain (compare Chapter 4.4.2). No heat flux over the model boundary is allowed. The injection temperature of the gas is simulated as a constant temperature boundary condition at the well locations during the individual injection phases of the storage operation. During shut-in or withdrawal phases the temperature boundary condition is deactivated. In the absence of a specific storage and power plant setup which would define the temperature of the H_2 gas, the injection temperature is set to 50 °C, which is around 25 °C above the initial temperature in the vicinity of the storage well.

The flow rates applied at the storage well are taken from the improved storage setup presented in Chapter 4.5.3. At first N_2 is injected at a rate of 15 000 sm³/d for 365 days, followed by a shut-in period of 60 days and the first H_2 injection at 25 000 sm³/d for 210 days. After a short shut-in period of 7 days the storage operation of 12 cycles begins. Each storage cycle consists of a withdrawal period of 7 days followed by a shut-in of 7 days and an injection period of 60 days. The

next storage cycle starts following another shut-in period of 30 days. The withdrawal rates applied at the storage well increase stepwise from initially 200 000 sm^3/d to ultimately 1 000 000 sm^3/d in the 11th cycle (see Fig. 4.18). Similarly, the injection rate is increased from 58 333 sm^3/d in the first cycle to the final target rate of 122 500 sm^3/d in the fourth cycle.

For the calculation of phase densities and viscosities a generalised formulation of the Peng-Robinson equation of state is used, which takes into account the temperature distribution within the model domain (Schlumberger 2015). Feedback of the temperature perturbation on the flow simulation is thus included in the simulation. OpenGeoSys assumes thermal equilibrium between the solid phased and all fluid phases.

4.6.2 Simulation results

The storage well is located so that at least 12 m of reservoir is available in vertical direction to accommodate sufficiently high injection rates. This positioning results in the more buoyant gas first filling the shallower and thinner sections of the storage formation. Consequently, only a thin layer of gas in the upper section of the storage formation is present at the end of the first H_2 injection after 645 days (Fig. 4.35a). The distribution of the gas phase does not correspond to the temperature perturbation caused during the storage initialization phase (Fig. 4.36). This initial filling phase of the storage with N_2 and H_2 marks the longest continuous injection phases during which the temperature at the well location is kept constant being 365 and 210 days, respectively. After 180 days of injection, which is about the half way point of the N_2 injection phase, the temperature of the storage formation is increased by at least 15 °C within the first 7 m from the injection well (Fig. 4.36a). As constant temperature boundary conditions are used, the maximum temperature differences in the storage formation are given directly by the difference between the initial temperature and the applied temperature, which is about 25 °C. The heat signal also conductively spreads into the overlying and underlying rock formations. The lateral extent of the temperature perturbation is slightly greater than the vertical extent. In the formations above the storage formation a change in temperature of at least 15 °C is observed in distances of about 2.5 m. The extent of the temperature perturbation into the underlying formations is much lower at around 1 m. The greater extent of the temperature perturbation towards the top of the storage forma-

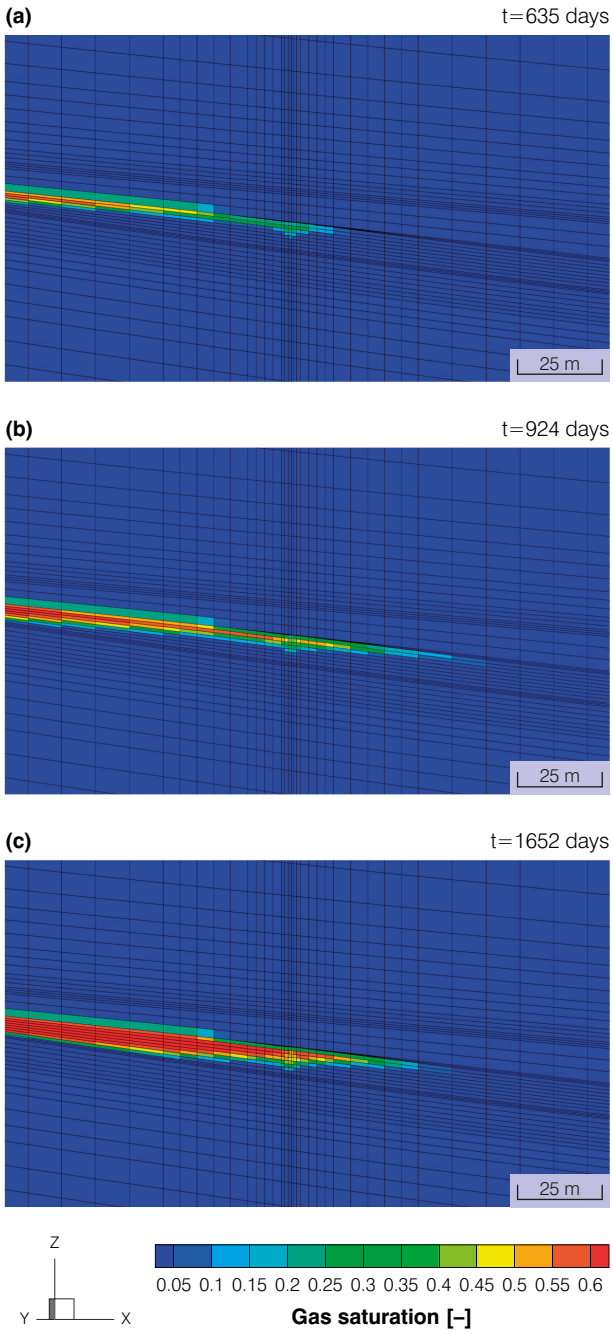

Fig. 4.35 Gas saturations at a vertical slice through the well position along the x-axis after ***(a)*** *the first H_2 injection,* ***(b)*** *prior to the fourth storage cycle and* ***(c)*** *prior to the 11th storage cycle, the first cycle at full capacity*

tion and the overlying caprock is a result of the gas rising in the vicinity of the storage well after injection, which leads to a increased transport of heat into this region. At this early stage of the simulation the maximum reach of the temperature perturbation as measured by a change of at least 1 °C is about 20 m from the well in lateral direction. Until the end of the N_2 injection at 365 days, the extent of the interval in which the temperature is increased by more than 15 °C remains similar, showing a more consistent vertical temperature distribution within the storage formation (Fig. 4.36b). Also, the space affected by high temperature changes in the cap rock is slightly increased. The absolute reach of the heat signal is about 25 m from the storage well, again in lateral direction. Within the caprocks above and below the storage formation the temperature is elevated by more than 1 °C in distances of about 10 m.

In the following shut-in period of 30 days the temperature boundary conditions at the injection site are deactivated. The temperature perturbations continuously spread further at the expense of the magnitude of the signal by heat conduction (Fig. 4.36c). A temperature increase of at least 1 °C is observed at distances of about 30 m from the injection well within the storage formation. The temperature perturbations in the overlying and underlying caprocks reach about 12.5 m. In the subsequent H_2 injection phase the temperature boundary conditions are reactivated, once again resulting in high temperature differences of more than 15 °C in the first 7.5 m from the injection well (Fig. 4.36d). The reach of the temperature signal increases further to about 35 m in lateral direction. No visible differences can be observed regarding the vertical reach of the signal. The distribution of the temperature perturbation

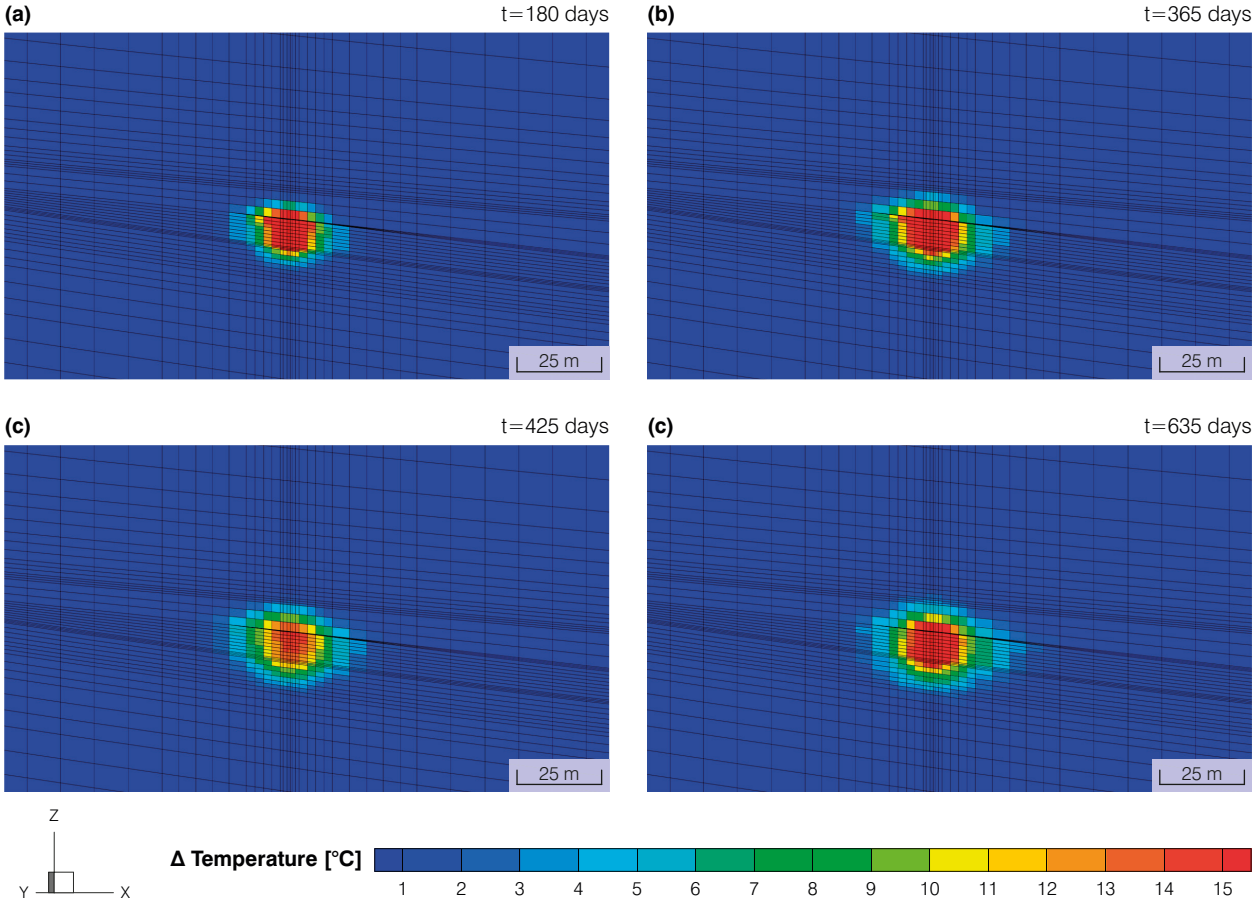

Fig. 4.36 Change in temperature to the initial distribution ***(a)*** *after half of the N_2 is injected,* ***(b)*** *after the N_2 injection,* ***(c)*** *after the 30 day shut-in period and* ***(d)*** *after the initial filling with H_2.*

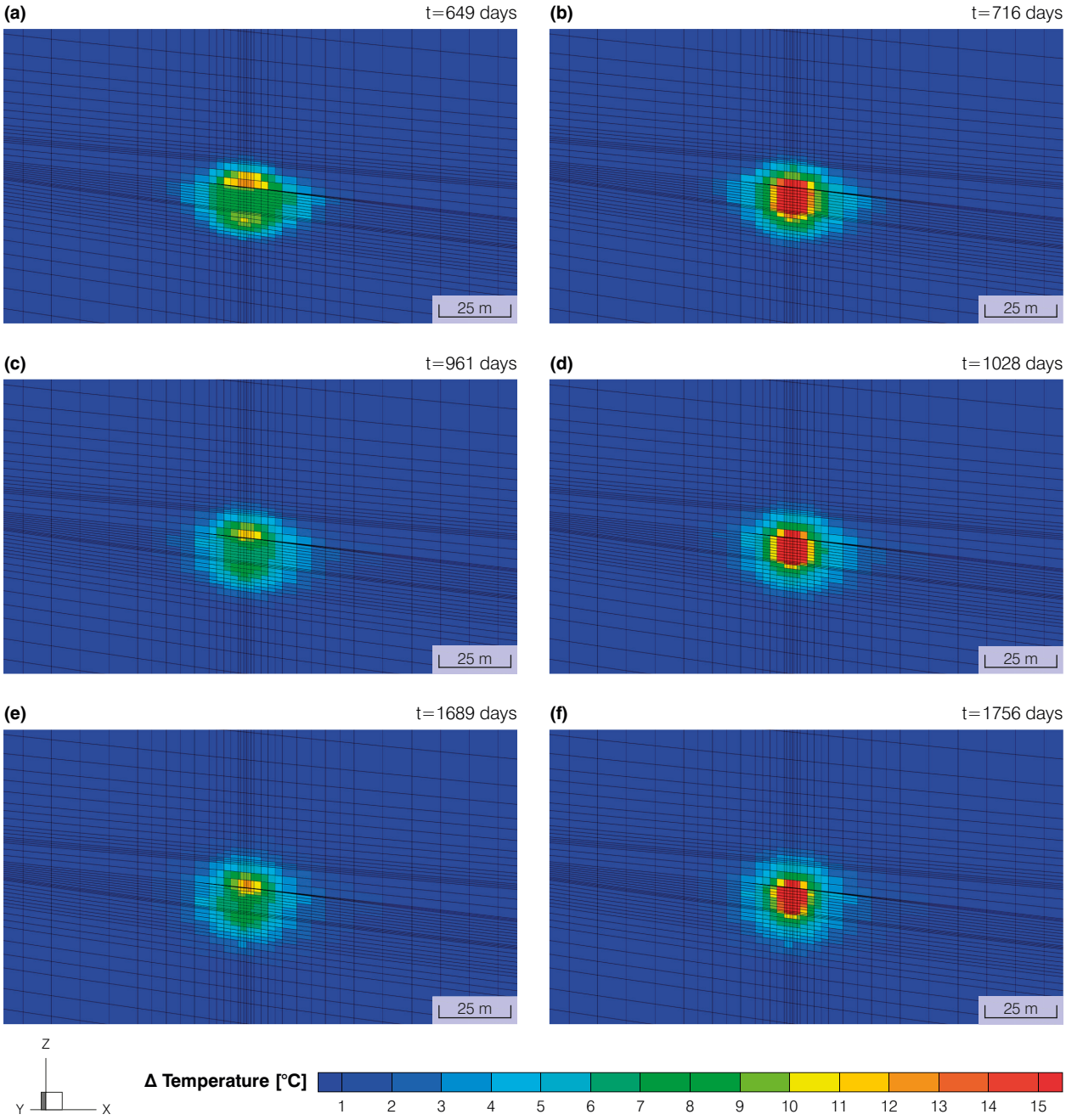

*Fig. 4.37 Change in temperature compared to the initial storage temperature after the withdrawal and replenishment with H_2 in the first cycle (**a, b**), the fourth cycle (**c, d**) and the 11th storage cycle (**e, f**).*

does not reflect the distribution of the gas phase (compare Fig. 4.35a, Fig. 4.36d).

During the subsequent withdrawal of gas in the first storage cycle from 642 days to 349 days, the production of reservoir fluids results in heat being taken out of the storage formation (Fig. 4.37a). The magnitude of the temperature perturbation decreases noticeably with temperatures in the storage formation being elevated by just 7 to 9 °C. The removal of heat around the well also results in a conductive transfer of heat from the caprocks back to the storage formation so that the maximum temperatures in the rock formations above and below the storage formation are less than 13 °C. The overall extent of the temperature perturbation is not affected by the withdrawal with the signal reaching about 35 m within the storage formation and 12.5 m in the

caprocks. Subsequently to the withdrawal and a short shut-in period the storage is replenished in H_2. In the used storage setup significantly more gas is injected than withdrawn in the first 11 storage cycles (compare Chapter 4.5.3). The refilling of the storage with gas again results in larger temperature differences near the well bore of at least 15 °C in the first 5 m after 716 days (Fig. 4.37b). Similar temperatures can be observed within the first 2.5 m in the adjacent formations above and below. The rock volume in which such high temperature changes can be observed is thus similar to the volume affected by the initial filling of the reservoir (compare Fig. 4.36d). The extent of the temperature perturbation in those formations is maintained around 12.5 m in the overlying formations and about 13 m in the underlying formations. In lateral direction the overall extent is also comparable to the previous observation times being around 35 m.

Over the course of the following storage cycles only meagre differences can be observed compared to the first storage cycle. The maximum temperature perturbations after the fourth withdrawal period are in the range of 7 to 9 °C, with the greatest temperature increase in the caprock rock above the storage formation being around 12 to 13 °C (Fig. 4.37c). The volume in which this stronger temperature perturbation occurs is however reduced compared to the first storage cycle. Below the storage formation the maximum change in temperature is less than that at around 9 °C. In contrast to the first cycle, the lateral extent of the temperature perturbation is increased to around 45 m. In vertical direction a change of more than 1 °C can be observed in distances of up to 15 m. In the subsequent injection period lasting from 968 to 1028 days the measure of the temperature perturbation remains constant in all directions (Fig. 4.37d). Again, the temperature in the storage formation up to a distance of about 5 m from the well is subjected to temperature increases of more than 15 °C. Such large temperature increases are also visible in the first 2.5 m of the overlying caprock.

From the fourth cycle onwards only minor differences can be observed between the storage cycles so that the temperature perturbations caused by the storage operation in the 11th cycle closely resemble the status of the fourth cycle (Fig. 4.37 e,f). Albeit significantly more gas is present in the reservoir at this time (compare Fig. 4.35d), the distribution of the temperature perturbation is not linked to the distribution of the gas phase. This is because the injected gas has a low volumetric heat capactiy, compared with the heat capacity provided by the rock and the connate water. Thus, the transport of heat is dampened by the remaining phases. Nevertheless, injection induced perturbations in the temperature distribution translate to increased temperatures in the storage formation and the overlying and underlying rock strata with the greatest extent being about 45 m in the simulated scenario. In vertical direction the reach of the temperature signal is less than that being around 13 m. The cyclicity of the storage operation results in a constant temperature fluctuations within the caprocks and the storage formation of several degrees in the near well bore region.

4.6.3 Conclusions

Thermal effects induced during porous media H_2 storage can be caused by various processes of which only the effect of the injection temperature was simulated and presented in this chapter. The Joule-Thomson effect, which results in a temperature change by gas expansion during flow within a reservoir, is discussed in Chapter 3 and is briefly summarized at this point. H_2 has a negative Joule-Thomson coefficient at the simulated reservoir conditions, leading to a temperature increase during gas expansion. Although the cyclic operation of the storage results in gas expansion along the flow path during injection and withdrawal, the overall temperature change induced by this effect is small at less than 1 K (or °C). This is primarily due to the small magnitude of the Joule-Thomson coefficients of H_2. Other gases which could be used for porous media energy storage such as air or CH_4 have greater Joule-Thomson coefficients which will result in larger temperature differences. Furthermore, the storage frequency does affect the overall temperature change so that larger temperature differences can be expected for i.e. a compressed air energy storage.

Obviously, temperature perturbations can also be caused by the temperature with which H_2 is

injected, which largely depends on the surface installations as the modes or methods of H_2 generation differ in operating pressures and temperatures. In case of a H_2 generation at low pressures, additional compression might be necessary prior to the injection of the gas depending on the initial reservoir pressure. While a temperature increase caused by such a compression can be moderated by coolers, differences between the injection temperature and the reservoir temperature can be expected already due to high operating temperatures of the H_2 generation facilities.

In this study, it is assumed that gas is injected at 50 °C, which is about 25 °C above the initial reservoir temperature. Given some modules used for H_2 production can be operated at temperatures of up to 100 °C, the assumed injection temperature is within the range of potential injection temperatures.

The simulation of the effect of such an injection temperature is carried out using the coupled OpenGeoSys-ECLIPSE simulator described in Chapter 3. The simulation model consists of one storage well and is based on the simulation model used for estimating storage performance and induced hydraulic effects of the small capacity H_2 storage. The injection temperature is simulated by applying constant temperature boundary conditions at the well locations during injection periods of the storage initialization and operation. The chosen boundary conditions resemble a conservative estimate of the heat added to the system as the predefined injection temperature is applied to all fluids and the rock phase present at the well location and not just the gas phase.

The maximum temperature difference occurring in the model is governed by the chosen injection temperature so that the maximum change is about 25 °C. The heat is transported away from the well by conduction and advection, with the latter being only relevant during injection phases. The extent of the induced thermal effects as measured by a difference of more than 1 °C is less than 25 m in lateral and 10 m in vertical direction after the initial filling of the storage. During the subsequent first couple of storage cycles, the reach of the induced thermal effects increases further, ultimately being about 45 m in lateral and 15 m in vertical direction. The differences between the storage cycles are rather small so that the extent of temperature perturbations is practically constant on these short time scales. The cyclic operation of the storage does however result in frequent temperature changes of more than 5 °C in the storage formation and the adjacent rock strata near the well location.

Overall the extent of the induced thermal effects around one storage well are minuscule when compared to the extent of hydraulic effects. Nevertheless, temperature perturbations are not restricted to the storage formation itself. At an actual storage site most likely more than one well would be used to provide high storage outputs. Given the hydraulic interference between the wells demands for a well spacing of more than 100 m, not one single volume in which significant temperature changes are occurring can be expected. The extent of the induced thermal effects is relatively independent on the applied well flow rates.

This analysis is based on several simplifications such as homogeneous thermal parameters and constant temperature boundary conditions. Through the assumption of local thermal equilibrium the applied boundary condition results in an overestimation of the amount of heat introduced into the system during the injection phases. For a more realistic boundary condition the heat content of the injected gas should be considered, e.g. by specifying a source term in the heat transport equation equivalent to the supplied heat. Doing so does however require additional code development as the automatic well flow rate reductions caused by a violation of the BHP limits have to be taken into account. Nevertheless, the presented simulation does provide a first conservative estimate of the induced thermal effects caused by an H_2 storage operation.

5 MONITORING ASPECTS OF POROUS MEDIA HYDROGEN STORAGE

In the following chapter geophysical monitoring techniques, namely seismic, geoelectric, and gravimetric methods are tested for the individual applicability to a porous media H_2 storage. For this an H_2 storage operation is simulated at a realistically parametrised, heterogeneous storage. The resulting gas phase distribution is used as input for forward simulations of the application of the various geophysical monitoring techniques. The results obtained with from the geophysical monitoring are then qualitatively compared to the input data to infer the limitations of the monitoring methods.
The storage demand on which the storage simulation is based and the simulation setup are consistent with those of Chapter 4. Nevertheless, the underlying storage scenario is briefly presented in Chapter 5.2. The geological model and the setup of the simulation model are presented in Chapter 5.3 and 5.4, respectively. The simulation results obtained for the heterogeneous storage and which are used to assess the geophysical monitoring techniques are presented in Chapter 5.5. The results obtained with the geophysical methods applied in this analysis are given in Chapter 5.6.
The content of the following chapter is published as

Pfeiffer W T, al Hagrey SA, Köhn D, Rabbel W, Bauer S (2016) Porous media hydrogen storage at a synthetic, heterogeneous field site: numerical simulation of storage operation and geophysical monitoring. Environ Earth Sci 75:1177. doi: 10.1007/s12665-016-5958-x

5.1 Introduction

A thorough site monitoring is a necessity both prior and during and field application of porous media H_2 storage to optimized the storage operation and ensure its integrity. The space required for such a site monitoring must be considered when assessing potential effects on and implications for other usages. Consequently, the specific monitoring requirements of a potential usage such as a porous media H_2 storage must be taken into account during a sustainable subsurface planning together with the dimension of the usage (Kahnt et al. 2015).

Various techniques can be used for monitoring a gas storage, each serving different purposes. Observation wells for example can be used for pressure monitoring to infer reservoir properties (Katz et al. 1959) or for direct monitoring of the gas distribution. Furthermore, pressure monitoring of carbon capture and storage (CCS) sites at observation wells within and outside of the storage formation can give information on the storage operation and possible leakages (e.g. Birkholzer et al. 2009; Benisch and Bauer 2013). Such measurements yield either point data such as local pressures or integral data such as flow rates and volumes. These point data based monitoring techniques can be enhanced by integrated geophysical monitoring concepts, which can detect and quantify gas phase bodies in the subsurface, enabling a more detailed 2D or 3D rendering of the gas phase distribution (al Hagrey et al. 2014; Benisch et al. 2015).

In a porous media gas storage, gas replaces the formation brine causing changes in elastic moduli, density and electric resistivity. These changes result in physical contrasts when employing geophysical monitoring techniques such as seismic full waveform inversion (FWI), electric resistivity tomography (ERT) and gravity measurements. CCS storage processes have been monitored using mainly seismic time-lapse imaging which estimates changes in P-wave velocity (Vp) and acoustic impedance (e.g. Eiken et al. 2000; Arts et al. 2002; Arts et al. 2003; Arts et al. 2004; Chadwick et al. 2005; Meadows 2008; Chadwick et al. 2009; Ghaderi and Landrø 2009; Hannis 2010; Lüth et al. 2011). In recent years, seismic FWI became a popular technique to resolve structures much smaller than the dominant seismic wavelength. The applicability of FWI to field data sets has been proven by imaging small-

scale leakage paths of a methane gas plume within the Valhall gas field using 3D acoustic FWI (Sirgue et al. 2010; Operto et al. 2015), demonstrating the potential to estimate material parameters and changes thereof with a high spatial resolution. As elastic material parameters can be linked to physical parameters of the gas phase via an appropriate rock physics model, this allows an estimation of the gas saturation. Queißer and Singh (2013a; 2013b) applied this approach using data from the Sleipner field site. Other successful acoustic FWI examples to image the migration of the CO_2 phase in the underground are based on crosswell (Zhang et al. 2012) and reflection seismic data (Zhang et al. 2013) from the Ketzin CCS site. The combination of seismic, ERT and gravity techniques has the potential of providing even better monitoring results as the individual techniques complement each other (Lüth et al. 2011; al Hagrey et al. 2013).

In theory, these concepts can be readily adapted to porous media H_2 storage as all gases have similar impacts on the electro-elastic properties used in the monitoring techniques. However, the low density of H_2 and the relatively unknown dimensions of a typical porous media H_2 storage pose additional challenges as they can result in thin gas phase bodies which are harder to detect. These unknowns are addressed in this chapter by first briefly describing a possible usage scenario of a H_2 storage operation and simulating the behaviour of a theoretical storage site in northern Germany during operation and then by investigating the applicability of FWI, ERT and gravity methods to a site monitoring.

5.2 Defintion of the storage demand

To be able to set the performance of a storage into context to potentially occurring deficits in power production, the overall storage demand has to be defined. The storage demand is a function of the required delivery rate of electrical energy and the duration of the energy withdrawal period, both of which are highly variable. The storage demand to which the reservoir simulation is evaluated to is identical to the demand defined in Chapter 4.2. For completeness, the underlying scenario is briefly presented here with more information available in the aforementioned chapter.

Simulations of power production from renewable sources in Germany based on actual meteorological data, forecast shortages in electric power supply of up to 14 days in months of unfavourable weather conditions most prevalent in the winter months (Klaus et al. 2010). It can however be assumed that several types of energy storage would be employed simultaneously, effectively shortening the period in which a H_2 gas storage site is the main source of power for the grid. In the absence of more detailed data, the period of demand from the storage site was set to one week.

In general, the required electrical power from the storage depends on the actual energy demand, the supply of electric power from all primary sources, which in most cases are fluctuating, and the number of storage facilities. The required delivery rate of the H_2 storage site was set to the average power demand of the state of Schleswig-Holstein, northern Germany, which corresponds to a population of about 2.8 million people. This approach neglects fluctuations in power demand and power production from other sources and can thus be seen as a worst-case scenario. In 2011 a total of 42.82 million GJ of electricity was consumed in Schleswig-Holstein (MELUR 2013), corresponding to 0.82 million GJ in one week. Additionally, the efficiency of the re-electrification process must be considered, as the supply of energy to the storage is not assumed to be a limiting factor. For the re-electrification of stored H_2 either fuel cells (Büchi et al. 2014) or gas turbines (Forsberg 2009) can be used. Both methods have similar real-world system efficiencies, which is assumed to be 60 % in this study. Using the specific energy density, also termed inferior calorific or lower heating value, of H_2 of 124 MJ/kg (Carden and Paterson 1979), the amount of H_2 that has to be retrieved from the storage site during one week is 129 million m^3 of H_2 at surface conditions (sm^3).

5.3 Storage site characterisation

For the numerical reservoir simulation of the H_2 storage operation the same structural and geological model as in the previously presented heterogeneous storage simulation is used (see Chapter 4.4). Thus, only a short overview is given on the geological background of the storage site.

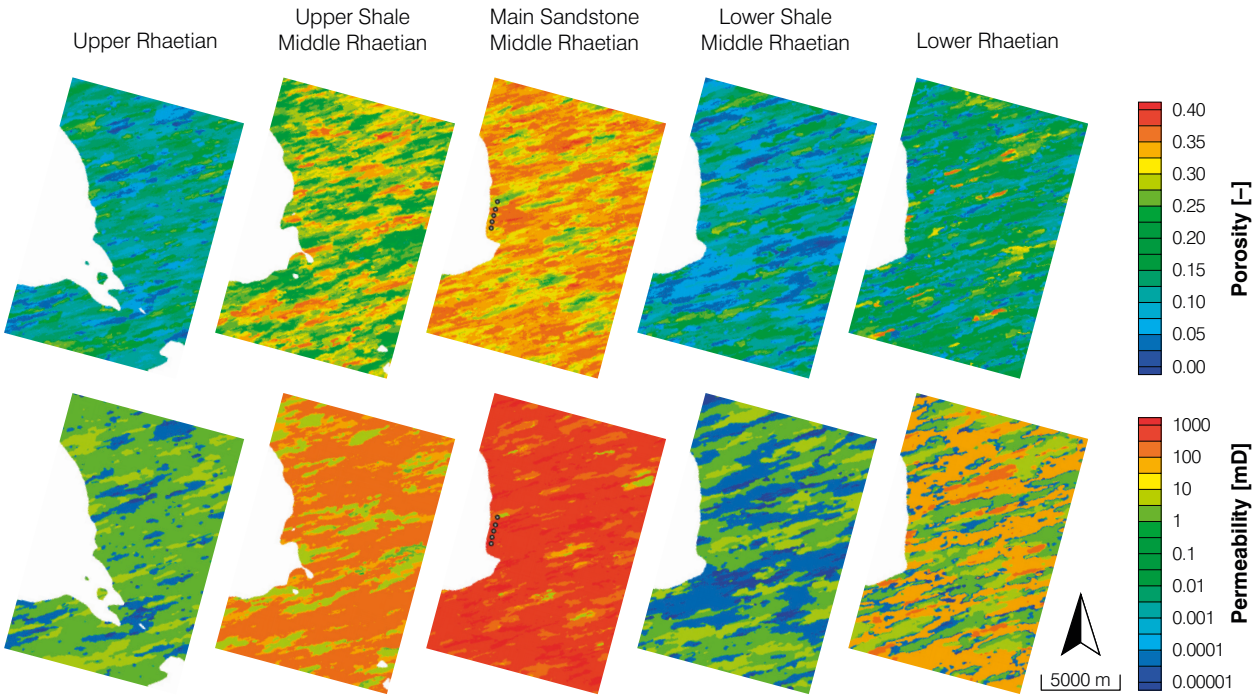

Fig. 5.1 *Vertically averaged porosity (top) and permeability (bottom) distribution of all sub-formations of the Rhaetian used in the scenario simulation.*

A potential storage site should provide a sufficient reservoir volume, competent sealing formations above and below the storage formation preventing gas migration into adjacent formations and a high intrinsic permeability to ensure well deliverability (Bennion et al. 2000). Due to the specific properties of H_2 gas it is prone to fingering. This quality makes a steeply dipping structure favourable (Paterson 1983).

Although the storage operation itself is hypothetical and represents a synthetic scenario, the storage site used in this analysis is based on an actual anticline structure located in Schleswig-Holstein, northern Germany. The anticline was formed by halokinesis of the Zechstein salts starting in the Triassic period (Baldschuhn et al. 2001). Hese (2012) proposed the deposits of the Middle Jurassic and the Lower Cretaceous as possible cap rocks and the Rhaetian sandstones of the Upper Triassic (Exter Formation) as a potential storage formation at this site for carbon dioxide storage. The Rhaetian deposits have already proven to be a reservoir formation suited for natural gas exploration in northwest Germany (Fahrion and Betz 1991).

The Rhaetian of North German Basin comprises the change from the non-marine environment of the Late Triassic to the marine environment of the Early Jurassic (Doornenbal and Stevenson 2010). The deposits consist of several distinct sandstone layers of varying thickness with intermediate shale layers (Gaupp 1991; Doornenbal and Stevenson 2010; Hese 2012).

The geological model created for this study is based on a regional structural model developed by (Hese 2012) into which the internal succession of Lower Rhaetian, lower shale of the Middle Rhaetian, main sandstone of the Middle Rhaetian, upper shale of the Middle Rhaetian and Upper Rhaetian are embedded (Fig. 4.1). The division of the Rhaetian into the sub-formations is based on facies descriptions given by Gaupp (1991) and Hese (2012). Of the sediments of the Middle Rhaetian, the Main Sandstone is the most favourable target formation for an underground gas storage operation, as it has a thickness of several meters and consist of middle to coarse grained, relatively pure quartzite (Fahrion and Betz 1991; Gaupp 1991; DSK 2005; Hese 2012).

Due to the halokinesis, early Cimmerian uplift and transgressional tectonics, the thickness of the sediments of the Upper Triassic varies throughout the North German Basin (Doornenbal and Stevenson 2010). As a result, the potential stor-

age represents a capped dome structure (Fig. 4.1 a, b). The depth of the Rhaetian base ranges from around 400 m at the top of the anticline structure to more than 3,000 m at the flanks. The shallower eastern flank of the anticline is chosen to accommodate the storage site.

The structural model of the storage site is used as a basis for a facies modelling, making use of both lateral and vertical trends, to obtain a heterogeneous set of parameters (see also Chapter 4.4, Tab. 4.1). The individual facies components clay, fine sand, medium sand and coarse sand were used to obtain the 25 equally likely heterogeneous parameter distributions of which one is used in this analysis (Fig. 5.1). Porosity and permeability ranges are available as on-site (Hese 2012) and off-site data from the North German Basin (Gaupp 1991). However, neither capillary pressure nor relative phase permeability data are openly accessible.

Due to the scarcity of detailed site specific data, necessary values like residual saturations, displacement pressures, maximum gas phase permeabilities and pore distribution indices are deduced from values typically found in literature for rocks of similar characteristics (e.g. Hildenbrand et al. 2002; Hildenbrand et al. 2004; Bachu and Bennion 2008; Wollenweber et al. 2010). For capillary pressure the standard Brooks & Corey formulation (Brooks and Corey 1946) is used. The capillary entry pressure data taken from literature has to be scaled to the phases used in the simulation. This is done using the Laplace equation (e.g. Helmig 1997) and assuming the rock to be water wet. The interfacial tension (IFT) depends on the component specific properties such as solubility, pressure and temperature (Schowalter 1979). Using the empirical formulation by Massoudi and King (1974) the IFT of H_2 and N_2 at 25 °C and 50 bars, which are fair approximations of the initial pressure and temperature in the reservoir, is 0.068 and 0.071 N/m, respectively. The similarity in the IFT of the two gas components results in comparable entry pressures under the given assumptions. Thus, the phase composition is not taken into account when calculating the capillary pressure data using the literature derived values given in Tab. 4.1. Relative phase permeabilities are determined using Corey-type equations by Burton et al. (2009).

5.4 Storage simulation setup

For simulation of the storage operation, the developed facies model is transferred to a simulation model using a spatial discretisation of 50 x 50 m in lateral direction. Each sub-formation is vertically discretised using a constant number of layers, with cell thickness varying from 0.2 to over 5 m. The storage operation is simulated using five wells, labelled 1 to 5 from north to south, placed near the top of the structure (Fig. 4.1, 5.5). Preliminary simulations on homogeneous models indicated that the formation thickness should be greater than 12 m in order to achieve the target well deliverability. Thus, the wells are completed over the whole formation thickness and are placed at the shallowest depth possible while still providing sufficient reservoir thickness.

Since the scenario used in this study is based on a saline aquifer with no initial gas present, the storage has to be initialised by filling it with cushion gas. Due to the high costs when H_2 is used as cushion gas, N_2 is used as it can be considered a cheaper alternative due to its great abundance in the geosphere. Additionally, N_2 is relatively inert to chemical reactions (Oldenburg 2003; Oldenburg and Pan 2013). Fluid properties such as density and viscosity are calculated during runtime using a generalised formulation of the Peng-Robinson equation of state (Schlumberger 2015). With the parameters used in this study (Tab. 4.2), the densities obtained for reservoir conditions are within 1.9 % and 1.3 % of the values given in Lemmon et al. (2016) for H_2 and N_2, respectively. Viscosity values for H_2 and N_2 deviate by up to 13.9 % and 1.9 % from those given in Lemmon et al. (2016), respectively. However, these values are still within the uncertainty range given in Lemmon et al. (2016), which are 15 % for H_2 and 2 % N_2. The multiphase-multicomponent simulation code Eclipse E300 (© Schlumberger) is used in this study. Diffusion within the gas phase is neglected while gas dissolution in the connate water is included in the simulation. Prior to injection, a hydrostatic pressure distribution is assumed throughout the simulation area. The northern, eastern and southern boundaries are assumed open by adding an infinite boundary pore volume and thus maintaining the initial hydrostatic pressure throughout the simulation run. The western

model boundary is assumed to be closed due to the fault system in the centre of the model domain. The caprocks above the Rhaetian deposits are assumed to be tight against the stored H_2 and N_2 and are thus represented in the simulation as a no-flow boundary.

The storage operation can be split into three stages, the injection of N_2 used as part of the cushion gas, the initial filling of the storage with the working gas (H_2) and the actual storage operation during which the H_2 gas is extracted and injected. The target injection and withdrawal rates for the individual storage phases were set based on preliminary injection and withdrawal tests based on homogeneous parametrizations. The first stage of the storage operation, the filling with the nitrogen gas, is carried out over a period of 710 days with a target injection rate of 55 625 sm^3/d/well. The target injection rate for the initial H_2 injection is 155 000 sm^3/d/well for a period of 210 days. The third stage comprises of six storage cycles. Based on the conducted energy demand analysis, the duration of the production or withdrawal period of each storage cycle is one week. The target withdrawal rate is set to 1 000 000 sm^3/d/well. Thus, under ideal conditions the dimensioning of the storage should be sufficient to meet around 27 % of the defined total storage demand of 129 million sm^3 H_2 gas required per week. This assumes that more than one storage site will be employed to balance the fluctuating power generation by renewable sources. However, this site storage capacity could be increased by adding more wells. The storage is replenished for 50 days at a target rate of 150 000 sm^3/d/well after a single day shut-in subsequent to each withdrawal period. The next storage cycle follows after an additional shut-in period of 30 days, resulting in one withdrawal phase every three months.

The initial hydrostatic bottom hole pressures (BHP) are calculated at 50.5, 49.3, 49, 47.5 and 48.6 bars with the uppermost connections being at a depth of 493, 481, 479, 463 and 474 m at wells 1 through 5, respectively. Determining accurate overpressure limits requires in-depth knowledge on the local stress state. Röckel and Lempp (2003) estimated the minimum horizontal stress gradient in the North German Basin (NGB) to be within 15 to 20 MPa/km for sediments above the Zechstein, which applies to the study site. This would allow for a pressure increase of 19 or 45 bars over the initial BHP at well 4 using the smaller and larger stress gradient. The average maximum pressure gradient in porous media gas storages in Germany is 16.8 MPa/km (Sedlacek 1999), corresponding to an allowable pressure increase of 30.3 bars over the initial BHP at the shallowest well 4. As no detailed site specific data is available, the maximum and minimum allowable BHPs are set to 65 and 30 bars in all wells. The maximum allowable pressure increase in the shallowest well 4 is thus 17.5 bars. The specified upper BHP limit corresponds to the minimum horizontal stress at the reference depth of well 4 as calculated using the lower estimate of the gradient given by Röckel and Lempp (2003) and 84 % of the average limit given by Sedlacek (1999), providing a conservative estimate. For the other wells, the given gradients allow a greater overpressure due to the greater depths of the wells, which consequently results in lower fractions being used as the BHP limits are applied uniformly for all wells. In case of a violation of the BHP limits, the flow rate of the individual well is automatically adapted by the simulator until the pressure is within the specified range. Skin effects on the well flow rates are neglected in this work.

5.5 Storage simulation results

The gas injections in the first two storage phases, from herein referred to as the storage initialization, comprising of the N_2 injection and the initial fill with H_2, result in increased fluid pressures within the storage formation. The overpressure signal spreads into the reservoir formation with a nearly concentric pattern (Fig. 5.2). Only in the area of reduced permeability north of well 1 a slightly smaller pressure change is observed. Due to the lower density of both gas components compared to the formation water, the gas accumulates in the top of the structure (Fig. 5.3, 5.5). However, the gas phase distribution is greatly affected by the reservoir heterogeneity. Especially around well 1 and the centre well 3 only low average gas saturations are achieved. While the N_2 gas is relatively far spread reaching up to 2 km from the storage wells, the H_2 is more concentrated around the wells (Fig. 5.3). Throughout the storage initialisation all wells are constantly operating at the upper

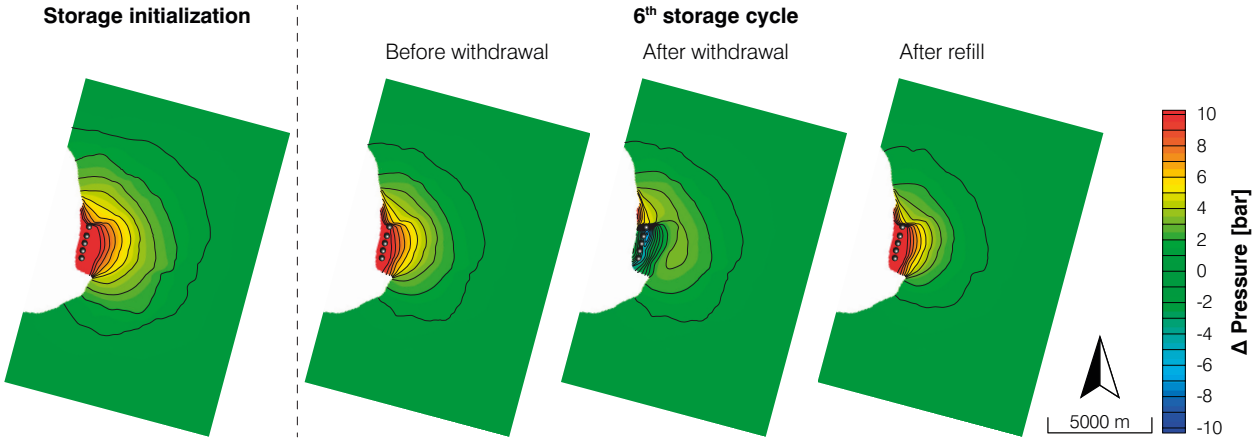

Fig. 5.2 Pressure change observed in the middle plane of the reservoir formation, the Main Sandstone of the Middle Rhaetian, after the storage initialization (t=920 days) and during the sixth and last storage cycle (t=1361, 1369 and 1419 days respectively). The black lines depict one bar increments.

BHP limit. As a consequence, the injection rates are reduced, which in turn results in less gas being injected overall (Tab. 5.1). In total only 43.3 % of the designated N_2 volume and 14.6 % of the H_2 volume are injected into the storage formation and thus available prior to the first withdrawal period. During an actual field deployment where well flow data would be available the injection periods would be extended as a consequence of the reduced well flow rates. However, for the sake of future comparison with other realisations, the simulation was continued as planned.

The low H_2 gas volume strongly affects the first withdrawal period that follows directly after the storage initialization, as the withdrawal results in strong pressure drops in some of the wells. The lower BHP limit of 30 bars is reached in well 1 within the first day of the withdrawal period at 922 days into the simulation run and remains at this level throughout this withdrawal phase until day 929 (Fig. 5.4). Consequently, the gas flow rate in this well is reduced to around 250 000 sm^3/d. Different to that, the target rate of 1 000 000 sm^3/d/well is achieved in wells 2, 4 and 5 throughout the withdrawal period as the BHP stays above the lower limit in these wells (Fig. 5.4). The target flow rate is also achieved in well 3 during most of this period. However, in the last time step of the withdrawal period the BHP reaches the lower limit and thus the well flow rate is reduced slightly to about 970 000 sm^3/d. During the first withdrawal period a total of 3839 m^3 of formation water is produced together with the gas in the five storage wells. The highest water fraction is obtained in well 3 with just over 0.03 %. In the following short shut-in period of one day the BHP of all wells quickly rebounds to the local reservoir pressure, which is affected by the permeability and the element volume, of about 45 bars and increases slowly from there onwards to a level close to the initial value of the hydrostatic equilibrium.

The composition of the produced gas phase varies during the following withdrawal period with high fractions of H_2 in the produced gas in in the beginning and lower values due to an insufficient volume of H_2 towards the end (data not shown). However, as the withdrawal rates also vary with time, volume averaged fractions are more representative. The lowest volume averaged H_2 fraction in the produced gas phase during the first withdrawal period is reached in well 1 with just slightly more than 33 % while the highest fraction of 60 % is reached in well 4. 54 %, 35 % and 42 % are achieved in wells 2, 3 and 5, respectively. Thus, despite the high withdrawal rates during the first cycle only a total of 14.48 million sm^3 H_2, corresponding to 92 100 GJ of electrical energy after re-electrification is withdrawn. Compared to the defined target amount of 35 million sm^3 this is less than half the envisaged value.

During the subsequent injection phase from day 930 to 980, in which the storage is replenished in H_2, the BHPs of the wells rise again, ultimately reaching the upper limit in all five wells. Different to the storage initialization, the achieved flow rates are equal to the target of 155 000 sm^3/d

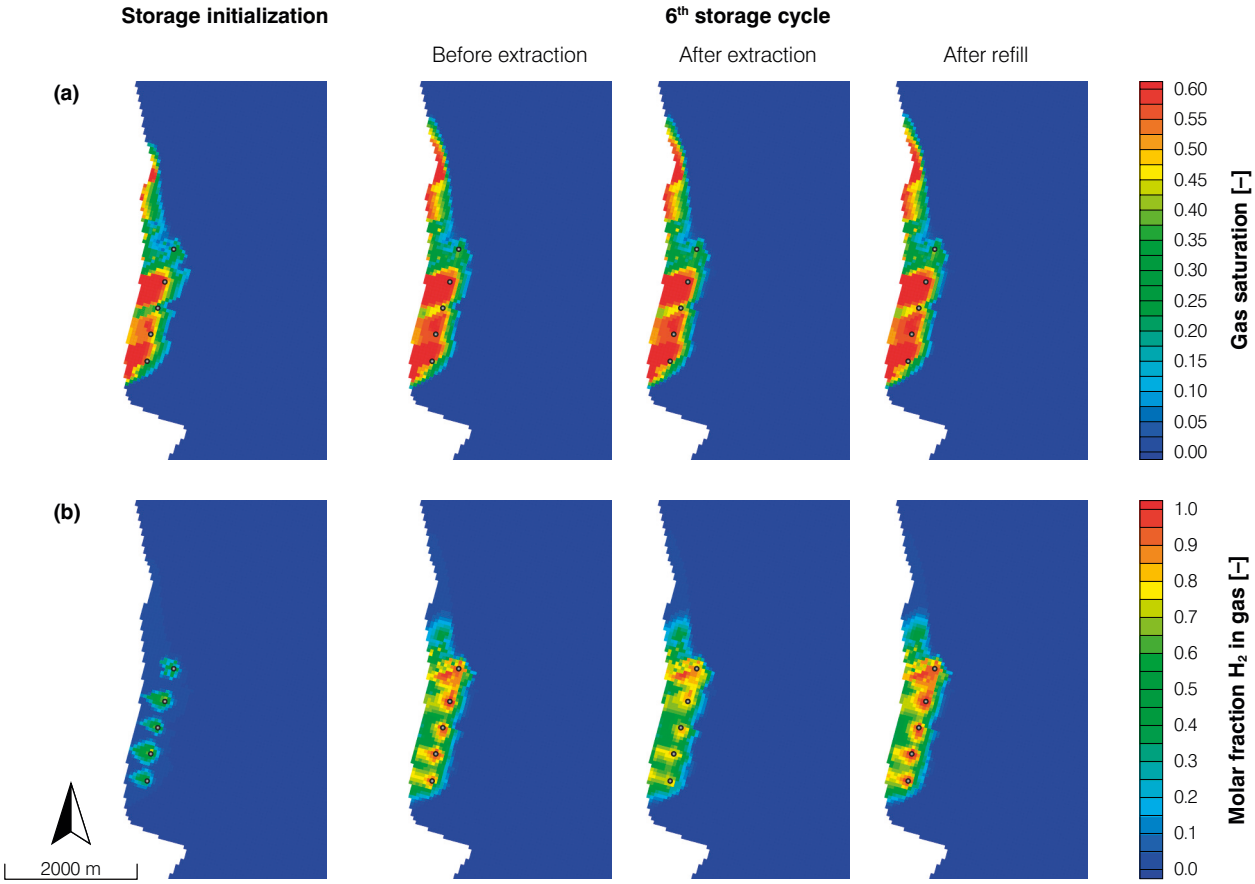

Fig. 5.3 (a) Vertically averaged gas phase saturations and (b) molar fractions of H_2 in the gas phase after the storage initialization (t=920 days) and during the sixth and last storage cycle (t=1361, 1369 and 1419 days respectively).

throughout most of the injection period. Only during the last 10 to 15 days the flow rates are reduced (Fig. 5.4). Thus, the amount of H_2 in place for the second storage cycle is considerably larger compared to the first cycle (Tab. 5.1). Clearly the pressure decrease caused by the prior withdrawal is beneficial for the refill phase. In the following shut-in phase from 980 to 1010 days, the BHP again quickly adapts to the local reservoir pressure. However, the pressure change of just around 1 bar is small compared to the pressure change observed after the first withdrawal period. Following this, the pressure slowly declines further towards the initial hydrostatic pressure level.

As slightly more H_2 is injected in each cycle compared to the volume of gas extracted during the subsequent withdrawal phase, the volume of gas in place increases with time. In the sixth and last simulated storage cycle, the amount of H_2 in place prior to withdrawal has increased by a factor of about 3.6 while the N_2 in place is reduced to around half of the initial value prior to the first storage cycle (Tab. 5.1, Fig. 5.3). Consequently, the target injection and withdrawal rates are matched in the subsequent storage cycles in most wells while BHP stays within the specified margin. Only in well 1 the BHP reaches the limits which consequently results in a reduction in flow rate (Fig. 5.4).

Interestingly well 1 shows the highest fraction of H_2 in the produced gas phase from the second cycle onwards reaching slightly more than 96 % while all other wells stay below 90 % until the end of the sixth cycle. This can most likely be attributed to the strong pressure reduction in the vicinity of this well during the first withdrawal period which subsequently helped with the distribution of the H_2 gas during the storage refill. The increased total gas in place, the larger H_2 fraction and a better distribution of the H_2 around the injection wells (Fig. 5.3) result in both increased well flow rates (Fig. 5.4) and increased storage performance regarding the extracted energy (Tab. 5.1). The vol-

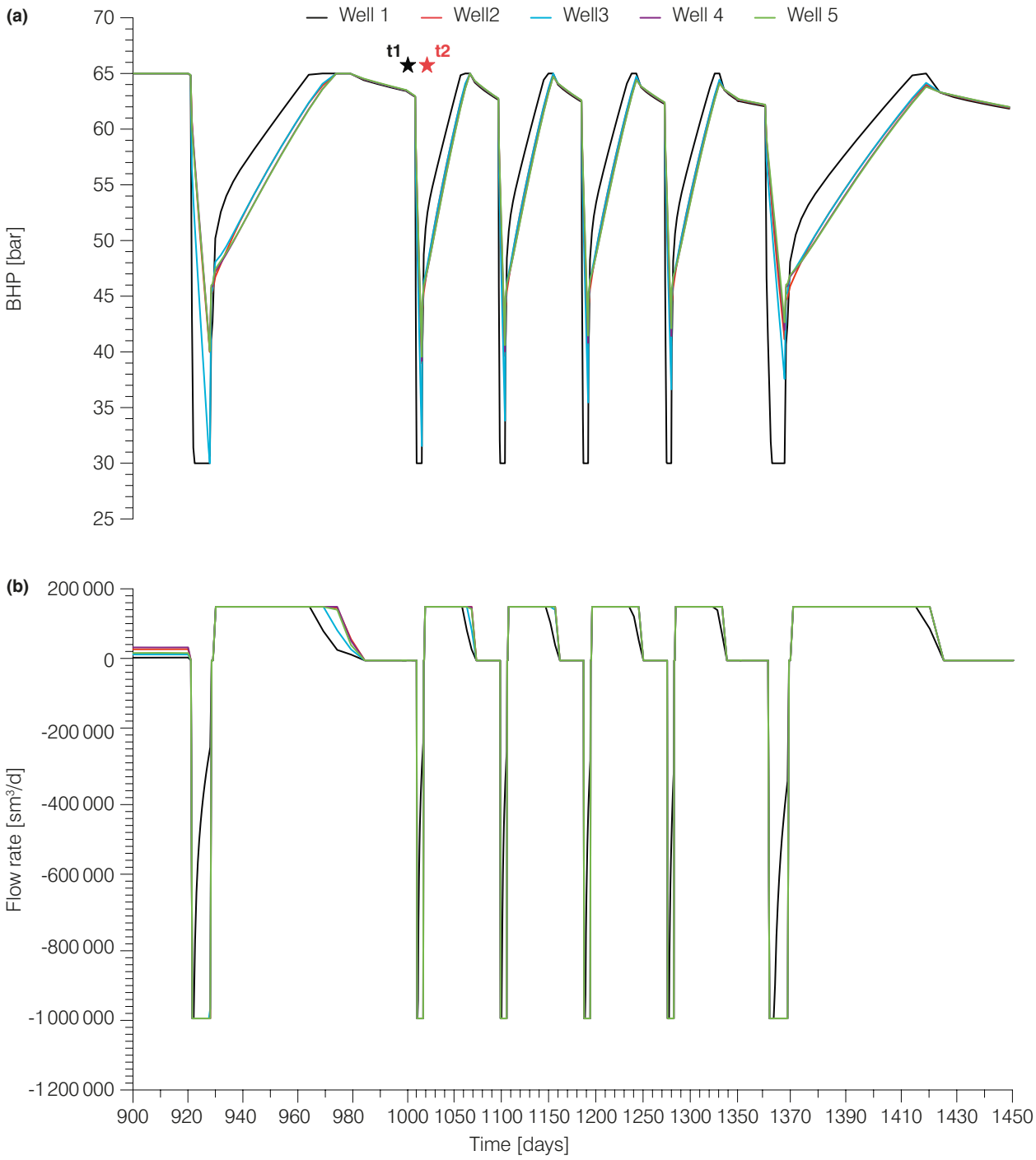

Fig. 5.4 (a) Down-hole pressures and (b) achieved gas flow rates for all wells during the third storage phase, the cyclic storage operation. The first and the last storage cycles are enlarged. Stars mark the times at which the acoustic FWI (t1), ERT (t1) and gravity mapping (t1 & t2) is conducted.

ume of retrieved H_2 in the sixth storage cycle is just over 29 million sm^3, equivalent to slightly more than 186 000 GJ of usable energy. Thus, the storage is capable of supplying around 22 % of the weekly energy demand defined in this scenario, which is slightly less than the predicted target of 27 %. The amount of H_2 trapped in the connate formation water due to dissolution increases with time. At the end of the simulation after about 4 years, the amount of dissolved H_2 is 141 tonnes, which is 1.75 % of the total H_2 present in the storage formation at the time.

Tab. 5.1 Results from the reservoir storage simulation for all six storage cycles. The equivalent energy is calculated assuming a 60 % efficiency of the re-electrification process.

Cycle	N_2 in place prior to withdrawal [sm^3]	H_2 in place prior to withdrawal [sm^3]	Av. gas withdrawal rate of storage [sm^3/d]	H_2 volume produced during withdrawal [sm^3]	Equivalent energy [GJ]
1	85 454 583	23 747 448	-4 512 524	14 482 659	92 110
2	68 349 573	42 708 131	-4 532 791	22 479 262	142 968
3	59 099 301	56 443 314	-4 579 213	25 451 249	161 870
4	52 496 061	67 689 265	-4 616 181	27 176 777	172 844
5	47 359 570	77 410 498	-4 650 400	28 407 313	180 671
6	43 214 081	86 065 805	-4 682 632	29 359 126	186 724

The amount of produced water continuously decreases during the simulation with a total of 862 m^3 being produced in last storage cycle with the highest water fraction being 0.024 % in well 1.

Despite the displacement of large gas volumes during the storage operation, only little differences in the distribution of the gas phase can be observed between before and after a withdrawal or injection phase, although the distribution of the H_2 near the wells varies considerably (Fig. 5.3). The gas-water contact is relatively stable during the storage cycles, showing that the gas phase does not expand downwards on the slope of the anticline. However, gas phase densities change during a cycle by approximately 20 %. Thus, the storage operation is mainly conducted through gas expansion and compression and is therefore controlled by the compressibility of the gas phase. This is further supported by the obtained BHP data as the pressure change in the wells between injection and withdrawal decreases with time whereas the withdrawal rates increase or are maintained at the target value.

As a result of the open boundary conditions to three sides of the model domain, the overpressure within the formation decreases slightly with time (Fig. 5.2), while a small pocket of over-pressurized formation water and gas north of the well gallery is persistent throughout the simulation. This effect can again be attributed to the slightly lower permeability in the vicinity of well 1 (compare Fig. 5.1). The regional pressure response is underestimated because of the specified constant pressure boundary conditions. However, simulations conducted using boundary pore volumes representing an extension of the storage formation by 0, 10 and 25 km show that the pressures obtained within the storage site during operation varies by less than 1.1, 0.6 and 0.4 bar, respectively. This small effect of the chosen boundary volume can be attributed to the large compressibility of the H_2 gas phase. Well BHPs and consequently storage flow rates are also only slightly affected, with the flow rates being reduced by less 2 % when the boundary pore volume is set to represent a lateral extension of 10 km and less than 1 % if the extension is assumed to be 25 km.

The data gathered at the storage and observation wells such as down-hole pressures, temperatures, flow rates and gas composition can be used for the monitoring and control of the storage operation (Katz et al. 1959). In the case of an underground storage operation, frequent well monitoring is essential as the cyclic stress in combination with high withdrawal rates can cause formation damage around the storage wells that could reduce the deliverability. Data obtained during the frequent shut-in periods of the storage operation can be used to determine any change in the formation damage zone around the wells (Bary et al. 2002) and to infer the expected flow rate for a given pressure drop in each well. As not additional observation wells are included in the simulation and formation damage due to the storage operation is neglected, the BHP data obtained at the storage wells can only be used to infer the reservoir pressure during the shut-in phases as described previously (pressure rebounds in Fig. 5.4). In addition to such point data, geophysical monitoring techniques can provide detailed multi-dimensional information on the undergoing storage operation.

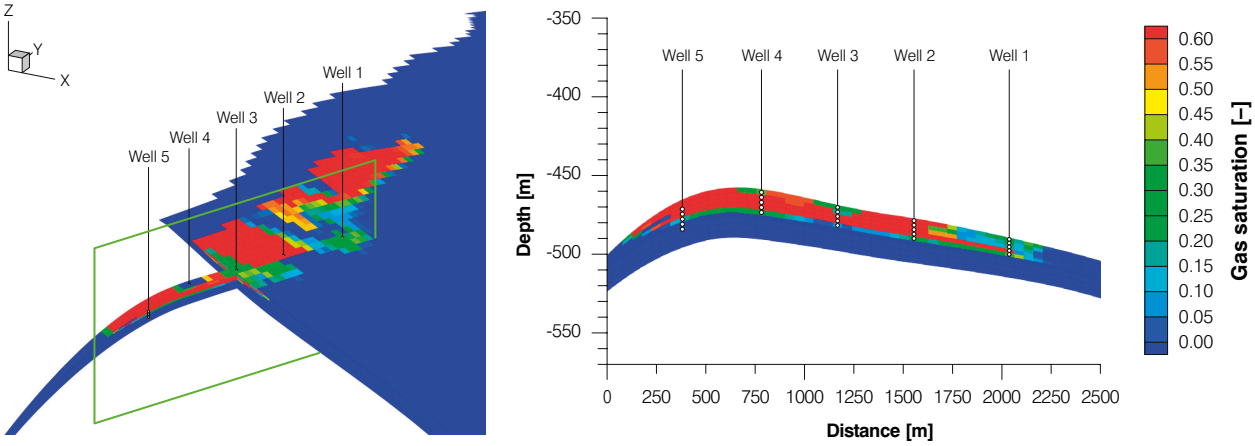

Fig. 5.5 Gas phase distribution in the model domain (left) and in a slice along the well gallery (right) before the second withdrawal period (t1=1009 days) which are used for the geophysical mapping modelling.

5.6 Geophysical monitoring

As mentioned before, geophysical methods of FWI, ERT and gravity can be applied to gas storage applications as the injected gas changes the electro-elastic properties and the density of the subsurface target in question. However, both gas components (N_2 and H_2) used in this work have similar influences on these properties of the system and thus may not be distinguished by neither the applied ERT nor FWI technique. As the overall gas phase distribution changes only slightly over the course of a storage cycle, the geophysical simulations are carried out predominately at one time step just before the second withdrawal period (t1, Fig. 5.4). Only the gravity modelling is also conducted right after the subsequent withdrawal period in order to test the methods ability to quantify the extracted gas volume (t2, Fig. 5.4).

5.6.1 Seismic FWI results

To estimate the impact of spatial gas saturation variations (Fig. 5.5) within the reservoir on the seismic wavefield, a P-wave velocity model (Fig. 5.6a) is derived via a petrophysical rock model. This consists of a Gassmann fluid substitution model (Gassmann 1951) assuming a patchy gas-distribution (Mavko and Mukerji 1998). The limited extension of the reservoir and small changes of the P-wave velocity with respect to the background model prohibit the application of a classical travel time based tomographic approach. Therefore, the proposed seismic mapping strategy is based on acoustic 2D FWI which can resolve structures down to approximately half of the seismic wavelength. The theoretical details of this approach are described in Asnaashari et al. (2015) and Al Hagrey et al. (2014). The frequency content of the excited seismic wavefield and consequently also the resolution of the FWI depends on the used acquisition geometry.

The monitoring boreholes in this study do not coincide with the injection wells and are significantly deeper in order to optimize ray coverage within the reservoir, signal-to-noise ratio and mitigate reduced resolution due to wavefront healing when applying high frequency seismic sources.

The resolution of two different acquisition geometries is tested. Acquisition geometry 1 consists of a walk-away Vertical-Seismic Profile (VSP) survey with 113 shot positions at the surface and 6 boreholes, each containing 41 multi-component receivers (Fig. 5.6). Due to the large distance from the surface to the receivers at reservoir level, the source signature is a band-limited spike wavelet with minimum and maximum frequencies of 5 Hz and 100 Hz, respectively.

Acquisition geometry 2 is based on a pure crosswell geometry. The acoustic wavefield is excited by 102 shots distributed in two boreholes and recorded by 50 multi-component receivers

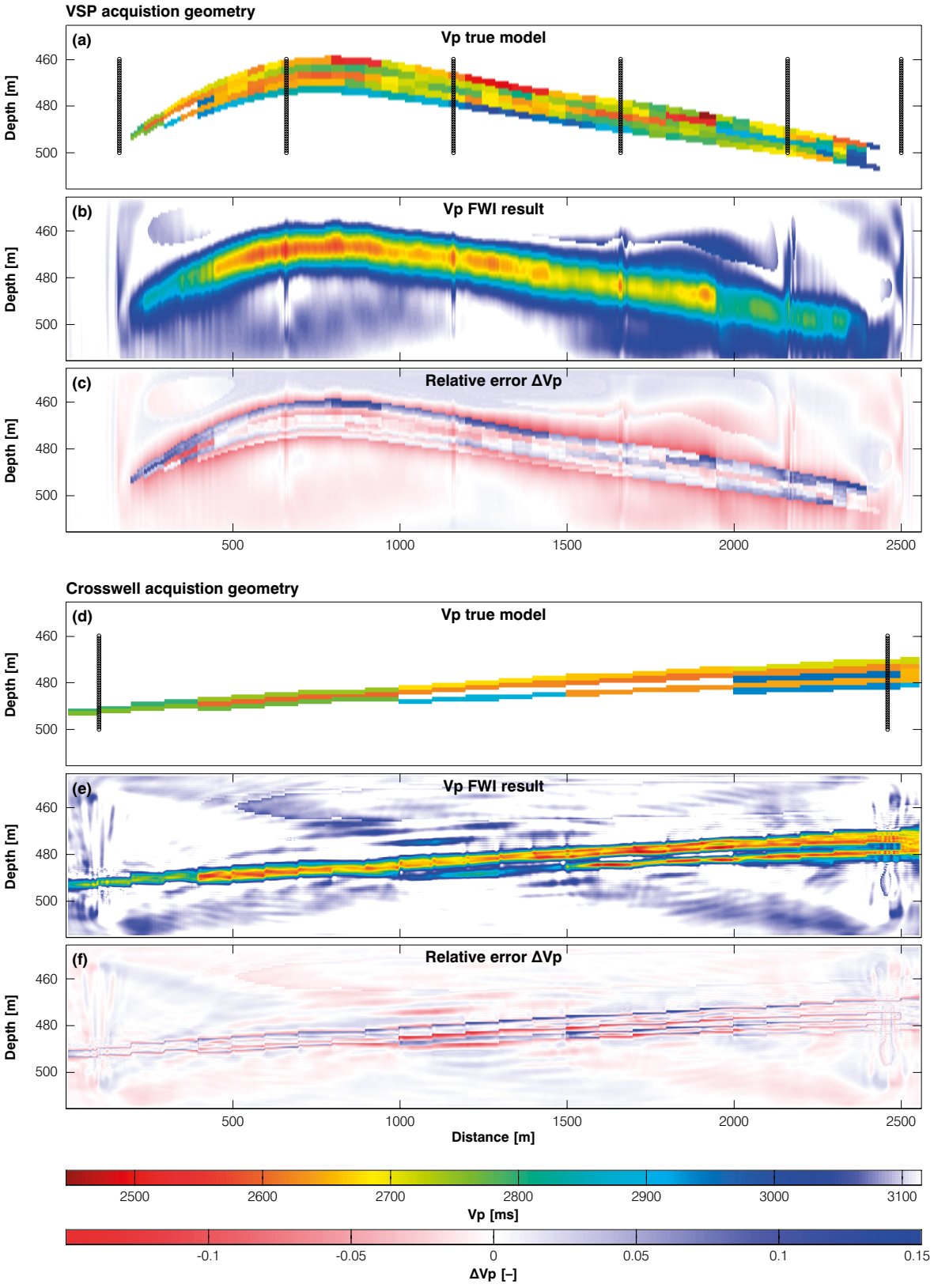

*Fig. 5.6 Comparison between the FWI mapping results, true P-wave velocity model Vp and relative error ΔVp for the H_2 storage formation using the VSP acquisition geometry (**a**)-(**c**) and crosswell acquisition geometry (**d**)-(**f**), respectively. Black dots denote receiver positions.*

in each borehole. Compared to acquisition geometry 1 the source-receiver distance in the pure crosswell geometry is much smaller and therefore a source wavelet covering minimum and maximum frequencies of 100 Hz and 1000 Hz, respectively, can be applied.

The propagation of the acoustic wavefield is modelled by a time-domain finite-difference scheme. The initial model for the FWI is a homogeneous half-space with Vp assumed as 3115 m/s and density being 2650 kg/m^3. To reduce the non-linearity of the multi-parameter inversion problem a sequential FWI approach of low-pass filtered data with different maximum frequencies of 25 Hz, 50 Hz and 100 Hz for acquisition geometry 1 and 250 Hz, 500 Hz and 1000 Hz for acquisition geometry 2 is applied, respectively. Furthermore, only the waveforms of the first arrivals are inverted by applying a time-window. The models for P-wave velocity and density are simultaneously improved. The P-wave velocity inversion result using the VSP geometry (Fig. 5.6 b) generally recovers the shape of the gas reservoir, however details of the P-wave velocity model cannot be resolved due to the lack of frequencies larger than 100 Hz in the seismic data. To quantify the error between true model Vp_{true} and FWI result Vp_{FWI}, we calculate the relative error ΔV_p via $\Delta V_p=(V_{p\,FWI}-Vp_{true})/Vp_{true}$

In case of the VSP geometry the relative error (Fig. 5.6 c) varies between ± 15 % and maximum errors occur at the boundaries of the gas body, while the average absolute ΔVp is 2 %. To improve the FWI mapping resolution, crosswell acquisition geometry 2 is applied. Due to the higher maximum frequencies in the recorded seismic data compared to acquisition geometry 1, the FWI result (Fig. 5.6 e) shows detailed changes of the P-wave velocity within the reservoir down to a size of roughly 2 m when compared with the true model (Fig. 5.6 d). The relative error (Fig. 5.6 f) still varies between ± 15 %, however these errors only occur at the sharp boundaries of the gas phase, which cannot be perfectly resolved by the FWI. Within the reservoir the error drops down to roughly ± 5 % and the average absolute ΔVp to 1 %, a significant improvement compared to the result estimated by the VSP acquisition geometry.

5.6.2 ERT results

Similar to the FWI, the ERT modelling starts with transforming the results from the flow simulation model (Fig. 5.4) into a geoelectric resistivity model (initial or input model ρ_{input}, Fig. 5.7 a) by applying an almost realistic parametrisation with hydrogeological and petrophysical values prevailing at the study site of the NGB (al Hagrey et al. 2014). The bulk resistivity (ρ) model is derived from the Archie equation for the sandstone reservoir and from subsurface data for the other formations (Archie 1942; al Hagrey et al. 2014).

Synthetic datasets are acquired using optimized electrode arrays with electrodes placed in boreholes at 10 m spacing within the depth range of the storage targets (caprock, reservoir and base layer), being 300 to 660 m (e.g. Loke et al. 2003; al Hagrey 2012). Optimized electrode configurations that maximize the resolution of survey results were found using a sensitivity analysis (e.g. McGillivray and Oldenburg 1990; Stummer et al. 2004). Optimized data sets of practical sizes (up to < 20 000 data points), which are nearly 2 % the comprehensive data set (of the highest possible resolution) but with almost similar results as the comprehensive set, are generated.

A 2.5D forward and inverse ERT modelling is carried out using the modern codes of RES2DMOD and RES2DINVx64 (e.g. Loke et al. 2003). The forward modelling code is applied to generate a synthetic dataset of 0.6 % average simulation error. ERT data are inverted once by including no constrains and once by incorporating mapping results of the subsurface to minimize the ambiguity problems of the non-unique solution (e.g. al Hagrey et al. 2013). These mapping results are usually known from other (e.g. seismic data) and baseline surveys. Constrained inversions are conducted once by incorporating boundaries and once by fixing resistivity regions. In both cases these constrains are applied outside of the reservoir layer with the unknown target of gas distributions.

Resulting inversion resistivity models (ρ_{output}) clearly resolve the thin resistive anomaly of both gas components (H_2 and N_2) within the conductive brine reservoir and the heterogeneous geologic setting (Fig. 5.7 b–d). The reliability of

the reconstructed ERT tomograms is evaluated quantitatively by calculating the relative model resistivity difference (residual misfit Δρ) by: $\Delta\rho=(\rho_{output}-\rho_{input})/\rho_{input}$

Resulting (inverse) misfit residuals Δρ (Fig. 5.7 e–g) express quantitatively the resolution of the applied technique for both of the spatial mapping capability and the recovering resistivity amplitude. Absolute misfit Δρ values are distributed mostly inside the thin gas layer and nearly zero outside it, indicating the dominance of the inaccuracy caused by this layer. The resolution (inverse Δρ) is least for the unconstrained case, intermediate when incorporating boundaries and best when fixing the resistivity region model, their average absolute Δρ value approaching 0.29, 0.14 and 0.08, respectively. The resolution of the resistive gas layer in such conductive media is governed by the equivalence of transverse resistance (ρh=constant, h= layer thickness), where the smearing effect blurs boundaries and increases the thickness on expenses of the amplitude (e.g. Day-Lewis et al. 2005). However, all these problems could be minimized here by applying the ERT technique of optimized data acquisitions and constrained inversions (e.g. al Hagrey et al. 2013).

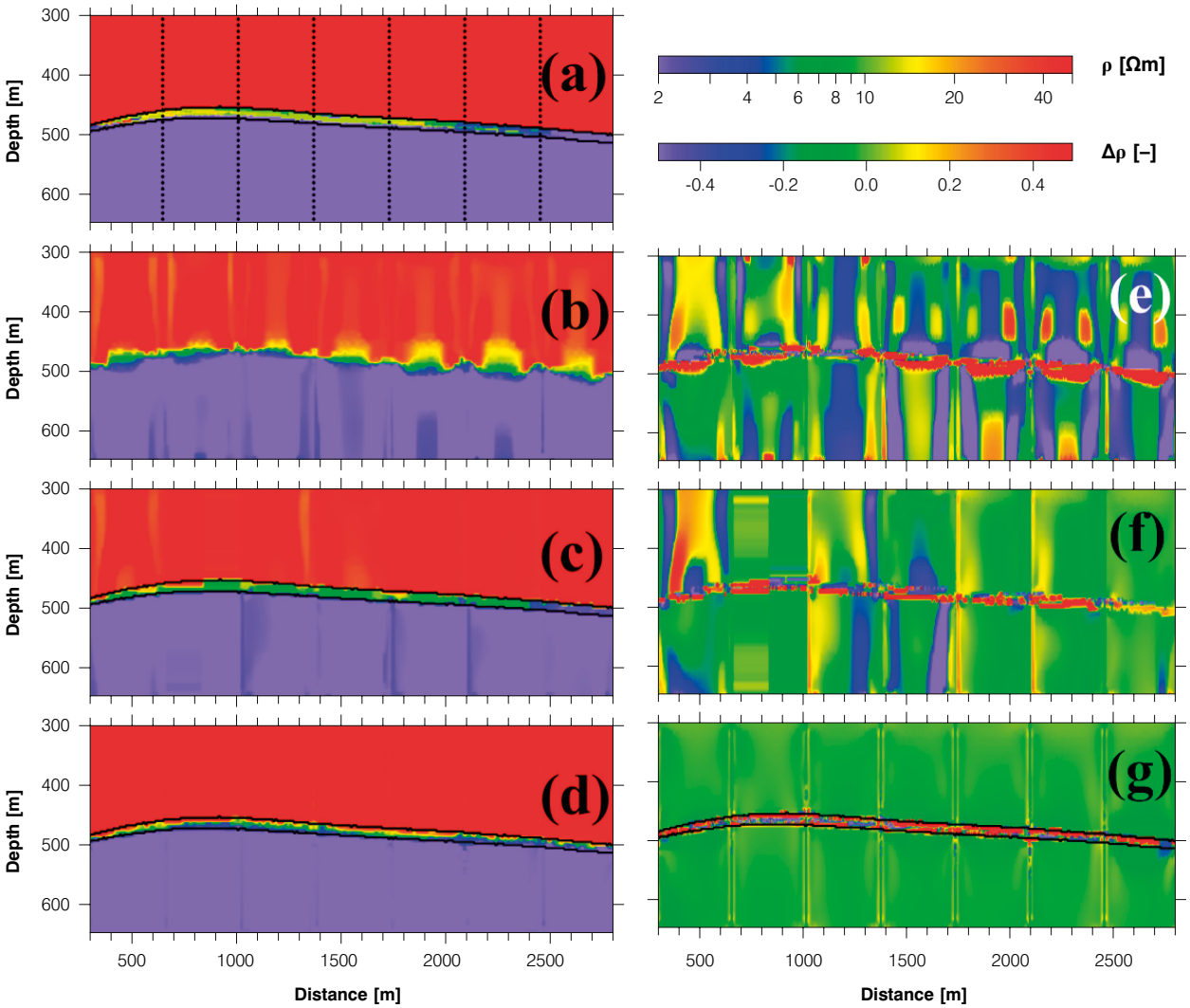

*Fig. 5.7 ERT mapping results for the simulated H_2 storage site. Shown is the input (**a**), inverted output models without constrains (**b**) with constraints in form of incorporated boundaries (**c**) and resistivity regions (**d**) outside the reservoir and the misfits Δρ corresponding to the output models (**e-g**). Black dots denote borehole electrodes.*

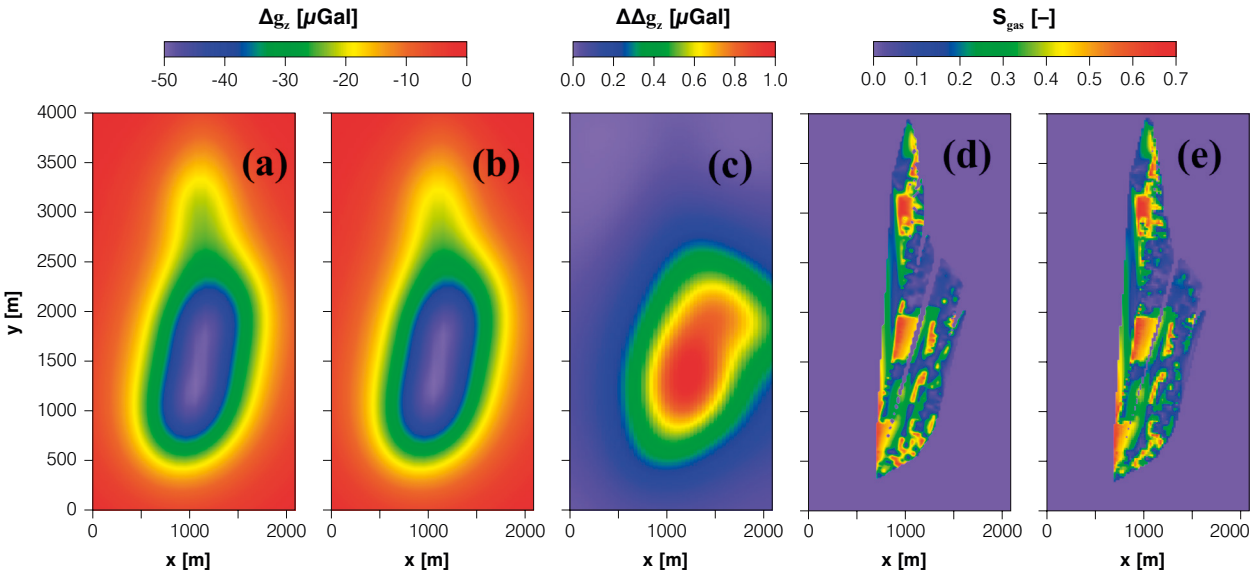

*Fig. 5.8 Results of 3D gravity modelling showing anomalies of the vertical component ([Δg]z) for the reservoir filled with (**a**) N_2 and H_2 (**b**) and after the gas withdrawal and (**c**) as their difference ([ΔΔg]z). For the purpose of comparison, the distribution of average gas saturations before (**d**) and after (**e**) the withdrawal period are projected on the corresponding xy-plane.*

5.6.3 Gravity results

For conducting the 3D gravity modelling, the two results of the reservoir flow simulation corresponding to the storage state before (t1) and after withdrawal (t2) in the second storage cycle are transformed into 3D density models using a realistic parametrisation for the study site based on data from the North German Basin (e.g. Baldschuhn et al. 2001; Hese 2012).

The gravity modelling aims at studying the sensitivity of the technique to distinguish the gas components and monitor the temporal variation due to the gas withdrawal and subsequent H_2 injections. Injecting H_2 or N_2 into a saline reservoir displaces the initially present pore water, resulting in a drop of the bulk density, which in turn causes a decrease in the gravity components and gradients. In this study the software IGMAS+ (Interactive Gravity and Magnetic Application System) designed for 3D gravity, gravity gradient and magnetic modelling is used (e.g. Götze and Lahmeyer 1988; Schmidt et al. 2011).

The gravity field components (g_x, g_y and g_z) and gradients (g_{zx}, g_{zy} and g_{zz}) and their residual anomalies (Δg_x, Δg_y and Δg_z) are calculated before and after the gas withdrawal. For an easier visualization, only the vertical component Δg_z maps at the surface reflecting the strongest anomalies as a result of the gas presence are shown.

The negative Δg_z anomalies relative to the background show a high sensitivity of the applied gravity technique to the gas storage operation (Fig. 5.8). All gravity anomalies Δg_z which result from the first H_2 re-injection and the subsequent gas withdrawal of the second storage cycle (Fig. 5.4) are well resolvable with amplitudes approaching 50 and 49 μGal, respectively (Fig. 5.8 a, b). However, their difference ($\Delta\Delta g_z$) of 1 μGal is unresolvable (immeasurable) by modern micro-gravimeters , which have accuracies of ±3-5 μGal (Fig. 5.8 c).

Consequently, this implies that the amount of extracted H_2 from the storage should be more than 3 times the applied value in this study for the method being able to distinguish between the individual gas components. Injections of H_2 into the N_2 phase in the reservoir increases the gas saturation and gas pressure in some regions slightly on the expenses of the pore water. However, the small quantities of H_2 cause only a small density contrast and thus a negligible gravity anomaly. In all cases, the gravity anomalies should be free from any other short-term temporal effects occurring within the operation cycles, e.g. abrupt fluctuations of the groundwater table.

5.7 Conclusions

Porous media H_2 storage is discussed as a viable option for long term and large scale energy storage. To evaluate the applicability of seismic, geoelectric and gravimetric monitoring techniques a realistically parametrised scenario simulation is carried out. The achieved delivery rate of H_2 was set in context with the average power demand of the state of Schleswig-Holstein, Northern Germany, which corresponds to about 2.8 million people. The site used for the simulation is based on an actual geological structure found in Northern Germany and parametrised using a facies modelling approach, that resulted in a strongly heterogeneous and realistic parameter distribution.

The storage simulation consists of three main phases, namely the cushion gas injection utilizing N_2, the initial filling of the reservoir with the working gas H_2 and the cyclic storage operation. All storage operations were carried out using five wells located at the top of the structure. Each withdrawal period in the storage phase is followed by a short shut-in period of 1 day, a refill period of 50 days and another shut-in period of 30 days. The operational mode of the storage wells alternates between withdrawal and injection with the intermediate shut-in periods representing short hiatuses associated with the switching of the flow regime. Prediction of the availability of renewable power production is possible for several days in advance (e.g. Foley et al. 2012), thus changes in the operating mode of a well can be anticipated up to a few days, which can be assumed to be sufficient time for the corresponding changes in well operation. Alternatively, dedicated injection and withdrawal wells could be used either in an alternating operating pattern as described or in a continuous operating pattern, i.e. a continuous injection and withdrawal, to cope with varying demand and supply. While this set-up is technically possible, it is uneconomical due to the larger numbers of wells required and because a direct use of H_2 without intermediate storage is more efficient.

Based on preliminary simulations using homogeneous parametrisations the target withdrawal and injection rates were set to 1 000 000 sm^3/d/well and 155 000 sm^3/d/well, respectively. It was found that the storage performance was initially poor due to the lower than expected H_2 gas volume in place but increased with the number of storage cycles as more H_2 was available. In the final storage cycle a total of 29 million sm^3 of H_2, equivalent to 186 000 GJ or around 51 667 MWh of power could be extracted. The storage site is therefore capable of supplying around 22 % of the weekly demand defined in this study, which is slightly less than the predicted 27 % because of gas impurities. It can be expected that performance of the simulated storage will increase further, ultimately topping out at the target of 35 million sm^3 of H_2, corresponding to 222 600 GJ (61 833 MWh) of power, if more storage cycles are simulated.

As discussed in Chapter 4.5.3 and 4.5.4, the deliverability of the storage site could be increased by either increasing the well flow rates or increasing the number of wells, both of which effectively enlarge the storage. As shown in Chapter 4.5.4, horizontal wells could be used instead of vertical wells to increase the individual well screen length, which would reduce the pressure drop around the wells associated with a given withdrawal or injection rate and thus allow for higher production or injection rates. The loss of H_2 due to dissolution in the connate water increases with the simulation time, ultimately being 141 tonnes after 4 years, which equates to 1.75 % of the total H_2 in the storage formation at the end of the simulation. This effect will abate with time, as pore waters equalize with the gas phase. Thus, the simulated porous media H_2 storage site is indeed a viable option for mitigating shortages in power production as defined in the usage scenario. However, geochemical reactions, which are not considered in the simulation, could limit the applicability of such an operation due to i.e. corrosive H_2S gas being produced.

Diffusion processes will also effect an H_2 storage, either due to loss of H_2 into the caprock through diffusion in the water phase, or if a separate cushion gas is used as in this study, through mixing by diffusion with the cushion gas. As the diffusion length is estimated at 2 m during a storage cycle, this effects is not represented in the simulations.

Due to the specified boundary conditions for the fluid flow the pressure build up in the far-field is underestimated in this simulation. Thus, for a more realistic assessment of the induced hydrau-

lic effects the simulations presented in Chapter 4.4 and 4.5 should be referred to. However, the boundary conditions specified in this simulation do not affect the pressure in the storage or the performance significantly.

In addition to down-hole pressure and temperature monitoring, integrative geophysical approaches, namely FWI, ERT and gravity methods can be employed for a site monitoring concept, depending on their individual capabilities in detecting changes in the gas inventory. Subject to the used acquisition geometry, the acoustic FWI can resolve P-wave velocity and subsequently gas saturation variations within the storage reservoir to a varying extent. A surface seismic walk-away VSP geometry is limited in the frequency content to 100 Hz, maximum. Theoretically, the FWI can resolve structures down to approximately half of the minimum wavelength. Assuming an average P-wave velocity of 2700 m/s within the reservoir, the VSP geometry can only resolve the general shape of the gas phase down to the size of 14 m, but no internal structures.

For a more detailed resolution of flow-paths and the gas phase distribution, a crosswell geometry with maximum frequencies of 1000 Hz in the seismic data is required, capable to resolve approximately 1.4 m features in size. While the theoretical resolution of the crosswell is much better than the VSP geometry, the acquisition of high quality data with a high signal-to-noise ratio is challenging and expensive due to the required small separation between the monitoring boreholes. Beside gas saturation and - density, the pore pressure can have a significant impact on the seismic P-wave velocity variations. In this study, these effects are not incorporated into the rock-model. Consequently, the amplitudes of the resulting seismic velocity anomalies in the real field application might be larger and easier to detect by seismic FWI. Furthermore, the highly-resolved structures derived from FWI can be used to constrain the ERT inversion.

The resulting geoelectric mapping resolution is comparable with that of the applied seismic method. Employing optimized data acquisitions and constrained inversions in the ERT technique minimizes the interpretation ambiguity and thus further enhances the mapping resolution. The inaccuracy of the FWI technique expressed by the relative misfit distribution is less than that of the ERT technique but both errors are still within a reasonable low range. Distinguishing the H_2 from the N_2 is practically impossible with both FWI and ERT techniques due to the similar influences on the electro-elastic properties by both gas components. Using the FWI or ERT techniques to quantify changes in the gas inventory because of the storage operation is not possible, as the volume change of the gas phase in the storage due to injection or withdrawal is not large enough for a detection with these methods.

The difference in mass contrast caused by the H_2 injection is too small to be measurable as a gravity anomaly. H_2 inventory in the storage formation can thus only be monitored by conventional mass balancing using the well flow rates. However, the gravity method may be able to resolve the gas phase if larger H_2 volumes of more than 3 times the current volume are present in the storage.

6 SUMMARY AND CONCLUSIONS

In this thesis, several aspects of H_2 storage in porous geological formations are investigated in the context of subsurface spatial planning. Sustainable subsurface spatial planning includes the a-priori determination of the storage dimensions, the induced hydraulic, thermal, mechanical and chemical effects of the storage operation and monitoring methods requirements. Such an assessment can be carried out using numerical scenario simulations, given adequate modelling tools are available.

The development of numerical modelling tools, which can be used for the assessment of coupled hydraulic, thermal and chemical processes occurring during H_2 storage in porous geological formations, is one aim of this thesis. To achieve this, a coupling approach for the scientific open source code OpenGeoSys and the proprietary reservoir simulator ECLIPSE (© Schlumberger) is developed, which can be used for numerical simulations of THMC-systems such as those encountered during porous media gas storage. In a coupled simulation, the multiphase-multicomponent flow and transport is solved for in ECLIPSE, while OpenGeoSys provides the facilities to include heat transport, geochemical reactions and aqueous transport of any non-major phase constituents. For an accurate representation of the induced effects, feedback on the multiphase-multicomponent flow and transport simulation, e.g. by geochemical reactions or temperature perturbations, can be included either using iterative or sequential process coupling. The Joule-Thomson effect, which describes temperature changes during isenthalpic gas expansion, is implemented in OpenGeoSys for gases consisting of N_2, O_2, H_2, CH_4 and CO_2. All implementations are successfully validated using reference simulations or data.

The developed coupled simulator can be used for the assessment of hydraulic, thermal and chemical effects during H_2 gas storage operations within the limits of the respective simulators. Thus one of the aims of this thesis, to provide modelling tools for the assessment of induced effects, is achieved. However, the developed simulator is not limited to use in H_2 storage scenarios. While the Joule-Thomson effect is currently only implemented for the noted components, the coupling between OpenGeoSys and ECLIPSE does not impose any limitations on future uses for the simulation of multiphase-multicomponent systems encountered in other gas storage scenarios such as e.g. compressed air energy storage.

Further improvements can be made to the heat transport modelling facilities of the coupled simulator. In the current version, the no injection data is transferred from ECLIPSE to OpenGeoSys during the simulation run. Thus, boundary conditions to the heat transport can either be a constant temperature or a pre-defined heat source term. However, for an accurate representation of induced thermal effects during gas storage operations the heat added to the system by the injected gas must be quantified, which requires knowledge on the injection volume per time step. Furthermore, heat transfer due to evaporation of formation water into the gas phase and redistribution or removal through the gas withdrawal remains to be implemented in a future development.

The assessment of potential dimension of H_2 storage in porous geological formations, one of the remaining aims of this thesis, is achieved through numerical scenario simulations of a hypothetical storage operation at an existing geological structure in the North German Basin, providing a realistic geological setting. At the storage site, the Rhaetian sandstones, one of the potentially suitable host formations for porous media gas storage in the NGB, are chosen as the target storage formations. To assess the variability of the simulations results due to the variability of the distribution of the reservoir properties such as permeability and porosity, 25 equally likely and realistic parameter distributions are created using a facies modelling approach.

It is found that the simulated storage site can on average supply H_2 at a rate of 2.2 to 4.1 million sm^3/d during a week-long withdrawal period

when using 5 storage wells. Assuming a 60 % efficiency for the re-electrification, which is a reasonable estimate based on current technology, the storage site can thus supply power on the order of 162 to 300 MW continuously for one week, depending on the distribution of the heterogeneity in the storage formation. During the withdrawal, a total of 23.3 to 31.6 million sm^3 H_2 are produced, which corresponds to about 41 000 to 55 900 MWh of energy.

The storage performance can be increased by adding storage wells and enlarging the volume of gas in the storage formation. Homogeneous simulations, which were found to provide a reasonable estimate of the variability of the storage performance seen in the heterogeneous cases, show that the storage can supply H_2 equivalent to about 210 400 to 234 300 MWh of energy when 11 horizontal storage wells are used. The sustainable H_2 flow rates are in the range of around 10.1 to 15.6 million sm^3, corresponding to a power output of about 744 to 1147 MW, depending on the distribution of the reservoir properties.

Thus, this one storage site can supply 90 to 102 % of the average weekly energy demand in electricity of the state of Schleswig-Holstein, which has a population of about 2.8 million people. The power output from the storage site is sufficient to supply around 55 to 85 % of the average weekly power demand of 1356 MW as defined in this scenario.

The large differences in the fractions of the required power and energy demand the storage site can supply are due to storage flow rates quickly decreasing towards the end of the withdrawal periods. Nevertheless, the storage capacity can be further increased as the spill points of the geological structure are not yet reached, implying that the storage site alone could potentially supply 100 % of the demand in power and energy. Given the widespread distribution of potential host rock formations in the NGB, H_2 storage in porous geological formations is thus a viable option for large-scale energy storage, capable of supplying high storage capacities in terms of energy and power.

Critical aspects of the storage dimensioning are the purity of the withdrawn gas and the storage flow rates, limiting both the storage capacity and the power output the storage site can provide. The major controlling factors are the storage setup, i.e. the number of storage wells, the storage schedule, and site specific properties such as pressure limits, the geometry of the storage formation and the distribution of the hydraulic parameters.

Numerical simulations as presented in this thesis can be used to investigate these factors and assess the dimensions of potential H_2 storage operations in a site-specific approach. If insufficient data are available, numerical simulation can still provide estimates of storage dimensions. Thus, they are a valuable tool for a planning of the limited resources the subsurface can provide.

Besides the estimation of storage dimensions, a sustainable subsurface spatial planning scheme also demands the a-priori quantification of induced hydraulic, thermal, geochemical and geomechanical effects induced by the operation and development of e.g. a porous media H_2 storage site. The aims of this thesis include the assessment of hydraulic effects induced by H_2 storage operations and the provision of a first estimate of induced thermal effects.

Hydraulic effects caused by such a H_2 storage operation are due to the distribution of the gas in the storage formation and the pressure perturbations caused by the storage operation. The distribution of the gas phase is strongly affected by the reservoir heterogeneity, with the gas being concentrated in the highly permeable sections of the storage formation. In an ideal scenario, the storage operation is compensated by the compressibility of the gas in the storage formation during injection and withdrawal, resulting in a stable gas-water contact. If such conditions are given, the extent of the gas phase remains constant in time once the storage site is operating at its target capacity. In the large-scale H_2 storage simulation, the lateral extent of the gas phase is about 7 km by 750 m.

The maximum and minimum pressure perturbations that can occur in the subsurface are governed by the pressure limits applied at the storage wells. Thus, an accurate estimation of these limits is not only required for estimating the storage dimensions, but also for the induced pressure perturbations. In the near-field of the storage wells, the fluid pressures are fluctuating due to the cyclic storage operation. For the investigated scenario, the resulting pressure changes in the near-field of the storage are about +20 bars and -15 bars

compared to the initial hydrostatic levels. In the far field of the wells the storage operation always results in an overpressure. At distances of 5 km, overpressures of less than 3 bars are observed in all simulations. In case of the large-scale simulations, the pressure-change due to the storage operation is about 1 bar in 10 km. These pressure-changes are low compared to the absolute pressures of more than 150 bars. The effect of reservoir heterogeneity on the pressure perturbations is minuscule compared to e.g. effects of reservoir heterogeneity on the distribution of the gas phase itself or the various storage performance metrics.

Given a sufficient reservoir volume the overpressure decreases with time. If, however, sealing faults or fractures limit the extent of a storage formation, the overpressure in the far field will be not only higher in magnitude but also more persistent in time. The magnitude of the overpressure signal in storage formation also depends on the injection pattern, with lower injection rates and thus longer storage build-up times resulting in reduced overpressures.

In the context of subsurface spatial planning, the assessment of mutual interactions between different subsurface uses is required for a sustainable allocation of the limited available space. Given the extensive reach of pressure perturbations, induced hydraulic effects are an important factor to consider when assessing mutual interactions between different uses on a case specific basis, e.g. using numerical simulations as presented in this thesis, with the scenario of a combined waste water injection and H_2 storage operation at the same geological structure.

Thermal effects of a H_2 storage operation are provided in this thesis in a form a first estimate. Several processes can induce thermal effects during a H_2 storage operation, of which the injection temperature of the gas is the primary. Temperature perturbations can also be a result of e.g. the Joule-Thomson effect and of heat transfer due to evaporation of formation water into the stored gas. Of these three processes, the effect of the first two are investigated in this thesis using the developed OpenGeoSys-ECLIPSE simulator.

The temperature at which H_2 is injected at the storage site is governed by the operating conditions required by the surface installations. Operating temperatures of e.g. electrolysers used to produce H_2 prior to injection can be up to 100 °C. Furthermore, the operating pressures may demand additional compression of the gas prior to injection, during which the gas heats up further. Coolers may be used to lower the gas temperature as it might be required by the surface installations. Nevertheless, the temperature of the gas could potentially differ significantly from typical reservoir temperatures, which are in the range of 20 to 50 °C.

The Joule-Thomson effect describes temperature changes of gas during isenthalpic expansion. During gas flow in a porous formation, gas is expanding along the flow path. Thus, the Joule-Thomson effect causes temperature changes whenever gas is injected or withdrawn from the storage site.

In the investigated scenario, the thermal effects caused by the Joule-Thomson effect are minuscule as the Joule-Thomson coefficients for H_2 only have a low magnitude. However, it is noteworthy that thermal effects caused by the Joule-Thomson accumulate several tens of metres away from the storage wells, in regions where the gas is primarily moving back and forth in the storage formation and is not withdrawn. The magnitude and the extent of the thermal effects are thus primarily governed by the specific surface installations which define the injection temperature.

Assuming a constant injection temperature of around 25 °C above the initial reservoir temperature results in temperature changes up to 50 m away from the storage wells. Furthermore, the cyclic operation of the storage results in pronounced temperature fluctuations in the rock formations adjacent to the storage wells. The spread of the temperature perturbations is primarily conductive. This is a result of the relatively low volumetric heat capacity of the gas and of the assumption in OpenGeoSys that local temperature are in equilibrium across all phases.

The simulated scenario does include further simplifications, such as a constant temperature boundary condition, high thermal dispersivities and a homogeneous distribution of the thermal properties. Because of these, the simulations can only provide a conservative estimate. Nevertheless, the developed OpenGeoSys-ECLIPSE simulator can be used to provide a first estimate of thermal effects induced by a H_2 storage opera-

tion. While the Joule-Thomson effect during a H_2 storage operation is most likely negligible, more pronounced temperature perturbations may be induced during other types of gas storage, e.g. because of larger Joule-Thomson coefficients or a higher frequency of the storage operation as for example in a compressed air energy storage site operated on a bi-daily schedule.

Given the developed OpenGeoSys-ECLIPSE simulator has no general limitations regarding the considered gas components and the Joule-Thomson being implemented for any mixture of N_2, H_2, O_2, CO_2 and CH_4, a large variety of storage scenarios can be investigated. However, some processes such as heat transfer through the evaporation of residual formation water are not yet implemented. To what degree this process affects the temperatures in the storage formation should be addressed in future research.

The applicability of monitoring methods to a H_2 storage operation must be determined for the application of a subsurface spatial planning scheme in addition to the aforementioned aspects of storage dimensioning and induced effects.

The most direct monitoring techniques are measurements taken at storage or observation wells, which can be measurements of fluid pressures, temperatures or compositions. Thus, wells can be used for the direct measurement of induced hydraulic, thermal and chemical effects. Suitable locations for observation wells can be determined using numerical scenario simulations as presented in this thesis. In addition to such point data, geophysical monitoring techniques can provide detailed multi-dimensional information on the undergoing storage operation.

In this thesis, seismic forward waveform inversion (FWI), geoelectric resistivity tomography (ERT) and gravimetric monitoring techniques are investigated for the use at a H_2 storage site. For the FWI method it is found that a surface acquisition geometry is sufficient to resolve the general shape of the gas phase distribution. To resolve internal structures, a detailed FWI survey using a crosswell acquisition geometry is required, with which structures of around 1.4 m in size can be discerned. However, besides the saturation of the gas phase, the pore pressure can significantly impact the p-wave velocity variations, which were not included in this assessment. Thus, the detectability of the gas phase may be increased in an actual field application. Geoelectric surveys are also restricted to a cross-well acquisition geometry. The detailed structures resolved with crosswell FWI can further enhance the application of geoelectric techniques through constraining the ERT inversion. In doing so the resolution obtained with the ERT technique is comparable to that of the FWI technique. Thus, FWI and ERT techniques can be used to locate and map the gas distribution at an H_2 storage site when using a crosswell acquisition geometry. Quantifying changes in the gas inventory due to withdrawal or injection periods is, however, not possible, as the change in volume is too small. For the given storage site the employed gravity technique shows anomalies resembling the gas phase. However, monitoring the filling state of the storage site is not possible as the differences in the gas inventory are not sufficient. Nevertheless, this study successfully demonstrates the applicability of such an integrative site investigation concept for porous media H_2 storage.

For the specific case of this H_2 storage site, the operational space can be defined by the distribution of the gas phase within the storage formation. This directly used space is, once the storage site is at its full capacity, stable in size. Within this space the fluid pressures are elevated by several bars over the initial hydrostatic pressure and the pore space is occupied by mobile gas and immobile residual formation water. The affected space is characterised in the lateral directions by the induced pressure perturbations and vertically by the induced thermal effects. For the estimation of the monitoring space further analyses are required to determine the effects of other uses or technical installations in the rock strata above the storage formation. In the studied case the geophysical methods include data acquired at the surface and thus intermediate uses might affect the resolution of the detection methods.

In the context of subsurface spatial planning, the results of this thesis show that numerical modelling tools are available to determine storage dimensions, induced hydraulic, thermal and chemical effects and the applicability of geophysical monitoring techniques for a given H_2 storage site. For this, sufficient data on the reservoir properties, the surface installations and the power and energy demand is indispensable.

Further model development is required to better represent the injection temperature of the gas and to account for heat transfers by phase changes. As shown in this thesis, H_2 storage in porous formations can provide large storage capacities in terms of power output and energy withdrawn. However, (bio)chemical reactions of the stored gas might diminish the storage performance. If reliable data is available, the developed OpenGeoSys-ECLIPSE simulator could be used to assess these effects. Furthermore, research on the integrity of caprocks and their capability to retain the stored gas is required.

Apart from the uncertainties of the geological parameter distribution, the actual storage demand and the site-specific setup of the surface facilities are the primary unknowns which affect the simulation results as these factors control the storage operation. Thus, future research should be aimed at a closer integration of the demand imposed onto the storage operation by the grid.

REFERENCES

Adamek F, Aundrup T, Glaunsinger W, Kleimaier M, Landinger H, Leuthold M, Lunz B, Moser A, Pape C, Pluntke H, Rotering N, Sauer U, Sterner M, Wellßow W (2012) Energiespeicher für die Energiewende - Speicherungsbedarf und Auswirkungen auf das Übertragungsnetz für Szenarien bis 2050. VDE, Frankfurt a. M.

al Hagrey SA (2012) 2D Optimized electrode arrays for borehole resistivity tomography and CO_2 sequestration modelling. Pure Appl Geophys 169:1283–1292. doi: 10.1007/s00024-011-0369-0

al Hagrey SA, Köhn D, Rabbel W (2014) Geophysical assessments of renewable gas energy compressed in geologic pore storage reservoirs. SpringerPlus 3:267. doi: 10.1186/2193-1801-3-267

al Hagrey SA, Strahser M, Rabbel W (2013) Seismic and geoelectric modeling studies of parameters controlling CO_2 geostorage in saline formations. Int J Greenh Gas Control 19:796–806. doi: 10.1016/j.ijggc.2013.01.041

Archie GE (1942) The Electrical Resistivity Log as an Aid in Determining Some Reservoir Characteristics. Trans AIME 146:54–62. doi: 10.2118/942054-G

ARL (2012) Nutzungen im Untergrund vorsorgend steuern – für eine Raumordnung des Untergrundes - Positionspapier Nr. 91. ARL, Hannover

Arts R, Chadwick A, Eiken O, Zweigel P (2003) Interpretation of the 1999 and 2001 time-lapse seismic data (WP 5.4). TNO Report NITG 03-064-B, TNO, Utrecht

Arts R, Eiken O, Chadwick A, Zweigel P, van der Meer L, Zinszner B (2004) Monitoring of CO_2 injected at Sleipner using time-lapse seismic data. Energy 29:1383–1392. doi: 10.1016/j.energy.2004.03.072

Arts R, Elsayed R, van der Meer L, Eiken O, Ostmo S, Chadwick A, Kirby G, Zinszner B (2002) Estimation of the mass of injected CO_2 at Sleipner using time-lapse seismic data. 64th EAGE Conf Exhib, Florence, Italy, 27 - 30 May 2002

Asnaashari A, Brossier R, Garambois S, Audebert F, Thore P, Virieux J (2015) Time-lapse seismic imaging using regularized full-waveform inversion with a prior model: Which strategy? Geophys Prospect 63:78–98. doi: 10.1111/1365-2478.12176

Bachu S, Bennion B (2008) Effects of in-situ conditions on relative permeability characteristics of CO_2-brine systems. Environ Geol 54:1707–1722. doi: 10.1007/s00254-007-0946-9

Baldschuhn R, Binot F, Fleig S, Kockel F (2001) Geologisches Jahrbuch A153: Geotektonischer Atlas von Nordwest-Deutschland und dem deutschen Nordseesektor. Schweizerbart'sche Verlagsbuchhandlung, Hannover

Ballarini E, Beyer C, Bauer RD, Griebler C, Bauer S (2014) Model based evaluation of a contaminant plume development under aerobic and anaerobic conditions in 2D bench-scale tank experiments. Biodegradation 25:351–371. doi: 10.1007/s10532-013-9665-y

Bary A, Crotogino F, Prevedel B, Berger H, Brown K, Henzell M, Mohmeyer K-U, Ren N-K, Stiles K (2002) Storing Natural Gas Underground. Oilfield Review, Summer 2002:2-17

Battermann K (1989) Das Rhät (oberer Keuper) im östlichen Niedersachsen. Zeitrschrift der Deutschen Geologischen Gesellschaft 140:101–116

Battino R (1982) IUPAC Solubility Data Series 10: Nitrogen and Air. Pergamon Press, Oxford

Bauer S, Beyer C, Dethlefsen F, Dietrich P, Duttmann R, Ebert M, Feeser V, Görke U, Köber R, Kolditz O, Rabbel W, Schanz T, Schäfer D, Würdemann H, Dahmke A (2013) Impacts of the use of the geological subsurface for energy storage: An investigation concept. Environ Earth Sci 70:3935–3943. doi: 10.1007/s12665-013-2883-0

Bauer S, Beyer C, Kolditz O (2006) Assessing measurement uncertainty of first-order degradation rates in heterogeneous aquifers. Water Resour Res 42:1–14. doi: 10.1029/2004WR003878

Bauer S, Class H, Ebert M, Feeser V, Götze H, Holzheid A, Kolditz O, Rosenbaum S, Rabbel W, Schäfer D, Dahmke A (2012) Modeling, parameterization and evaluation of monitoring methods for CO_2 storage in deep saline formations: the CO_2-MoPa project. Environ Earth Sci 67:351–367. doi: 10.1007/s12665-012-1707-y

Bear J, Bachmat Y (1990) Introduction to modelling of transport phenomena in porous media. Kluwer Academic Publisher, Dordrecht

Benisch K, Bauer S (2013) Short- and long-term regional pressure build-up during CO_2 injection and its applicability for site monitoring. Int J Greenh Gas Control 19:220–233. doi: 10.1016/j.ijggc.2013.09.002

Benisch K, Graupner B, Bauer S (2013) The coupled opengeosys-eclipse simulator for simulation of CO_2 storage - Code comparison for fluid flow and geomechanical processes. Energy Procedia 37:3663–3671. doi: 10.1016/j.egypro.2013.06.260

Benisch K, Köhn D, al Hagrey S, Rabbel W, Bauer S (2015) A combined seismic and geoelectrical monitoring approach for CO_2 storage using a synthetic field site. Environ Earth Sci 73:3077–3094. doi: 10.1007/s12665-014-3603-0

Bennion DB, Thomas FB, Ma T, Imer D (2000) Detailed Protocol for the Screening and Selection of Gas Storage Reservoirs. SPE/CERI Gas Technol Symp Calgary, Canada, 3-5 April 2000. doi: 10.2118/59738-MS

Beyer C, Bauer S, Kolditz O (2006) Uncertainty assessment of contaminant plume length estimates in heterogeneous aquifers. J Contam Hydrol 87:73–95. doi: 10.1016/j.jconhyd.2006.04.006

Beyer C, Konrad W, Rügner H, Bauer S, Liedl R, Grathwohl P (2009) Model-based prediction of long-term leaching of contaminants from secondary materials in road constructions and noise protection dams. Waste Manag 29:839–850. doi: 10.1016/j.wasman.2008.06.025

Beyer C, Li D, De Lucia M, Kühn M, Bauer S (2012) Modelling CO_2-induced fluid–rock interactions in the Altensalzwedel gas reservoir. Part II: coupled reactive transport simulation. Environ Earth Sci 67:573–588. doi: 10.1007/s12665-012-1684-1

Beyer C, Popp S, Bauer S (2016) Simulation of temperature effects on groundwater flow, contaminant dissolution, transport and biodegradation due to shallow geothermal use. Environ Earth Sci 75:1244. doi: 10.1007/s12665-016-5976-8

Birkholzer JT, Oldenburg CM, Zhou Q (2015) CO_2 migration and pressure evolution in deep saline aquifers. Int J Greenh Gas Control 40:203–220. doi: 10.1016/j.ijggc.2015.03.022

Birkholzer JT, Zhou Q (2009) Basin-scale hydrogeologic impacts of CO_2 storage: Capacity and regulatory implications. Int J Greenh Gas Control 3:745–756. doi: 10.1016/j.ijggc.2009.07.002

Birkholzer JT, Zhou Q, Cortis A, Finsterle S (2011) A sensitivity study on regional pressure buildup from large-scale CO_2 storage projects. Energy Procedia 4:4371–4378. doi: 10.1016/j.egypro.2011.02.389

Birkholzer JT, Zhou Q, Tsang CF (2009) Large-scale impact of CO_2 storage in deep saline aquifers: A sensitivity study on pressure response in stratified systems. Int J Greenh Gas Control 3:181–194. doi: 10.1016/j.ijggc.2008.08.002

BMWi (2016) Die Energie der Zukunft, Fünfter Monitoring-Bericht zur Energiewende, Berichtsjahr 2015. Bundesministerium für Wirtschaft und Energie, Berlin, 172p

BMWi (2015) Vierter Monitoring-Bericht zur Energiewende - Ein gutes Stück Arbeit. Die Energie der Zukunft. Bundesministerium für Wirtschaft und Energie, Berlin, 112p

Boockmeyer A, Bauer S (2014) High-temperature heat storage in geological media: high-resolution simulation of near-borehole processes. Géotechnique Lett 4:151–156. doi: 10.1680/geolett.13.00060

Börgesson L (1996) ABAQUS. Dev Geotech Eng 79:565–570. doi: 10.1016/S0165-1250(96)80047-2

Borup R, Meyers J, Pivovar B, Kim YS, Mukundan R, Garland N, Myers D, Wilson M, Garzon F, Wood D, Zelenay P, More K, Stroh K, Zawodzinski T, Boncella J, Mcgrath JE, Inaba OM, Miyatake K, Hori M, Ota K, Ogumi Z, Miyata S, Nishikata A, Siroma Z, Uchimoto Y, Yasuda K, Kimijima K, Iwashita N (2007) Scientific Aspects of Polymer Electrolyte Fuel Cell Durability and Degradation. Chemical Scientific Aspects of Polymer Electrolyte Fuel Cell Durability and Degradation. Chem Rev 107:3904–3951. doi: 10.1021/cr050182l

Böttcher N, Singh AK, Kolditz O, Liedl R (2012) Non-isothermal, compressible gas flow for the simulation of an enhanced gas recovery application. J Comput Appl Math 236:4933–4943. doi: 10.1016/j.cam.2011.11.013

Bovet J (2014) Notwendigkeit und Steuerungsmöglichkeiten einer unterirdischen Raumordnung. UPR Umwelt- und Planungsrecht 34:418–425

Brooks RH, Corey AT (1946) Hydraulic Properties of Porous Media. Hydrological Papers Color State University 3, 61p

Büchi FN, Hofer M, Peter C, Cabalzar UD, Bernard J, Hannesen U, Schmidt TJ, Closset A, Dietrich P (2014) Towards re-electrification of hydrogen obtained from the power-to-gas process by highly efficient H_2/O_2 polymer electrolyte fuel cells. RSC Adv 4:56139–56146. doi: 10.1039/C4RA11868E

Burton M, Kumar N, Bryant SL (2009) CO_2 injectivity into brine aquifers: Why relative permeability matters as much as absolute permeability. Energy Procedia 1:3091–3098. doi: 10.1016/j.egypro.2009.02.089

Carden PO, Paterson L (1979) Physical, chemical and energy aspects of underground hydrogen storage. Int J Hydrogen Energy 4:559–569. doi: 10.1016/0360-3199(79)90083-1

Cardwell Jr. WT, Parsons RL (1945) Average Permeabilities of Heterogeneous Oil Sands. Trans Am Inst Mining, Metall Pet Eng 160:34–42. doi: 10.2118/945034-G

Carlson J, Gurley D, King G, Price-Smith C, Waters F (1992) Sand Control: Why and How? Oilfield Review October 1992:41–53

Carr S, Premier GC, Guwy AJ, Dinsdale RM, Maddy J (2014) Hydrogen storage and demand to increase wind power onto electricity distribution networks. Int J Hydrogen Energy 39:10195–10207. doi: 10.1016/j.ijhydene.2014.04.145

Chadwick RA, Arts R, Eiken O (2005) 4D seismic quantification of a growing CO_2 plume at Sleipner, North Sea. Petroleum Geology Conference series 6:1385–1399. doi: 10.1144/0061385

Chadwick RA, Noy D, Arts R, Eiken O (2009) Latest time-lapse seismic data from Sleipner yield new insights into CO_2 plume development. Energy Procedia 1:2103–2110. doi: 10.1016/j.egypro.2009.01.274

Chiesa P, Lozza G, Mazzocchi L (2005) Using hydrogen as gas turbine fuel. J Eng Gas Turbines Power 127:73–80. doi: 10.1115/1.1787513

Clark JE, Bonura DK, Van Voorhees RF (2005) An Overview of Injection Well History in the United States of America. Dev Water Sci 52:3–12. doi: 10.1016/S0167-5648(05)52001-X

Cord-Ruwisch R, Seitz H-J, Conrad R (1988) The capacity of hydrogentrophic anaerobic bacteria to compete for traces of hydrogen depends on the redox potential of the electron acceptor. Arch Microbiol 149:350–357

Crotogino F, Donadei S, Bünger U, Landinger H, Crotogino F, Donadei S, Ut KBB, Bünger U, Landinger H (2010) Large-Scale Hydrogen Underground Storage for Securing Future Energy Supplies. In: Stolten D, Grube T (eds): 18th World Hydrogen Energy Conference 2010, Parallel Sessions Book 4:37-45

Crotogino F, Mohmeyer K-U, Scharf R (2001) Huntorf CAES: More than 20 Years of Successful Operation. Solution Mining Research Institute (SMRI) Spring Meeting 2001, Orlando, 15-18 April

Day-Lewis FD, Singha K, Binley AM (2005) Applying petrophysical models to radar travel time and electrical resistivity tomograms: Resolution-dependent limitations. Journal of Geophysical Research B: Solid Earth 110:1–17. doi: 10.1029/2004JB003569

Delfs JO, Nordbeck J, Bauer S (2016) Upward brine migration resulting from pressure increases in a layered subsurface system. Environ Earth Sci 75:1–13. doi: 10.1007/s12665-016-6245-6

Dethlefsen F, Beyer C, Feeser V, Köber R (2016) Parameterizability of processes in subsurface energy and mass storage. Environ Earth Sci 75:1–25. doi: 10.1007/s12665-016-5626-1

Diersch H-JG (2014) FEFLOW. Springer, Berlin

Doornenbal HJ, Stevenson A (eds) (2010) Petroleum geological atlas of the southern permian basin area. EAGE Publications b. v, Houten

DSK (ed) (2005) Stratigraphie von Deutschland IV - Keuper. E. Schweizerbart'sche Vertragsbuchhandlung, Stuttgart

Dussaud M (1989) New Techniques in Underground Storage of Natural Gas. In: Tek MR (ed) Underground Storage of Natural Gas. Kluwer Academic Publisher, Dordrecht, pp 371–383

Eiken O, Brevik I, Arts R, Lindeberg E, Fagervik K (2000) Seismic monitoring of CO_2 injected into a marine acquifer. In: SEG Technical Program Expanded Abstracts 2000. Society of Exploration Geophysicists, pp 1623–1626

Evans DJ, West JM (2008) An appraisal of underground gas storage technologies and incidents, for the development of risk assessment methodology. Britisch Geological Survey, Nottingham

Fahrion H, Betz D (1991) Geologischer Rahmen, Fund- und Fördergeschichte. In: Achilles H, Ahrendt H (eds) Das Gasfeld Thönse in Niedersachsen - Ein Unikat. Schweizerbart Science Publishers, Stuttgart, pp 7–10

Feldmann F, Hagemann B, Ganzer L, Panfilov M (2016) Numerical simulation of hydrodynamic and gas mixing processes in underground hydrogen storages. Environ Earth Sci 75:1165. doi: 10.1007/s12665-016-5948-z

Flemisch B, Darcis M, Erbertseder K, Faigle B, Lauser A, Mosthaf K, Müthing S, Nuske P, Tatomir A, Wolff M, Helmig R (2011) DuMux: DUNE for multi-{phase,component,scale,physics,...} flow and transport in porous media. Adv Water Resour 34:1102–1112. doi: 10.1016/j.advwatres.2011.03.007

Foh S, Novil M, Rockar E, Randolph P (1979) Underground Hydrogen Storage. Brookhaven National Laboratory, Upton, New York, 145p

Foley AM, Leahy PG, Marvuglia A, McKeogh EJ (2012) Current methods and advances in forecasting of wind power generation. Renew Energy 37:1–8. doi: 10.1016/j.renene.2011.05.033

Forsberg CW (2009) Sustainability by combining nuclear, fossil, and renewable energy sources. Prog Nucl Energy 51:192–200. doi: 10.1016/j.pnucene.2008.04.002

Freiboth S, Class H, Helmig R, Graf T, Ehlers W, Schwarz V, Vrettos C (2009) A model for multiphase flow and transport in porous media including a phenomenological approach to account for deformation-a model concept and its validation within a code intercomparison study. Comput Geosci 13:281–300. doi: 10.1007/s10596-008-9118-6

Gahleitner G (2013) Hydrogen from renewable electricity: An international review of power-to-gas pilot plants for stationary applications. Int J Hydrogen Energy 38:2039–2061. doi: 10.1016/j.ijhydene.2012.12.010

Gallo AB, Simões-Moreira JR, Costa HKM, Santos MM, Moutinho dos Santos E (2016) Energy storage in the energy transition context: A technology review. Renew Sustain Energy Rev 65:800–822. doi: 10.1016/j.rser.2016.07.028

Gasem KAM, Gao W, Pan Z, Robinson RL (2001) A modified temperature dependence for the Peng-Robinson equation of state. Fluid Phase Equilibria 181:113–125. doi: 10.1016/S0378-3812(01)00488-5

Gassmann F (1951) Über die Elastizität poröser Medien. Vierteljahresschrift der Naturforschenden Gesellschaft Zürich 96:1–23

Gaupp R (1991) Zur Fazies und Diagenese des Mittelrhät-Hauptsandsteins im Gasfeld Thönse. In: Achilles H, Ahrendt H (eds) Das Gasfeld Thönse in Niedersachsen - Ein Unikat. Schweizerbart Science Publishers, Stuttgart, p 34–55

Ghaderi A, Landrø M (2009) Estimation of thickness and velocity changes of injected carbon dioxide layers from prestack time-lapse seismic data. Geophysics 74:O17–O28. doi: 10.1190/1.3054659

Götze H-J, Lahmeyer B (1988) Application of three-dimensional interactive modeling in gravity and magnetics. Geophysics 53:1096–1108

Graupner BJ, Li D, Bauer S (2011) The coupled simulator ECLIPSE–OpenGeoSys for the simulation of CO_2 storage in saline formations. Energy Procedia 4:3794–3800. doi: 10.1016/j.egypro.2011.02.314

Gregory DP, Pangborn JB (1976) Hydrogen energy. Annu Rev Energy 1:279–310. doi: 10.1098/rsta.2006.1965

Gutjahr AL, Gelhar LW, Bakr AA, MacMillan JR (1978) Stochastic analysis of spatial variability in subsurface flows: 2. Evaluation and application. Water Resour Res 14:953–959. doi: 10.1029/WR014i005p00953

Hagemann B, Rasoulzadeh M, Panfilov M, Ganzer L, Reitenbach V (2015) Mathematical modeling of unstable transport in underground hydrogen storage. Environ Earth Sci 73:6891–6898. doi: 10.1007/s12665-015-4414-7

Hagemann B, Rasoulzadeh M, Panfilov M, Ganzer L, Reitenbach V (2016) Hydrogenization of underground storage of natural gas: Impact of hydrogen on the hydrodynamic and bio-chemical behavior. Comput Geosci 20:595–606. doi: 10.1007/s10596-015-9515-6

Hannis S (2010) Monitoring technologies used at some geological CO_2 storage sites. In: Innovation for Sustainable Production (i-SUP), Bruges, Belgium, 18-21 April 2010

He W, Beyer C, Fleckenstein JH, Jang E, Kolditz O, Naumov D, Kalbacher T (2015) A parallelization scheme to simulate reactive transport in the subsurface environment with OGS#IPhreeqc 5.5.7-3.1.2. Geosci Model Dev 8:3333–3348. doi: 10.5194/gmd-8-3333-2015

Hein P, Kolditz O, Görke UJ, Bucher A, Shao H (2016) A numerical study on the sustainability and efficiency of borehole heat exchanger coupled ground source heat pump systems. Appl Therm Eng 100:421–433. doi: 10.1016/j.applthermaleng.2016.02.039

Helmig R (1997) Multiphase flow and transport processes in the suburface. Springer, Berlin

Hermansen H, Landa GH, Sylte JE, Thomas LK (2000) Experiences after 10 years of waterflooding the Ekofisk Field, Norway. J Pet Sci Eng 26:11–18. doi: 10.1016/S0920-4105(00)00016-4

Hese F (2011) Geologische 3D-Modelle des Untergrundes Schleswig-Holsteins – ein Beitrag für Potenzialstudien zur Nutzung von tiefen salinen Aquiferen. Zeitschrift der Deutschen Gesellschaft für Geowissenschaften 162:389–404. doi: 10.1127/1860-1804/2011/0162-0389

Hese F (2012) 3D Modellierungen und Visualisierung von Untergrundstrukturen für die Nutzung des unterirdischen Raumes in Schleswig-Holstein. Dissertation, Kiel University

Hettema M, Papamichos E, Schutjens P (2002) Subsidence delay: Field observations and analysis. Oil Gas Sci Technol 57:443–458. doi: 10.2516/ogst:2002029

Hildenbrand A, Schlömer S, Krooss BM (2002) Gas breakthrough experiments on fine-grained sedimentary rocks. Geofluids 2:3–23. doi: 10.1046/j.1468-8123.2002.00031.x

Hildenbrand A, Schlömer S, Krooss BM, Littke R (2004) Gas breakthrough experiments on pelitics rocks:

comparitive study with N_2, CO_2 and CH_4. Geofluids 4:61–80. doi: 10.1111/j.1468-8123.2004.00073.x

IEA (2016) Energy, Climate Change & Environment - 2016 Insights. International Energy Agency, Paris

IGU/WOC (2006) Underground Storage of Gas. Report of Working Committee 2, Trienneium 2003-2006, International Gas Union, 23rd World Gas Conference, Amsterdam, 5-9 June 2006

IPCC (2014) Climate Change 2014: Mitigation of Climate Change. Working Group III Contribution tot he Fifth Assessment Report on the Intergovernmental Panel on Climate Change, Cambridge University Press, Cambridge

IRENA (2015) Renewable Energy Target Setting. International Renewable Energy Agency.

Jessen K, Kovscek AR, Orr FM (2005) Increasing CO_2 storage in oil recovery. Energy Convers Manag 46:293–311. doi: 10.1016/j.enconman.2004.02.019

Johnston HL, Bezman II, Hood CD (1946) Joule-Thomson Effects in Hydrogen at Liquid Air and at Room Temperatures. J Am Chem Soc 68:2367–2373. doi: 10.1021/ja01215a069

Jolley SJ, Dijk H, Lamens JH, Fisher QJ, Manzocchi T, Eikmans H, Huang Y (2007) Faulting and fault sealing in production simulation models: Brent Province, northern North Sea. Pet Geosci 13:321–340. doi: 10.1144/1354-079306-733

Joule JP, Thomson W (1854) On the Thermal Effects of Fluids in Motion. Part II. Philos Trans R Soc London 144:321–364. doi: 10.1098/rstl.1854.0016

Kabuth A, Dahmke A, Beyer C, Dethlefsen F, Dietrich P, Duttmann R, Ebert M, Feeser V, Görke U, Köber R, Kolditz O, Rabbel W, Schanz T, Schäfer D, Würdemann H, Bauer S (2017) Energy storage in the geological subsurface: dimensioning, risk analysis and spatial planning – The ANGUS+ project. Environ Earth Sci. doi: 10.1007/s12665-016-6319-5

Kahnt R, Gabriel A, Seelig C, Freund A, Homilius A (2015) Unterirdische Raumplanung Vorschläge des Umweltschutzes zur Verbesserung der über- und untertägigen Informationsgrundlagen, zur Ausgestaltung des Planungsinstrumentariums und zur nachhaltigen Lösung von Nutzungskonflikten - Teilvorhaben 1: Geologische Daten. Umweltbundesamt, Dessau-Roßlau

Katz D, Cornell D, Kobayashi R, Poettmann FH, Vary JA, Elenbaas JR, Weinaug CF (1959) Handbook of Natural GasEngineering-Katz. McGraw-Hill Book Company, New York

Kaufhold H, Hable R, Liebsch-Dörschner T, Thomsen C, Taugs R (2011) Distribution and properties of mesozoic sandstones and barrier rocks in Schleswig-Holstein and Hamburg – Basic informations on possible energetic utilisation of the deeper subsurface. Schriftenreihe der Deutschen Gesellschaft für Geowissenschaften 74:38–60. doi: 10.1127/sdgg/74/2011/38

Kaye G, Laby T (2016) Tables of physical and chemical constants (16th edition). 3.5. Critical Constants and Second Virial Coefficients of Gases. Kaye and Laby Online, v1.0, http://www.kayelaby.npl.co.uk [last accessed 14 March 2016].

Kempka T, Kühn M, Class H, Frykman P, Kopp A, Nielsen CM, Probst P (2010) Modelling of CO_2 arrival time at Ketzin - Part I. Int J Greenh Gas Control 4:1007–1015. doi: 10.1016/j.ijggc.2010.07.005

Klaus T, Vollmer C, Werner K, Lehmann H, Müschen K (2010) Energieziel 2050 : 100 Prozent Strom aus erneuerbaren Quellen. Umweltbundesamt, Dessau-Roßlau

Kolditz O, Bauer S (2004) A process-oriented approach to computing multi-field problems in porous media. Journal of Hydroinformatics 6:225–244

Kolditz O, Bauer S, Bilke L, Böttcher N, Delfs JO, Fischer T, Görke UJ, Kalbacher T, Kosakowski G, McDermott CI, Park CH, Radu F, Rink K, Shao H, Shao HB, Sun F, Sun YY, Singh AK, Taron J, Walther M, Wang W, Watanabe N, Wu Y, Xie M, Xu W, Zehner B (2012a) OpenGeoSys: An open-source initiative for numerical simulation of thermo-hydro-mechanical/chemical (THM/C) processes in porous media. Environ Earth Sci 67:589–599. doi: 10.1007/s12665-012-1546-x

Kolditz O, Bauer S, Böttcher N, Elsworth D, Görke UJ, McDermott CI, Park CH, Singh AK, Taron J, Wang W (2012b) Numerical simulation of two-phase flow in deformable porous media: Application to carbon dioxide storage in the subsurface. Math Comput Simul 82:1919–1935. doi: 10.1016/j.matcom.2012.06.010

Kolditz O, Görke U-J, Shao H, Wang W, Bauer S (eds) (2016) Thermo-Hydro-Mechanical-Chemical Processes in Fractured Porous Media: Modelling and Benchmarking. Springer, Heidelberg

Kolditz O, Shao H, Wang W, Bauer S (eds) (2015) Thermo-Hydro-Mechanical-Chemical Processes in Fractured Porous Media: Modelling and Benchmarking. Springer, Heidelberg

Korpås M, Greiner CJ (2008) Opportunities for hydrogen production in connection with wind power in weak grids. Renew Energy 33:1199–1208. doi: 10.1016/j.renene.2007.06.010

Kosakowski G, Watanabe N (2014) OpenGeoSys-Gem: A numerical tool for calculating geochemical and porosity changes in saturated and partially saturated media. Phys Chem Earth 70–71:138–149. doi: 10.1016/j.pce.2013.11.008

Kroniger D, Madlener R (2014) Hydrogen storage for wind parks: A real options evaluation for an optimal investment in more flexibility. Appl Energy 136:931–946. doi: 10.1016/j.apenergy.2014.04.041

Laille JP, Molinard JE, Wents A (1988) Inert Gas Injection as Part of the Cushion of the Underground Storage of Saint-Clair-Sur-Epte, France. SPE Gas Technology Symposium, Dallas, 13-15 June. doi: 10.2118/17740-MS

LBEG (2015) Erdöl und Erdgas in der Bundesrepublik Deutschland Niedersachsen 2015. Landesamt für Bergbau, Energie und Geologie, Hannover

Leachman JW, Jacobsen RT, Penoncello SG, Lemmon EW (2009) Fundamental Equations of State for Parahydrogen, Normal Hydrogen, and Orthohydrogen. J Phys Chem Ref Data 38:721–747.

Lee MC, Seo S Bin, Yoon J, Kim M, Yoon Y (2012) Experimental study on the effect of N_2, CO_2, and steam dilution on the combustion performance of H_2 and CO synthetic gas in an industrial gas turbine. Fuel 102:431–438. doi: 10.1016/j.fuel.2012.05.028

Leith W (2001) Geologic and Engineering Constraints on the Feasibility of Clandestine Nuclear Testing by Decoupling in Large Underground Cavities - Open file report 01-28. U.S. Geological Survey

Lemmon EW, McLinden MO, Friend DG (2016) Thermophysical Properties of Fluid Systems. In: Linstrom PJ, Mallard WG (eds) NIST Chemistry WebBook, NIST Standard Reference Database Number 69. National Institute of Standards and Technology, Gaithersburg, MD, USA, http://webbook.nist.gov [last accessed 14 March 2016].

Li D, Bauer S, Benisch K, Graupner B, Beyer C (2014) OpenGeoSys-ChemApp: A coupled simulator for reactive transport in multiphase systems and application to CO_2 storage formation in Northern Germany. Acta Geotech 9:67–79. doi: 10.1007/s11440-013-0234-7

Loke MH, Acworth I, Dahlin T, Loke MH, Acworth I, Dahlin T (2003) A comparison of smooth and blocky inversion methods in 2D electrical imaging surveys. Explor Geophys 34:182. doi: 10.1071/EG03182

Lüth S, Bergmann P, Cosma C, Enescu N, Giese R, Götz J, Ivanova A, Juhlin C, Kashubin A, Yang C, Zhang F (2011) Time-lapse seismic surface and down-hole measurements for monitoring CO_2 storage in the CO2SINK project (Ketzin, Germany). Energy Procedia 4:3435–3442. doi: 10.1016/j.egypro.2011.02.268

Ma X, Gildin E, Plaksina T (2015) Efficient optimization framework for integrated placement of horizontal wells and hydraulic fracture stages in unconventional gas reservoirs. J Unconv Oil Gas Resour 9:1–17. doi: 10.1016/j.juogr.2014.09.001

Mallman EP, Zoback MD (2007) Subsidence in the Louisiana coastal zone due to hydrocarbon production. Journal of Coastal Research 50

Massoudi R, King AD (1974) Effect of pressure on the surface tension of water. Adsorption of low molecular weight gases on water at 25°. J Phys Chem 78:2262–2266. doi: 10.1021/j100615a017

Mavko G, Mukerji T (1998) Bounds on low frequency seismic velocities in partially saturated rocks. Geophysics 63:918–924

McDermott CI, Randriamanjatosoa ARL, Tenzer H, Kolditz O (2006) Simulation of heat extraction from crystalline rocks: The influence of coupled processes on differential reservoir cooling. Geothermics 35:321–344. doi: 10.1016/j.geothermics.2006.05.002

McGillivray P, Oldenburg D (1990) Methods for calculating Fréchet derivatives and sensitivities for the nonlinear inverse problem: a comparative study. Geophys Prospect 38:499–524. doi: 10.1111/j.1365-2478.1990.tb01859.x

Meadows M (2008) Time-lapse seismic modelling and inversion of CO_2 saturation for storage and enhanced oil recovery. The Leading Edge 27:506–516

MELUR (2013) Energiebilanz Schleswig-Holstein 2011. Ministerium für Energiewende, Landwirtschaft, Umwelt und ländliche Räume, Kiel

Michels A, de Graaff W, Wolkers GJ (1964) Thermodynamic properties of hydrogen and deuterium at temperatures between –175°C and 150°C and at pressures up to 2500 atmospheres. Appl Sci Res Sect A 12:9–32. doi: 10.1007/BF03184744

Mitiku AB, Bauer S (2013) Optimal use of a dome-shaped anticline structure for CO_2 storage: A case study in the North German sedimentary basin. Environ Earth Sci 70:3661–3673. doi: 10.1007/s12665-013-2580-z

Morse DG (1994) Siliciclastic reservoir rocks. In: Magoon LB, Dow WG (eds) The Petroleum System – From Source to Trap. American Association of Petroleum Geologists Memoirs 60:121–139

Müller C, Reinhold K (eds) (2011) Geologische Charakterisierung tiefliegender Speicher- und Barrierehorizonte in Deutschland - Speicher-Kataster

Deutschland. Schweizerbart Science Publishers, Stuttgart, Germany

Nachiappan N, Kalaignan GP (2013) Effect of nitrogen and carbon dioxide as fuel impurities on PEM fuel cell performances. 351–354. doi: 10.1007/s11581-012-0730-z

Nagel NB (2001) Compaction and subsidence issues within the petroleum industry: From Wilmington to Ekofisk and beyond. Physics and Chemistry of the Earth, Part A: Solid Earth and Geodesy 26:3–14. doi: 10.1016/S1464-1895(01)00015-1

Nurmi R, Kuchuk F, Cassell B, Chardac J-L, Marguet P (1996) Horizontal Highlights. Middle East Well Evaluation Review 16:7–25.

Ogden JM (1999) Prospects for building a hydrogen energy infrastructure. Annu Rev Energy Env 24:227–279. doi: 10.1146/annurev.energy.24.1.227

Oldenburg CM (2003) Carbon Dioxide as Cushion Gas for Natural Gas Storage. Energy & Fuels 17:240–246. doi: 10.1021/ef020162b

Oldenburg CM (2006) Joule-Thomson cooling due to CO_2 injection into natural gas reservoirs. In: PROCEEDINGS, TOUGH Symposium 2006 Lawrence Berkeley National Laboratory, Berkeley, May 15–17, 2006

Oldenburg CM (2007) Joule-Thomson cooling due to CO_2 injection into natural gas reservoirs. Energy Convers Manag 48:1808–1815. doi: 10.1016/j.enconman.2007.01.010

Oldenburg CM, Pan L (2013) Porous Media Compressed-Air Energy Storage (PM-CAES): Theory and Simulation of the Coupled Wellbore-Reservoir System. Transp Porous Media 97:201–221. doi: 10.1007/s11242-012-0118-6

Oldenburg CM, Webb SW, Pruess K, Moridis GJ (2004) Mixing of stably stratified gases in subsurface reservoirs: A comparison of diffusion models. Transp Porous Media 54:323–334. doi: 10.1023/B:TIPM.0000003748.74155.48

Onaisi A, Samier P, Koutsabeloulis N, Longuemara P (2002) Management of Stress Sensitive Reservoirs Using Two Coupled Stress-Reservoir Simulation Tools: ECL2VIS and ATH2VIS Proceedings of Abu Dhabi International Petroleum Exhibition and Conference 1–13. doi: 10.2523/78512-MS

Operto S, Miniussi A, Brossier R, Combe L, Métivier L, Monteiller V, Ribodetti A, Virieux J (2015) Efficient 3-D frequency-domain mono-parameter full-waveform inversion of ocean-bottom cable data: application to Valhall in the visco-acoustic vertical transverse isotropic approximation. Geophys J Int 202:1362–1391. doi: 10.1093/gji/ggv226

Orlic B (2016) Geomechanical effects of CO_2 storage in depleted gas reservoirs in the Netherlands: Inferences from feasibility studies and comparison with aquifer storage. J Rock Mech Geotech Eng 8:846–859. doi: 10.1016/j.jrmge.2016.07.003

Panfilov M (2010) Underground Storage of Hydrogen: In Situ Self-Organisation and Methane Generation. Transp Porous Media 85:841–865. doi: 10.1007/s11242-010-9595-7

Paterson L (1983) The implications of fingering in underground hydrogen storage. Int J Hydrogen Energy 8:53–59. doi: 10.1016/0360-3199(83)90035-6

Pfeiffer WT, al Hagrey SA, Köhn D, Rabbel W, Bauer S (2016) Porous media hydrogen storage at a synthetic, heterogeneous field site: numerical simulation of storage operation and geophysical monitoring. Environ Earth Sci. doi: 10.1007/s12665-016-5958-x

Pfeiffer WT, Bauer S (2015) Subsurface Porous Media Hydrogen Storage - Scenario Development and Simulation. Energy Procedia 76:565–572. doi: 10.1016/j.egypro.2015.07.872

Pickard WF, Shen AQ, Hansing NJ (2009) Parking the power: Strategies and physical limitations for bulk energy storage in supply-demand matching on a grid whose input power is provided by intermittent sources. Renew Sustain Energy Rev 13:1934–1945. doi: 10.1016/j.rser.2009.03.002

Plaat H (2009) Underground gas storage: Why and how. Geol Soc London, Spec Publ 313:25–37. doi: 10.1144/SP313.4

Pollok L, Gast S, Hölzner M, Fleig S, Hammer J, Riesenberg C, von Goerne G (2015) Projekt „InSpEE " – Speicherpotenzial für erneuerbare Energien (CAES & H_2). Einblicke in das Inventar norddeutscher Salzstrukturen. In: 79. Tagung der Arbeitsgemeinschaft Norddeutscher Geologen. Landesamt für Umwelt, Naturschutz und Geologie Mecklenburg-Vorpommern, Güstrow, Germany, pp 129–130

Pruess K (2004) The TOUGH Codes—A Family of Simulation Tools for Multiphase Flow and Transport Processes in Permeable Media. Vadose Zone Journal 3:738. doi: 10.2136/vzj2004.0738

Queißer M, Singh SC (2013a) Localizing CO_2 at Sleipner — Seismic images versus P-wave velocities from waveform inversion. Geophysics 78:B131-B146. doi: 10.1190/geo2012-0216.1

Queißer M, Singh SC (2013b) Full waveform inversion in the time lapse mode applied to CO_2 storage at Sleipner. Geophys Prospect 61:537–555. doi: 10.1111/j.1365-2478.2012.01072.x

Reinhold K, Müller C (2011) Storage potential in the deeper subsurface - Overview and results from the

project Storage Catalogue of Germany. Schriftenreihe der Deutschen Gesellschaft für Geowissenschaften 74:9–27. doi: 10.1127/sdgg/74/2011/9

Reitenbach V, Ganzer L, Albrecht D, Hagemann B (2015) Influence of added hydrogen on underground gas storage: a review of key issues. Environ Earth Sci 73:6927–6937. doi: 10.1007/s12665-015-4176-2

Renard P, de Marsily G (1997) Calculating equivalent permeability: a review. Adv Water Resour 20:253–278. doi: 10.1016/S0309-1708(96)00050-4

Ringrose P, Bentley M (2015) Reservoir Model Design. Springer, Dordrecht

Roberts D V. (1996) Sustainable development and the use of underground space. Tunnelling and Underground Space Technology 11:383–390. doi: 10.1016/S0886-7798(96)00039-9

Röckel T, Lempp C (2003) Der spannungszustand im Norddeutschen Becken. Erdöl Erdgas Kohle 119:73–80

Rönkä K, Ritola J, Rauhala K (1998) Underground space in land-use planning. Tunnelling and Underground Space Technology 13:39–49. doi: 10.1016/S0886-7798(98)00029-7

Rutqvist J (2012) The geomechanics of CO_2 storage in deep sedimentary formations. Geotech Geol Eng 30:525–551. doi: 10.1007/s10706-011-9491-0

Rutqvist J, Birkholzer JT, Tsang CF (2008) Coupled reservoir-geomechanical analysis of the potential for tensile and shear failure associated with CO_2 injection in multilayered reservoir-caprock systems. Int J Rock Mech Min Sci 45:132–143. doi: 10.1016/j.ijrmms.2007.04.006

Rutqvist J, Wu Y, Tsang C, Bodvarsson G (2002) A modeling approach for analysis of coupled multiphase fluid flow , heat transfer , and deformation in fractured porous rock. Int J Rock Mech Min Sci 39:429–442

Schäfer D, Schlenz B, Dahmke A (2004) Evaluation of exploration and monitoring methods for verification of natural attenuation using the virtual aquifer approach. Biodegradation 15:453–465. doi: 10.1023/B:BIOD.0000044600.81216.00

Schäfer F, Walter L, Class H, Müller C (2012) The regional pressure impact of CO_2 storage: A showcase study from the North German Basin. Environ Earth Sci 65:2037–2049. doi: 10.1007/s12665-011-1184-8

Schiebahn S, Grube T, Robinius M, Tietze V, Kumar B, Stolten D (2015) Power to gas: Technological overview, systems analysis and economic assessment for a case study in Germany. Int J Hydrogen Energy 40:4285–4294. doi: 10.1016/j.ijhydene.2015.01.123

Schlichtenmeyer M, Klafki M (2016) Differences and challenges in salt cavern design for hydrogen, air and natural gas. In: Wuttke F, Bauer S, Sánchez M (eds) Energy Geotechnics: Proceedings of the 1st International Conference on Energy Geotechnics. CRC Press, pp 65–69

Schlumberger (2015) ECLIPSE v2015.2 - Technical Description

Schmidt R, Wagner W (1985) A new form of the equation of state for pure substances and its application to oxygen. Fluid Phase Equilib 19:175–200

Schmidt S, Plonka C, Götze H-J, Lahmeyer B (2011) Hybrid modelling of gravity, gravity gradients and magnetic fields. Geophys Prospect 59:1046–1051. doi: 10.1111/j.1365-2478.2011.00999.x

Schowalter TT (1979) Mechanics of secondary hydrocarbon migration and entrapment. Am Assoc Pet Geol Bull 5:723–760. doi: 10.1306/2F9182CA-16CE-11D7-8645000102C1865D

Schulze F, Kleimeyer F, Schöne R, Westphal I, Jannssen G, Bartel S, Seiffert S (2015) Unterirdische Raumplanung – Vorschläge des Umweltschutzes zur Verbesserung der über- und untertägigen Informationsgrundlagen, zur Ausgestaltung des Planungsinstrumentariums und zur nachhaltigen Lösung von Nutzungskonflikten - Teilvorhaben 2: planerische und rechtliche Aspekte. Umweltbundesamt, Dessau-Roßlau

Sedlacek R (1999) Untertage Erdgasspeicherung in Deutschland. Erdöl Erdgas Kohle 114:526–535

Setzmann U, Wagner W (1991) A New Equation of State and Tables of Thermodynamic Properties for Methane Covering the Range from the Melting Line to 625 K at Pressures up to 1000 MPa. J Phys Chem Ref Data 20:1061–1155

Shao H, Kosakowski G, Berner U, Kulik DA, Mäder U, Kolditz O (2013) Reactive transport modeling of the clogging process at Maqarin natural analogue site. Phys Chem Earth 64:21–31. doi: 10.1016/j.pce.2013.01.002

Singh A, Delfs JO, Görke UJ, Kolditz O (2014) Toward physical aspects affecting a possible leakage of geologically stored CO_2 into the shallow subsurface. Acta Geotech 9:81–86. doi: 10.1007/s11440-013-0237-4

Singh AK, Baumann G, Henninges J, Goerke U-J, Kolditz O (2012) Numerical analysis of thermal effects during carbon dioxide injection with enhanced gas recovery: a theoretical case study for the Altmark gas field. Environ Earth Sci 67:497–509. doi: 10.1007/s12665-012-1689-9

Sirgue L, Barkved OI, Dellinger J, Etgen J, Albertin U, Kommedal JH (2010) Full waveform inversion: the next leap forward in imaging at Valhall. First Break 28:65–70. doi: 10.3997/1365-2397.2010012

Smolinka T, Günther M, Garche J (2010) Stand und Entwicklungspotenzial der Wasserelektrolyse zur Herstellung von Wasserstoff aus regenerativen Energien. NOW-Studie 2010, 53p

Sørensen B (1975) Energy and resources. Science 189:255–260.doi:10.1126/science.189.4199.255

Sørensen B, Petersen AH, Juhl C, Ravn H, Søndergren C, Simonsen P, Jørgensen K, Nielsen LH, Larsen H V., Morthorst PE, Schleisner L, Sørensen F, Pedersen TE (2004) Hydrogen as an energy carrier: Scenarios for future use of hydrogen in the Danish energy system. Int J Hydrogen Energy 29:23–32. doi: 10.1016/S0360-3199(03)00049-1

Span R, Lemmon EW, Jacobsen RT, Wagner W, Yokozeki A (2000) A Reference Equation of State for the Thermodynamic Properties of Nitrogen for Temperatures from 63.151 to 1000 K and Pressures to 2200 MPa. J Phys Chem Ref Data 29:1361–1433

Span R, Wagner W (1996) A New Equation of State for Carbon Dioxide Covering the Fluid Region from the Triple-Point Temperature to 1100 K at Pressures up to 800 MPa. J Phys Chem Ref Data 25:1509–1595

Steinke F, Wolfrum P, Hoffmann C (2013) Grid vs. storage in a 100% renewable Europe. Renew Energy 50:826–832. doi: 10.1016/j.renene.2012.07.044

Sterner M, Stadler I (2014) Energiespeicher. Springer, Berlin

Stummer P, Maurer H, Green AG (2004) Experimental design: Electrical resistivity data sets that provide optimum subsurface information. Geophysics 69:120–139. doi: 10.1190/1.1649381

Takasaki H, Chikahisa H, Yuasa Y (2000) Planning and mapping of subsurface space in Japan. Tunn Undergr Sp Technol 15:287–301. doi: 10.1016/S0886-7798(00)00057-2

Taku Ide S, Jessen K, Orr FM (2007) Storage of CO_2 in saline aquifers: Effects of gravity, viscous, and capillary forces on amount and timing of trapping. Int J Greenh Gas Control 1:481–491. doi: 10.1016/S1750-5836(07)00091-6

Taron J, Elsworth D (2009) Thermal-hydrologic-mechanical-chemical processes in the evolution of engineered geothermal reservoirs. Int J Rock Mech Min Sci 46:855–864. doi: 10.1016/j.ijrmms.2009.01.007

Teatini P, Castelletto N, Ferronato M, Gambolati G, Janna C, Cairo E, Marzorati D, Colombo D, Ferretti A, Bagliani A, Bottazzi F (2011) Geomechanical response to seasonal gas storage in depleted reservoirs: A case study in the Po River basin, Italy. J Geophys Res Earth Surf 116:1–21. doi: 10.1029/2010JF001793

Tenthorey E, Vidal-Gilbert S, Backé G, Puspitasari R, John Pallikathekathil Z, Maney B, Dewhurst D (2013) Modelling the geomechanics of gas storage: A case study from the Iona gas field, Australia. Int J Greenh Gas Control 13:138–148. doi: 10.1016/j.ijggc.2012.12.009

Thibeau S, Bachu S, Birkholzer J, Holloway S, Neele F, Zhou Q (2014) Using pressure and volumetric approaches to estimate CO_2 storage capacity in deep saline aquifers. Energy Procedia 63:5294–5304. doi: 10.1016/j.egypro.2014.11.560

Ursúa A, Gandia LM, Sanchis P (2012) Hydrogen Production From Water Electrolysis: Current Status and Future Trends. Proc IEEE 100:410–426. doi: 10.1109/JPROC.2011.2156750

VDI (2010) Thermal use of the underground: fundamentals, approvals, environmental aspects. VDI4640. Verein Deutscher Ingenieure, Düsseldorf

Wagner W, Cooper JR, Dittmann A, Kijima J, Kretzschmar H-J, Kruse A, Mareš R, Oguchi K, Sato H, Stöcker I, Šifner O, Takaishi Y, Tanishita I, Trübenbach J, Willkommen T (2000) The IAPWS Industrial Formulation 1997 for the Thermodynamic Properties of Water and Steam. J Eng Gas Turbines Power 122:150. doi: 10.1115/1.483186

Wang B, Bauer S (2016) Converting heterogeneous complex geological models to consistent finite element models: methods, development, and application to deep geothermal reservoir operation. Environ Earth Sci 75:1349. doi: 10.1007/s12665-016-6138-8

Wang X, Economides M (2009) Advanced natural gas engineering. Gulf Publishing Company, Houston

White J a., Chiaramonte L, Ezzedine S, Foxall W, Hao Y, Ramirez A, McNab W (2014) Geomechanical behavior of the reservoir and caprock system at the In Salah CO_2 storage project. Proceedings of the National Academy of Sciences of the United States of America 111:8747–8752. doi: 10.1073/pnas.1316465111

Wollenweber J, Alles S, Busch A, Krooss BM, Stanjek H, Littke R (2010) Experimental investigation of the CO_2 sealing efficiency of caprocks. Int J Greenh Gas Control 4:231–241. doi: 10.1016/j.ijggc.2010.01.003

Xie M, Bauer S, Kolditz O, Nowak T, Shao H (2006) Numerical simulation of reactive processes in an experiment with partially saturated bentonite. J Contam Hydrol 83:122–147. doi: 10.1016/j.jconhyd.2005.11.003

Young CL (1981) IUPAC Solubility Data Series 5/6: Hydrogen and Deuterium. Pergamon Press, Oxford

Zemke J, Stöwer M, Borgmeier M (2005) Injection of Brine from Cavern Leaching into Deep Saline Aquifers: Long-Term Experiences in Modeling and Reservoir Survey. Developments in Water Science 52:403–412. doi: 10.1016/S0167-5648(05)52028-8

Zhang F, Juhlin C, Cosma C, Tryggvason A, Pratt RG (2012) Cross-well seismic waveform tomography for monitoring CO_2 injection: a case study from the Ketzin Site, Germany. Geophys J Int 189:629–646. doi: 10.1111/j.1365-246X.2012.05375.x

Zhang F, Juhlin C, Ivandic M, Lüth S (2013) Application of seismic full waveform inversion to monitor CO_2 injection: modelling and a real data example from the Ketzin site, Germany. Geophys Prospect 61:284–299. doi: 10.1111/1365-2478.12021

Zhao C, Hobbs BE, Ord A, Hornby P, Peng S, Liu L (2007) Mineral precipitation associated with vertical fault zones: the interaction of solute advection, diffusion and chemical kinetics. Geofluids 7:3–18. doi: 10.1111/j.1468-8123.2006.00156.x

Zoback MD (2010) Reservoir geomechanics. Cambridge University Press, Cambridge

ENCLOSED PUBLICATIONS

Chapter 3

Pfeiffer WT, Graupner B, Bauer S (2016) The coupled non-isothermal, multiphase-multicomponent flow and reactive transport simulator OpenGeoSys-ECLIPSE for porous media gas storage. Environ Earth Sci 75:1347. doi: 10.1007/s12665-016-6168-2

Abstract
Numerical simulations are a viable tool to gain insights into complex coupled THMC processes prevailing in many geoscientific applications. In this work, a coupling approach for OpenGeoSys and ECLIPSE is presented, which combines the multiphase flow simulations of ECLIPSE with heat and reactive geochemical component transport simulations of OpenGeoSys. The coupled simulator is capable of dealing with multiphase-multicomponent systems with no specific limitations regarding the components used. Furthermore, thermal effects like the Joule-Thomson effect and geochemical feedback on fluid flow and mass transport are accounted for by the coupled simulator. The developed coupled code is validated in a series of benchmarks. It is found that the results of the coupled simulator are in very close agreement with those obtained from the reference simulations with the relative errors being smaller than 0.00001 %, 0.0002 % and 0.003 % for phase pressures, saturations and component concentrations, respectively. Validation of the thermal coupling of the simulators shows the same good agreement, if no thermal feedback on fluid flow is considered with a maximum relative error of 0.0015 %. Including thermal feedback on fluid flow shows increased relative differences of up to 0.3 % due to the slightly different equations of states used in the simulators. Given the good accuracy of the validation runs, the coupled code can thus now be applied for reservoir simulations of coupled processes occurring in the subsurface.

Chapter 4

Pfeiffer WT, Beyer C, Bauer S (2017) Hydrogen storage in a heterogeneous sandstone formation – Dimensioning and induced hydraulic effects. Petroleum Geoscience doi: 10.1144/petgeo2016-050

Abstract
Large-scale energy storage in the geological subsurface (e.g. by storing hydrogen gas) may help to mitigate effects of a fluctuating energy production arising from the extensive use of renewable energy sources. The applicability of hydrogen ($H_{2)}$ storage in a porous sandstone formation is investigated by defining a usage scenario and a subsequent numerical simulation of a storage operation at an existing anticlinal structure in the North German Basin. A facies modelling approach is used to obtain 25 heterogeneous and realistic parameter sets. The storage operation consists of the initial filling with nitrogen used as cushion gas, the initial filling with H_2, and six withdrawal periods with successive refilling and shut-in periods. It is found that, on average, the storage can sustain a continuous power output of 245 MW for 1 week when using five storage wells, while peak performance can be as high as 363 MW, indicating that the storage is mainly limited by the achievable extraction rates. The median of the maximum pressure perturbation caused by this storage is around 3 bars and can be observed at a distance of 5 km from the wells.

Chapter 5

Pfeiffer WT, al Hagrey SA, Köhn D, Rabbel W, Bauer S (2016) Porous media hydrogen storage at a synthetic, heterogeneous field site: numerical simulation of storage operation and geophysical monitoring. Environ Earth Sci 75:1177. doi: 10.1007/s12665-016-5958-x

Abstract

Large-scale energy storage such as porous media hydrogen storage will be required to mitigate shortages originating from fluctuating power production if renewables dominate the total supply. In order to assess the applicability of this storage option, a possible usage scenario is defined for an existing anticlinal structure in the North German Basin and the storage operation is numerically simulated. A heterogeneous and realistic parameter distribution is generated by a facies modelling approach. The storage operation, which is performed using five wells, consists of an initial filling of the storage with nitrogen used as cushion gas and hydrogen as well as several weeklong withdrawal periods each followed by a refill and a shut-in period. Storage performance increases with the number of storage cycles and a total of 29 million m3 of hydrogen gas at surface conditions can be produced in the long term, equating to 186,000 GJ of energy when assuming a re-electrification efficiency of 60 %. In addition to downhole pressure monitoring geophysical techniques such as seismic full waveform inversion (FWI), electrical resistivity tomography (ERT) and gravity methods can be used for site monitoring, if their individual detecting capabilities are sufficient. Investigation of the storage scenario by virtual application of these methods shows that FWI and ERT can be used to map the thin gas phase distribution in this heterogeneous formation with the individual methods conforming each other. However, a high spatial density of receivers in a crosswell geometry with less than 500 m distance between the observation wells is required for this. Gravity mapping also shows anomalies indicating mass changes caused by the storage operation. However, monitoring the filling state of this hydrogen storage site is not possible.